Structure of Brightest Cluster Galaxies and Intracluster Light

Matthias Kluge

München 2020

Structure of Brightest Cluster Galaxies and Intracluster Light

Matthias Kluge

Dissertation der Fakultät für Physik
Dissertation of the Faculty of Physics

der Ludwig-Maximilians-Universität München
at the Ludwig Maximilian University of Munich

für den Grad des
for the degree of

Doctor rerum naturalium

vorgelegt von Matthias Kluge
presented by

Munich, 03.03.2020

1^{st} Evaluator: Prof. Dr. Ralf Bender
2^{nd} Evaluator: Prof. Dr. Harald Lesch
Date of the oral exam: 13.05.2020

Zusammenfassung

Der erste Teil dieser Arbeit stellt die Ergebnisse einer photometrischen Beobachtungsstudie von hellsten Clustergalaxien (BCGs) vor, die speziell auf das sie umgebende Intracluster-Licht (ICL) mit geringer Oberflächenhelligkeit (SB) abzielt. Es handelt sich hierbei um die bisher tiefste und größte Untersuchung von 170 lokalen ($z \lesssim 0.08$) Galaxienclustern auf der Nordhemisphäre. Die Beobachtungen wurden mit der Großfeldkamera (WWFI) am 2m-Teleskop des Wendelstein Observatoriums durchgeführt.

Die Grenzhelligkeit der gemessenen SB-Profile liegt bei $SB = 30\ g'$ mag arcsec^{-2}, ungefähr 2000 mal leuchtschwächer als der Himmel in einer dunklen, mondlosen Nacht. Daher ist eine sorgfältige Kalibrierung entscheidend, um Systematiken auszuschließen. Streulichtinduzierte Inhomogenitäten des Hintergrundes werden durch weites Bewegen des Teleskops zwischen den Aufnahmen und Subtraktion von Nachthimmelsmodellen auf SBs von weniger als $\Delta SB > 31\ g'$ mag arcsec^{-2} reduziert. Die ausgedehnten Flügel der Punktspreizfunktion heller Vordergrundsterne werden subtrahiert, Variationen des Kamerasensor-Nullniveaus werden korrigiert und Ladungspersistenz wird maskiert. Erstmals wird auch der Verbreiterungseffekt der Punktspreizfunktion bestimmt und bis hin zu den schwächsten SBs korrigiert.

Vor 23% der Galaxiencluster wurden durch galaktischen Zirrus verursachte, verbleibende Inhomogenitäten des Hintergrundes detektiert, die heller sind als $SB_\sigma < 27{,}6$ g' mag arcsec^{-2}. Das große Gesichtsfeld des WWFI ermöglicht jedoch die Unterscheidung zwischen Akkretionsmerkmalen und galaktischem Zirrus. Erstere wurden in Form von Gezeitenströmen in 22% der BCGs gefunden, schalenförmige Strukturen in 9,4%, Mehrfachkerne in 47% und 7% der Cluster enthalten zwei BCGs.

Mithilfe von Archivaufnahmen des Hubble-Weltraumteleskops und entfalteten WWFI Aufnahmen wird die räumliche Auflösung in den inneren Regionen verbessert. Die SB-Profile von 71% der BCG+ICL-Systeme lassen sich gut durch eine einzige Sérsic (SS)-Funktion beschrieben. Die restlichen 29% benötigen eine doppelte Sérsic (DS)-Funktion. SS-BCGs besitzen symmetrischere Isophotenformen und weniger detektierte Akkretionsmerkmale als DS-BCGs und sie weisen eine etwas relaxiertere Morphologie auf. DS-BCGs beherbergen $S2 = 52 \pm 21\%$ ihres gesamten Lichtes in der äußeren Sérsic Komponente. Es gibt eine breite Streuung in den Übergangsradien $r_\times$ zwischen den beiden Sérsic-Komponenten und in den SBs an diesen Übergangsradien $SB(r_\times)$. Die Gesamthelligkeiten der BCG+ICL-Systeme korrelieren nur schwach mit $S2$, $r_\times$ und $SB(r_\times)$. Da BCG+ICL-Systeme derzeit überwiegend in ihren Außenbereichen wachsen, deutet dies darauf hin, dass die äußere Sérsic Komponente vermutlich nicht das dynamisch heiße ICL nachzeichnet.

Die Skalierungsrelationen der BCGs unterscheiden sich deutlich von denen normaler elliptischer Galaxien, was höchstwahrscheinlich auf ihre ununterscheidbare Einbettung in das ICL zurückzuführen ist. Die Gesamthelligkeiten und Radien der ausgedehntesten BCG+ICL-Systeme sind vergleichbar mit denen ganzer Galaxiencluster. Im Durchschnitt ist das ICL, gemessen an Positionswinkel und Zentrierung, besser als die BCG an ihrem Cluster ausgerichtet. Dies qualifiziert das ICL als einen potentiellen Marker der Dunklen Materie. Die gefundenen, positiven Korrelationen zwischen der BCG+ICL-Helligkeit und der Clustermasse, dem Clusterradius, der Anzahl an Satellitengalaxien und deren integrierter Helligkeit bestätigen, dass das BCG/ICL-Wachstum tatsächlich an das Clusterwachstum gekoppelt ist.

Die Lichtmenge in der ICL-Komponente wird anhand eines Gesamthelligkeitsschwellenwertes, SB-Schwellenwerten und Profilzerlegungen abgeschätzt. Die Gültigkeit der Schlussfolgerungen über die Eigenschaften des ICL beeinflusst dies nicht.

Der zweite Teil dieser Arbeit dokumentiert die WWFI-Datenreduktionspipeline, die im Zuge dieser Dissertation entwickelt wurde und zur Verarbeitung von Beobachtungsrohdaten dient. Sie ist für die Photometrie ausgedehnter Objekte mit geringer SB optimiert und kann darüber hinaus auch zur Aufbereitung beliebiger WWFI-Bilder verwendet werden. Diese Dokumentation enthält detaillierte technische Beschreibungen aller grundlegenden und weiterführenden Funktionen und soll als Referenz und Anleitung für die Pipeline dienen.

Abstract

The first part of this thesis presents the results of a photometric survey of Brightest Cluster Galaxies (BCGs), specifically targeting their low-surface-brightness Intracluster Light (ICL) outskirts. It is the deepest and largest sample of galaxy clusters to this date, consisting of 170 local ($z \lesssim 0.08$) clusters in the northern hemisphere. The observations have been obtained with the Wendelstein Telescope Wide Field Imager (WWFI).

Surface brightness (SB) profiles are measured down to ∼2000 times fainter levels than the sky brightness in a dark, moonless night. Precise calibration is crucial here to exclude systematics. Background inhomogeneities induced by scattered light are reduced down to $\Delta SB > 31$ g' mag arcsec^{-2} by large dithering and subtraction of night-sky flats. The extended wings of bright foreground stars are subtracted, relative bias offsets between the readout ports of the CCDs are corrected, and charge persistence is masked. For the first time, the broadening effect of the point-spread function is determined and corrected down to the faintest SBs.

Residual background inhomogeneities brighter than $SB_\sigma < 27.6$ g' mag arcsec^{-2} caused by galactic cirrus are detected in front of 23% of the clusters. However, the large field of view allows discrimination between accretion signatures and galactic cirrus. I detect accretion signatures in form of tidal streams in 22%, shells in 9.4% and multiple nuclei in 47% of the brightest cluster galaxies (BCGs) and find two BCGs in 7% of the clusters.

Semimajor-axis SB profiles of the BCGs and their surrounding ICL are measured down to a limiting SB of $SB = 30$ g' mag arcsec^{-2}. The spatial resolution in the inner regions is increased by combining the WWFI light profiles with those that we measured from archival Hubble Space Telescope images or deconvolved WWFI images. I find that 71% of the BCG+ICL systems have SB profiles that are well described by a single Sérsic (SS) function, whereas 29% require a double Sérsic (DS) function to obtain a good fit. SS BCGs, having more symmetric isophotal shapes and fewer detected accretion signatures than DS BCGs, appear to have slightly more relaxed morphology than their DS counterparts. Members of the latter type encompass $S2 = 52 \pm 21$% of their total light in the outer Sérsic component. There is a wide scatter in transition radii $r_\times$ between the two Sérsic components and SB at the transition radii $SB(r_\times)$. The integrated brightnesses of the BCG+ICL systems correlate only weakly with $S2$, $r_\times$ and $SB(r_\times)$. That indicates that the outer Sérsic component is unlikely to trace the dynamically hot ICL since BCG+ICL systems grow at present epoch predominantly in their outskirts.

I find that BCGs have scaling relations that differ markedly from those of normal ellipticals, likely due to their indistinguishable embedding in the ICL. The most extended BCG+ICL systems have luminosities and radii comparable to whole clusters. I use different plausible estimates for the ICL component (based on an integrated brightness threshold, SB thresholds and profile decompositions), and find that they do not affect the conclusions about the ICL properties. On average, the ICL seems to be better aligned than the BCG with the host cluster in terms of position angle and centering. That makes it a potential Dark Matter tracer. I find positive correlations between BCG+ICL brightness and cluster mass, cluster radius, cluster richness and integrated satellite brightness, confirming that BCG/ICL growth is indeed coupled with cluster growth.

The second part of this thesis documents the WWFI data reduction pipeline, which I have developed during the course of this PhD thesis project and applied to process the raw observational data. It is optimized for low-SB photometry of extended objects. However, its utility is not limited to that specific science case. It can be used as a standard pipeline to reduce any WWFI images. This documentation provides detailed technical descriptions about all basic and advanced features. It is meant to serve as both a reference and a manual for the pipeline.

Contents

List of Figures

List of Tables

Preamble

Most of the following Part I has been published as Kluge et al. (2019) in ApJS. Additional material are the host cluster properties presented in Chapters 6 and 7.5 and Appendices C, D, E and F, as well as the photometric dissections between the BCGs and ICL in Chapters 7.4 and 8.4 and the discussion on ICL as a Dark Matter tracer in Chapter 8.5. The conclusions in Chapter 9 are extended by those derived from the not yet published material.

For the published article, I have exclusively performed the data reduction and analysis, and developed the data reduction pipeline, which is documented in detail in Part II. Moreover, most of the scientific analysis and interpretation were done by myself. Contributions from co-authors are:

- Bianca Neureiter provided the calibrated comparison dataset of A2589 (in Fig. 5.4) obtained with the Wendelstein 40cm telescope. She also tested the masking algorithm in Chapter 19 and developed the background subtraction method described in Sec. 18.10.
- Arno Riffeser helped improving the early code for the WWFI data reduction pipeline for which Daniel Grün laid the foundations. He also engaged in technical discussions.
- Ralf Bender provided the isophote fitting tools and guidance throughout the project.
- Claus Gössl contributed through maintenance of the WWFI and technical discussions.
- Ulrich Hopp contributed through scientific discussions.
- Michael Schmidt and Christoph Ries have done most of the Wendelstein 2m Telescope observations.
- Noah Brosch provided the raw comparison dataset of A1177 (in Fig. 5.4), obtained with the Jay Baum Rich 70cm telescope.

The first five mentioned co-authors have further contributed by proofreading the paper.

Part I

Structure of Brightest Cluster Galaxies and Intracluster Light

Chapter 1

Introduction

Following the first detection of an "extended mass of luminous intergalactic matter of very low surface brightness" in the Coma cluster (Zwicky, 1951), numerous early studies have confirmed that "subgroupings of galaxies in clusters [...] often share a common outer envelope several hundred kiloparsecs in diameter" (Kormendy & Bahcall 1974; also Arp & Bertola 1971; Welch & Sastry 1971; Thuan & Kormendy 1977). A similar envelope was discovered to surround the Virgo cluster galaxy M87 (Arp & Bertola 1969; de Vaucouleurs 1969).

Today, we know that many galaxy clusters are populated by an outstandingly bright and extended elliptical galaxy near the geometric and kinematic cluster center. They are referred to as brightest cluster galaxies (BCGs). The definition of this galaxy type is similar to the historic definition of cD galaxies (Matthews et al. 1964; Morgan & Lesh 1965). cD galaxies form a subset of BCGs that are surrounded by an extended, diffuse stellar envelope. That envelope is part of the ex-situ stellar population that was accreted during mass assembly (Cooper et al., 2013, 2015; Pillepich et al., 2018). It is probably mixed with the intracluster light (ICL) which is kinematically unbound from the BCG. In this work, we do not distinguish between stellar envelope, stellar halo, and ICL because they are probably indistinguishable with photometric data alone. Oegerle & Hill (2001) classify 20% of BCGs as cD galaxies. The issue with this subset definition is that the detection of an existing envelope depends on the depth of the observation. Moreover, large samples of BCGs are Gaussian distributed in their brightnesses (Postman & Lauer 1995; Hansen et al. 2009; Donzelli et al. 2011; Lauer et al. 2014), which implies that the transition between cD and non-cD BCGs is continuous. Hence, it makes sense to study BCGs as a generalized class of galaxies.

Contrary to what the name suggests, a BCG is in our adopted definition not necessarily the brightest galaxy in a cluster: it must also lie close to the cluster center as traced by the satellite galaxy distribution or the intracluster medium. Between 20% and 40% of central galaxies are not the brightest galaxy in their host clusters (Skibba et al. 2011; Hoshino et al. 2015). A famous example is M87 in the Virgo cluster. The brightest galaxy is M49, but it is located far off the cluster center. M87 is (in projection) near the X-ray gas emission peak (e.g., Kellogg et al. 1971), which is a good tracer for the potential minimum of the cluster. Moreover, the rising velocity dispersion profile of the surrounding planetary nebulae is steeper for M87 (Longobardi et al., 2018) than for M49 (Hartke et al., 2018), showing that intracluster planetary nebulae are more centered on M87 than on M49. The velocity dispersion profile of the globular clusters rises toward the outskirts of M87 (Côté et al., 2001), but it falls toward

the outskirts of M49 (Sharples et al., 1998), showing that the intracluster globular clusters are also more centered on M87. All of the arguments above agree that M87 qualifies better as the BCG of the Virgo cluster in our adopted definition.

Several methods have been developed and applied to dissect the ICL from the BCG. Empirical methods are driven by photometric observations. They encompass surface brightness cuts (Feldmeier et al. 2004; Burke et al. 2012) and the fitting of double de Vaucouleurs (1948), double Sérsic (1968) or similar functions to the SB profiles (Gonzalez et al. 2005; Seigar et al. 2007; Donzelli et al. 2011) or fitting only the central part and defining the excess luminosity in the outskirts as ICL (Schombert 1986; Zibetti et al. 2005). A different approach is to consider stellar velocities. It is motivated by the rising radial velocity dispersion profiles that approach the cluster dispersion, i.e., the relative velocities of the cluster galaxies (Ventimiglia et al. 2010; Toledo et al. 2011; Arnaboldi et al. 2012; Melnick et al. 2012; Murphy et al. 2014; Bender et al. 2015; Barbosa et al. 2018; Spiniello et al. 2018). The ICL is hereby the dynamically hot component that is kinematically controlled by the gravitational potential of the whole cluster, i.e., unbound from the BCG. Bender et al. (2015) have applied a simplified approach to observational data of NGC 6166 by assuming constant velocity dispersions for both components.

In a more complex form, the kinematic approach is often applied in numerical simulations where full phase-space information of the particles is accessible. A BCG+ICL system is decomposed by fitting a double Maxwell distribution to the particle velocities. The component with the higher characteristic velocity is called the diffuse stellar component (DSC, e.g., Dolag et al. 2010). Contrary to expectation, the "photometrically" determined ICL does not necessarily resemble the DSC (Puchwein et al. 2010; Rudick et al. 2011; Cui et al. 2014; Remus et al. 2017). A different set of components alternative to the bound / unbound criterion are in-situ formed / accreted stars. The in-situ stars were formed directly from the cluster cooling flow whereas accreted stars have been stripped from satellite galaxies. Cooper et al. (2015) showed that in their used N-body simulations, 80–95% of stellar mass found below $SB \gtrsim 26.5$ V mag arcsec^{-2} is associated with accreted stars. The question whether the outer photometric component traces the DSC and/or the accreted stellar mass or none of them is a matter of on-going research and will be discussed in this paper.

The currently widely accepted two-phase formation scenario (e.g., Contini et al. 2014, 2018) states that the BCG formed first by galactic mergers and the ICL was accreted afterward by a mixture of (1) galaxy harassment, that is, high-velocity encounters between satellite galaxies (Moore et al., 1996); (2) tidal stripping induced by effects of dynamical friction against the whole cluster potential (Byrd & Valtonen 1990; Gnedin 2003); and (3) preprocessing in smaller groups (Mihos 2004; Rudick et al. 2006). Remnants of these violent processes are predicted by simulations to occur at low surface brightnesses (SBs), mostly below $SB \gtrsim 29$ g' mag arcsec^{-2} (Rudick et al. 2009; Puchwein et al. 2010; Harris et al. 2017; Mancillas et al. 2019), and are confirmed by observations (e.g., Arnaboldi et al. 2012; Kormendy & Bender 2012; Iodice et al. 2017; Mihos et al. 2017). We refer to these remnants as accretion signatures.

Tension between simulations and observations persists regarding the amount of ICL. Numerical simulations generally reproduce too much ICL (Puchwein et al. 2010; Ragone-Figueroa et al. 2013), especially for very massive clusters (Cooper et al., 2015).

The build-up, shape, and substructure of BCG+ICL light profiles, as well as the types and abundances of accretion signatures, are sensitive probes for the dynamical evolution of galaxy clusters (e.g., Puchwein et al. 2010; Cui et al. 2014). To constrain formation models,

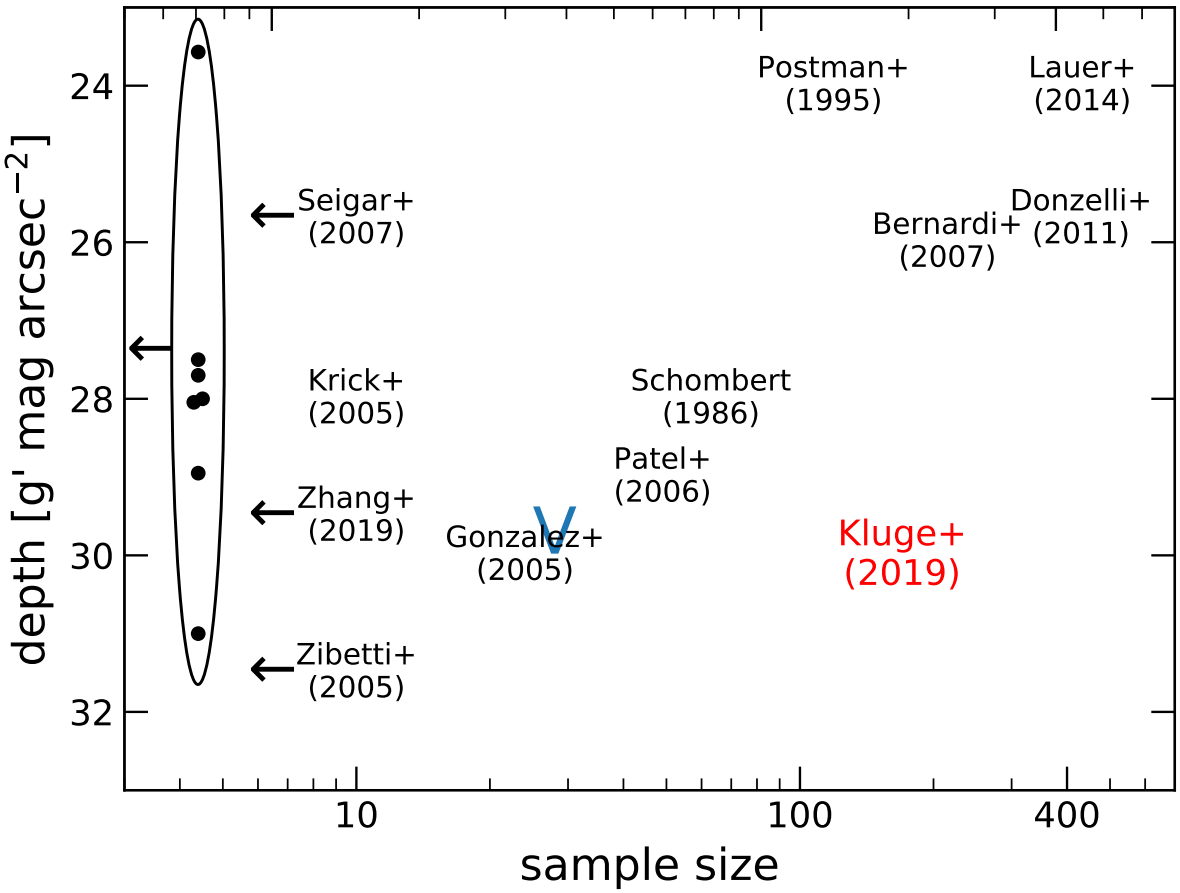

Figure 1.1: Overview of photometric low-redshift BCG surveys: Seigar et al. (2007), Krick & Bernstein (2005), Zhang et al. (2019), Zibetti et al. (2005), Gonzalez et al. (2005), Patel et al. (2006), Schombert (1986), Postman & Lauer (1995), Bernardi et al. (2007), Lauer et al. (2014), Donzelli et al. (2011). The so-far published VST survey of Early-type GAlaxieS (VEGAS) sample is shown by a blue "V" (Capaccioli et al. 2015, Spavone et al. (2017), Spavone et al. (2018), Cattapan et al. (2019)). The dots embedded in the ellipse represent single- or double-target BCGs observations. From top to bottom: Jorgensen et al. (1992), Bender et al. (2015), Ferrarese et al. (2012), Feldmeier et al. (2002), Kormendy et al. (2009), Mihos et al. (2005), Iodice et al. (2016). The arrows indicate that the sample size is smaller than the label position in the plot. Our survey (red) populates an unexplored parameter space region in sample size and depth.

especially in the faint outskirts of BCGs, a large sample of BCGs with deep light profiles is needed. Fig. 1.1 illustrates that so far, either the studied sample was relatively small (Gonzalez et al. 2005; Krick & Bernstein 2005; Patel et al. 2006; Seigar et al. 2007) or the surface brightness at the transition radius between the two photometric components of double Sérsic (DS) BCGs is mostly below the limiting magnitude of the surveys (Postman & Lauer 1995; Bernardi et al. 2007; Donzelli et al. 2011; Lauer et al. 2014). In this paper, we present a study that fulfills both criteria.

This paper is organized as follows. In section 2, we present our sample and selection criteria. The data and data reduction are described in section 3 with a detailed documentation of the data reduction pipeline in section 10. Our methods to measure and combine the surface brightness profiles are described in section 4. Sections 3 and 4 and especially 10 are dedicated to readers who are interested in the image processing techniques necessary for deep imaging. An extensive error analysis is given in section 5. The procedures for measuring host cluster properties are described in chapter 6. We present our results in section 7. They are discussed in section 8 and summarized in section 9.

Throughout the paper, we assume a flat cosmology with $H_0 = 69.6$ km s^{-1} Mpc^{-1} and $\Omega_\mathrm{m} = 0.286$. Distances and angular scales were calculated using the web tool from Wright (2006). Virgo infall is not considered. If not stated otherwise, then three types of flux corrections were applied: (1) dust extinction using the maps from Schlafly & Finkbeiner (2011), (2) K corrections following Chilingarian et al. (2010) and Chilingarian & Zolotukhin (2012), and (3) cosmic $(1 + z)^4$ dimming. Magnitudes are always given in the AB system.

Chapter 2

The survey

2.1 Sample selection

Our sample is based on the Abell–Corwin–Olowin (ACO) catalog (Abell et al., 1989). It contains 4073 rich galaxy clusters, out of which we selected 141 by the following criteria:

1. redshift $z \lesssim 0.08$,
2. galactic latitude $|b| > 13.5°$,
3. decl. $> +5°$,
4. no bright stars nearby.

Regarding the fourth criterion, a stellar brightness limit in the range $5 < g < 9$, where g is the stellar magnitude in the g-band, is applied, depending on the projected distance $2.6° < d < 0.08°$ from the BCG. Additionally, we allow 15 exceptions from the redshift constraint because of preobservational misidentification of the BCG and one exception from the decl. constraint: A85 was observed for a different program. The sample is extended with nine clusters from the Von Der Linden et al. (2007) catalog, three clusters from the Albert et al. (1977) catalog, and one group from the Morgan et al. (1975) catalog. The final sample of 170 BCGs is listed in Tab. 2.1, and its spatial distribution is shown in Fig. 2.1.

In order to investigate the completeness of our sample, we plot the BCG redshifts against the total BCG+ICL brightness in Fig. 2.2. A slight Malmquist bias is seen by the upward trend of the average brightness with increasing redshift, shown by the red line.

Furthermore, we compare the completeness of our sample to that of the most comprehensive samples available in the literature, Lauer et al. (2014) and Donzelli et al. (2011). After applying the same volume-limiting constraints, the overlap of Lauer et al.'s sample on our sample is 90%. An overall agreement is expected because both Lauer et al.'s and our samples are mainly drawn from the ACO catalogs. Following the same criteria, the overlap with the sample of Donzelli et al. is 89%, and vice versa 80%.

The selection of the BCG in each cluster was done manually while inspecting the deep Wendelstein Telescope Wide Field Imager (WWFI) images. We always chose the most extended elliptical galaxy (at the ~ 27 g' mag arcsec^{-2} isophote) that is located close to the cluster center, as traced by the X-ray gas or satellite galaxy distribution. It usually coincides

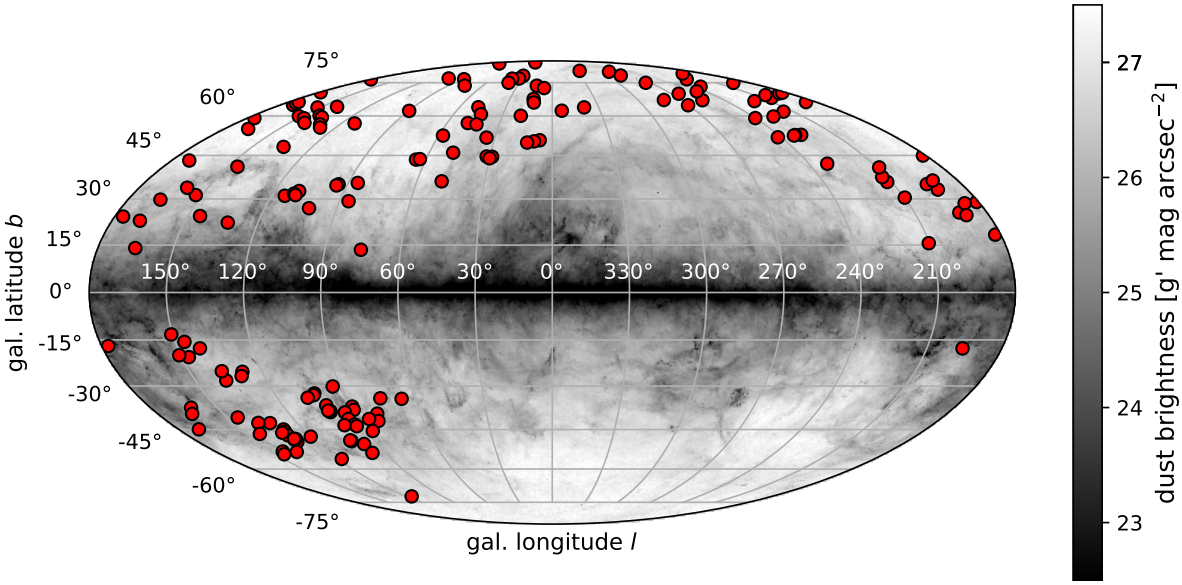

Figure 2.1: Our sample. The observed galaxy clusters are marked as red points. The background is the far-infrared dust emission map from Planck Collaboration et al. (2014). It is scaled to match the emission of the galactic cirrus (see Sec. 5.2).

with the brightest galaxy in the cluster, but that is not a stringent criterion. Our choices differ in 26 (20%) out of the 127 clusters that overlap with the Lauer et al. (2014) sample, who select the brightest galaxy measured in a metric aperture of 10 h^{-1} kpc radius. That is a consequence of the more cD-like definition of BCGs that we adopted. Out of those 26 galaxies, 15 are marked as the second-brightest galaxy in the Lauer et al. sample.

Private discussion with Tod Lauer and Marc Postman revealed that the choice of the BCG in those clusters is debatable. That is mainly due to (1) the Abell cluster number does not unambiguously identify a cluster in the case of line-of-sight overlap (three cases); (2) there is disagreement on the distance to the cluster center, usually in case of ongoing mergers of clusters (four cases); (3) the BCG is fainter in the metric aperture but brighter in terms of total luminosity (eight cases); (4) the criteria "brightest in the metric aperture" and "most extended" stand in conflict with each other (11 cases); and (5) the criteria "brightest in the metric aperture" and "central" stand in conflict with each other (three cases). The sometimes-occurring conflict between "brightest" and "central" was also pointed out by Von Der Linden et al. (2007).

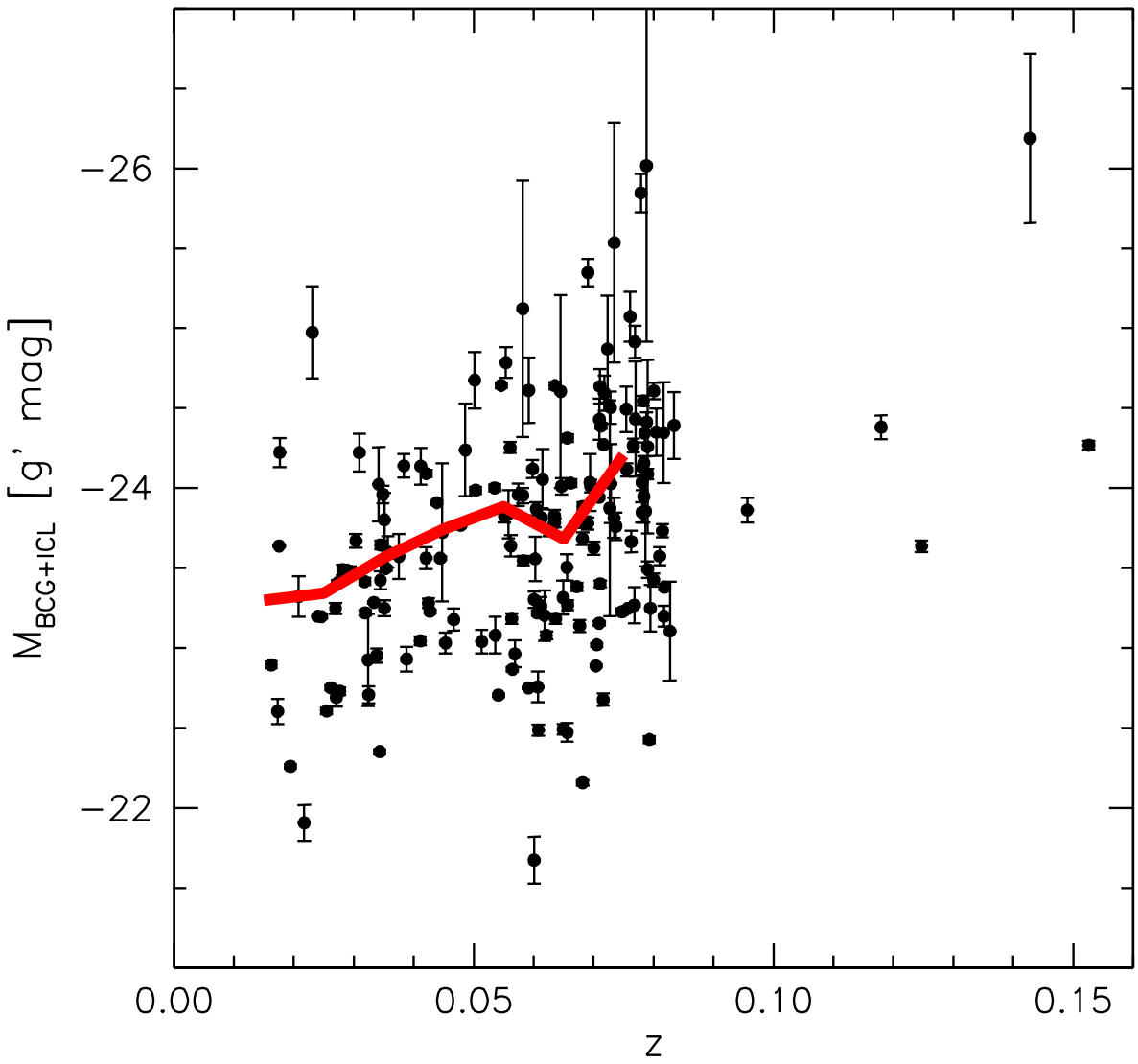

Figure 2.2: Redshift z of the BCG plotted against the total brightness of the BCG+ICL $M_{\rm BCG+ICL}$ measured in this paper. The red line shows the average brightness in each redshift bin with width $\Delta z = \pm 0.005$. Four outliers with $M_{\rm BCG+ICL} < -27$ g' mag were neglected because total brightness depends heavily on the extrapolation of the upward-curved light profiles that are unlikely to continue to infinite radius.

Table 2.1: The BCG sample.

Cluster	BCG	R.A. (J2000)	Decl. (J2000)	z	Angular Scale (kpc arcsec^{-1})	L14 Selection	HST Available
(1)	(2)	(3)	(4)	(5)	(6)	(7)	(8)
A76	IC 1565	00:39:26.3	+06:44:04	0.038372	0.765	✓	✓
A85	MCG-02-02-086	00:41:50.4	-09:18:11	0.055380	1.083	✓	–
A150	UGC 716	01:09:18.4	+13:10:09	0.061321	1.190	✓	–
A152	UGC 727	01:10:03.1	+13:58:42	0.058280	1.135	✓	–
A154	IC 1634	01:11:02.9	+17:39:47	0.069478	1.336	M2	–
A158	LEDA 1518776	01:11:46.3	+16:51:29	0.064500	1.248	other	–
A160	MCG+02-04-010	01:12:59.6	+15:29:29	0.043830	0.869	✓	✓
A161	LEDA 2098391	01:15:22.3	+37:20:24	0.076954	1.467	✓	–
A171	MCG+03-04-014	01:17:17.9	+16:15:57	0.071670	1.375	✓	–
A174	2MASX J01201619+3548272	01:20:16.1	+35:48:27	0.078056	1.486	✓	–
A179	2MASX J01223283+1931312	01:22:32.8	+19:31:32	0.056194	1.097	M2	–
A193	IC 1695	01:25:07.6	+08:41:58	0.050171	0.987	✓	✓
A225	NVSS J013848+184931	01:38:48.9	+18:49:32	0.069375	1.334	✓	–
A240	UGC 1191	01:42:06.0	+07:39:54	0.062534	1.212	✓	–
A245	2MASX J01435285+0624499	01:43:52.8	+06:24:51	0.079310	1.508	other	–
A257	2MASX J01490841+1357474	01:49:08.3	+13:57:48	0.070540	1.355	✓	–
A260	IC 1733	01:50:42.9	+33:04:56	0.035680	0.714	✓	✓
A262	NGC 708	01:52:46.3	+36:09:07	0.016220	0.332	✓	✓
A292	UGC 1518	02:02:18.9	+19:04:02	0.064648	1.250	✓	–
A347	NGC 910	02:25:26.9	+41:49:23	0.017302	0.354	✓	✓
A376	UGC 2232	02:46:03.9	+36:54:19	0.048610	0.958	✓	✓
A397	UGC 2413	02:56:28.7	+15:54:58	0.034447	0.690	✓	✓
A399	UGC 2438	02:57:53.1	+13:01:52	0.071239	1.367	✓	–
A400	NGC 1128	02:57:41.6	+06:01:21	0.023980	0.487	✓	✓
A407	2MASX J03015146+3550283	03:01:51.8	+35:50:20	0.047820	0.943	✓	–
A426	NGC 1275	03:19:48.1	+41:30:43	0.017560	0.359	–	✓
A498	2MASX J04375071+2112203	04:37:50.7	+21:12:21	0.059823	1.163	✓	–
A505	UGC 3197	04:59:55.6	+80:10:44	0.053504	1.048	✓	–
A539	LEDA 17025	05:16:37.3	+06:26:27	0.028142	0.568	M2	–
A553	2MASX J06124115+4835445	06:12:41.1	+48:35:45	0.069059	1.329	–	–
A559	2MASX J06395117+6958332	06:39:51.0	+69:58:34	0.075700	1.445	–	–
A568	MCG+06-16-019	07:07:41.5	+35:03:32	0.081702	1.549	✓	–
A569	NGC 2329	07:09:08.0	+48:36:56	0.019420	0.396	✓	✓
A582	2MASX J07280080+4155074	07:28:00.8	+41:55:08	0.060245	1.171	✓	–
A592	2MASX J07424058+0922207	07:42:40.6	+09:22:21	0.065651	1.268	other	–
A595	MCG+09-13-062	07:49:27.2	+52:02:33	0.070938	1.362	M2	–
A600	2MASX J07563560+6344237	07:56:35.5	+63:44:25	0.080997	1.537	✓	–
A602	2MASX J07532661+2921341	07:53:26.6	+29:21:35	0.060420	1.174	M2	–
A607	SDSS J075724.71+392106.6	07:57:24.7	+39:21:07	0.095620	1.784	–	–
A612	2MASX J08011329+3440311	08:01:13.2	+34:40:31	0.082720	1.567	–	–
A634	UGC 4289	08:15:44.8	+58:19:16	0.027090	0.548	✓	✓
A671	IC 2378	08:28:31.6	+30:25:53	0.050320	0.990	✓	✓
A688	SDSS J083734.33+154907.6	08:37:34.3	+15:49:08	0.152620	2.672	–	–
A690	ICRF J083915.8+285038	08:39:15.8	+28:50:39	0.079020	1.503	✓	–
A695	2MASX J08411308+3224596	08:41:13.1	+32:25:00	0.071103	1.365	✓	–
A734	2MASX J09003199+1614213	09:00:32.0	+16:14:26	0.074717	1.428	–	–
A744	2MASX J09072049+1639064	09:07:20.5	+16:39:07	0.072850	1.395	✓	–
A757	2MASX J09130775+4742307	09:13:07.7	+47:42:31	0.051350	1.009	✓	–
A834	2MASX J09413277+6642376	09:41:32.7	+66:42:39	0.070910	1.361	✓	–
A883	2MASX J09511516+0529170	09:51:15.1	+05:29:17	0.078983	1.502	–	–
A999	MCG+02-27-004	10:23:23.7	+12:50:07	0.032490	0.653	✓	✓
A1003	MCG+08-19-026	10:25:01.5	+47:50:31	0.063660	1.233	✓	–
A1016	IC 613	10:27:07.8	+11:00:39	0.032370	0.650	✓	✓
A1020	2MASX J10274949+1026306	10:27:49.5	+10:26:31	0.067702	1.305	✓	–
A1056	LEDA 2186592	10:38:01.7	+41:46:26	0.124670	2.251	–	–
A1066	2MASX J10393872+0510326	10:39:38.7	+05:10:33	0.068170	1.313	✓	–
A1100	MCG+04-26-010	10:48:45.6	+22:13:05	0.046666	0.922	✓	–
A1108	NGC 3405	10:49:43.3	+16:14:20	0.021740	0.442	–	–
A1142	IC 664	11:00:45.3	+10:33:12	0.033860	0.679	✓	✓
A1155	2MASX J11043955+3513477	11:04:39.5	+35:13:49	0.076788	1.464	✓	–
A1173	2MASX J11091531+4133412	11:09:15.3	+41:33:42	0.076620	1.461	–	–
A1177	NGC 3551	11:09:44.4	+21:45:33	0.031830	0.640	✓	✓
A1185	NGC 3550	11:10:38.4	+28:46:04	0.035094	0.703	✓	–
A1187	2MASX J11110955+3935522	11:11:09.6	+39:35:53	0.078380	1.492	✓	–
A1190	MCG+07-23-031	11:11:43.6	+40:49:15	0.078150	1.488	✓	–
A1203	2MASX J11134824+4017083	11:13:48.2	+40:17:09	0.075510	1.442	✓	–
A1213	2MASX J11162274+2915086	11:16:22.7	+29:15:09	0.045300	0.896	✓	–
A1218	2MASX J11184993+5144291	11:18:49.9	+51:44:30	0.079470	1.511	✓	–
A1228	UGC 6394	11:22:56.4	+34:06:42	0.042710	0.847	other	–
A1257	MCG+06-25-069	11:26:17.3	+35:20:25	0.034320	0.688	other	–
A1270	MCG+09-19-084	11:28:41.9	+54:10:21	0.070400	1.352	✓	–
A1275	2MASX J11292709+3638189	11:29:27.1	+36:38:19	0.060690	1.179	✓	–
A1279	2MASX J11313927+6714296	11:31:39.3	+67:14:31	0.054130	1.060	✓	–
A1314	IC 712	11:34:49.3	+49:04:40	0.033350	0.669	✓	–
A1324	LEDA 2557423	11:37:16.3	+57:06:49	0.117960	2.146	–	–
A1356	2MASX J11422978+1028327	11:42:29.8	+10:28:33	0.071612	1.374	✓	–
A1365	NVSS J114430+305259	11:44:30.5	+30:53:01	0.076260	1.455	✓	–
A1367	NGC 3842	11:44:02.1	+19:57:00	0.020830	0.424	✓	–
A1371	MCG+03-30-100	11:45:22.2	+15:29:44	0.068220	1.314	M2	–
A1400	2MASSJ11520578+5458171	11:52:05.7	+54:58:18	0.060070	1.168	other	–
A1413	MCG+04-28-097	11:55:18.0	+23:24:18	0.142800	2.527	–	✓
A1423	2MASX J11574738+3342438	11:57:47.3	+33:42:44	0.080010	1.520	✓	–
A1424	MCG+01-31-003	11:57:28.9	+05:05:21	0.080446	1.528	✓	–
A1435	MCG+02-31-009	12:00:14.3	+10:41:49	0.061220	1.189	–	–
A1436	MCG+09-20-056	12:00:13.8	+56:15:03	0.067212	1.296	M2	–
A1452	MCG+09-20-071	12:03:07.1	+51:40:31	0.065544	1.266	M2	–
A1507	NGC 4199A	12:14:48.6	+59:54:23	0.060070	1.168	✓	–

A1516	2MASX J12185235+0514443	12:18:52.3	+05:14:45	0.078342	1.491	–	–
A1526	2MASX J12214375+1345168	12:21:43.8	+13:45:17	0.081740	1.550	–	–
A1534	MCG+10-18-041	12:24:42.7	+61:28:15	0.070010	1.345	✓	–
A1569	2MASX J12362580+1632181	12:36:25.7	+16:32:19	0.068464	1.318	other	–
A1589	MCG+03-32-083	12:41:17.4	+18:34:29	0.071800	1.377	✓	–
A1610	IC 822	12:47:45.5	+30:04:39	0.060622	1.178	✓	–
A1656	NGC 4874	12:59:35.7	+27:57:34	0.023100	0.469	M2	✓
A1668	IC 4130	13:03:46.6	+19:16:18	0.063510	1.230	✓	–
A1691	MCG+07-27-039	13:11:08.6	+39:13:37	0.072300	1.386	✓	–
A1749	IC 4269	13:29:21.0	+37:37:23	0.055785	1.090	✓	–
A1767	MCG+10-19-096	13:36:08.3	+59:12:24	0.071062	1.364	✓	–
A1775	MCG+05-32-063	13:41:49.1	+26:22:25	0.075460	1.441	✓	✓
A1795	MCG+05-33-005	13:48:52.5	+26:35:35	0.063550	1.231	✓	✓
A1800	UGC 8738	13:49:23.5	+28:06:27	0.078288	1.490	✓	–
A1809	2MASX J13530637+0508586	13:53:06.4	+05:09:00	0.078850	1.500	✓	–
A1812	2MASX J13522099+3730370	13:52:21.0	+37:30:38	0.061810	1.199	–	–
A1825	UGC 8888	13:58:00.4	+20:37:57	0.062135	1.205	✓	–
A1828	2MASX J13581472+1820457	13:58:14.7	+18:20:47	0.064913	1.255	✓	–
A1831	MCG+05-33-033	13:59:15.1	+27:58:35	0.076110	1.452	✓	–
A1890	NGC 5539	14:17:37.7	+08:10:47	0.058180	1.134	✓	–
A1899	MCG+03-37-008	14:21:41.7	+17:45:09	0.056445	1.102	✓	–
A1904	MCG+08-26-024	14:22:10.2	+48:34:15	0.070980	1.363	✓	–
A1913	2MASX J14263943+1641139	14:26:39.4	+16:41:15	0.053610	1.050	other	–
A1982	MCG+05-35-020	14:51:14.4	+30:41:33	0.056322	1.100	✓	–
A1983	MCG+03-38-044	14:52:55.3	+16:42:11	0.044764	0.886	M2	✓
A2022	MCG+05-36-002	15:04:15.9	+28:29:48	0.058189	1.134	✓	–
A2029	IC 1101	15:10:56.1	+05:44:42	0.077900	1.484	✓	✓
A2052	UGC 9799	15:16:44.5	+07:01:18	0.034470	0.691	✓	✓
A2061	2MASX J15212054+3040154	15:21:20.6	+30:40:16	0.078820	1.499	✓	–
A2063	MCG+02-39-020	15:23:05.3	+08:36:34	0.034170	0.685	✓	–
A2065	MCG+05-36-020	15:22:24.0	+27:42:52	0.069020	1.328	✓	–
A2107	UGC 9958	15:39:39.0	+21:46:58	0.042060	0.835	✓	–
A2122	UGC 10012	15:44:59.0	+36:06:35	0.066210	1.278	✓	–
A2147	UGC 10143	16:02:17.0	+15:58:29	0.035380	0.708	✓	✓
A2151	NGC 6041	16:04:35.8	+17:43:18	0.035100	0.703	✓	–
A2152	MCG+03-41-095	16:05:29.2	+16:26:10	0.044440	0.880	✓	–
A2162	NGC 6086	16:12:35.5	+29:29:06	0.031900	0.641	✓	–
A2197	NGC 6173	16:29:44.9	+40:48:42	0.029380	0.592	✓	✓
A2199	NGC 6166	16:28:39.1	+39:33:11	0.030920	0.622	✓	✓
A2247	UGC 10638	16:50:58.6	+81:34:30	0.038809	0.774	M2	–
A2248	2MASX J16573834+7703462	16:57:38.4	+77:03:46	0.065641	1.268	M2	–
A2255	2MASXI J1712287+640338	17:12:28.8	+64:03:39	0.073440	1.406	–	–
A2256	UGC 10726	17:04:27.1	+78:38:26	0.059170	1.152	✓	–
A2271	MCG+13-12-022	17:18:16.6	+78:01:07	0.057439	1.120	✓	–
A2293	2MASX J18012131+5739016	18:01:21.3	+57:39:02	0.073396	1.405	M2	–
A2308	2MASX J18340865+7057188	18:34:08.5	+70:57:20	0.083424	1.579	✓	–
A2319	MCG+07-40-004	19:21:10.0	+43:56:45	0.054588	1.068	–	–
A2388	LEDA 140981	21:53:39.3	+08:15:10	0.061500	1.194	✓	–
A2469	-	22:40:34.3	+12:17:56	0.065600	1.267	other	–
A2495	MCG+02-58-021	22:50:19.7	+10:54:13	0.080060	1.521	✓	✓
A2506	NGC 7432	22:58:01.9	+13:08:05	0.025464	0.516	–	–
A2513	NGC 7436	22:57:57.5	+26:09:01	0.024600	0.499	–	–
A2516	2MASX J23001449+1835027	23:00:14.5	+18:35:03	0.081825	1.551	–	–
A2524	2MASX J23031792+1740232	23:02:55.8	+17:45:01	0.081490	1.546	✓	–
A2558	2MASX J23124349+1021435	23:12:43.5	+10:21:44	0.064900	1.255	✓	–
A2572	NGC 7597	23:18:30.2	+18:41:21	0.037540	0.749	other	–
A2589	NGC 7647	23:23:57.4	+16:46:38	0.041170	0.818	✓	✓
A2593	NGC 7649	23:24:20.0	+14:38:50	0.042042	0.835	✓	✓
A2618	2MASX J23340547+2259000	23:34:05.5	+22:59:00	0.072813	1.395	✓	–
A2622	2MASX J23350151+2722203	23:35:01.5	+27:22:21	0.063441	1.229	✓	–
A2625	2MASX J23374932+2048340	23:37:49.3	+20:48:34	0.059118	1.151	✓	–
A2626	IC 5338	23:36:30.6	+21:08:51	0.055108	1.078	✓	✓
A2630	2MASX J23380105+1554022	23:38:01.0	+15:54:02	0.068170	1.313	other	–
A2634	NGC 7720	23:38:29.4	+27:01:54	0.030350	0.611	✓	✓
A2637	2MASXI J2338533+212752	23:38:53.3	+21:27:53	0.073702	1.410	✓	–
A2657	2MASX J23445742+0911349	23:44:57.4	+09:11:36	0.041081	0.817	M2	✓
A2665	MCG+01-60-039	23:50:50.5	+06:08:59	0.056100	1.096	✓	–
A2666	NGC 7768	23:50:58.5	+27:08:51	0.026955	0.545	✓	✓
A2675	2MASX J23554260+1120355	23:55:42.6	+11:20:36	0.076893	1.466	✓	–
A2678	2MASX J23554532+1139135	23:55:45.3	+11:39:14	0.078125	1.487	M2	–
AWM1	NGC 2804	09:16:50.0	+20:11:55	0.027670	0.559	–	–
AWM5	NGC 6269	16:57:58.1	+27:51:16	0.034891	0.699	–	–
AWM7	NGC 1129	02:54:25.2	+41:34:37	0.017639	0.361	–	✓
L2027	LEDA 1479941	00:43:11.8	+15:16:03	0.078650	1.497	–	–
L2030	NGC 7237	22:14:46.9	+13:50:28	0.026180	0.530	–	–
L2069	2MASX J01072180+1416240	01:07:21.8	+14:16:24	0.078512	1.494	–	–
L2093	2MASX J01092719+1415359	01:09:27.2	+14:15:37	0.060780	1.181	–	–
L2211	NGC 7651	23:24:26.0	+13:58:21	0.042460	0.843	–	–
L3009	2MASX J09204890+4039516	09:20:48.8	+40:39:52	0.072690	1.393	–	–
L3055	2MASX J07464283+3059493	07:46:42.9	+30:59:50	0.056850	1.109	–	–
L3152	NGC 6338	17:15:22.9	+57:24:41	0.027300	0.552	–	✓
L3186	2MASX J17153003+6439511	17:15:30.0	+64:39:52	0.079040	1.503	–	–
MKW4	NGC 4104	12:06:39.0	+28:10:29	0.028605	0.577	–	–

Table 2.1: The BCG sample. Clusternames beginning with "AWM", "L" and "MKW" are taken from the Albert et al. (1977), Von Der Linden et al. (2007) and Morgan & Lesh (1965) catalogs, respectively. A comparison to the BCG selection by Lauer et al. (2014) (hereafter L14) is given in column (7). The items mean: agreement (✓), our BCG choice is the second-ranked galaxy L14 (M2), the cluster is not present in L14 (–) and our choice is neither the first- nor the second-ranked galaxy in L14. The last column states whether Hubble Space Telescope images were used increase the spatial resolution of the inner light profiles.

Chapter 3

Data

The observations have been carried out with the 2m Fraunhofer telescope at the Wendelstein Observatory. It is located in the Bavarian Alps, 70 km southeast from Munich, Germany. The telescope is a modern Alt-Az instrument that has been in operation since late 2013. We have utilized the Wendelstein Wide Field Imager (WWFI; Kosyra et al. 2014) for our survey, which also is its first light instrument. Its optical components are designed to minimize ghost intensities (Hopp et al., 2014), which qualifies the setup well for a deep imaging study.

The field of view with $27.6' \times 28.9'$ in combination with the large dither pattern is wide enough to cover the ICL down to an SB of 30 g' mag arcsec^{-2} while still providing sufficient sky coverage (see Fig. 3.1, left panel) to model the background accurately. That corresponds to a median semimajor axis radius of $a = 350 \pm 128$ kpc for our sample.

The camera consists of four 4096×4109 pixel sized e2v CCD detectors installed in a camera by Spectral Instruments. The detectors are aligned in a 2×2 mosaic (see Fig. 3.2). On the sky, the gaps between the CCDs are $98''$ in the north–south direction and $22''$ in the east–west direction. A large 52-step dither pattern is chosen for the observations to fill up the gaps and provide sufficient sky coverage. It is illustrated in Fig. 3.1. For the first four exposures, the BCG is centered on each CCD, then shifted by two arcminutes in R.A. or decl. direction before repeating the four exposures off-center. That procedure is repeated 13 times whereby the shifting direction changes for each step. In other words, the dither pattern is a 13-step spiral where each step is repeated on all four CCDs. This strategy allows us to model any time-stable background pattern accurately, which is especially important near the location of the BCG. The total integration time per target is 52 minutes and is split into 60 s single exposures.

We have chosen the g'-band for all observations because the night-sky brightness is more stable in that filter band compared to redder bands, due to the absence of strong emission lines. The fact that optical reflections have lower intensities is also important.

The pixel scale of $0.2''$/pixel oversamples the seeing-limited data. The typical seeing of FWHM $\simeq 1.2 \pm 0.2''$ allows us to resolve the inner cores of BCGs after deconvolving the central image regions. If available, we use high resolution Hubble Space Telescope imaging data downloaded from the Hubble Legacy Archive (https://hla.stsci.edu) to measure the central light profiles and combine them with the profiles measured from wide-field WWFI data.

As the main interest of this work is the faint outskirts of BCGs, the observing constraints

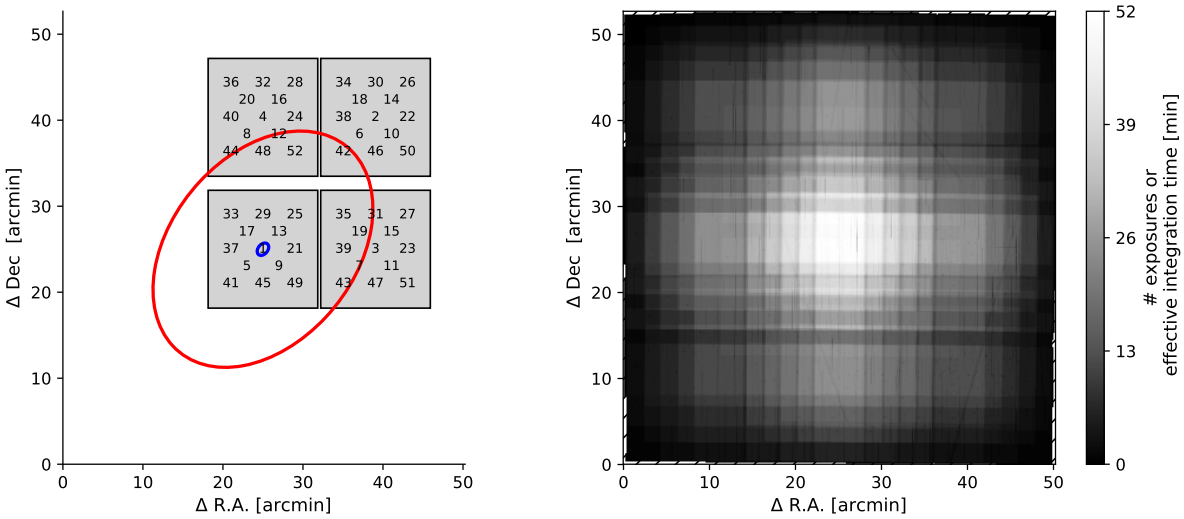

Figure 3.1: *Left:* illustration of the dither pattern. The four CCDs are represented by gray squares. The illustrated pointing corresponds to the first element of the dither pattern. The position of the BCG on the detectors is indicated by the number i for each dither element i. Blue and red ellipses correspond to the isophotes with $SB = 30$ g' mag arcsec^{-2} for the apparently smallest BCG, A2630 (semimajor axis radius $a = 50''$), and the apparently largest BCG, A1367 ($a = 955''$), respectively, that were observed with this dither pattern. *Right:* stacked weight file of A600. The spatially dependent number of exposures that were added are color coded.

were prioritized more on dark and photometric conditions than on excellent seeing. Hence, the median seeing for our survey is worse than the median site seeing of $0.8''$ reported by Hopp et al. (2008).

3.1 Data reduction

The data reduction pipeline was specifically developed and assembled for the WWFI. It includes bias subtraction, flat-fielding, charge persistence, bad pixel and cosmic-ray masking, photometric zero-point calibration, background subtraction, bright star removal, resampling, and coadding. The photometric zero-points are calibrated using Pan-STARRS1 DR2 catalogs (Flewelling et al., 2016) and provide SB profiles consistent with the Sloan Digital Sky Survey (SDSS). A comparison of 10 BCG SB profiles with those measured from SDSS DR12 image data shows that the SB profiles agree within 0.02 mag arcsec^{-2} before point-spread function (PSF) debroadening correction. Dark current is negligible at the low CCD operating temperature of –115°C. Detailed descriptions of all important aspects regarding deep surface photometry follow in the next subsections.

3.1.1 Bias

Bias exposures show a chess field–like pattern. Each of the 16 readout amplifiers places a unique bias offset on the corresponding data region. A time-stable vertical line pattern is hidden beneath these offsets. To get rid of this line pattern, we subtract a master-bias image that was created by averaging all the bias images taken in the relevant month. The offsets are subtracted beforehand. Cosmic rays are removed with the tool `cosmicfits` (Gössl & Riffeser, 2002).

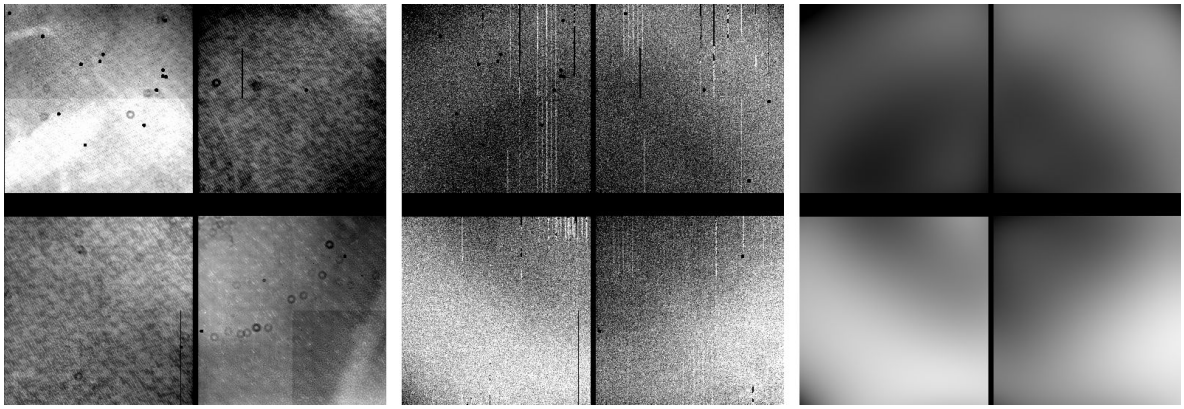

Figure 3.2: *Left:* example master flat in the g'-band. Variations are on the 3% level. *Middle panel:* example night-sky flat, also in the g'-band. Variations are on the 2% level. Charge persistence stripes are visible as vertical white lines. *Right panel:* fit of the night-sky flat with 2D fourth-order polynomials for each of the four CCDs.

The values of the offsets themselves are not stable over time. They fluctuate mildly on minute time-scales. We measure ~ 0.1 ADU residuals even after the clipped average of the corresponding overscan regions had been subtracted. The origin of this effect could be a heating up of the readout electronics, which is correlated to the number of charges being read out. An alternative explanation is based on electromagnetic interferences from a nearby transmitting antenna. In order to eliminate the varying offsets from the science images, we match the background fluxes along 30-pixel-wide adjacent stripes along the borders of each quadrant to the average value of these stripes. This is done for each CCD independently. Regions affected by charge persistence are masked beforehand in order to dismiss contaminated pixels (see Sec. 3.1.3).

3.1.2 Flat-fielding

We correct for large-scale illumination inhomogeneities and small-scale patterns like dust using calibration images that were taken each night during twilight. These twilight flats are flux-aligned with fourth-order polynomials to each other and then combined into a master flat (Fig. 3.2, left panel). Every bias-subtracted science image is divided by this master flat. However, large-scale residuals on a 2% level remain (Fig. 3.2, middle panel). That is common for wide-field imagers. The residual patterns are almost (but not perfectly!) point-symmetric around the center and stable for one pointing in one night. We have identified three properties of this pattern that point toward a color effect as its origin: (1) the closer to dark time the flats are taken, the weaker is the pattern structure; (2) it is weaker in narrowband filters; (3) the quotient of two exposures that were taken while first a green and second a red LED illuminated the inner dome shows a similar pattern with $\sim$2% large-scale variation.

We conclude that the bluer color of the twilight sky compared to the redder night sky, in combination with color-dependent stray light originating inside the optical path, led to inhomogeneities in the flat-fielding process. No improvement in flatness was accomplished by using dome flats instead of twilight flats. Even though the chosen lamp produced redder light than the twilight sky, the difficulty of illuminating a large inner dome surface homogeneously from a short distance limits the possibility of achieving perfect flatness.

The multiplicative scaling of the flat-field pattern correlates positively with the night-sky

brightness. Color changes toward a bluer night sky that are du to airglow, city lights, or lunar twilight invoke an inversion of the pattern. We factor in that behavior by scaling night-sky flats (NSFs) accordingly (see Eq. 3.6 in Sec. 3.1.5).

3.1.3 Charge persistence masking

Bright foreground stars from the Galaxy are unavoidable in all observed fields, especially due to the wide field of the WWFI camera. The extreme numbers of photons arriving from these stars trigger a tremendous release of free electrons into the valence band of the CCD detector. A small fraction of them gets trapped inside defects in the silicon lattice. These trapped electrons are then released over time where the release rate follows a power law $\dot{N} \propto t^{-1}$. That process can last for hours, depending on the severity of saturation. After the trapped electrons are released, they are stored inside the pixels' potential wells until readout.

When the electrons are being shifted toward the readout register as part of the readout process, they temporarily affect the pixel values along their path. More precisely, the electron bulk loses a fraction in lattice defects of the pixels along the readout direction. Many of these secondarily trapped electrons are released over the first 2 μs, which is the length of a readout step. As a result, a saturation stripe appears in the same exposure where saturation happened, but opposite to the shifting direction. Another charge persistence stripe appears in subsequent exposures in the shifting direction because the damaged pixels slowly release the remaining trapped electrons (see Fig. 3.2, middle panel). Over time, these artificial signals contaminate an increasing fraction of the total field of view because of the dithering strategy.

Our masking strategy is to store the locations where stars saturated and check the corresponding stripes' background flux relative to the ±15-pixel-wide areas alongside them. The charge persistence stripe is being masked when the contaminating signal is higher than the local background plus 0.2 times the rms background scatter. The factor 0.2 was empirically determined to minimize false-positive detections. The location information of a positive detection is forwarded to the subsequent images until the stripe is no longer detectable.

3.1.4 Bright star removal

Bright foreground stars have to be removed from the images for two reasons. Some of the PSFs' extended wings (see Fig. 3.3, and e.g., Kormendy 1973) overlap in projection with the targeted ICL, and they furthermore complicate the background modeling. We follow the strategy from Slater et al. (2009) to model and subtract the ∼100 brightest stars in the observed fields. Their approach has been successfully applied for the Burrell Schmidt Deep Virgo Survey (Mihos et al., 2017). Duc et al. (2015) and later Karabal et al. (2017) performed a similar correction for the `MATLAS` survey data, but with time-consuming manual modeling.

We split the cleaning procedure into two steps. First, we subtract the circular PSF light profile from every star, and second, we model and subtract the out-of-focus reflections, which are location dependent. The circularly symmetric light profile for a zeroth magnitude star is shown in Fig. 3.3. It spans ∼14′ in radius and ∼ 19 g' mag arcsec^{-2} dynamic range in surface brightness. The blue line is a Moffat (1969) fit to the core and depends on the seeing. The outer components are time-stable because they are due to the optics. Surprisingly, they can be modeled by three $r^{1/4}$ profiles. The outermost $r^{1/4}$ component is extrapolated to the edge of the field of view. We are mostly interested in removing the wings accurately. A single PSF model is therefore sufficient for all observations. The analytic SB profile shown by the red

j	s	$r_{\rm outer}$ (arcsec)	SB (g' mag arcsec^{-2})
1	0.04371	37.4	17.03
2	0.08649	23.8	17.98
3	0.10602	92.6	17.28
4	0.11811	102.6	17.40
5	0.12555	109.6	18.22
6	0.26040	74.0	19.12
7	0.28365	87.6	19.12
8	0.31713	86.4	20.04

Table 3.1: Reflection properties for a zeroth magnitude star. The relative shift s, given in column (2), is defined in Eq. 3.4 as the offset of a ring with respect to the source divided by its distance from the optical axis. The outer radius of each reflection ring j is given in column (3). The inner radius is always $r_{\rm inner} = 0.424 r_{\rm outer}$. The surface brightness normalized to a zeroth magnitude star of each ring is given in column (4).

line in Fig. 3.3 is used to model all stars that are listed in the Tycho-2 catalog (Høg et al., 2000) and located inside of a circular aperture with radius $r < 1.3°$ around the center of the field. Stellar magnitudes are converted from the Tycho B_T and V_T to the Johnson B_J and V_J filter system using Eq. 1.3.20 from ESA (1997):

$$V_J = V_T - 0.09(B-V)_T, \tag{3.1}$$

$$(B-V)_J = 0.85(B-V)_T \tag{3.2}$$

and are then converted to SDSS g-band magnitudes using the equation derived by Jester et al. (2005):

$$g = V_J + 0.60(B_J - V_J) - 0.12. \tag{3.3}$$

Our photometric zero-points are calibrated to the Pan-STARRS photometric filter system. The difference between SDSS g and Pan-STARRS g' magnitudes (e.g., $g - g' = 0.09$ for the Sun; Willmer 2018) is not relevant here because the reference g'-band PSF SB profile is assigned its g-band catalog magnitude. It is scaled for different stars according to their g-band magnitudes. However, the uncertainties of the color transformations propagate an error to the individual scaling of the model stars. Further relevant effects are intrinsic stellar variabilities and the uncertainty of the preliminary photometric zero-point calibration at that intermediate step of the data reduction. We want to minimize the average residuals of the brightest stars. That is achieved by introducing an empirically determined scaling factor $f^i_{\rm scaling}$ for all stars in each cluster pointing i. Our manual choices vary in $0.9 \lesssim f^i_{\rm scaling} \lesssim 1.1$.

Reflections are considered separately. They are particularly prominent in wide-field imagers, due to the need for multiple corrector optics in order to correct for field distortions. They arise from light that is reflected at various surfaces during its path through the telescope system. These surfaces are the front and back sides of filter glasses, corrector lenses, and the CCD entrance window. The longer path lengths result in out-of-focus duplicates next to bright light sources, so-called ghosts (Fig. 3.3, top panel). For the WWFI g'-band, we calculate that 1.78% of the PSF's light is redistributed into these ghosts, which is consistent with the findings of Hopp et al. (2014). We identify eight rings with parameters listed in Tab. 3.1. The rings are only concentric if the light source is located on the optical axis, that is,

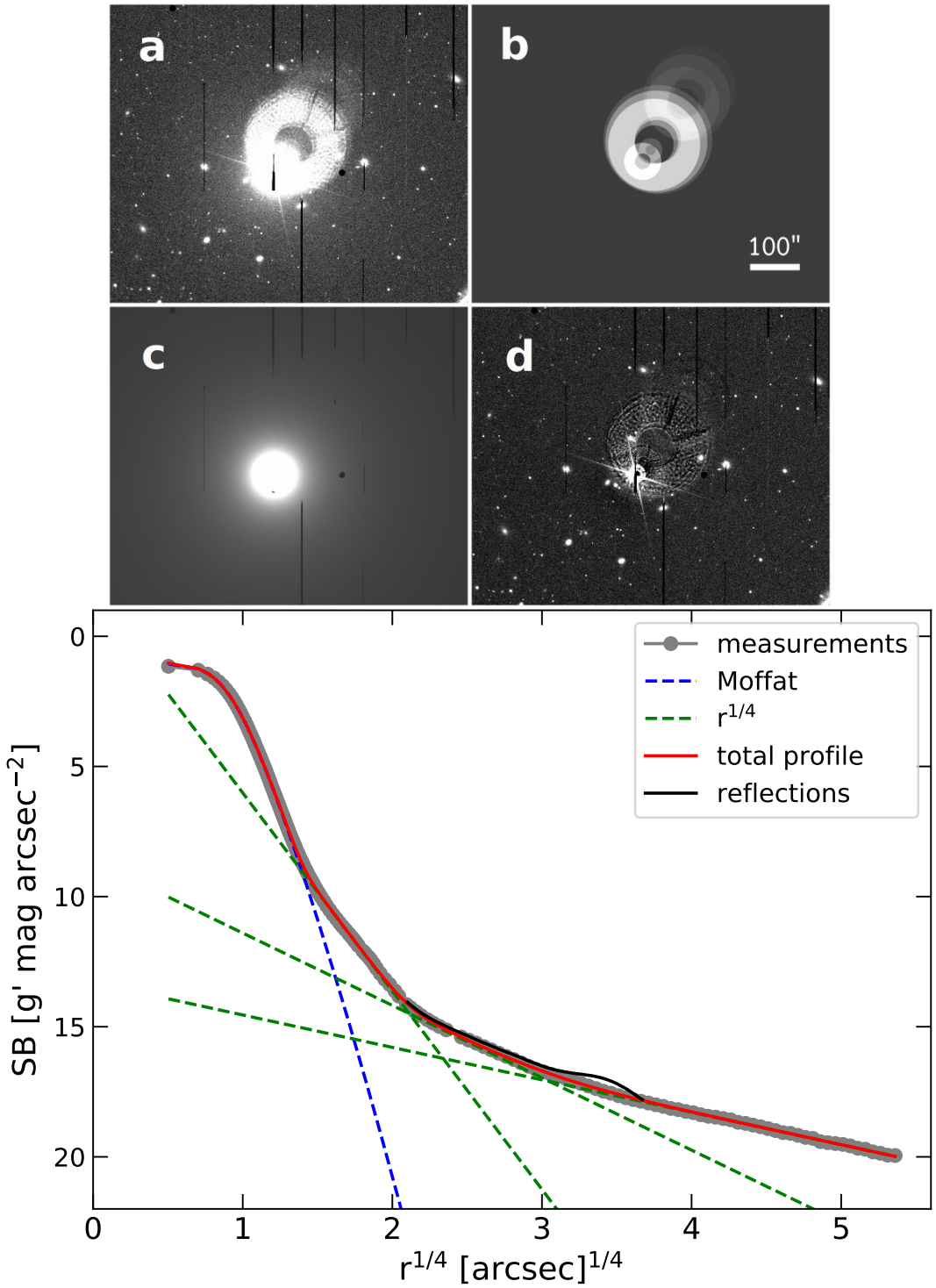

Figure 3.3: *Top panel:* (a) example cutout of a bright star, (b) model of the ghosts, (c) model of the point-symmetric component of the PSF, (d) residual after subtracting both models. *Bottom panel:* SB profile of a zeroth magnitude star. The multicomponent fit to the data points is shown as a red line and it is used for the modeling. The FWHM of the Moffat fit (blue dashed line) to the central region is FWHM $= 1.05''$. The outer three $r^{1/4}$ components (green dashed lines) are formed by the optical elements in the telescope. The contribution from the reflections is plotted separately as the black line.

close to the field center. They are shifted radially outward in any other case. The relative shift s of ring j is in good approximation linearly dependent on the distance of the star at position $\boldsymbol{r}_{\rm star}$ from the optical axis at position $\boldsymbol{r}_{\rm oa}$:

$$\boldsymbol{r}_j = \boldsymbol{r}_{\rm star} + s \cdot (\boldsymbol{r}_{\rm star} - \boldsymbol{r}_{\rm oa}^{q_i}) \tag{3.4}$$

with

$$\begin{aligned} \boldsymbol{r}_{\rm oa}^{q_1}[\rm px] &= (4011, 4162), \\ \boldsymbol{r}_{\rm oa}^{q_2}[\rm px] &= (4007, -433), \\ \boldsymbol{r}_{\rm oa}^{q_3}[\rm px] &= (-195, -443), \\ \boldsymbol{r}_{\rm oa}^{q_4}[\rm px] &= (-195, 4159), \end{aligned} \tag{3.5}$$

being the position of the optical axis in the coordinate system of each CCD q_i. The central coordinates of the rings are $\boldsymbol{r}_j$. The outer radii $r_{\rm outer}$ are tabulated in Tab. 3.1. The inner radii are always $0.424 r_{\rm outer}$, corresponding to the shaded area of the support for the secondary mirror. The surface brightness of the ring j is $SB_j + g'$ for a star with a g'-band magnitude g'. The values for SB_j are given in Tab. 3.1 and are estimated by scaling the brightness of each ring model independently so that the total residual after subtraction is minimal.

3.1.5 Background subtraction

After flat-fielding, large-scale variations in the background pattern are apparent on a 2% level (see Fig. 3.2, middle panel). That corresponds to a surface brightness of $SB \sim 26$ g' mag arcsec^{-2}. In order to measure accurate SBs at the 30 g' mag arcsec^{-2} level, the background has to be flat on the same level. The necessary calibration has to be performed on the individual images because the dithering between observations would otherwise result in sharp-edged jumps in the background pattern of the coadded mosaic.

The delicacy for every background subtraction method lies in the risk of accidentally subtracting the incompletely masked ICL, which mimics an artificial background pattern. The easiest method to follow would be simple surface polynomial or surface spline fitting (e.g., Capaccioli et al. 2015) of the source-masked images. We have discarded this approach because of its severe risk of subtracting part of the ICL. This method is furthermore fairly unstable when the polynomials or splines are unconstrained, due to large masks. This can lead to overshooting, especially when an edge of the image is masked. A detailed explanation of our masking procedure is given in Sec. 3.2.

We apply the more robust method of subtracting an average model of the background pattern, a so-called night-sky flat (NSF). This is only possible because the background pattern is to zeroth order time-stable (see Sec. 3.1.2). A separate NSF is created for every visit, i.e., for each target in each night. The major advantage of this method is that the background pattern is known at and around the masked BCG. That is because masked regions in individual images are filled up in the NSF by averaging numerous dithered exposures. Moreover, the issue of incomplete masks is reduced because only a small number of images are contaminated by undetected PSF or galaxy halos at a specific, fixed image location, again thanks to the large dither pattern.

The NSF can either be created from separate sky pointings (Iodice et al. 2017; Spavone et al. 2017) or from the target pointings themselves. The first option is safer because the risk

of including part of the ICL in the NSF is eliminated. The necessary observing strategy is, on the other hand, twice as time-consuming. We take advantage of the $\sim 4\times$ larger field of view compared to the extent to which we measure ICL. An optimized dithering strategy (see Sec. 3) ensures that the background can be determined from the target exposures themselves while maximizing the exposure time on-target and minimizing the contribution of the incompletely masked ICL on the NSFs.

The PSF-subtracted (see Sec. 3.1.4) and source-masked single images are normalized and averaged to an NSF. The normalization is necessary because fluctuations in the sky brightness on a 2% level are common between exposures, and the normalization is allowed since the background pattern is to first order multiplicative because of its origin in flat-fielding residuals (see Sec. 3.1.2).

A number of undetected charge persistence stripes usually becomes visible in the deep NSFs (see Fig. 3.2, middle panel, and Sec. 3.1.3). We therefore fit two-dimensional fourth-order polynomials to each CCD region in order to improve the NSFs' smoothness (see Fig. 3.2, right panel). The smoothed NSF is then rescaled in flux back to the individual images i from which it was created. The scaling formula is

$$\mathrm{NSF}_i(x, y) = \mathrm{NSF}(x, y) \times a_i + b_i. \tag{3.6}$$

We allow for an additive b_i and multiplicative a_i scaling. Two fitting parameters are needed to account for the gradual flipping of an outward-increasing to an outward-decreasing brightness of the background pattern as the night-sky color becomes bluer (see Sec. 3.1.2).

Every NSF is scaled slightly too high because incomplete masks are more present in the individual images than in the averaged NSF. That leads to a small, negative background constant on the order of negative $\sim$30 g' mag arcsec^{-2} that remains in the coadded mosaics (see Sec. 5.1). This constant is later-on determined as the value to which the linear light profiles converge at large radii (cf. e.g., Spavone et al. 2017).

3.2 Source masking

Two situations require source masking: (1) before averaging images to create NSFs and (2) before measuring the BCG/ICLs light profiles. Both situations require different masking techniques, but both resulting masks need to be as complete and on large scales as homogeneous as possible. Tools that are being used by other authors include the IRAF task `objmasks` (Mihos et al., 2017) or `ExAM` (Huang et al. 2011; Spavone et al. 2017), which is based on SExtractor (Bertin & Arnouts, 1996) catalogs.

We have developed our own technique specifically to tackle the requirement of homogeneity. Our adopted, large dither pattern causes a spatially varying signal-to-noise ratio of $\Delta\mathrm{S/N} > 2$. That is a severe problem for the choice of masking thresholds:

1. A constant signal masking threshold leads to a more frequent masking of noise peaks as false-positive detections in the low-S/N regions.

2. A constant S/N masking threshold leads to fewer detections of sources in the low-S/N regions.

While choice (1) results in a decrease of the average flux value in the low-S/N regions, choice (2) evokes the opposite. Both options therefore introduce a significant bias in the NSF scaling and isophotal flux measurements. A compromise between the two options, that is, a spatially dependent scaling of the masking threshold $T(x, y)$ by the square root of the local background rms scatter $\mathrm{rms}(x, y)$, results in satisfyingly homogeneous masks for a low average masking threshold T_0:

$$T(x,y) \geq T_0 \cdot \left(\frac{\sqrt{\mathrm{rms}(x,y)}}{\mathrm{median}(\sqrt{\mathrm{rms}(x,y)})} \right). \tag{3.7}$$

The information of the local background noise $\mathrm{rms}(x, y)$ is stored in the stacked weight maps generated by `SWarp` (see Fig. 3.1, right panel, for an example).

We now explain our choices for the average masking thresholds for each of the two scenarios that were mentioned in the beginning of this subsection.

§1) Masks for background modeling

The basis for this type of mask is a roughly background-subtracted, coadded image. This is in our case a mosaic that was created after subtracting second-order 2D polynomials from the masked single exposures. We mention here that this procedure is iterative. Since there can be no celestial sources with sizes smaller than the seeing, we smooth the stack using a 2D Gaussian filter with standard deviation $\sigma = 11$ px in order to avoid mask fragmentation. All pixels get masked that have greater values than the locally calculated threshold $T(x, y)$, where T_0 in Eq. 3.7 corresponds to a surface brightness of 27.5 g' mag arcsec^{-2}. The regions around the BCG and around bright stars are conservatively enlarged by hand to a size where we expect the $29 \sim 30$ g' mag arcsec^{-2} isophote to be. We again stress here that ICL residuals at these levels are damped in the NSF by averaging the widely dithered single exposures. That is confirmed by the recovery of a mock-BCG SB profile down to $SB > 30$ g' mag arcsec^{-2}, as presented in Sec. 5.1.

§2) Masks for light profile measurements

Before measuring the flux from a BCG+ICL, we have to mask all other sources except for the BCG+ICL itself. Our approach to this problem is to subtract a model for the BCG+ICL before creating the mask. We exploit the fact that the BCG+ICL system is usually the largest object in the field of view and has the shallowest SB profile gradient. Thus, it can be approximately modeled by a medium-scale background fitting method. That model is created by performing a bicubic spline interpolation to a grid of points that was generated by calculating the clipped median in (51×51) pixel sized square apertures around the corresponding locations. After subtracting this model from the stack, we generate and combine one mask for the small and one mask for the medium-sized sources. The stack is smoothed with a 2D Gaussian filter with $\sigma = 5$ px (which is the typical seeing) for the first mask and $\sigma = 21$ px (which is about half of the background interpolation step size) for the second mask. All pixels are masked that have values greater than

$$T(x,y) \geq T_0 \cdot \mathrm{rms}(x,y) \cdot \left(\frac{\sqrt{\mathrm{rms}(x,y)}}{\mathrm{median}(\sqrt{\mathrm{rms}(x,y)})} \right)^{-1}, \tag{3.8}$$

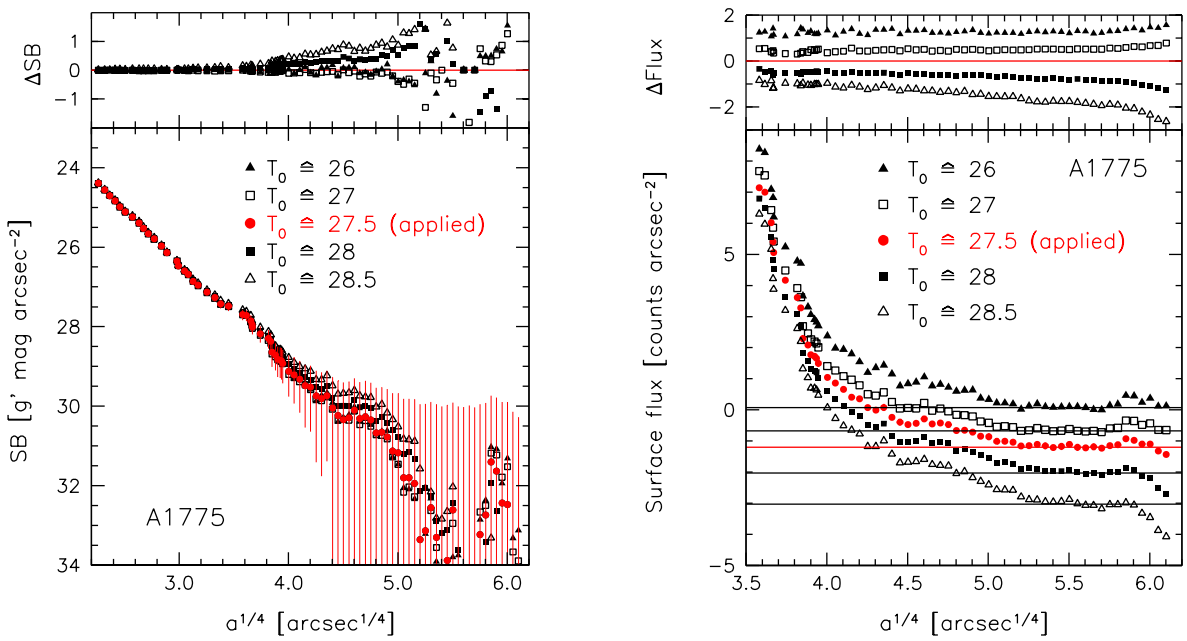

Figure 3.4: Surface brightness (left) and surface flux (right) profiles of the BCG in A1775 measured for different masking thresholds T_0 (Eq. 3.8) converted to units of g' mag arcsec^{-2}. The residual differences from the measurements done with the applied masking threshold (red) are shown in the top panels. The residual background choices are shown for each masking threshold as the horizontal lines in the right panel.

where this time, $T_0 = 0.15$ is given in units of the local S/N per pixel. We emphasize here that the threshold is extremely low because of the preceding smoothing. Also note that the scaling term is now inverted because the threshold is expressed differently. The chosen threshold $T_0 = 0.15$ corresponds on average to a surface brightness of $27 \,\widehat{\lesssim}\, T_0 \,\widehat{\lesssim} 27.5$ g' mag arcsec^{-2} (see Fig. 3.4, red label). We decided to fix the masking threshold this time in units of (scaled) S/N because it provides a more consistent mask homogeneity between stacks of different integration times. In practice, fainter average thresholds result to zeroth order in a higher residual background constant (see the horizontal lines in Fig. 3.4, right panel). That is because the overall distribution of background galaxies is largely homogeneous on the spatial scales of the outermost isophotes. This constant is determined in any case during the measurement of the light profile and thus introduces no bias. A first-order effect of a too-faint masking threshold is a downward bending of the outer surface flux profile (see the slope of the residuals in Fig. 3.4, right panel). That is due to the outward-decreasing signal-to-noise ratio, as explained in the beginning of this subsection. The fainter the threshold, the more sensitive the mask homogeneity becomes toward spatially varying S/N ratios. The effect is reduced by $\sim 50\%$ by the spatial scaling of the threshold T_0 (Eq. 3.8) but not fully eliminated. The downward bending also biases the background constant choice to too-low values. Both effects combined result in too-bright SB data points in $3.6 < (a[\mathrm{arcsec}])^{1/4} < 5.5$ (empty triangles and filled squares in Fig. 3.4, left panel). The same panel also shows that the SB profiles derived with masking thresholds $26 \,\widehat{\leq}\, T_0 \,\widehat{\leq}\, 27.5$ are consistent with each other. The explained effects are less important for shallower thresholds because fewer pixels are affected. The optimal threshold is therefore the faintest one that produces a surface flux profile that is still consistent with those derived with shallower thresholds. For the case of A1775, we find the optimal threshold to be $T_0 = 0.15 \,\widehat{=}\, 27.5$ g' mag arcsec^{-2}.

The masks are expanded by convolving them with a circular kernel with radius $r = 9$ px for the first mask and $r = 11$ px for the second mask so that no light around small and medium-sized sources leaks visibly out of the expanded masks. The spline interpolation produces artifacts in the central areas of the BCG. We unmask and remask these regions by hand. Finally, the regions around bright and extended sources excluding the BCG+ICL are conservatively expanded by hand to a size where we expect the $29 \sim 30$ g' mag arcsec^{-2} isophotes to be. The average masked fraction in the final masks is $33 \pm 5\%$.

3.3 Astrometry, Resampling, and Stacking

The astrometric solutions were calculated with `SCAMP` (Bertin, 2006). The resampling and coadding of the calibrated images is performed with `SWarp` (Bertin, 2010). The individual images are weighted by their inverse background rms scatter squared to obtain an optimal S/N for extended sources.

Chapter 4

Surface brightness profiles and isophotal shape parameters

4.1 Fitting ellipses to the isophotes

Azimuthally averaged surface brightness (SB) profiles of all BCGs are measured by fitting ellipses to the galaxies' isophotes with the code `ellfitn` from Bender & Moellenhoff (1987). All ellipses have five degrees of freedom: semimajor axis radius a, ellipticity $\epsilon = 1 - b/a$ where b is the semiminor axis radius, central coordinates X_0 and Y_0, and position angle PA.

Deviations Δr_i of the ith isophote from a perfect ellipse are expanded in a Fourier series,

$$\Delta r_i = \sum_{k=3}^{19} [a_k \cos(k\theta_i) + b_k \sin(k\theta_i)], \tag{4.1}$$

where θ is the eccentric anomaly.

The routine breaks down usually around $SB \sim 27$ g' mag arcsec^{-2} where the low-SB halos of satellite galaxies deform the ICL isophotes on the one hand, but too conservative masking on the other hand prevents the routine from finding enough sampling points for the ellipse fitting. In order to estimate the light profiles beyond that SB, we fix the isophotal shape parameters ϵ, PA, X_0 and Y_0 for all ellipses that are larger than the one where the scatter in these parameters increases significantly. The semimajor axis radius for that ellipse is on average 207 ± 141 kpc with a median of 178 kpc. No isophotal parameters besides the flux are determined beyond this radius. The fluxes along all elliptical isophotes in the extended WWFI profiles are then determined by the method described in Sec. 4.2.

Systems with strong overlap between the BCG and satellite galaxies (e.g., A1656) are handled by mirroring parts of the uncontaminated side of the BCG on the contaminated side before measuring the isophotal shapes.

4.2 Isophotal flux measurement

The tools for the flux measurements are developed by us on the basis of Python scripts. They use the output isophotal shape tables that are provided by `ellfitn`. The flux along an isophote is measured in an elliptical annulus centered around that isophote. The annulus has

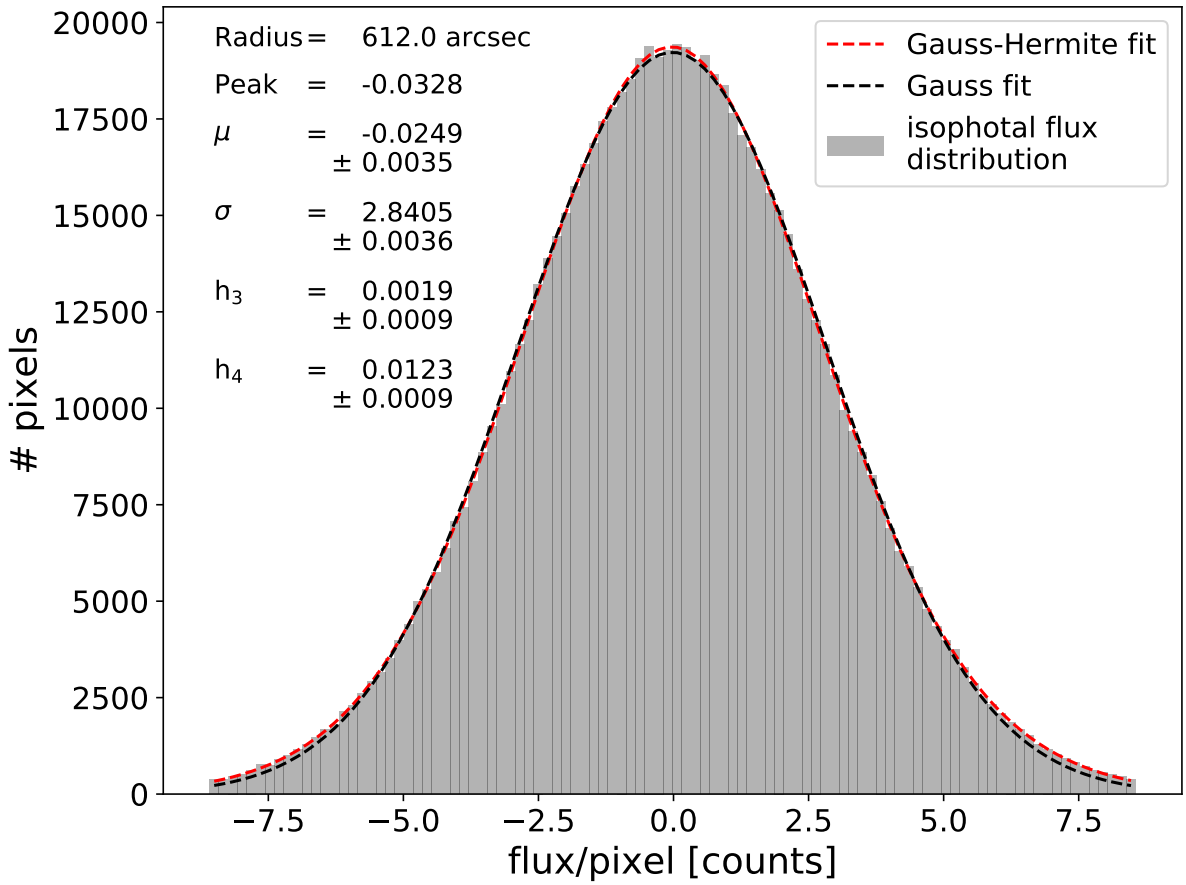

Figure 4.1: Pixel histogram of an example isophote with $SB = 30\ g'$ mag arcsec^{-2}. The flux units are calibrated for a pixel scale of $0.2''$/px and a photometric zero-point of $ZP = 30\ g'$ mag. The Gaussian fit is overplotted as a black dashed line, and the Gauss–Hermite fit that includes two higher orders h_3 and h_4 is overplotted as a red dashed line. The value μ is used to the calculate the SB of the isophote. The negative background constant is not yet subtracted here.

a thickness of the average separation between two consecutive isophotes, calculated in $r^{1/4}$ units and evaluated at the isophotal radius. In other words, the annuli are not overlapping but all together cover the full area. We measure the isophotal flux by fitting a Gaussian with two higher-order moments (van der Marel & Franx, 1993) to the pixel histogram (see Fig. 4.1). The distribution is $\kappa - \sigma$ clipped on both sides at three times the standard deviation. The third and fourth Gauss–Hermite moments are given by

$$f(F) = A \exp(-0.5F^2) \times [1 + h_3(c_1 F + c_3 F^3) + h_4(c_0 + c_2 F^2 + c_4 F^4], \tag{4.2}$$

where $F = (x - \mu)/\sigma$ with μ being the mean and σ being the standard deviation of the standard Gaussian. The normalization coefficient is A, and the other coefficients are given as $c_0 = \sqrt{6}/4$, $c_1 = -\sqrt{3}$, $c_2 = -\sqrt{6}$, $c_3 = 2\sqrt{3}/3$, and $c_4 = \sqrt{6}/3$. We use μ as the final value for the flux measurement.

The wings of the distribution are larger than what would be estimated from a simple Gaussian fit. Incompletely masked stellar halos, galactic outskirts, or cirrus introduce an asymmetry of the distribution toward more positive values, which we describe by the h_3 component. Noisier than average images are weighted less during coaddition. The result on the pixel histogram is similar to adding a second Gaussian component of low amplitude but with larger standard deviation to the high-S/N data. We quantify that behavior with the symmetric h_4 component.

The systematic errors in the light profile of the mock galaxy (see Sec. 5.1) were smallest when using the mean of the higher order Gaussian μ as a robust estimator for the flux. We therefore calculate all SBs from this parameter.

A residual, negative background constant remains in every coadded mosaic (see Sec. 3.1.5). We estimate this constant as the value to which the linear light profile converges at large radii. An example is shown in Sec. 5.1. That constant is subtracted from all flux data points before these are converted into magnitudes.

4.3 Composite SB profiles

To improve the spatial resolution of the inner light profiles, we deconvolve the innermost $80 \times 80''$ of our WWFI data using the `MIDAS` task `deconvolve/image`. The task uses 40 iterations of the Richardson–Lucy (1974) algorithm. If available (see Tab. 2.1), we use instead archival Hubble Space Telescope (HST) data in the filter band that is closest to the g'-band. The background constant is poorly calibrated in the HST imaging data. We vary it manually until the inferred SB profile agrees best and over the largest radial interval with the WWFI-determined SB profile. The photometric zero-point of the HST data is also adjusted in the same way.

A transition region is defined for each light profile where both the HST or deconvolved WWFI profile and the extended WWFI profile overlap well (horizontal lines in Fig. 4.2). Both profiles are merged in this transition region by weighted averaging of the data points.

The merging and replacing of the inner data points are done for all isophotal shape parameters.

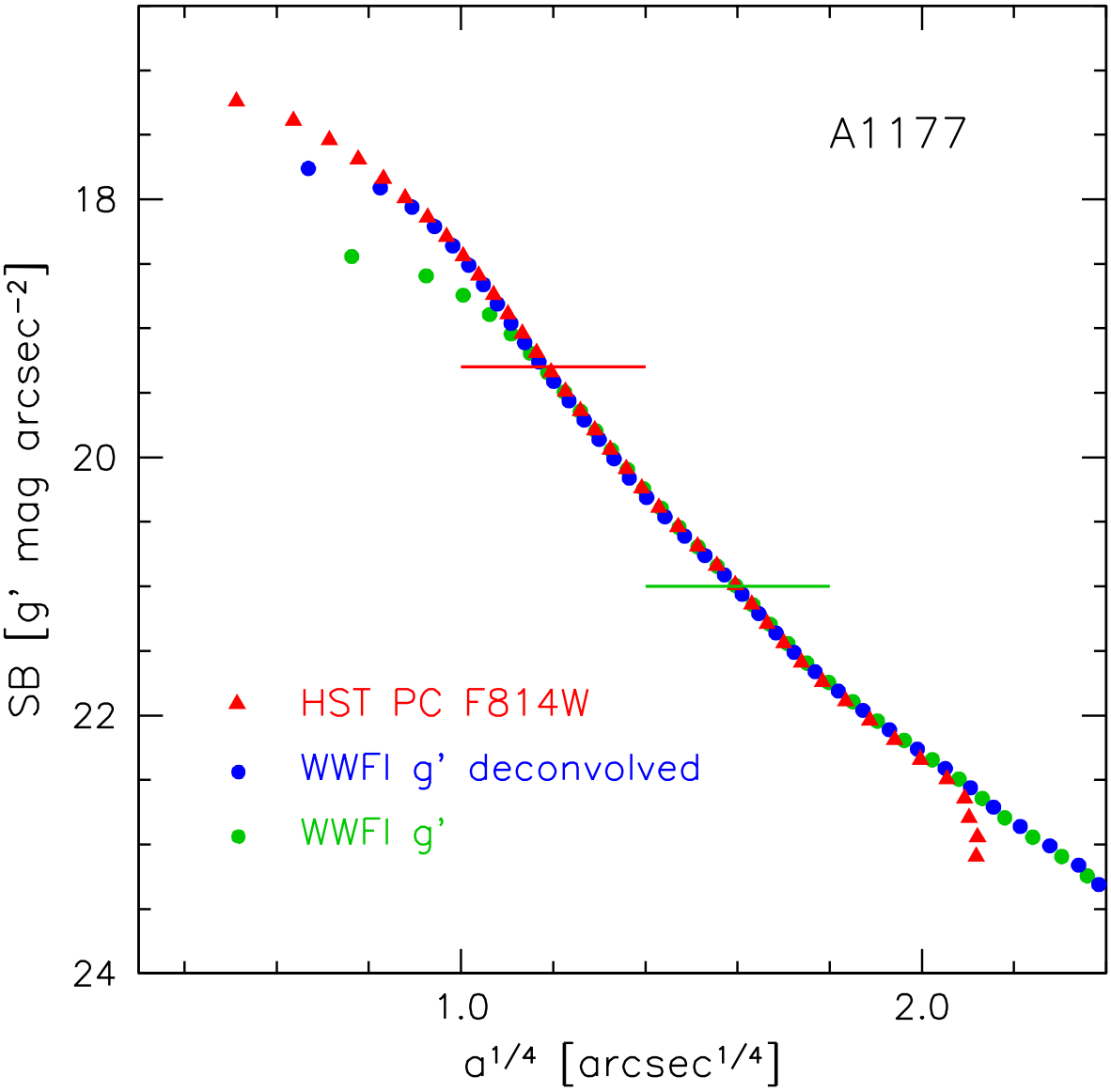

Figure 4.2: Inner light profile of NGC 3551 in A1177. The green and blue data points are obtained from WWFI data before and after deconvolution, respectively. The Nyquist sampling limit is reached at $a^{1/4} = 0.8''^{1/4} \widehat{=} 0.4'' = a$. The red data points are from archival HST data. The transition region between HST and nondeconvolved WWFI data is in between the two horizontal lines. A manual zero-point shift is applied to the HST data points to make the profiles overlap in the transition region.

4.4 Sérsic fits

The Sérsic (1968) function is an empirical description for SB profiles of elliptical galaxies. It fits the semimajor-axis profile shapes of elliptical and spheroidal galaxies overwhelmingly well over a large radial range that, for most galaxies, covers $93-99\%$ of the total galaxies' light (Kormendy et al., 2009). It was first used to fit SB profiles of BCGs by Graham et al. (1996), who demonstrated its superiority to the hitherto preferentially used de Vaucouleurs ($n=4$) profile because the Sérsic indices of BCGs are usually $n>4$. The Sérsic function is given by

$$SB(a) = SB_{\rm e} + c(n)\cdot\left[\left(\frac{a}{a_{\rm e}}\right)^{\frac{1}{n}} - 1\right], \tag{4.3}$$

where $a_{\rm e}$ is the effective radius, that is, the semimajor axis radius of the isophote that encloses one-half of the galaxies' total light. The effective surface brightness $SB_{\rm e} = SB(a_{\rm e})$ is the SB at radius $a_{\rm e}$. Half of each galaxy's total light is below this SB. It is not to be confused with $< SB_{\rm e} >$, the average surface brightness inside of $a_{\rm e}$, which is often used in the literature and significantly brighter than $SB_{\rm e}$. The normalization constant $c(n) = 2.5\times(0.868n-0.142)$ ensures that $a_{\rm e}$ encloses half of the total light. Finally, the Sérsic index n controls the outer upward bend of the profile. Higher Sérsic indices hint at a more dominant halo.

If the curvature becomes too strong, then n diverges. For instance, the SB profile of the L3009 BCG ($n=77\pm111$) has a curvature close to that critical value. The power-law slope of the SB profile for divergent n is +5. Stronger curvatures cannot be fitted by a single Sérsic function. We then extend the fitting formula by a second Sérsic function SB_2 to account for an outer light excess above the inner Sérsic function SB_1:

$$SB(a) = -2.5\log_{10}(10^{-0.4SB_1(a)} + 10^{-0.4SB_2(a)}). \tag{4.4}$$

The radius where both Sérsic profiles cross, that is, where their SBs are equal, is referred to as transition radius $r_\times$. The SB at that point is the transition surface brightness $SB_\times$.

The outer component is sometimes interpreted as the ICL, which is thereby assumed to be photometrically distinct. The (non)justification of this interpretation is discussed in Sec. 8. The BCGs whose light profile can be fitted well enough by only one Sérsic function are referred to as *single Sérsic BCGs* (SS BCGs), and the BCGs that need two additive Sérsic functions are referred to as *double Sérsic BCGs* (DS BCGs).

An alternative explanation for the origin of some DS profile shapes could be due to a central poststarburst stellar population that formed after a wet merger, as it is often seen in extra-light ellipticals (e.g., Faber et al. 1997; Kormendy 1999; Kormendy et al. 2009; Kormendy & Bender 2013). The origin of the DS shape would then be unrelated to the ICL phenomenon. Those BCGs have small DS transition radii relative to their effective radii $r_\times < 0.1 r_{\rm e}$ and small DS transition SBs of $SB_\times < 23$ g' mag arcsec^{-2} (Hopkins et al., 2009; Kormendy et al., 2009). We neglect those inner regions for the fits.

The composite SB profiles including the Sérsic fits are shown in Appendix A and the best-fit parameters are presented in Sec. 7.3. They are corrected for the broadening effects of the PSF wings (see Sec. 5.3). The fits are performed using the `python scipy` routine `curve_fit`, which is based on a nonlinear least squares method using the Levenberg–Marquardt algorithm. As pointed out by many authors (e.g., Seigar et al. 2007; Kormendy et al. 2009; Spavone et al. 2017), a simple χ^2 minimization based on measurement uncertainties is not optimal. The reasons are as follows: (1) the Sérsic model is empirical and does not describe the SB

profile shapes perfectly, especially not the intrinsic "wiggles"; (2) the brightest SB data points have negligible uncertainties compared to the faintest, outermost ones, which would therefore render the outermost data points useless; (3) errors are strongly correlated; and (4) symmetric uncertainties in the background constant are asymmetric in magnitude units. The SB profiles in Appendix A show that the scatter and systematic deviations from the Sérsic fits increase at faint SB levels. Therefore, we want to lower their weight but not neglect them for the fits. To achieve that, we minimize the function $\chi^2 = \sum_i (SB_i - SB_i^{\rm fit})/\Delta SB_i$ where SB_i is the ith SB data point, $SB_i^{\rm fit}$ is the value from the fit, and ΔSB_i are the uncertainties in SB that depend on SB_i itself. The latter do not represent the measurement uncertainties but still increase toward fainter SBs. We use a combination of two uncertainties. One is the background uncertainty of $\Delta BG = \pm 1$ count arcsec^{-2}, given for a photometric zero-point of $ZP = 30$ g' mag (see Sec. 5.1). Since the linear error bars are asymmetric in magnitude units, we mirror the upper error bars downward. We also added quadratically a systematic uncertainty of 0.18 g' mag arcsec^{-2} which is on the order of stronger intrinsic "wiggles" in the SB profiles. We get

$$\Delta SB = SB + 2.5 \log(10^{-0.4(SB-ZP)} + \Delta BG) + ZP + 0.18. \tag{4.5}$$

The errors of the best-fit parameters are estimated using Monte Carlo simulations. They are on the same order of magnitude as the uncertainties due to profile cropping (see Sec. 5.4).

The cores below a median major-axis radius of $a = 0.86 \pm 0.26''$ are excluded from the fits. The (usually) missing light has negligible influence on the structural parameters.

4.5 2D profile integration

We calculate the total flux $F_{\rm tot}$ and half-light parameters $r_{\rm e}$ and $SB_{\rm e}$ of the galaxies by integrating the 2D light profiles numerically while considering the radially varying ellipticities. The SB and ellipticity profiles are spline-interpolated and then evaluated on a grid with equidistant step sizes $\Delta a[''']^{1/4} = 0.001$. The ellipticities below (beyond) the first (last) measured data point are kept fixed. The SBs fainter than the last measured data point or below the limiting magnitude of our survey, $SB_{\rm lim} = 30$ g' mag arcsec^{-2} are replaced by the single or double Sérsic fit. The two outer limits to which we integrate the light profiles are $SB = 30$ g' mag arcsec^{-2} and effectively infinity.

The step sizes $a_{i+1} - a_i$ are smaller than the scales on which the flux F and ellipticity ϵ change significantly. In that limit holds the approximation

$$F_{\rm tot} \simeq \frac{1}{2}(F_{\rm tot}^{\rm lower} + F_{\rm tot}^{\rm upper}), \tag{4.6}$$

where

$$F_{\rm tot}^{\rm upper} = \sum_i F_{i+1} \cdot \pi(a_{i+1}^2(1-\epsilon_i) - a_i^2(1-\epsilon_i)), \tag{4.7}$$

$$F_{\rm tot}^{\rm lower} = \sum_i F_i \cdot \pi(a_{i+1}^2(1-\epsilon_i) - a_i^2(1-\epsilon_i)). \tag{4.8}$$

The effective radius r_e is the semimajor axis radius of the isophote that encircles one-half of the galaxy's integrated flux $F_{tot}/2$. The effective surface brightness SB_e is the SB at that isophote.

Chapter 5

Error analysis and correction for systematic effects

5.1 Background subtraction

The extended and faint nature of the ICL makes it susceptible to being subtracted in the progress of background subtraction. We examine the magnitude of this effect with the help of mock data. An empty sky region was observed with the same strategy as the galaxy clusters. Then we insert a mock BCG with a perfect Sérsic light profile ($r_{\rm e} = 100''$, $SB_{\rm e} = 26$ g' mag arcsec^{-2}, $n = 9$) into the raw data and reduce the data. The deviation of the measured light profile from the input profile provides a measure of the errors that we introduce by background subtraction and masking.

In Fig. 5.1 we show that the light profile of the mock galaxy is well preserved down to $SB = 31$ g' mag arcsec^{-2}. The main source of error is the choice of the residual background constant. It is always negative because of the flux-scaling of the NSF to the incompletely masked individual exposures (see Sec. 3.1.5). We conservatively estimate it to be ± 1 count arcsec^{-2}, based on the outermost surface flux profile flatnesses of the worst 75$^{\rm th}$ percentile of all BCGs in our sample. There is a tendency to choose a too-high value because of the finite field of view. The uncertainty corresponds to a limiting surface brightness of $SB_{\rm lim} = 30$ g' mag arcsec^{-2}. That estimation is in agreement with the comparison of the SB profiles measured from WWFI data and larger field-of-view data from the 40cm Wendelstein Telescope and 70cm Jay Baum Rich Telescope (JBRT; Sec. 5.5). The effect of choosing a too-high background constant is a drop in the outermost SB data points. That error only concerns surface brightnesses that are below our limiting magnitude $SB_{\rm lim} = 30$ g' mag arcsec^{-2}.

5.2 Galactic cirrus

Foreground dust in the Galaxy fundamentally limits the depth of optical imaging data (e.g., Miville-Deschênes et al. 2016 and references therein). It reflects the integrated stellar light of the Galaxy and becomes visible as filamentary structures that are easily misinterpreted as stellar streams. The dust emits at far-infrared and radio wavelengths and is thus easy to identify as not of extragalactic origin (Duc et al. 2015; Besla et al. 2016).

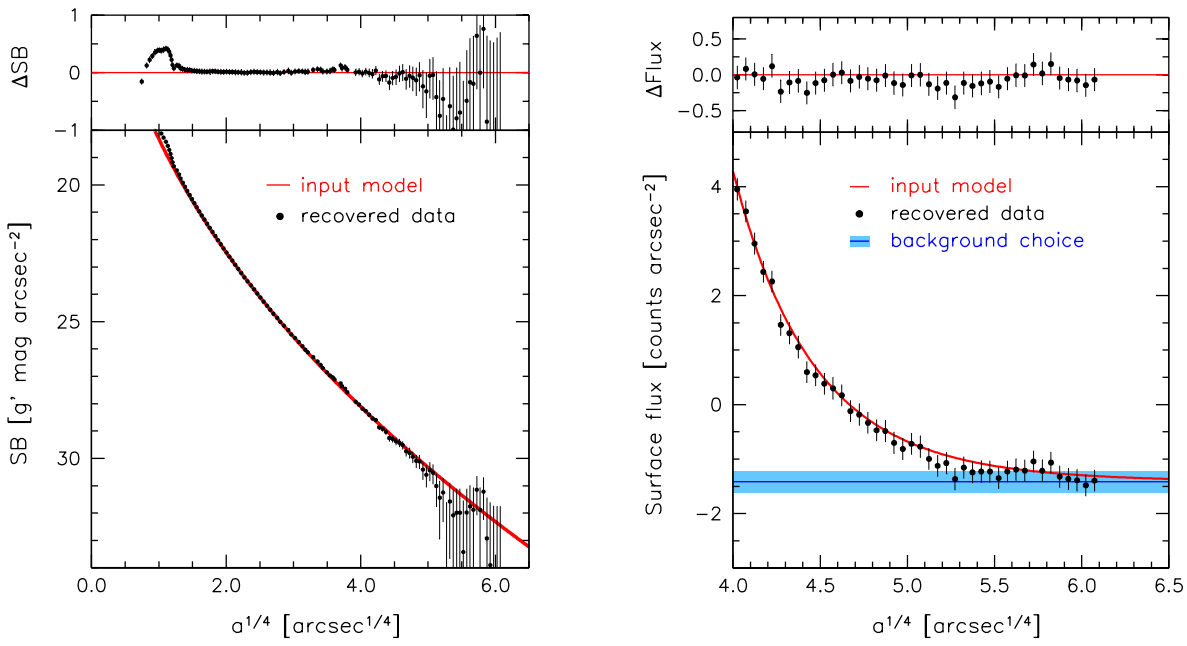

Figure 5.1: Recovered SB profile of a mock BCG that was inserted into raw data of a sky pointing. The regular data reduction including background subtraction was performed after that. The profile of the input model is plotted as a red line. The error bars are defined by the subjective uncertainty (blue shades) of the residual background constant (blue line).

We estimate the cirrus flux in our observations by scaling the 857 GHz (350 μm) far-infrared emission maps published by Planck Collaboration et al. (2014) so that the overall variations in dust flux match the ones of the galactic cirrus in our most strongly contaminated cluster A407 (see Fig. 5.2):

$$F^{g'}_{\rm cirrus}\ [\rm counts] \approx 0.5 F_{857\rm GHz}\ [\rm MJy\ sr^{-1}], \tag{5.1}$$

where the units on the left-hand side are calibrated to a photometric zero-point of $ZP = 30\ g'$ mag and a pixel scale of $0.2''$/pixel. We match the variations in flux and not the absolute flux because the average background was already subtracted from the WWFI stacks during data reduction. The residual cirrus is visible down to a surface brightness of $SB \sim 28\ g'$ mag arcsec^{-2} to which level we mask it by hand. Hidden cirrus below this SB level can evoke a systematic scatter in the outermost data points of the light profiles.

We define three categories of increasing cirrus contamination: A (invisible in the optical images), B (weak contamination), and C (strong contamination; see Fig. 5.2). Not the total dust flux but its large-scale variations have the strongest influence on the light profiles. We estimate these variations as the standard deviation σ of the dust surface flux in binned, 15×15 px sized thumbnails of the one-square-degree fields of view. The thresholds are expressed as surface brightness variations SB_σ in units of g' mag arcsec^{-2}:

$$\begin{aligned} &\text{Category A :} && 27.6 < SB_\sigma \\ &\text{Category B :} && 26.9 < SB_\sigma < 27.6 \\ &\text{Category C :} && SB_\sigma < 26.9. \end{aligned} \tag{5.2}$$

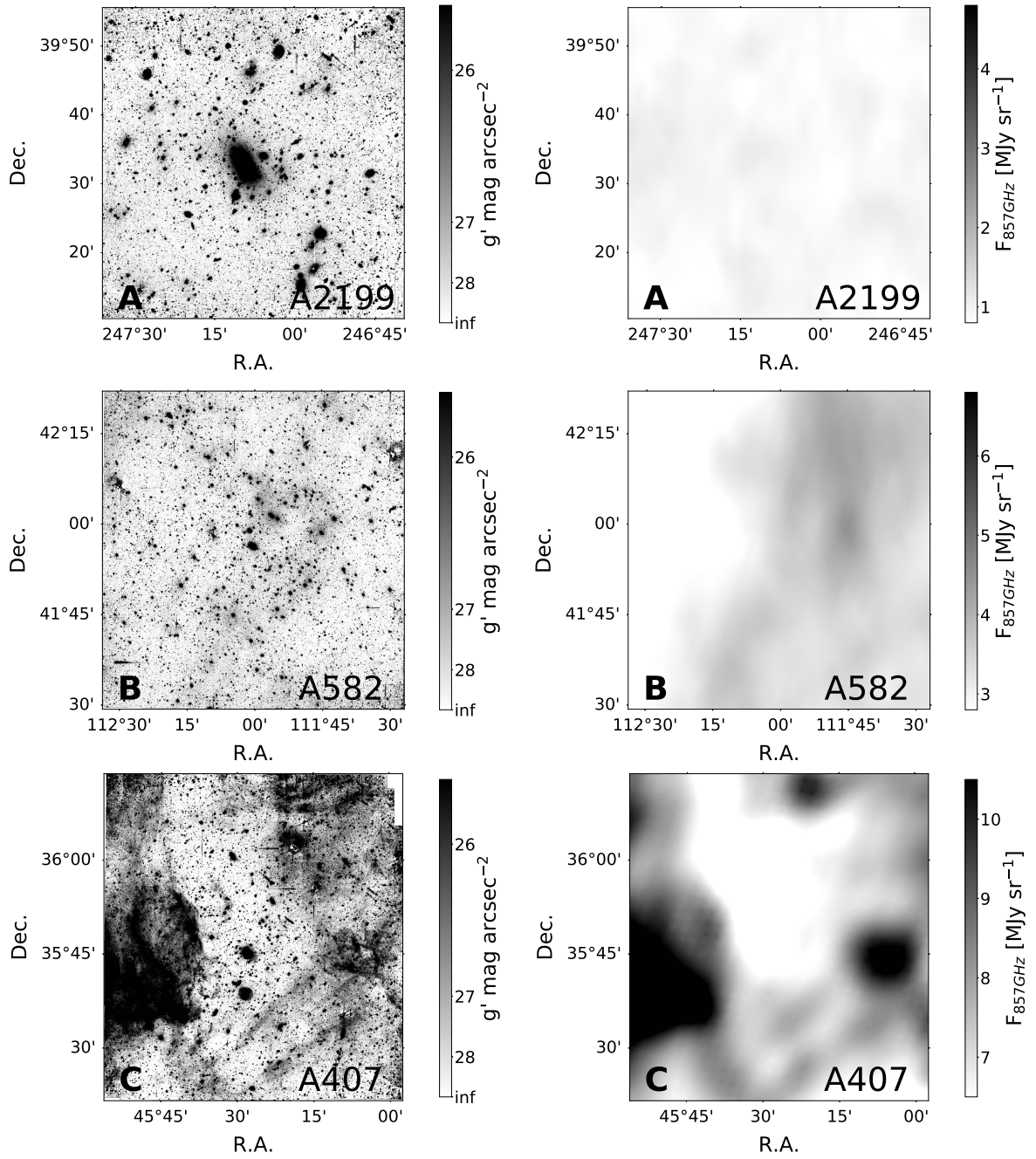

Figure 5.2: *Left panels from top to bottom:* three examples for contamination by Galactic cirrus across the fields of view of A2199, A582, and A407. All image cutouts are centered on the BCG. Contamination categories increase from A to C. *Right panels:* far-infrared 857 GHz maps of the same regions from Planck Collaboration et al. (2014). Note that the background constant and gradient in the optical images were modeled and subtracted by the night-sky flat procedure (see Sec. 3.1.5). The full-sized images of all observed clusters are shown in Appendix C.

The cirrus-contamination category of each cluster is labeled on the image cutouts in Appendix B. In our sample, 131 clusters (77%) belong to category A, 28 clusters (16.5%) to category B, and 11 clusters (6.5%) to category C.

That strength of contamination is reduced (1) by manual masking, (2) by applying a robust estimator on the pixel histogram (see Sec. 4.2), (3) because the flux is averaged along the large isophotes in the low-SB galactic outskirts, and (4) because large-scale variations, that is, a gradient across the field of view is included in the NSFs and subtracted.

An all-sky map of the scaled far-infrared map is shown in Fig. 2.1.

5.3 PSF effects

Seeing has a distorting influence on the light profiles: central galaxy light is redistributed toward larger radii. This effect manifests itself as (1) a flattening and circularization in the inner few arcseconds and (2) brighter SB in the range $1 \lesssim r \lesssim 4$ PSF FWHM. The effect is of the order of the core sizes of the local BCGs that we aim to resolve. As explained in Sec. 4, we therefore replace the central part of the light profiles by the ones that we either measured from archival (undeconvolved) Hubble Space Telescope imaging data or deconvolved WWFI data. As shown in Fig. 4.2, the deconvolved profiles are accurate to almost Nyquist sampling quality, that is, $\gtrsim 0.4''$ resolution. The cores with sizes of order $1''$ are therefore real and not resolution artifacts.

Not only the PSF's center but also its outer wings distort the galaxy light profiles (see Duc et al. 2015 and references therein or Trujillo & Fliri 2016). The PSF's wings and reflections from the BCG's center overlap with the ICL. In other words, light is redistributed from the center to the outskirts. We refer to this effect as PSF broadening. It becomes a problem when the galaxy's center is bright compared to its outer halo. Fig. 5.3 shows the severity of this effect. SB profiles of two (red and black) representative model BCGs are plotted as dotted lines. The SB profiles after 2D convolution with the PSF are overplotted as dashed lines. The systematic error due to PSF broadening is $0.1 > \Delta SB > 0.5$ g' mag arcsec^{-2} and increasing with galaxy size.

We now describe our correction method for the broadening effect. The accurate approach would be to deconvolve the imaging data prior to the SB profile measurement. However, this is computationally challenging considering the large kernel size of $\sim 2000 \times 2000$ pixels and Richardson–Lucy deconvolution (Lucy, 1974) being an iterative procedure. We use a computationally faster method that is based on the approximation that the amount of scattered light is small (1.78%, see Sec. 3.1.4) compared to the total light. Under these circumstances, a secondary convolution $i * t$ by image processing results in similar light scattering even after the primary convolution $i = r * t$ by the telescope optics is already inherent to the images. That is quantified by

$$i = r * t, \tag{5.3}$$

$$r \approx i - (i * t - i), \tag{5.4}$$

where r is the unknown intrinsic light distribution, t is the kernel, that is, the PSF, and i is the image data after primary convolution. We apply a 2D convolution[1] to images that

[1]We also experimented with a 1D convolution using the `python` package `scipy.signal.convolve`. A simple

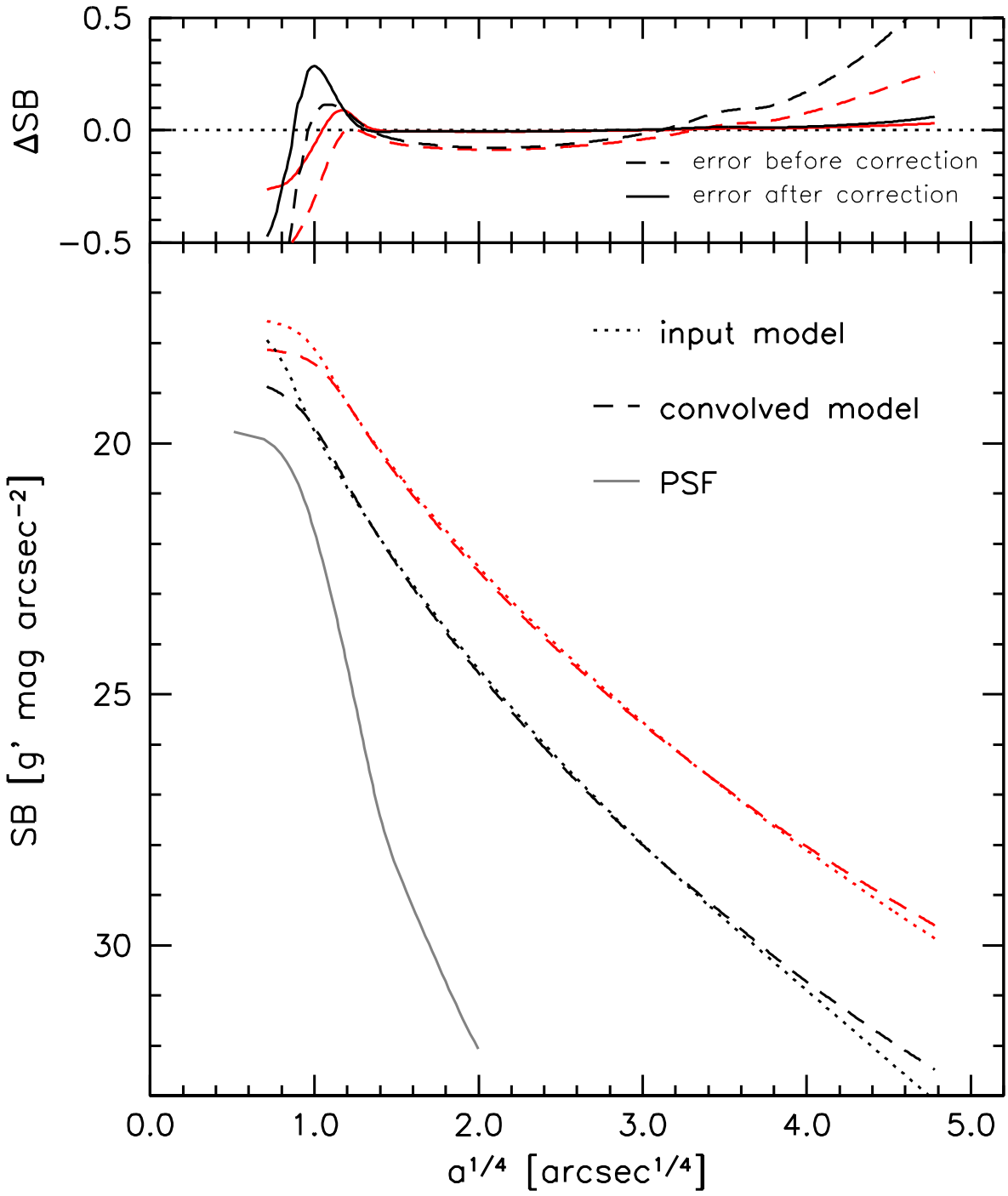

Figure 5.3: Effect of PSF broadening on SB profiles of two different mock BCGs (red and black). The dotted lines show the original SB profiles, and the dashed lines show the profiles after convolution with the PSF. The dashed and continuous lines in the top panel show the residuals before and after correction, respectively.

were regenerated from the isophotal shape parameters. The scattered light is reconstructed by subtracting the twice-convolved image $i * t$ from the primary convolved image i. Then, by subtracting this scattered light from the primary convolved image, the intrinsic light distribution is recovered (see Eq. 5.4).

The deviation of the corrected from the original (intrinsic) light profiles of the mock BCGs is shown in Fig. 5.3 (top panel) as continuous lines. The SB data points at radii $a > 4''$ agree well with the input model. The inner regions are badly recovered because the small-influence approximation fails there. However, these regions of the profiles are replaced by those derived from HST or deconvolved WWFI data (see Sec. 4.3).

Each SB profile of the real BCGs is corrected individually. The median correction for the structural parameters that are determined by direct integration of the light profiles (i.e., independent of the Sérsic fits) is

$$r_{\rm e,30}^{\rm corrected}/r_{\rm e,30}^{\rm uncorrected} = 0.94 \pm 0.03, \tag{5.5}$$
$$SB_{\rm e,30}^{\rm corrected} - SB_{\rm e,30}^{\rm uncorrected} = -0.11 \pm 0.05, \tag{5.6}$$
$$M_{\rm tot,30}^{\rm corrected} - M_{\rm tot,30}^{\rm uncorrected} = 0.03 \pm 0.02, \tag{5.7}$$

where the index "30" indicates that the parameters were determined by integrating the light profiles out to the isophote with $SB = 30$ g' mag arcsec^{-2} (for details, see Sec. 4.5). As expected, only a small influence on the integrated brightness is found. The integration aperture is sufficiently large that the redistribution of the light is close to negligible. The effective radii are increased and the effective surface brightnesses are dimmed by the broadening effect.

After fitting Sérsic functions to the SB profiles before and after PSF broadening correction, we calculate the median corrections for the Sérsic parameters of the SS BCGs:

$$r_{\rm e,SS}^{\rm corrected}/r_{\rm e,SS}^{\rm uncorrected} = 0.88 \pm 0.06, \tag{5.8}$$
$$SB_{\rm e,SS}^{\rm corrected} - SB_{\rm e,SS}^{\rm uncorrected} = -0.25 \pm 0.06, \tag{5.9}$$
$$n_{\rm SS}^{\rm corrected}/n_{\rm SS}^{\rm uncorrected} = 0.94 \pm 0.03, \tag{5.10}$$

and for the Sérsic parameters of the DS BCGs:

$$r_{\rm e,DS1}^{\rm corrected}/r_{\rm e,DS1}^{\rm uncorrected} = 0.99 \pm 0.04, \tag{5.11}$$
$$SB_{\rm e,DS1}^{\rm corrected} - SB_{\rm e,DS1}^{\rm uncorrected} = -0.03 \pm 0.08, \tag{5.12}$$
$$n_{\rm DS1}^{\rm corrected}/n_{\rm DS1}^{\rm uncorrected} = 0.99 \pm 0.04, \tag{5.13}$$
$$r_{\rm e,DS2}^{\rm corrected}/r_{\rm e,DS2}^{\rm uncorrected} = 0.95 \pm 0.03, \tag{5.14}$$
$$SB_{\rm e,DS2}^{\rm corrected} - SB_{\rm e,DS2}^{\rm uncorrected} = -0.04 \pm 0.08, \tag{5.15}$$
$$n_{\rm DS2}^{\rm corrected}/n_{\rm DS2}^{\rm uncorrected} = 0.96 \pm 0.04. \tag{5.16}$$

test applied to a slice along the major axis of a BCG and PSF light profiles results in a stronger broadening effect than for the 2D convolution and, hence, erroneous results.

5.4 Undetected ICL below the limiting magnitude

The SB limit of our survey is $SB_{\rm lim} = 30$ g' mag arcsec^{-2}. Below that limit, we have no reliable information on how the SB profiles continue. An educated guess is the extrapolation of the fitted Sérsic profiles because there is no indication for a truncation just above this limit (see Sec. 7.2). The following median corrections have to be applied when the lower SB boundaries are increased from 30 to infinity g' mag arcsec^{-2}:

$$r_{\rm e,\infty}/r_{\rm e,30} = 1.20 \pm 0.15, \tag{5.17}$$

$$SB_{\rm e,\infty} - SB_{\rm e,30} = 0.31 \pm 0.22, \tag{5.18}$$

$$M_{\rm tot,\infty} - M_{\rm tot,30} = -0.09 \pm 0.06. \tag{5.19}$$

The indices "30" and "∞" indicate the SB of the outermost considered isophote. **The averages of both values are listed in Appendix D, and the uncertainties derived from both integration limits are taken as the error.** We stress again that all median correction factors in Sec. 5.3 and 5.4 are only given for illustrative purposes. Each SB profile was corrected individually.

5.5 Comparison to data obtained with other telescopes

The key obstacle for deep imaging is the task of background subtraction. In addition to the mock-BCG test described in Sec. 5.1, we perform another test to make sure that the ICL is not oversubtracted in the WWFI data. For a control sample, we have obtained independent imaging data for A1177 with the 70cm JBRT at the WISE observatory (2 hr target integration time) and for A2589 with the 40cm telescope at the Wendelstein observatory (12 hr integration time). Both imagers span an even wider field of view than the WWFI and are made of one single CCD chip. That makes them less susceptible to systematic errors during background subtraction because the BCG+ICLs cover a smaller fraction of the field of view and less masking is required.

The control sample data were observed, dithered, and reduced in a similar way to the WWFI data. The only difference is the method of background subtraction. The background in the 70cm JBRT data was modeled by fourth-order 2D polynomials in each exposure. Nonphotometric observing conditions degraded the stability of the background pattern so that the NSF method failed. However, the polynomial approach works sufficiently well because of the large field of view.

The background in the 40cm WST data was modeled by scaling and averaging the two bracketing source-masked exposures that were taken before and after each exposure. No offset sky exposures were taken. The sky background is modeled from the science exposures themselves. The large dither pattern ensures that empty sky regions in the bracketing exposures always fall around the BCG's position so that the sky is modeled accurately across the whole field of view. Regions that happen to be masked in both bracketing exposures are replaced by fourth-order 2D polynomials that were fitted to the whole average sky images.

Figure 5.4 shows a comparison of the SB profiles measured in both datasets. The WWFI-obtained profiles are plotted before (gray) and after (black) PSF broadening correction (see Sec. 5.3). The two comparison profiles are not PSF broadening corrected. The overall agreement especially in the outermost data points provides further confidence in the accuracy

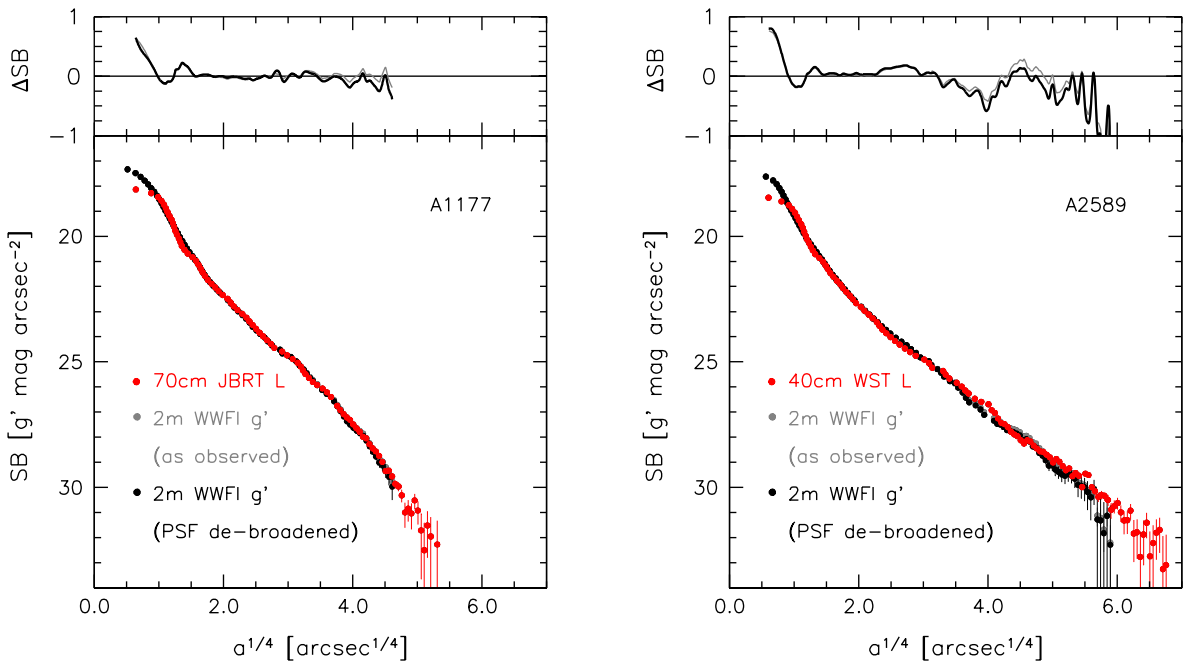

Figure 5.4: Control sample of two BCGs that were observed independently with different telescopes (red data points). *Left panel:* 70 cm Jay Baum Rich Telescope (JBRT) at the WISE observatory, owned and operated by Tel Aviv University. *Right panel:* 40 cm telescope at the Wendelstein observatory. The photometric zero-points of the L-band profiles are adjusted so that the L-band profiles match the WWFI g'-band profiles for comparison. Color gradients in the two filters are assumed to be negligible. The WWFI g'-band profiles are shown with (black) and without (gray) PSF debroadening correction. The deviations of the spline-interpolated comparison profiles from the WWFI profiles are shown in the top panels.

of the background subtraction method. Moreover, it confirms that <1m class telescopes can be sufficient to perform deep imaging projects by reaching the 30 g' mag arcsec^{-2} SB limit.

Chapter 6

Host cluster properties

6.1 Physical parameters

In order to understand the connection between BCG/ICL and cluster formation, we calculate and measure various parameters that describe the current evolutionary state of the host clusters of our BCG sample.

The cluster dispersions $\sigma_{\rm C}$, i.e., the dispersion of line-of-sight velocities of the cluster satellite galaxies are taken from Lauer et al. (2014). The satellite galaxies' positions were retrieved from the `SIMBAD` database. The search radius is $r_{\rm max} = 2$ Mpc in transversal and $v_{\rm BCG} \pm 3000$ km s^{-1} (using spectroscopic or photometric redshifts) along the line of sight direction around the BCG. The satellite galaxy samples are inhomogeneous with respect to the detection thresholds. However, we assume that this adds only a statistical error to our inferred correlations.

Following Tully (2015), we define the projected gravitational radius $r_{\rm g}$ as

$$r_{\rm g} = \frac{S^2}{\sum_{i<j} 1/r_{ij}} \tag{6.1}$$

where S is the total number of `SIMBAD` satellite galaxies inside $r_{\rm max} = 2$ Mpc, i.e., the cluster richness, and r_{ij} is the projected distance between galaxy pairs. The gravitational radius resembles the characteristic separation between two satellite galaxies. We estimate the error of $r_{\rm g}$ by using two different radial boundaries on the satellite galaxy samples:

$$\delta r_{\rm g} = |r_{\rm g}(r_{\rm max} = 2.5) - r_{\rm g}(r_{\rm max} = 1.5)| \tag{6.2}$$

The gravitational mass $\mathcal{M}_{\rm g}$ is given by

$$\mathcal{M}_{\rm g} = \alpha \sigma_{\rm p}^2 \times (\pi/2) r_{\rm g}/G \tag{6.3}$$

where G is the gravitational constant. The factors $(\pi/2)$ and α arise from the deprojection of the galaxy positions and velocity dispersion, respectively. The value of $\alpha = 2.4$ is adopted from Mamon et al. (2010) for an anisotropy model (Mamon & Łokas, 2005) that is a good fit to ΛCDM halos.

We further calculate the cluster mass density

$$\rho = \mathcal{M}_{\rm g}/(4/3\pi r_{\rm g}^3), \tag{6.4}$$

the satellite galaxy number density

$$s = S/(4/3\pi r_{\rm g}^3), \tag{6.5}$$

the mass phase space density

$$f_{\mathcal{M}_{\rm g}} = \rho/\sigma_{\rm C}^3, \tag{6.6}$$

and the galaxy number phase space density

$$f_{\rm s} = S/(4/3\pi r_{\rm g}^3 \times \sigma_{\rm C}^3). \tag{6.7}$$

The integrated brightness of all satellite galaxies $M_{\rm sat}$ is measured directly from the WWFI images and independent of the `SIMBAD` sample. The average field of view spans 1.64±0.49 Mpc in radius centered on the BCG. The procedure is the following: we mask all foreground stars that are listed in the Tycho-2 (Høg et al., 2000) and Pan-STARRS PV3 catalogs (Flewelling et al., 2016) catalogs, as well as in the source catalogs created with `SExtractor` from the WWFI images. We then multiply the masks which were created to measure the isophotal flux of the BCGs (see Sec. 3.2, §2) onto the WWFI stacks. That product image is then subtracted from the WWFI stacks so that only galaxies (excluding the BCG+ICL) remain in the difference image. The remaining flux is then measured in circular apertures centered around the BCG. The background is subtracted from the light profiles analogous to the procedure described in Sec. 4.2. These light profiles are then integrated and the uncertainties in the flux are estimated from the uncertainty of the background level choice.

All derived cluster properties are listed in Appendix E.

6.2 Alignment

Since the BCG, the ICL and the cluster galaxy density distribution are all to first order elliptical (or triaxial in 3D), we can measure the centers $\boldsymbol{r}_0$ and position angles PA for all three components by fitting ellipses to the isophotes or isodensity contours.

For the clusters, we use the satellite galaxy catalogs that are described in Sec. 6.1 to measure the galaxy density distribution. Firstly, we Voronoi bin the projected galaxy positions. Each voronoi cell is then divided by its surface area to obtain a galaxy density map. These maps are then smoothed using a Gaussian kernel with a standard deviation of 4 kpc $< \sigma_{\rm K} <$ 80 kpc which is optimized for each cluster by hand. The isodensity contours of the smoothed galaxy density maps are then fitted using `ellfitn` (see Sec. 4.1). Since substructures deform the isodensity contours, we manually select the fitted contour which resembles the overall cluster center and PA best by hand.

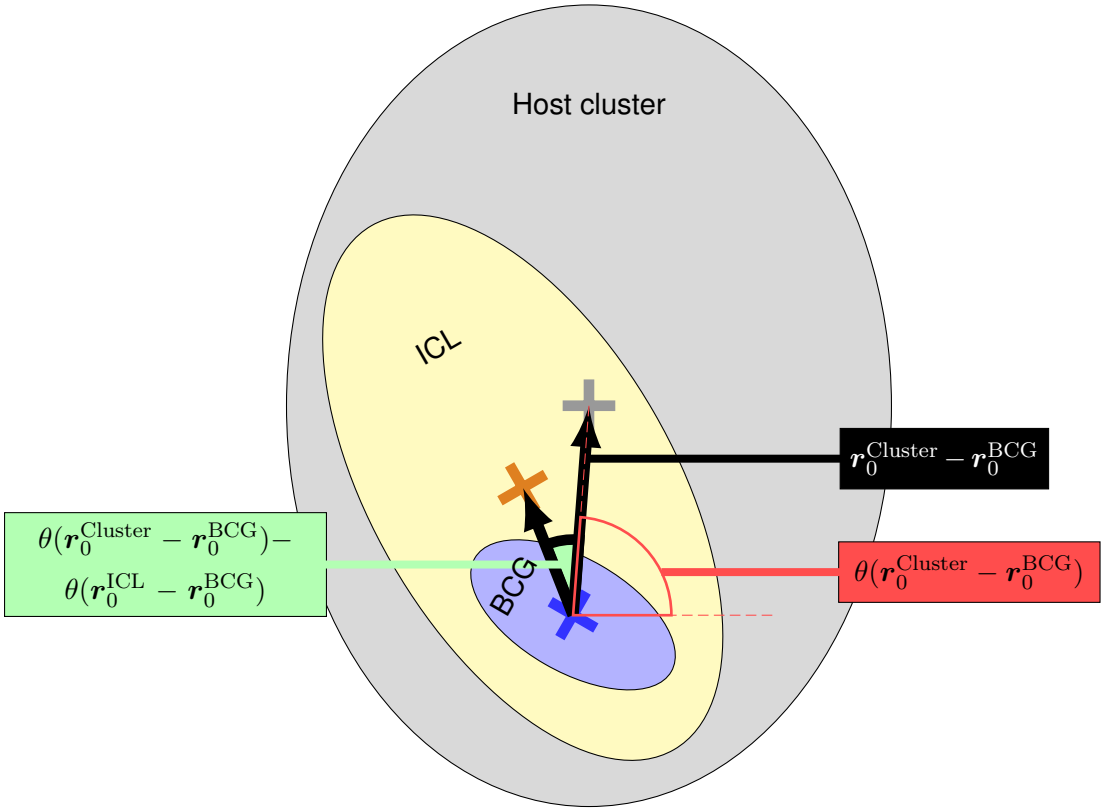

Figure 6.1: Schematic alignment between BCG (blue), ICL (yellow) and host cluster (gray). All three components have different position angles PA, which are measured independently from the offset direction. The two black arrows point from the BCG center towards the ICL- or host cluster-center, each marked with a cross. The angle θ of these vectors is counted anti-clockwise from the horizontal, red dashed line. However, only the absolute difference (green) between the two angles is of interest because it is the offset direction of the ICL with respect to the BCG. If the ICL is offset towards the host cluster center, then $|\theta(\boldsymbol{r}_0^{\mathrm{Cluster}} - \boldsymbol{r}_0^{\mathrm{BCG}}) - \theta(\boldsymbol{r}_0^{\mathrm{ICL}} - \boldsymbol{r}_0^{\mathrm{BCG}})| = 0°$.

The projected offset between the center of one component i with respect to a second component j is given as

$$\boldsymbol{r}_0^i - \boldsymbol{r}_0^j = \begin{pmatrix} \Delta R.A. \times \cos(Dec) \\ \Delta Dec \end{pmatrix}, \tag{6.8}$$

where i and j are either the BCG, ICL or the cluster galaxy density distribution. The angle of that resulting vector is

$$\theta(\boldsymbol{r}_0^i - \boldsymbol{r}_0^j) = \arctan\left(\frac{\Delta Dec}{\Delta R.A. \times \cos(Dec)}\right). \tag{6.9}$$

A schematic illustration for these quantities is shown in Fig. 6.1. Both, $\boldsymbol{r}_0$ and PA have measurement uncertainties which are especially large at large radii. In order to obtain a high S/N measurement for the BCG and ICL, we average PA and $\boldsymbol{r}_0$ below a major-axis radius $a < 30$ kpc for the BCG and beyond $a > 30$ kpc for the ICL. That radius is technically motivated so that roughly the same amount of data points are averaged in each interval. No averaging was done for the galaxy density distribution; the isophote which resembles the cluster PA best is chosen by hand.

Chapter 7

Results

7.1 Accretion and merging signatures

The advent of low-surface-brightness photometry has unveiled a myriad of fine structure in the outskirts of galaxies. These relics of violent accretion have been predicted by numerical simulations as the most direct evidence for hierarchical clustering (Bullock & Johnston 2005; Johnston et al. 2008; Rudick et al. 2009; Cooper et al. 2010; Puchwein et al. 2010; Cooper et al. 2013; Rodriguez-Gomez et al. 2016; Harris et al. 2017; Mancillas et al. 2019). They have been discovered around local late-type galaxies (e.g., Martínez-Delgado et al. 2010; Chonis et al. 2011; Foster et al. 2014; Ibata et al. 2014; Amorisco et al. 2015; Merritt et al. 2016) and local early-type galaxies (Tal et al. 2009; Duc et al. 2015; Bílek et al. 2016; Crnojević et al. 2016; Duc 2017), as well as galaxy groups (Da Rocha & Mendes de Oliveira, 2005; Da Rocha et al., 2008; Watkins et al., 2014, 2015; Okamoto et al., 2015; Spavone et al., 2018) and galaxy clusters (Feldmeier et al. 2002; Arnaboldi et al. 2012; Iodice et al. 2016, 2017, 2019; Mihos et al. 2017). A review on the topic can be found in Carlin et al. (2016). For a comparison between literature data on the frequency of disturbed morphologies, see Atkinson et al. (2013).

We visually inspect the clusters for accretion and merging signatures and classify them into four categories: (1) two BCGs, (2) shells, (3) tidal streams, and (4) multiple nuclei. There was no a priori knowledge of the galaxies' Sérsic type during the identification procedure. To maximize our likelihood of finding structures on various surface brightnesses, we have visually scanned linearly and logarithmically scaled, minimum filtered (Bílek et al., 2016), isophote-model and parametric-model subtracted images. The 2D models for the latter two methods are created from the isophotal shape profiles. For the parametric models, we replaced the SB values in the data tables by their corresponding SS or DS fit values.

One prototypical example for each category is shown in Fig. 7.1, top panel. An explanation of the characteristics of each category follows.

The "two BCGs" category is not a direct sign of interactions between galaxies, but a likely indicator for merging clusters, as is the case for the Coma cluster. Since the appearance of at least two similar-sized BCGs is a hint of a nonrelaxed state of the cluster, we include this category in our analysis. We find that 7.0% of the clusters have two BCGs (4.1% for SS BCG clusters and 12.2% for DS BCG clusters).

Shells are accumulations of stars that align in circle segments around the BCG center (e.g.,

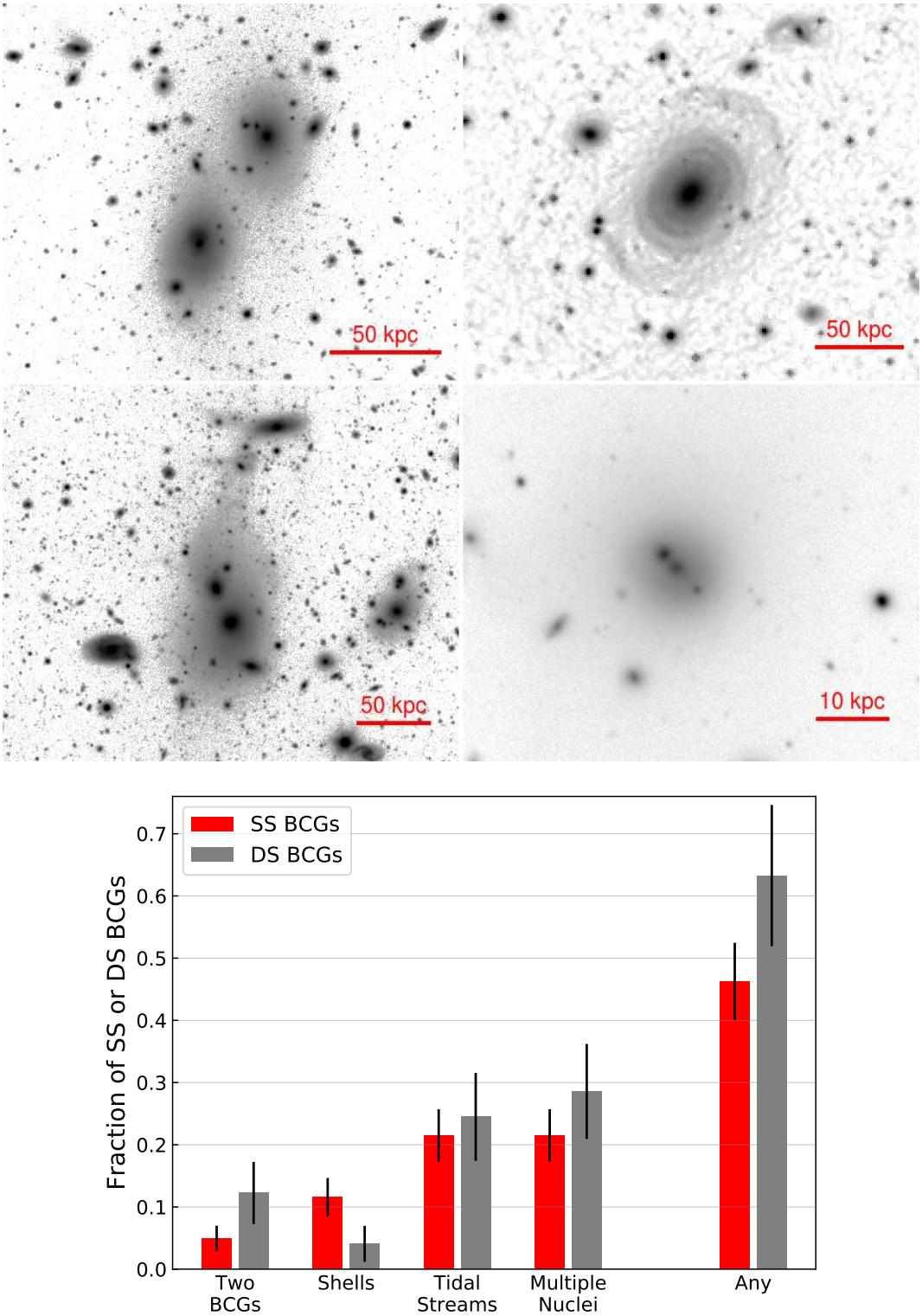

Figure 7.1: Accretion and merging signatures. *Top panel:* representative examples for each category. Top left: two BCGs in A1190. Top right: shells in A2197. Bottom left: tidal Streams in A1257. Bottom right: multiple nuclei in A1185. *Bottom panel:* relative abundance of each of the four features and of any of the four features.

Malin & Carter 1980, 1983; Hernquist & Quinn 1988, 1989 and many more). These segments can be more or less concentric, depending on the type of shell system. They form when a satellite galaxy falls onto the BCG on a nearly radial trajectory with pericentric distance < 15 kpc (Karademir et al., 2019) and is disrupted (Bílek et al. 2016; Pop et al. 2018). The shells mark the turnaround lines in the orbits of the progenitor's stars. Shells have been reproduced in simulations with mass ratios of the merging galaxies ranging from 1/100 (Quinn, 1984; Karademir et al., 2019) to $> 1/3$ (Karademir et al. 2019; Pop et al. 2018). See also Bílek et al. (2015) for a review. Shells are found in between $\sim 10\%$ (Schweizer & Seitzer, 1988) and $\sim 22\%$ of elliptical galaxies (Tal et al., 2009). The frequency in the Illustris simulation is $18 \pm 3\%$, which increases with increasing mass cut (Pop et al., 2018). We find that 9.4% of our analyzed BCGs show shells (11.6% of SS BCGs and 4.1% of DS BCGs). A lower frequency could be explained with the degrading angular resolution because the BCGs in our sample are a factor of $\sim$10 more distant than the local ellipticals in the Tal et al. (2009) sample, which decreases the detectability of existing shells. Our result should therefore be understood as a lower boundary for the abundance of shells in BCGs.

Tidal streams are made of stars that were liberated from a satellite galaxy by a collision (Moore et al., 1996) or due to the mean tidal field of the cluster (Merritt, 1984). These unbound stars then virialize in the cluster and add up to the ICL budget. For instance, unprecedentedly deep photometric surveys of the Virgo (Mihos et al., 2017) and Fornax clusters (Iodice et al., 2016, 2017, 2019) have unveiled multitudes of tidal streams. Other examples have been discovered in the Coma and Centaurus clusters (Gregg & West 1998; Trentham & Mobasher 1998; Calcáneo-Roldán et al. 2000). We do not make a strict differentiation between tidal tails and tidal streams as proposed by Duc et al. (2015) because we lack color information. Finally, we find that 22% of our observed BCGs show some form of stream-like features (21% of SS BCGs and 24% of DS BCGs). The features are usually dynamically hotter than the ones reported for field galaxies (e.g., Martínez-Delgado et al. 2010) and thus dissolve quicker. The observed abundance therefore implies ongoing ICL accretion.

Multiple nuclei are in $\sim 47\%$ of the cases simply chance superpositions as concluded from their undisturbed morphology (Lauer, 1988). The remaining half is split into high-velocity unbound interactions (24%) with radial velocity differences $\Delta V \gtrsim 400$ km s^{-1} that lead to tidal stripping of the secondaries' envelopes and possible low-velocity, strong merger interactions (29%) that lead to cannibalism of the secondary nucleus (Lauer 1988; see also Tonry 1985a,b; Beers & Tonry 1986). Without differentiating between the cases of real interactions and pure projections, we identify at least one secondary nucleus in 24% of all BCGs (21% of SS BCGs and 24% of DS BCGs). That is a slightly lower fraction than values reported in the literature (28%, Hoessel 1980; 45%, Schneider et al. 1983).

The relative abundances of the four discussed types of accretion signatures are also shown in Fig. 7.1. The error bars are determined using Poisson statistics. We cannot tell whether SS or DS BCGs have higher abundances of specific accretion signature types, due to small-number statistics. However, the total frequency of accretion signatures is 46% for SS BCGs and 63% for DS BCGs. The latter show more indications of ongoing merging processes with a 1σ certainty. The frequency for all BCGs is 51%.

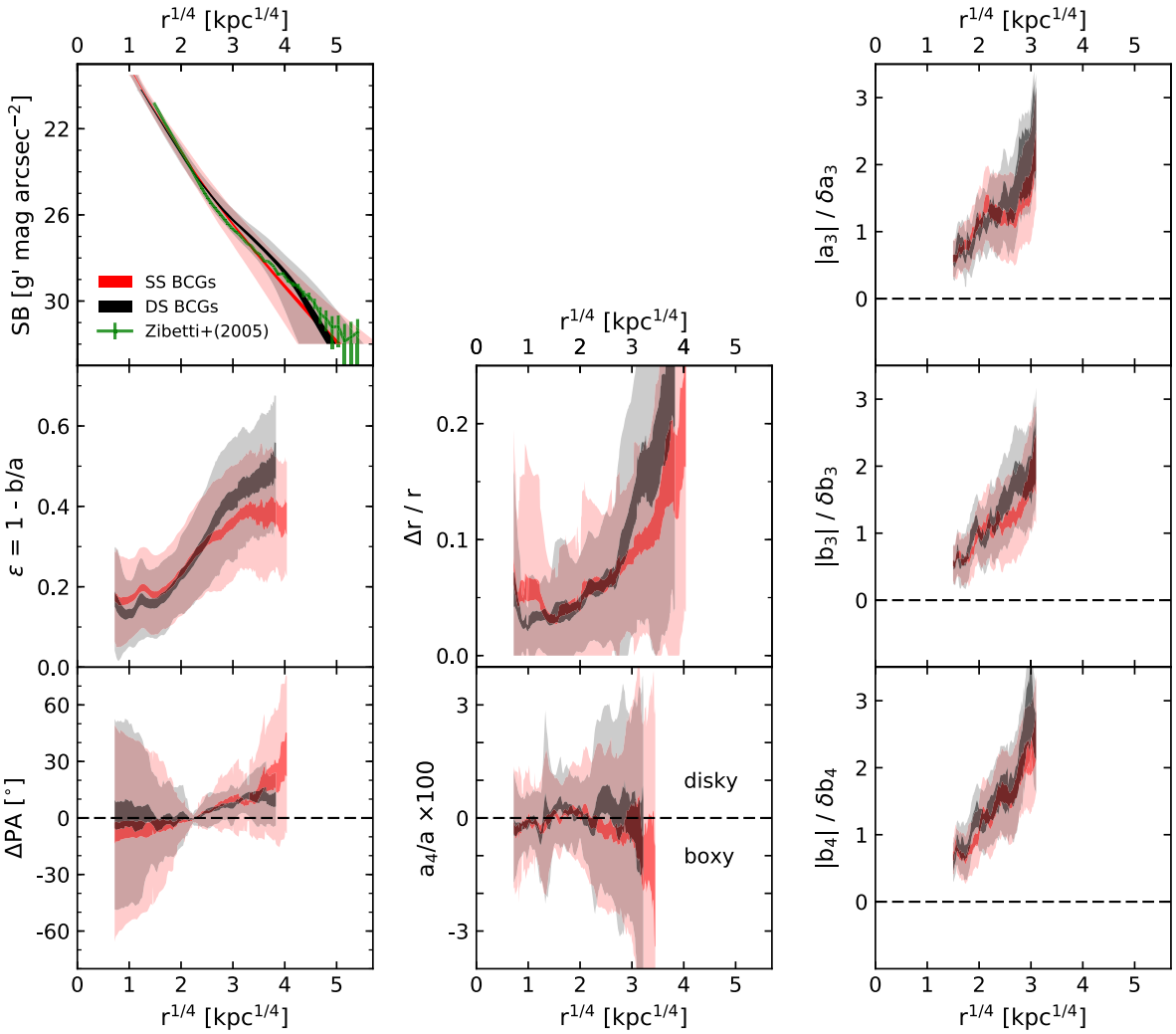

Figure 7.2: Average profiles of SS (DS) BCGs in red (black). The radius on the x-axis is given along the effective axis $r = \sqrt{ab}$. The more transparent shades correspond to the intrinsic 1σ scatter, and the more opaque shades correspond to the standard error of the mean. The average SB profiles are created by averaging the measured SB data points of all BCG+ICLs inside of $a < 16$ kpc and the extrapolated Sérsic fits outside of that that semimajor axis radius. Isophote twist ΔPA profiles are normalized to the median in the range $16 < r[\mathrm{kpc}] < 40$. Profiles with a negative gradient are flipped. Coefficients of the Fourier expansion of the deviations from elliptical isophotes (see Eq. 4.1) are plotted in the bottom middle and right panels. The diskyness/boxiness indicator a_4 is expressed as a percentage of the semimajor axis radius a. The more transparent error shades describe the 1σ intrinsic scatter. The other three Fourier coefficients a_3, b_3 and b_4 are expressed differently because they quantify asymmetric distortions that are randomly oriented and therefore average to zero for large samples. Their absolute value is divided by the measurement uncertainty. This is a measure of the significance that the corresponding deviations are detected. The error shades correspond to the 1σ measurement uncertainty. The comparison between SS and DS BCGs is only fair because the measurement scatter is almost identical .

7.2 Average profiles

The average light profiles and isophotal shape parameter profiles are presented in Fig. 7.2. All profiles are averaged in radial intervals besides the SB profiles, which were calculated by averaging in SB intervals. The different method is necessary because the limited depth would otherwise result in an artificial upward trend in the SB profiles below $SB \gtrsim 28$ g' mag arcsec^{-2}. Before averaging, outliers in every radius (or SB) interval are rejected that deviate more than 6.5 standard deviations from the mean. If data points for a minimum of 14 BCGs remain, then the average is plotted. The 1σ standard deviations of the intrinsic scatter are shown as shaded regions for SB, ϵ, ΔPA, $\Delta r/r$, and a_4. The shaded regions for a_3, b_3 and b_4 correspond to the measurement uncertainties.

The SB profiles are a composite of data and fits. Inner regions below $r < 16$ kpc are taken directly from the measured light profiles, and the outer regions are replaced by the Sérsic fits. The radius is given along the effective axis $r = \sqrt{ab}$. This is equivalent to measuring the profiles in circular apertures. It allows direct comparison to the SB profile that was measured by Zibetti et al. (2005) by combining 683 galaxy cluster images from the SDSS-DR1. We apply a K-correction of g'[rest frame] = [observed frame] $- 0.71$ mag to the r-band data from Zibetti et al. (Chilingarian et al. 2010; Chilingarian & Zolotukhin 2012), a color correction of $g = r + 1.2$, derived from their multiband SB profiles and corrected for cosmic dimming. The average profile from Zibetti et al. is inconsistent with our average profiles within the standard error of the mean, that is, the thickness of the red and black lines. We unsuccessfully tried to match our average SB profiles with the profile from Zibetti et al. by applying various total brightness cuts on our sample: after discarding all BCGs fainter than $M_{\rm tot} > -23$ g' mag, the average SBs around $SB \sim 30$ g' mag arcsec^{-2} match well, but the slope below $r < 40$ kpc is too shallow. Instead, if we discard all BCGs brighter than $M_{\rm tot} < -23$ g' mag, then the slopes match well at these radii but the profiles are too faint, especially in the ICL outskirts. We conclude from this analysis that the deviations cannot be attributed to sample selection alone. A possible explanation is the different age of the galaxies. The mean redshift $\bar{z}_{\rm Z} = 0.25$ of Zibetti et al.'s sample is higher than ours ($\bar{z}_{\rm K} = 0.06$). That equals 2.16 Gyr in time evolution after which the BCG's SB profiles might have evolved to become smoother.

The overall shape and scatter of SS and DS BCGs are fairly similar. The largest difference occurs around $r = 240$ kpc, where DS BCGs are on average 0.65 ± 0.18 g' mag arcsec^{-2} brighter than SS BCGs. The difference decreases again toward larger radii and becomes zero at $r = 470$ kpc.

We now move on to discuss the isophotal shape parameters. As explained in Sec. 4, these parameters are kept fixed beyond the last plausible radius. Hence, the average profiles for these parameters do not extend as far out as the averaged surface brightnesses.

The ellipticities $\epsilon = 1 - b/a$ rise with radius. The slope is slightly shallower for SS BCGs.

The position angles PA are counted counterclockwise starting from the north–south axis. It is unambiguously defined in the range $0° \leq PA < 180°$. It flips $\pm 180°$ when it is crossing the north–south axis. These jumps are eliminated by the following procedure: if the difference between two subsequent PA data points is greater than $PA_i - PA_{i+1} > 90°$, an offset of 180° is subtracted from all data points at greater radii. The opposite is done when $PA_i - PA_{i+1} < -90°$. All PA profiles are normalized to the median in the range $16 < r$[kpc] < 40. Since PAs are randomly oriented, their profiles average to constant zero for a large sample. To avoid this, we flip PA profiles with negative gradients. The gradients are determined between the median of the range $16 \leq r$[kpc] < 40 and the median of the range $r \geq 40$ kpc. We find

average isophote twists of order $\Delta PA/\Delta r \sim 10^\circ/100$ kpc for both SS and DS BCGs. The scatter beyond $r \gtrsim 50$ kpc is about twice as high for DS BCGs than for SS BCGs. The higher scatter below $r \lesssim 20$ kpc can be explained by the lower ellipticities of DS BCGs at these radii.

The ICL offset $\Delta r(r)$ is the distance between the center of the BCG and the center of the isophotal ellipse with radius r along the effective axis. The average and relative ICL offsets increase with radius. At $r = 150$ kpc, they reach 10% (i.e., 15 kpc) for SS BCGs and 20% (i.e., 30 kpc) for DS BCGs. The spatial direction of these offsets is discussed in Sec. 7.5.2.

Isophotal distortions from perfect ellipses are expanded in a Fourier series (see Sec. 4.1). The most informative coefficient a_4 is expressed as a percentage of semimajor axis radius a (see Fig. 7.2, bottom middle panel). It quantifies the diskyness ($a_4 > 0$) or boxiness ($a_4 < 0$) of the isophotes (e.g., Bender & Moellenhoff 1987).

We find that the inner isophotes in 10 kpc $\lesssim r \lesssim 25$ kpc are on average slightly disky. SS BCGs become boxy in the outskirts beyond $r \gtrsim 40$ kpc, whereas DS BCGs are slightly disky at that radius.

We show the first three coefficients of the Fourier expansion a_3, b_3 and b_4 in Fig. 7.2. The two parameters a_3 and b_3 quantify the triangularity of the isophotal shapes. The last parameter b_4 quantifies distortions similar to the disky/boxy parameter a_4, but includes a $\sim 45^\circ$ rotation because it is the amplitude of the sine component from the Fourier expansion (see Eq. 4.1). The values of all of these parameters average to zero for a large sample because asymmetric distortions are randomly oriented. In order to gain knowledge from them, we have to look at their moduli. What makes the analysis difficult is that the measurement errors are of the order of the values themselves. A better diagnostic is the significance whether a_3, b_3 and b_4 type deviations are detected at all. We therefore express these parameters in the form of their modulus, divided by the measurement uncertainty. The error shades in the bottom three panels on the right are the average measurement uncertainties and, like for the other parameters, the intrinsic scatter. A comparison between SS and DS profiles is only fair because the average uncertainties are very similar, as it is expected for a large sample size of similar galaxies. We find that SS BCGs are characterized by lower values for a_3, b_3 and b_4 than DS BCGs. In other words, SS BCGs have less pronounced asymmetric isophotal distortions, indicating a more relaxed state of SS BCGs.

7.3 Structural parameters

In this section, we examine first how BCGs populate the parameter space (r_e, SB_e, M_tot) and second how the Sérsic indices n are distributed. We therefore overplot the structural parameters listed in columns (9), (10), and (11) in Tab. D.1 on Fig. 2 from Kormendy & Bender (2012). The result is shown in Fig. 7.3. The literature parameters are determined by integrating the extrapolated SB profiles down to $SB \sim 29.7$ V mag arcsec^{-2} for core ellipticals and down to an arbitrarily faint SB for coreless ellipticals and dwarp spheroidal galaxies (Kormendy et al., 2009). Hence, they include most of the stellar halos. Since no attempt at a galaxy–halo decomposition was done for the literature parameters, we avoid doing so for the BCGs, too i.e., use the structural parameters determined for the whole light distribution including ICL for a consistent comparison.

The average corrections for PSF broadening and the average systematic error due to the finite depth of our survey are indicated by the arrows. These average corrections and also

Galaxy Type	X	Y	Slope α	Offset β
(1)	(2)	(3)	(4)	(5)
Regular Es	M	$\log(r_\mathrm{e})$	-0.309 ± 0.020	-6.02 ± 0.43
SS BCGs	M	$\log(r_\mathrm{e})$	-0.550 ± 0.037	-11.29 ± 0.87
DS BCGs	M	$\log(r_\mathrm{e})$	-0.547 ± 0.060	-11.10 ± 1.43
All BCGs	M	$\log(r_\mathrm{e})$	-0.563 ± 0.032	-11.57 ± 0.75
Regular Es	M	SB_e	-0.75 ± 0.13	5.47 ± 2.65
SS BCGs	M	SB_e	-1.90 ± 0.20	-20.32 ± 4.70
DS BCGs	M	SB_e	-1.96 ± 0.35	-20.95 ± 8.26
All BCGs	M	SB_e	-2.02 ± 0.18	-22.93 ± 4.26
Regular Es	$\log(r_\mathrm{e})$	SB_e	2.44 ± 0.22	20.18 ± 0.12
SS BCGs	$\log(r_\mathrm{e})$	SB_e	3.61 ± 0.13	18.61 ± 0.22
DS BCGs	$\log(r_\mathrm{e})$	SB_e	3.58 ± 0.26	18.77 ± 0.51
All BCGs	$\log(r_\mathrm{e})$	SB_e	3.63 ± 0.11	18.61 ± 0.88

Table 7.1: The correlations are in the form of $Y = \alpha X + \beta$. Orthogonal distance regression was applied to find the best-fit parameters. All values are for the g'-band. The galaxies of type "regular Es" are from Bender et al. (1992), i.e., the dark gray data points in Fig. 7.3.

the individual errors are neglected for the fitting of the parameter correlations. Otherwise, a significant number of data points had almost zero weight, due to the high inhomogeneity of the errors. We find that BCGs extend the population of regular ellipticals in parameter space to larger integrated brightnesses, dimmer effective SBs, and larger effective radii, but their parameter correlations have different slopes (see Tab. 7.1). In the next paragraphs, we compare our derived parameter correlations to those derived by Donzelli et al. (2011) and Bernardi et al. (2007) from shallower datasets and offer an explanation for the discrepancies. Later, we argue that the broken slopes appear because the growth of BCGs, compared to regular ellipticals, is more dominated by accretion of stellar material in their outskirts.

The Kormendy (1977) relation $SB_\mathrm{e} = \alpha \log(r_\mathrm{e}) + \beta$ that we fit to our data has a slope of $\alpha = 3.61 \pm 0.13$ for the SS BCGs and $\alpha = 3.58 \pm 0.26$ for the DS BCGs (see Tab. 7.1). Both results are in tension with the Kormendy relations found by Donzelli et al. (2011). Using shallower imaging data, they measured a slope of $\alpha = 3.29 \pm 0.06$ for the SS BCGs and $\alpha = 2.79 \pm 0.08$ for the DS BCGs. By also taking the offsets β after color corrections into consideration, we notice that the data points from Donzelli et al. are systematically shifted off our measured Kormendy relation toward smaller effective radii. A plausible explanation for this offset is the underestimation of the ICL amount in Donzelli et al.'s data because some upward curvature of the light profiles remained undetected. Their limiting SB converted to the g'-band is $SB_\mathrm{lim}^\mathrm{Donzelli+2011} = 25.7$ g' mag arcsec^{-2}. It can be recognized from inspecting Fig. 7.6, bottom panel, that about half of the transitions between the two Sérsic components (and therefore a strong upward curvature in the SB profiles) occur below Donzelli et al.'s detection limit. The authors themselves pointed out that their measured correlation coefficients depend on the applied radius or surface brightness cuts.

Our measured size-luminosity relation $\log(r_\mathrm{e}) = \alpha M + \beta$ has a slope $\alpha = -0.550 \pm 0.037$ for SS BCGs and $\alpha = -0.547 \pm 0.060$ for DS BCGs. That is significantly steeper than $\alpha = -0.354$ as measured by Bernardi et al. (2007). They fit SS functions to the semimajor axis SB profiles of 215 BCGs ($z < 0.12$), measured on SDSS DR2 r-band data. The average total brightness of the BCGs in the Bernardi et al. sample is 1–2 g' mag fainter than the BCGs in our

sample. A different sample selection, preferentially toward lower mass clusters, could explain that discrepancy. Unfortunately, direct comparison of individual BCGs was not possible. Furthermore, the authors concluded from mock observations that undetected ICL shifts the data points along the size-luminosity relation but does not change its slope. However, our results disagree with their conclusion. For the brightest BCGs, we find larger effective radii than predicted by the size-luminosity relation as measured by Bernardi et al. (2007). In Fig. 7.5, we show that the fraction of light that is encompassed in the low-SB outskirts increases with total BCG+ICL brightness. That can lead to a shallower size-luminosity relation when that trend is not included in the models of Bernardi et al.

The trend that brighter BCGs have larger luminosity fractions in their low-SB outskirts offers an explanation for the broken slope in the size-luminosity relation and consequently also in the other two relations shown in Fig. 7.3 and listed in Tab. 7.1. If BCGs are unique in growing predominantly by accreting stellar material into their outskirts, then their effective radii increase for a fixed brightness.

The same argument can also be made for galaxy clusters as a whole that grow purely by accretion. The slope of the size-luminosity relation is broken here once more. Compared to the BCGs, they are located at much larger radii but only slightly larger brightnesses (blue data points in Fig. 7.3).

We notice from further inspecting Fig. 7.3 that SS BCGs have a smaller median effective radius and a brighter median effective surface brightness (45 ± 24 kpc; 22.4 ± 0.9 g' mag arcsec^{-2}) compared to their DS counterparts (72 ± 31 kpc; 25.5 ± 0.8 g' mag arcsec^{-2}). The slightly more compact shape of SS BCGs is also seen in the average SB profiles in Fig. 7.2. In integrated brightnesses, SS BCGs are 14.8% fainter (-23.68 ± 0.53 g' mag) than DS BCGs (-23.83 ± 0.41 g' mag).

The distribution of Sérsic indices n for all SS BCGs is shown in Fig. 7.4. Most SS BCGs have $n \geq 4$, but 20/121 (17%) have significantly lower n. That value approximately separates the two classes of disky–coreless–rotating ellipticals (denoted extra-light ellipticals in the histogram) and boxy–core–nonrotating ellipticals (Kormendy et al., 2009). We further elaborate on that dichotomy in the next subsection. The high Sérsic indices can be explained by accretion that is predominantly happening in the outskirts, which subsequently increases the upward curvature of the SB profiles and consequently the Sérsic indices.

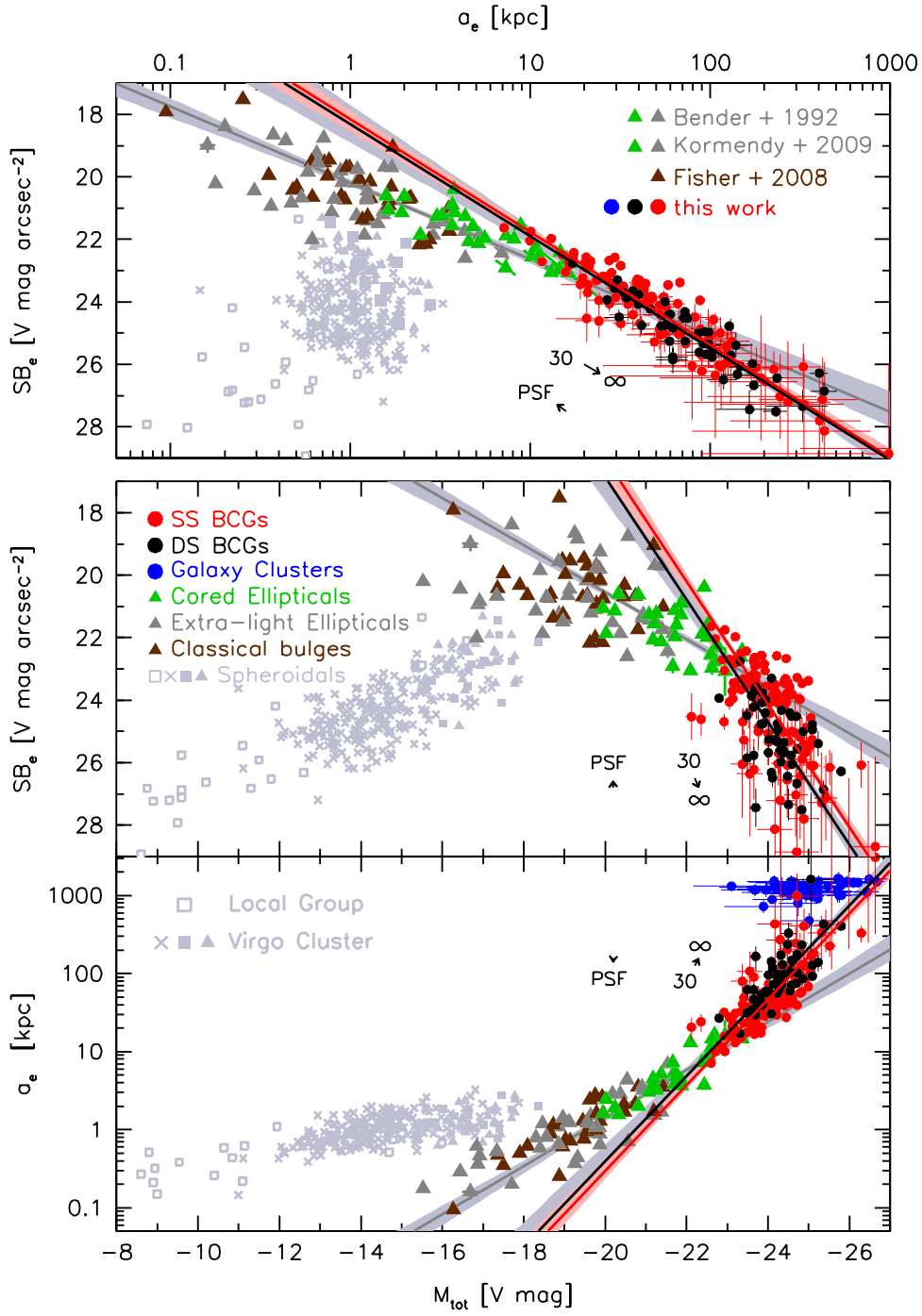

Figure 7.3: Comparison between integrated absolute brightnesses $M_{\rm tot}$, effective radii $a_{\rm e}$ along the major axis, and effective SB $SB_{\rm e}$ of BCGs, regular ellipticals, and galaxy clusters. The basis for this plot is Fig. 37 in Kormendy et al. (2009) with updates in Fig. 2 in Kormendy & Bender (2012) and Fig. 14 in Bender et al. (2015). The galaxy data points from the literature and from this work are calculated from 2D profile integration and evaluated along the major axes. For the clusters, the (circular) gravitational radius $r_{\rm g}$ (Eq. 6.1) is used. The arrow $30 \rightarrow \infty$ shows the median shift of the BCG parameters when using no upper integration limit compared to $SB_{\rm lim} = 30$ g' mag arcsec^{-2}. The arrow $\rightarrow$ PSF shows the median shift of the BCG parameters due to the PSF broadening correction. g'-band magnitudes were converted to V-band magnitudes via $V = g - 0.45$ mag (Jester et al., 2005) for $g - r = 0.78$ (Tojeiro et al., 2013).

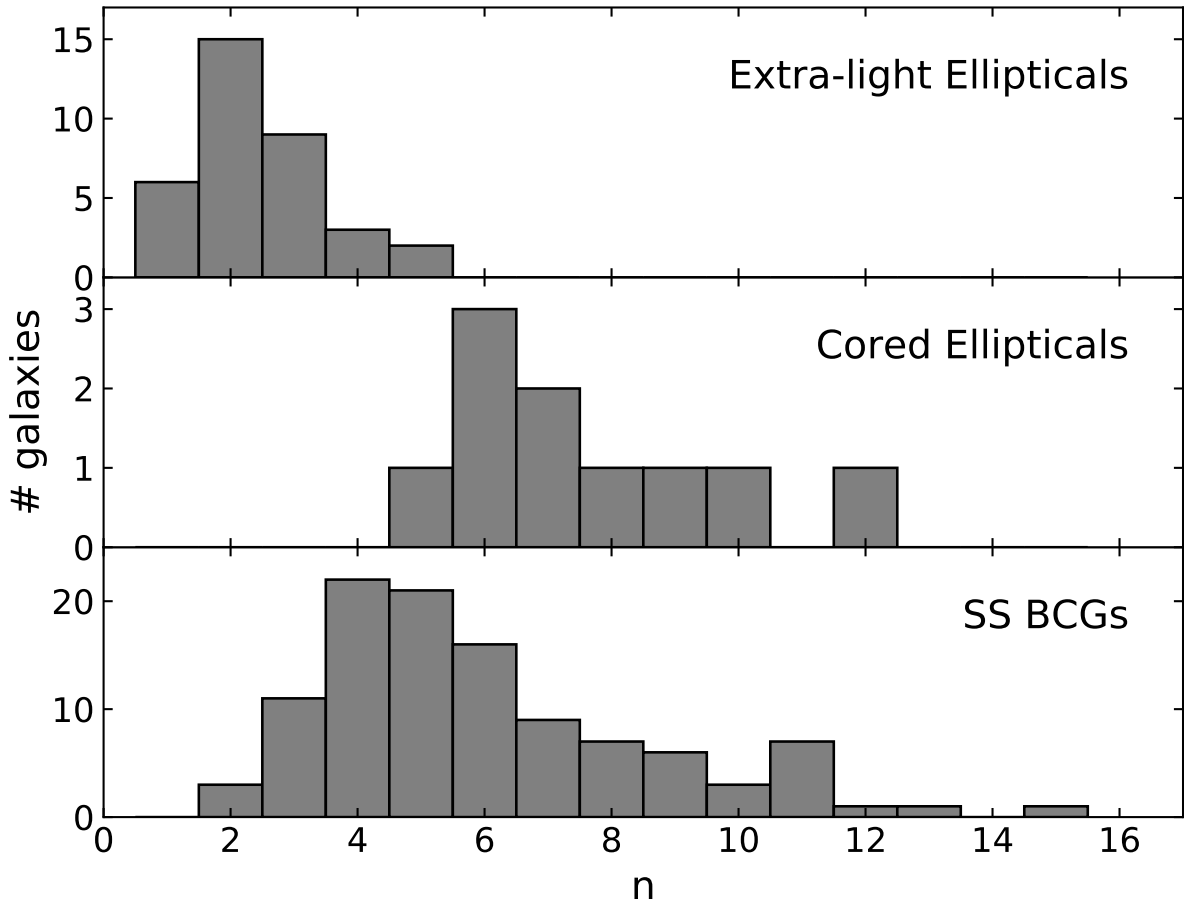

Figure 7.4: Distribution of Sérsic indices n for extra-light ellipticals (top panel), cored ellipticals (middle panel), and SS BCGs (bottom panel). The data for the extra-light and cored ellipticals are taken from Kormendy et al. (2009).

7.4 ICL fractions by photometric decomposition

For all observed clusters, we calculate a fiducial ICL fraction

$$f_{\rm ICL} = L_{\rm ICL}/(L_{\rm BCG} + L_{\rm ICL}) \tag{7.1}$$

as the luminosity of the photometric component that we define as ICL, relative to the total luminosity of the combined BCG+ICL system. We again stress that this probably includes at least part of the stellar halos of the BCGs.

The ICL brightness is then calculated as

$$M_{\rm ICL} = M_{\rm BCG+ICL} - 2.5\log(f_{\rm ICL}). \tag{7.2}$$

To separate the ICL from the BCG, we apply a simple integrated brightness cut (1) and three methods that are commonly used in the literature (2), (3) and (4). The ICL is either defined as

1. all stellar light above a given integrated brightness,
2. all stellar light below a given SB threshold,
3. the excess light above a de Vaucouleurs profile or as
4. the outer component determined by a SB profile decomposition into two Sérsic functions.

Whether or not these methods actually dissect the real, dynamically hot ICL from the BCG is an ongoing debate. We join that discussion later in Sec. 8.

7.4.1 Integrated brightness threshold

The brightness where the slope of the size-luminosity relation breaks (see Sec. 7.3) separates regular ellipticals from BCGs quite well. We therefore assume that there is a maximum brightness for regular ellipticals at the knee $M_{\rm max} = -21.85$ g' mag. All light above that brightness is defined as ICL:

$$M^{(1)}_{\rm ICL} = -2.5\log(10^{-0.4\times M_{\rm BCG+ICL}} - 10^{-0.4\times M_{\rm max}}) \tag{7.3}$$

We calculate an average ICL fraction of $f^{(1)}_{\rm ICL} = 71 \pm 22\%$.

7.4.2 Surface brightness threshold

We apply a surface brightness threshold on the light profiles. The faint light below this threshold is defined as the ICL in this context. We calculate the ICL fraction by integrating the light profiles numerically while considering the radially varying ellipticity. The results are strongly sensitive towards the choice of the brightness threshold (see Tab. 7.2). So which threshold separates the ICL from the BCG most accurately? Cooper et al. (2015) have shown that a SB threshold of $SB_{\rm cut} = 26.5\ V$ mag arcsec^{-2} attributes 80 – 95 % of the accreted stars to the ICL in their N-body simulations. We transform this V-band magnitude into a g'-band magnitude using a color transformation derived for NGC6166. By matching the V-band SB profile measured by Bender et al. (2015) to our g'-band SB profile, we get $g' \simeq V + 0.45$ mag.

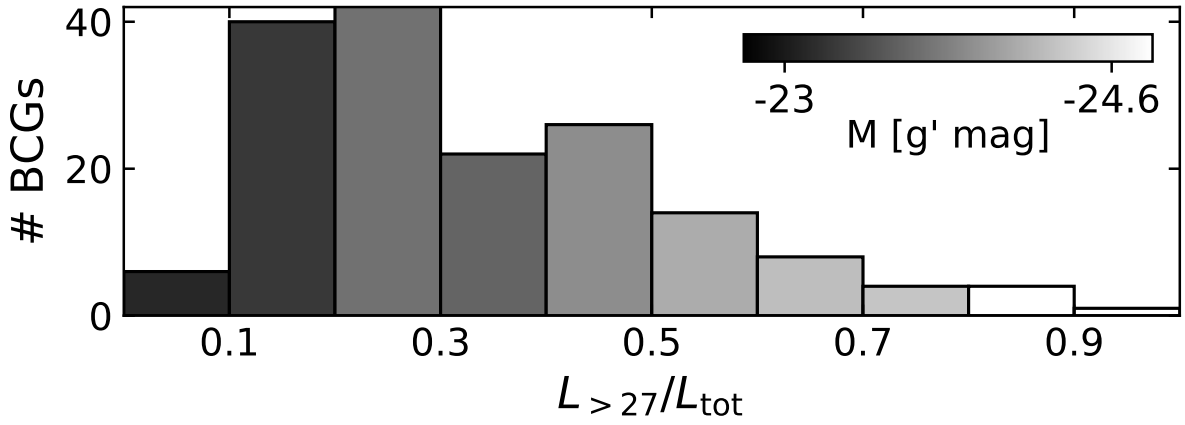

Figure 7.5: Luminosity fraction of the light below $SB > 27$ g' mag arcsec^{-2} in relation to the total BCG luminosity $L_{\rm tot}$. The average absolute BCG+ICL brightness in the bins is coded in the gray-shading of each bar.

The threshold in the g'-band is therefore set to $SB_{\rm cut} = 27$ g' mag arcsec^{-2}, for which we calculate an average ICL fraction $f^{(2)}_{\rm ICL} = 34 \pm 19\%$. That agrees well with the result from Cui et al. (2014) $f^{(2)}_{\rm ICL} \sim 30\%$ for the hydrodynamical simulations that include AGN feedback. However, that promising consistency has to be taken with caution because the combined BCG+ICL systems are too massive in the simulations (cf. column 5 in Tab. 7.2).

The results of Feldmeier et al. (2004) for five BCGs are between $f^{(2)}_{\rm ICL} = 28\%$ for $SB_{\rm cut} = 26$ V mag arcsec^{-2} and $f^{(2)}_{\rm ICL} = 2\%$ for $SB_{\rm cut} = 27.5$ V mag arcsec^{-2}. Both values are lower than ours, likely because Feldmeier et al. studied only non-cD clusters.

We discover a trend that brighter BCGs have larger ICL fractions (see Fig. 7.5) with a relatively high absolute value of the Spearman coefficient $R = -0.5$. That indicates that the recent growth of BCGs happens predominantly by accreting stellar material in their low-SB outskirts.

7.4.3 Excess light above the inner de Vaucouleurs profile

The Sérsic indices for SS BCGs are often (83%) significantly larger than $n > 4$ (see Sec. 7.3). That is about the transition value between lower mass (Faber et al., 1997; Lauer et al., 2007) disky-extralight-rotating ($n < 4$) and higher mass boxy-core-nonrotating ($n > 4$) ellipticals in the Virgo cluster (Kormendy et al., 2009). It is also known that the velocity dispersion profiles of large ellipticals flatten out towards larger radii instead of drop like those of lower-mass ellipticals (Veale et al., 2017). One could therefore hypothesize that large Sérsic indices are due to the presence of intragroup- or ICL (e.g., Bender et al. 2015).

By assuming that the BCG has a de Vaucouleurs ($n = 4$) SB profile, we define the ICL in this approach as the excess light above the outwards extrapolation of that profile. The de Vaucouleurs profile is fitted to the inner SB profile of all SS and DS BCGs below $SB < 23$ g' mag arcsec^{-2}. A larger fitting range would lead to large errors $\Delta SB \gtrsim 0.1$ g' mag arcsec^{-2} in the inner regions due to the $n > 4$ curvature of the SB profiles. As for the Sérsic fits, we exclude the cores from the fitting.

The average ICL fraction is $f^{(3)}_{\rm ICL} = 42 \pm 33\%$. That value is not directly comparable to the result from Zibetti et al. (2005). The authors measured the SB profile in an averaged SDSS-DR1 image of 683 BCG+ICLs. The de Vaucouleurs fit to the inner $\sim 15 - 80$ kpc

gives $r_e = 19.29$ kpc and $SB_e = 23.39$ g' mag arcsec^{-2} (after K-, color- and cosmic dimming correction). They calculate an average ICL fraction of $f_{ICL} = 33 \pm 6\%$. The fit to our averaged SB profile along the effective axis in the same radial interval gives $r_e = 35.44 \pm 0.24$ kpc and $SB_e = 24.61 \pm 0.01$ g' mag arcsec^{-2} and the ICL fraction is $f_{ICL} = 21 \pm 12\%$. The uncertainty of f_{ICL} is estimated from the SB uncertainty of the averaged SB profile. We assume a flux uncertainty that corresponds to a SB of 31 g' mag arcsec^{-2}.

Our calculated average ICL fraction is consistent within the measurement uncertainties with the average ICL fraction for the Zibetti et al. sample. The decomposition is much clearer for the SB profile measured by Zibetti et al. (see Fig. 7.2, top left panel) because its shape is much closer to a double de Vaucouleurs profile. Note that the sample of Zibetti et al. is at a higher average redshift: $\bar{z}_Z = 0.25$ compared to the sample of this work $\bar{z}_K = 0.06$ and therefore 2.16 Gyrs younger. As discussed in Sec. 7.2, the different average shapes might be the result of a time-evolution in which the SB profiles have evolved to become smoother. The increase in effective radius of the inner de Vaucouleurs component by 84% and the large fraction (71%) of smooth SS BCGs today are presumably a direct consequence of that.

7.4.4 Double Sérsic decomposition

The third approach to determine ICL fractions is by decomposing the SB profiles into two Sérsic functions. Both components are independently integrated from the 2D isophote models. The same ellipticity profile $\epsilon(r)$ is used for both components. PSF-correction is applied beforehand (see Sec. 5.4). The outer integration limit is set once to the isophote with $SB_{lim} = 30$ g' mag arcsec^{-2} and once to infinite radius. The ICL fraction is then determined for both cases to estimate the error by the undetected ICL. It is of order $|f_{ICL}^{30}/f_{ICL}^{\infty}| \sim 1\%$. We find that the outer component encompasses $f_{ICL}^{(4)} = 52 \pm 21\%$ of the total light. The intrinsic scatter is huge. We show a more detailed histogram of the distribution in the top panel of Fig. 7.6. The integrated brightness M of the BCG+ICL is coded in the gray-scaling of the bars. Only a weak correlation is found between f_{ICL} and M (Spearman $R = -0.20$).

The other two histograms show the transition point where the Sérsic components intersect. Only weak correlations with BCG+ICL brightness are found for the transition radii $r_\times$ (Spearman $R = -0.26$) and for the transition surface brightnesses $SB_\times$ (Spearman $R = -0.07$). The transition SBs between the BCGs and the DSCs (Diffuse Stellar Component = kinematically confirmed ICL) in the simulations used by Cui et al. (2014) have similar scatter around $SB_\times \sim 25$ g' mag arcsec^{-2}, but the non-negligible fraction of $SB_\times > 27$ g' mag arcsec^{-2} is not found there.

We now compare our results with those from previously published work by other authors. An overview of the derived ICL fractions and the limiting depths of the corresponding surveys can be found in Tab. 7.2.

The largest sample so far was compiled by Donzelli et al. (2011). They derived 430 BCGs light profiles from data taken between 1989 and 1995 and fitted them using either one or two Sérsic functions. The limiting depth of the survey is relatively shallow with $SB_{lim} = 24.5$ R mag arcsec^{-2}. Our averaged result $f_{ICL}^{(4)} = 52\% \pm 21\%$, agrees with the value of $f_{ICL} = 40\% \pm 14\%$, calculated from the S/e column in Donzelli et al. (2011). However, closer examination of the results for individual clusters reveals large discrepancies. Sérsic fits to SB profiles that were derived from shallow data are unconstrained at large radii. The goodness of fit can sometimes be improved significantly in the inner regions by choosing a

different set of parameters. They however often fail to describe the shape of the outer ICL halos.

Gonzalez et al. (2005) observed 24 galaxy clusters in drift-scan mode similar to SDSS. Background inhomogeneities are largely averaged out by that technique. The limiting magnitude of the survey corresponds an equivalent of $SB_{\rm lim} = 30$ g' mag arcsec^{-2} in the g'-band and is therefore as deep as our survey. They found a typical ICL contribution of ∼80-90% for 24 BCGs by decomposing their light profiles into two de Vaucouleurs profiles. That is larger than our result, but still consistent with our large error bars. We cannot compare individual galaxies because none of their observed clusters are visible in the northern sky.

Seigar et al. (2007) calculated between 59% and 98% ICL fractions for the extrapolated DS profiles of four BCGs which we will discuss now individually. NGC 6173 in A2197 classified by both, Seigar et al. and us as a SS BCG. Both results for NGC 3551 in A1177 ($f^{(4)}_{\rm ICL} = 53\pm14\%$, Seigar et al.; $f_{\rm ICL} = 55\pm4\%$, this work) are also consistent within the uncertainties. However, there is disagreement for the NGC 4874 in A1656 (Coma cluster). Seigar et al. found $f_{\rm ICL} = 98 \pm 1\%$ whereas we chose to fit it with a SS function because the transition radius would be close to the nucleus (see Sec. 4.4 and 8 §3). The results for UGC 9799 A2052 also disagree. Even though the galaxy has a relaxed morphology at first glance, there is strong intrinsic scatter in the radial light profile. The addition of a second Sérsic component improves the fit at small radii but provides no significant gain considering the overall, almost linear $r^{1/4}$ profile shape. Donzelli et al. (2011) agree with our perception since they also classify UGC 9799 as a SS BCG.

The fractions calculated from the hydrodynamical simulations of Puchwein et al. (2010) $f_{\rm ICL} \sim 70 - 90\%$ are slightly higher than what we determined from our observations. The authors decomposed the projected r-band light profiles into two de Vaucouleurs profiles instead of two Sérsic profiles like we did. The comparison is therefore not entirely fair.

The large intrinsic scatter of photometrically determined ICL fractions is reproduced in the Magneticum simulation. Remus et al. (2017) decomposed the mass profiles of simulated BCGs into two Sérsic functions. They discovered that there is no correlation between perceived ICL fractions that are determined by mass profile decompositions and the true ICL fractions derived by kinematic separation of the particles. That evokes skepticism on the validity of the physical interpretation that the outer Sérsic component traces the ICL.

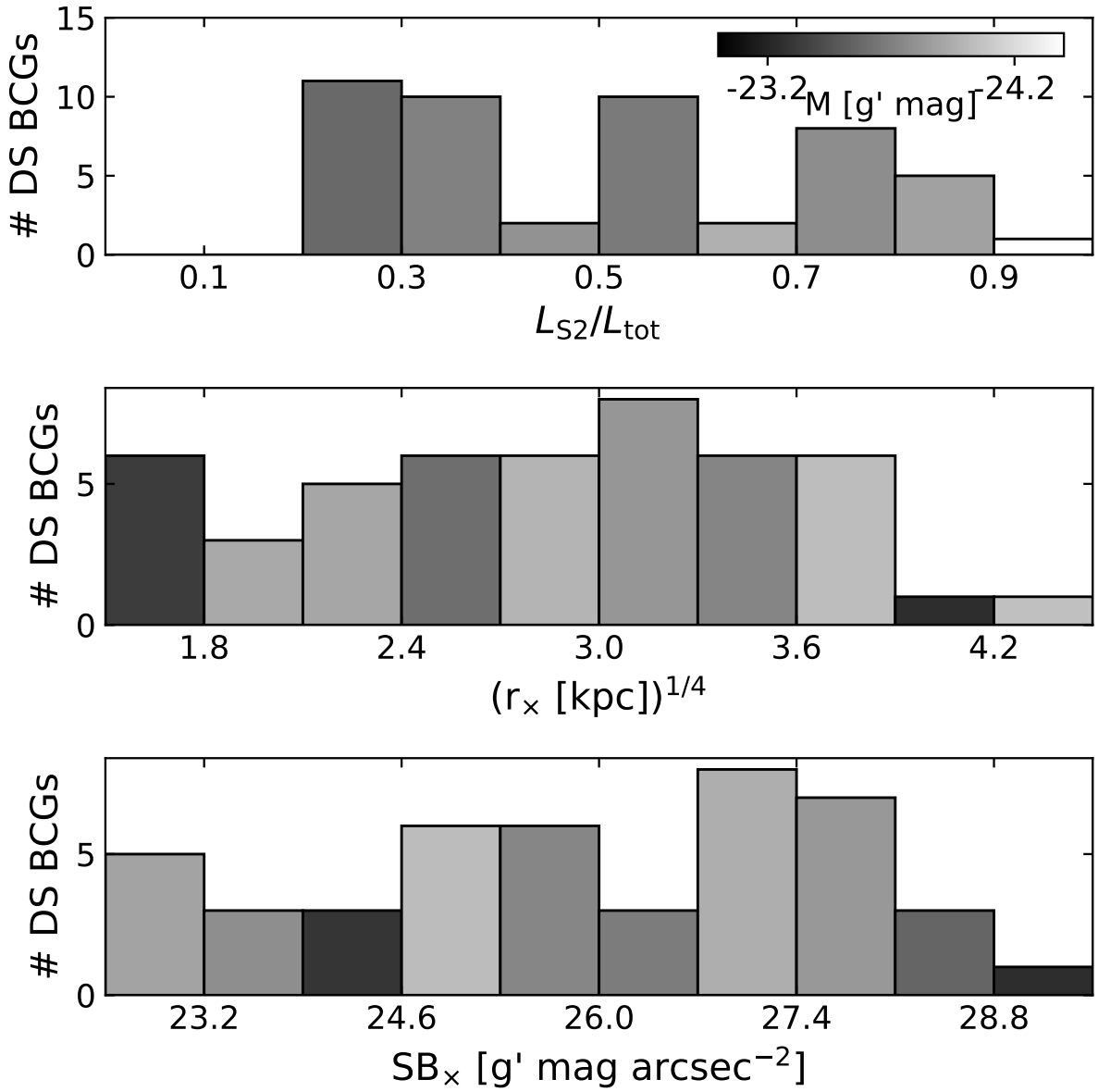

Figure 7.6: *Top panel:* Luminosity fraction of the outer Sérsic component $L_{\rm S2}$ in relation to the total BCG+ICL luminosity $L_{\rm tot}$. That is column (8) in Tab. D.1. *Middle panel:* Radius $r_\times$ beyond which the outer Sérsic component is brighter than the inner. *Bottom panel:* SB of the transition point $SB(r_\times)$. Only DS BCGs were considered. The average absolute BCG+ICL brightness in the bins is coded in the gray-shading of each bar.

Author	Method	$L_{\rm ICL}/(L_{\rm BCG+ICL})$	$L_{\rm ICL}/L_{\rm Cluster}$	$(L_{\rm BCG+ICL})/L_{\rm Cluster}$	lim. mag	filter	lim. mag (g')
OBSERVATIONS:							
this work	$M < -21.85$	$71\% \pm 22\%$	$20\% \pm 12\%$	$28\% \pm 17\%$	30	g'	...
this work	$SB_{\rm cut} = 25$	$52\% \pm 17\%$	$16\% \pm 14\%$	$28\% \pm 17\%$	30	g'	...
this work	$SB_{\rm cut} = 26$	$43\% \pm 19\%$	$13\% \pm 13\%$	$28\% \pm 17\%$	30	g'	...
this work	$SB_{\rm cut} = 27$	$34\% \pm 19\%$	$10\% \pm 12\%$	$28\% \pm 17\%$	30	g'	...
this work	$SB_{\rm cut} = 28$	$26\% \pm 18\%$	$8\% \pm 12\%$	$28\% \pm 17\%$	30	g'	...
this work	$SB_{\rm cut} = 29$	$19\% \pm 17\%$	$7\% \pm 11\%$	$28\% \pm 17\%$	30	g'	...
this work	$SB_{\rm cut} = 30$	$15\% \pm 16\%$	$5\% \pm 11\%$	$28\% \pm 17\%$	30	g'	...
Feldmeier et al. (2004)	$SB_{\rm cut} = 26$	$\sim 20\%$	...	...	26.5	V	27
Feldmeier et al. (2004)	$SB_{\rm cut} = 27.5$	$\sim 2\%$	...	...	26.5	V	27
this work	dV+excess	$42\% \pm 33\%$	$12\% \pm 8\%$	$28\% \pm 17\%$	30	g'	...
Zibetti et al. (2005)	dV+excess	$33\% \pm 6\%$	$10.9\% \pm 5.0\%$	$33\% \pm 16\%$	32	$r+i$	31.5
Zhang et al. (2019)	...	...	...	$44\% \pm 17\%$	30	r	29.5
this work	DS	$52\% \pm 21\%$	$18\% \pm 17\%$	$28\% \pm 17\%$	30	g'	...
Seigar et al. (2007)	DS	59% – 98%	...	...	26.5	R	26.0
Donzelli et al. (2011)	S+Exp	$40\% \pm 14\%$	...	...	24.5	R	25.7
Gonzalez et al. (2005)	2dV	80% – 90%	...	...	28.4	I	30
Gonzalez et al. (2007)	...	...	...	$33\% \pm 16\%$	24.5	R	25.7
SIMULATIONS:							
Puchwein et al. (2010)							
(w/ AGN feedback)	2dV	$\sim$ 70 – 90%	$\sim$ 42% – 66%	$\sim$ 55% – 80%	...	r	...
(w/o AGN feedback)	2dV	$\sim$ 70 – 85%	$\sim$ 39% – 62%	$\sim$ 50% – 80%	...	r	...
Rudick et al. (2011)	$SB_{\rm cut} = 26.5$	...	$11\% \pm 1\%$	...	...	V	...
Cui et al. (2014)							
(w/ AGN feedback)	$SB_{\rm cut} = 26.5$	$\sim$ 25% – 35%	$\sim$ 19% – 32%	$\sim$ 70% – 100%	...	V	...
(w/o AGN feedback)	$SB_{\rm cut} = 26.5$	$\sim$ 10% – 18%	$\sim$ 6% – 15%	$\sim$ 55% – 100%	...	V	...
Contini et al. (2014)	...	...	20% – 35%	25% – 55%	...	mass	...
Cooper et al. (2015)	...	...	...	15% – 40%	...	mass	...

Table 7.2: Comparisons of ICL fractions with published values from the literature. The methods to dissect the ICL from the BCG are either by applying a surface brightness cut, where the SB threshold in the filterband (5) is given in the second column (2), by decomposing the light profiles into two Sérsic functions (DS), two de Vaucouleurs function (2dV), an inner Sérsic and outer exponential function (S+Exp) or by fitting the inner light profile with a de Vaucouleurs function and counting the excess light above that (dV+excess) or by applying a brightness cut at $M_{\rm BCG+ICL} < -21.85$ g' mag. The limiting magnitudes given by the authors (6) are converted to g'-band (8) by matching the photometric zero-points of individual light profiles to our data (for Seigar et al. 2007 and Donzelli et al. 2011), by converting $g' = V + 0.45$ mag (for Feldmeier et al. 2004), by applying the color transformations derived by Lupton (2005, `https://www.sdss.org/dr12/algorithms/sdssUBVRITransform/`) (for Gonzalez et al. 2005) or by using the multiband light profiles measured by the authors and applying K- and for cosmic dimming correction (for Zibetti et al. 2005 and Zhang et al. 2019). The cluster luminosities in Zibetti et al. are calculated inside 500 kpc around the BCG, in Zhang et al. inside 1 Mpc around the BCG and for Gonzalez et al. (2007) inside r_{200}. The simulation results from Puchwein et al. (2010) and Cui et al. (2014) are calculated inside r_{500} and from Cooper et al. (2015) inside r_{200}. The $L_{\rm ICL}/L_{\rm Cluster}$ fraction is calculated for Contini et al. (2014) inside r_{200} and for $L_{\rm BCG+ICL}/L_{\rm Cluster}$ inside r_{500}.

7.5 Correlations between BCG/ICL and host cluster properties

7.5.1 Structural parameters

The widely accepted two-phase formation scenario of BCGs and ICL states that the ICL is made mostly of stellar material that has been accreted from cluster satellite galaxies. Consequently, we expect to find correlations between the satellite galaxies distribution of the host clusters and ICL properties. The results are shown in Fig. 7.7 and Appendix F.

After standardizing the variables, we fit only the slope and convert the result back to the non-standardized form. The Spearman coefficients, which give a measure for the strength of a correlation, are overplotted as a text label in each subplot. The measurement errors are neglected for the fitting of the parameter correlations. Otherwise, a significant amount of data points had almost zero weight due to the high inhomogeneity of the errors, especially for the brightnesses.

We distinguish between direct and indirect observables. Indirect observables (gravitational mass $\mathcal{M}_\mathrm{g}$, mass density ρ, satellite galaxy number density s, mass phase space density $f_{\mathcal{M}_\mathrm{g}}$ and galaxy number phase space density f_s) are constructed from a combination of direct observables (cluster dispersion σ_C, richness S, gravitational radius r_g and brightness of all satellite galaxies M_sat). They are defined in Sec. 6.1.

The first column in Fig. 7.7 shows the integrated brightnesses of the BCGs+ICL. The BCG luminosity is known to increase with cluster mass (Lin et al., 2004; Yang et al., 2005; Zheng et al., 2007; Popesso et al., 2007; Brough et al., 2008; Hansen et al., 2009). Hansen et al. (2009) found that $L_\mathrm{BCG} \propto \mathcal{M}_{200}^{0.30\pm0.01}$ for 13 823 SDSS clusters. We find a significantly steeper slope: $L_\mathrm{BCG+ICL} \propto \mathcal{M}_\mathrm{g}^{1.14\pm0.24}$. Under the assumption that the gravitational mass scales linearly with $\mathcal{M}_{200}$, the discrepancy must arise from the measured BCG luminosities. A previously underestimated ICL contribution is likely the cause. We show in Fig. 7.5 that the luminosity fraction below $SB > 27$ g' mag arcsec^{-2} increases with total BCG+ICL luminosity. Therefore, the luminosities of the brightest BCGs will be underestimated the most from shallow data. That will consequently lead to a shallower slope in the BCG luminosity – cluster mass relation.

The BCG+ICL (and also solely ICL-) brightness correlates positively with the gravitational mass and satellite brightness of the host cluster. That indicates that the growth of the ICL is indeed coupled to the growth of the cluster. Growth is also quantified in cluster gravitational radius, cluster richness and cluster velocity dispersion. All of those parameters have positive correlations with the ICL brightness.

We confirm that BCGs+ICL grow slower in brightness than their host cluster satellite brightness: $M_\mathrm{sat} = 1.19(\pm0.12)\ M_\mathrm{BCG+ICL} + \mathrm{const.}$ (cf. Appendix F and e.g., Fig. 14 in Hansen et al. 2009). But we find a stronger increase in ICL brightness at low surface brightnesses: $M_\mathrm{sat} = 0.69(\pm0.07)\ M_\mathrm{ICL}^\mathrm{SB28} + \mathrm{const.}$ That is another way of quantifying that BCGs grow predominantly in their outskirts at present epoch. Subsequently, the correlations between the ICL brightness (columns 2–5) and cluster properties are expected to be stronger than the correlations between the BCG+ICL brightness and the cluster properties. However, we find no significant improvements of the correlation strengths. That indicates that the virialization time-scales for the accreted stellar material are relatively short.

The bottom four rows of subplots in Fig. 7.7 show expressions for densities. Strong correlations are found between the ICL brightness and the phase-space densities $f_\mathcal{M}$ and f_s.

The stripping efficiency is proportional to the phase space density because tidal forces are strongest at short separations and more material can be accumulated when interaction timescales are long. Surprisingly, instead of an expected positive correlation, we find a negative correlation. The reason is possibly that we do not see the former host cluster properties but rather the effect that the phase space density decreases after energy is deposited into the clusters by mergers.

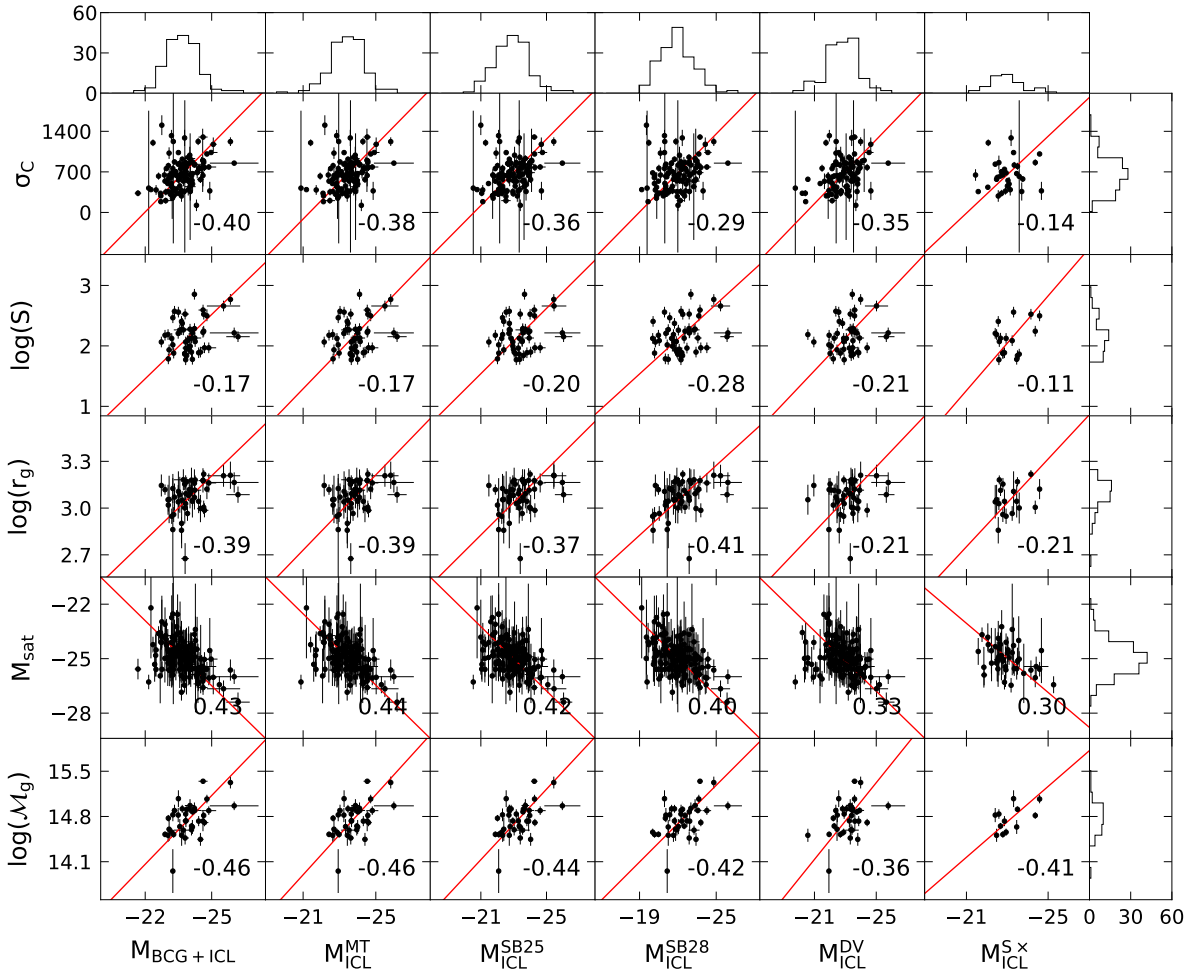

Figure 7.7: Correlations between BCG/ICL parameters (horizontal) and cluster parameters (vertical). The columns show (1) the absolute brightness of the BCGs+ICL $M_{\rm BCG+ICL}$ [g' mag], the absolute brightness of the ICL only $M_{\rm ICL}$ [g' mag], dissected (2) via the total magnitude threshold of –21.85 g' mag $M_{\rm ICL}^{\rm MT}$, (3) via the surface brightness threshold of 25 g' mag $M_{\rm ICL}^{\rm SB25}$, (4) via the surface brightness threshold of 28 g' mag $M_{\rm ICL}^{\rm SB28}$, (5) via the light excess above the inner de Vaucouleurs fit $M_{\rm ICL}^{\rm DV}$, and (6) via the double Sérsic fit $M_{\rm ICL}^{\rm S\times}$. The methods are explained in Sec. 7.4. The rows show (1) the velocity dispersion of the satellite galaxies $\sigma_{\rm C}$ [km s^{-1}] (taken from Lauer et al. 2014), (2) richness S, i.e., number of satellite galaxies, (3) gravitational radius $r_{\rm g}$ [kpc], (4) integrated absolute brightness of all satellite galaxies (excluding the BCG+ICL) $M_{\rm sat}$ [g' mag], and (5) gravitational mass $\mathcal{M}$ [M$_\odot$]. The histograms show the number of data points in each bin from the subplot containing either $M_{\rm sat}$ or $M_{\rm BCG+ICL}$.

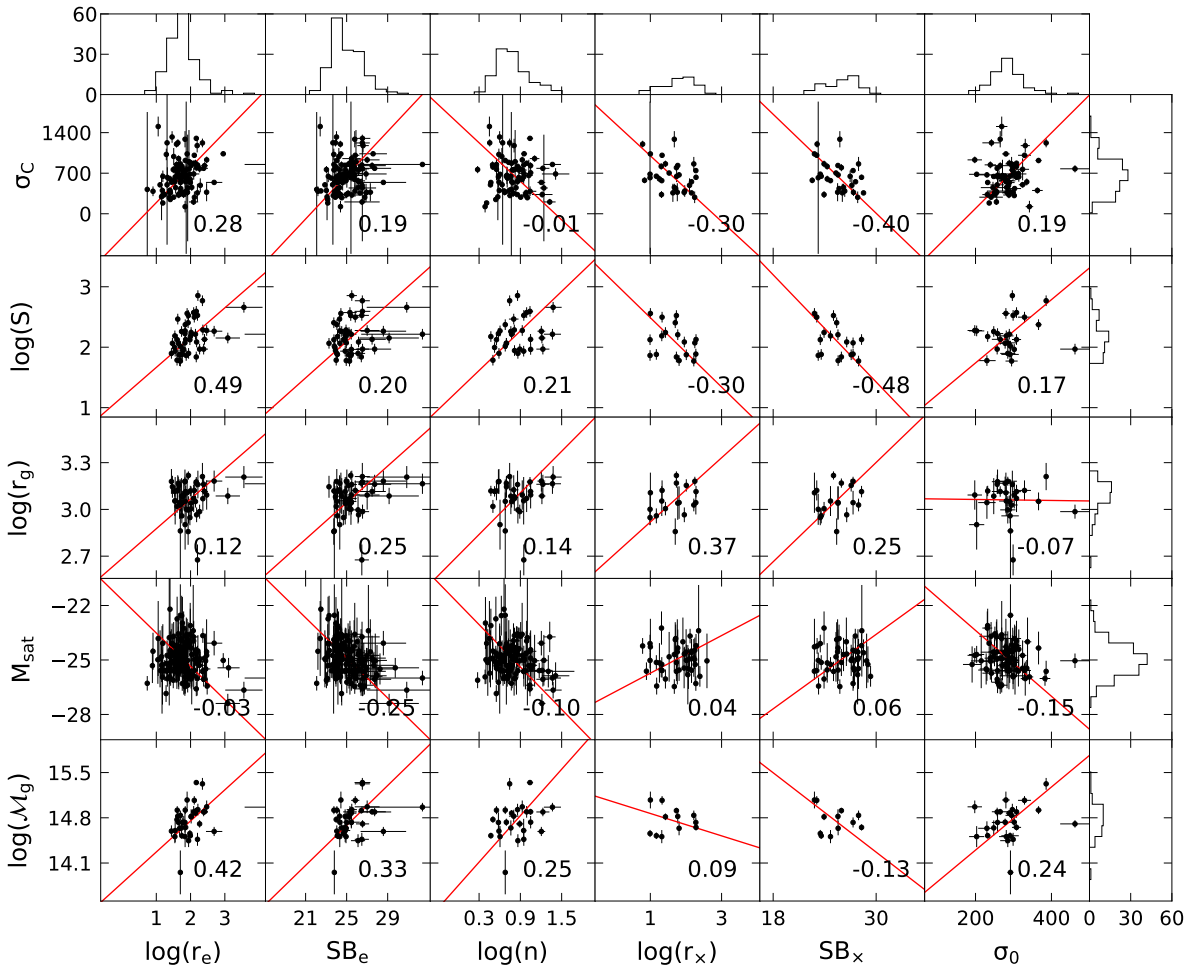

Figure 7.8: Correlations between BCG/ICL parameters (horizontal) and cluster parameters (vertical). The columns show (1) the effective radius $r_{\rm e}$ [kpc] along the major axis and (2) corresponding effective surface brightnesses $SB_{\rm e}$ [g' mag arcsec^{-2}], (3) Sérsic indices n of the SS BCGs, (4) transition radii $r_\times$ [kpc] and (5) transition surface brightnesses $SB_\times$ [g' mag arcsec^{-2}] between the two Sérsic profiles of the DS BCGs, and (6) central velocity dispersion (data taken from Lauer et al. 2014). The rows show (1) the velocity dispersion of the satellite galaxies $\sigma_{\rm C}$ [km s^{-1}] (taken from Lauer et al. 2014), (2) richness S, i.e., number of satellite galaxies, (3) gravitational radius $r_{\rm g}$ [kpc], (4) integrated absolute brightness of all satellite galaxies (excluding the BCG+ICL) $M_{\rm sat}$ [g' mag], and (5) gravitational mass $\mathcal{M}$ [M$_\odot$]. The histograms show the number of data points in each bin from the subplot containing either $M_{\rm sat}$ or $M_{\rm BCG+ICL}$.

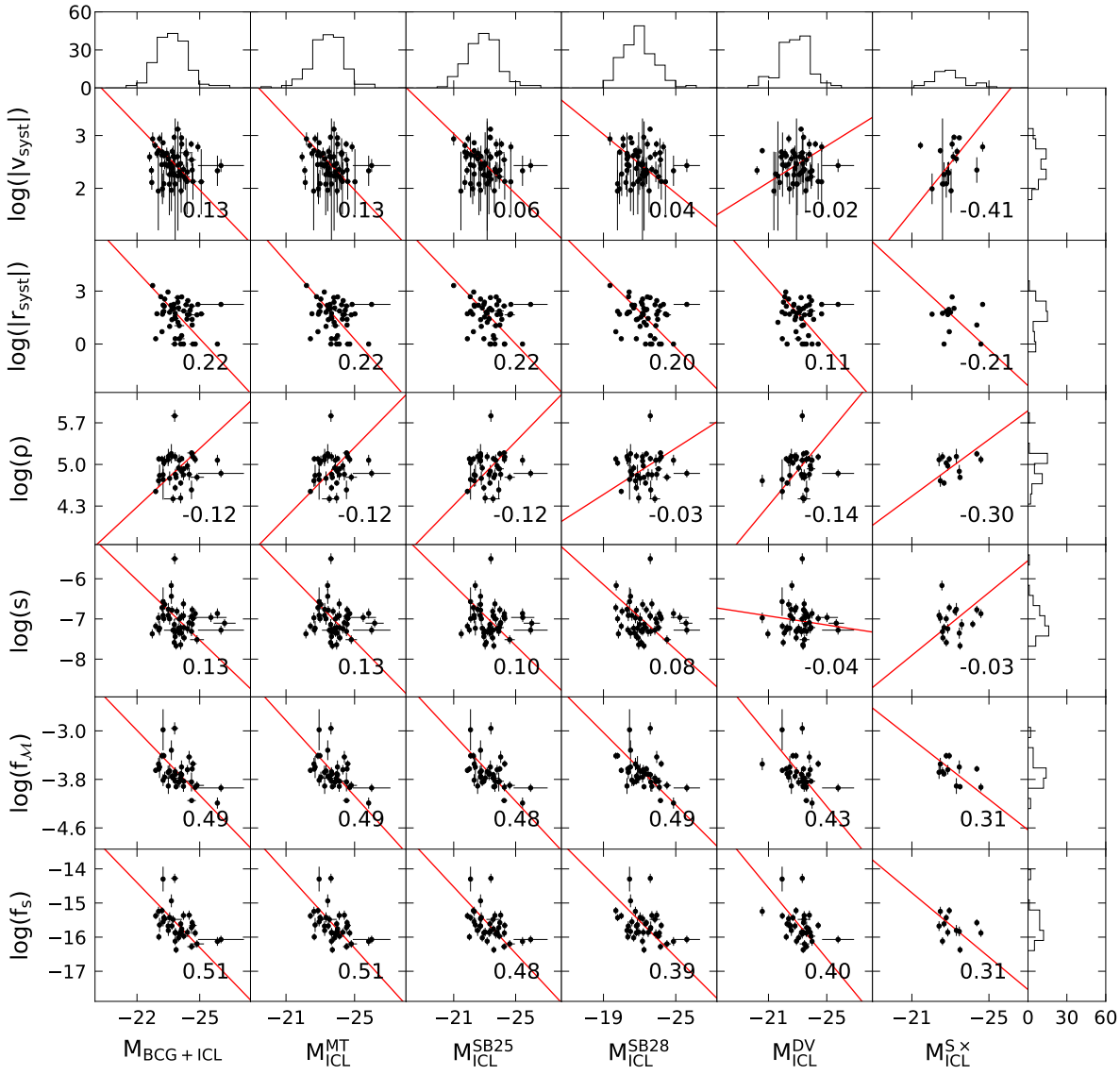

Figure 7.9: Correlations between BCG/ICL parameters (horizontal) and cluster parameters (vertical). The columns show (1) the absolute brightness of the BCGs+ICL $M_{\rm BCG+ICL}$ [g' mag], the absolute brightnesses of the ICL only $M_{\rm ICL}$ [g' mag], dissected (2) via the total magnitude threshold of –21.85 g' mag $M_{\rm ICL}^{\rm MT}$, (3) via the surface brightness threshold of 25 g' mag $M_{\rm ICL}^{\rm SB25}$, (4) via the surface brightness threshold of 28 g' mag $M_{\rm ICL}^{\rm SB28}$, (5) via the light excess above the inner de Vaucouleurs fit $M_{\rm ICL}^{\rm DV}$, and (6) via the double Sérsic fit $M_{\rm ICL}^{\rm S\times}$. The methods are explained in Sec. 7.4. The rows show (1) the absolute systemic velocity offset $v_{|\rm syst|}$ (data taken from Lauer et al. 2014), (2) radial X-ray emission peak offset $r_{|\rm syst|}$ (data also taken from Lauer et al. 2014), (3) mass density ρ [$M_\odot$ kpc^{-3}], (4) number density of satellite galaxies s [kpc^{-3}], (5) mass phase space density $f_{\mathcal{M}}$ [M$_\odot$ kpc^{-3} km^{-3} s^3], and (6) number phase space density of the satellite galaxies $f_{\rm s}$ [kpc^{-3} km^{-3} s^3] (6). The histograms show the number of data points in each bin from the subplot containing either $M_{\rm sat}$ or $M_{\rm BCG+ICL}$ (cf. Fig. 7.7).

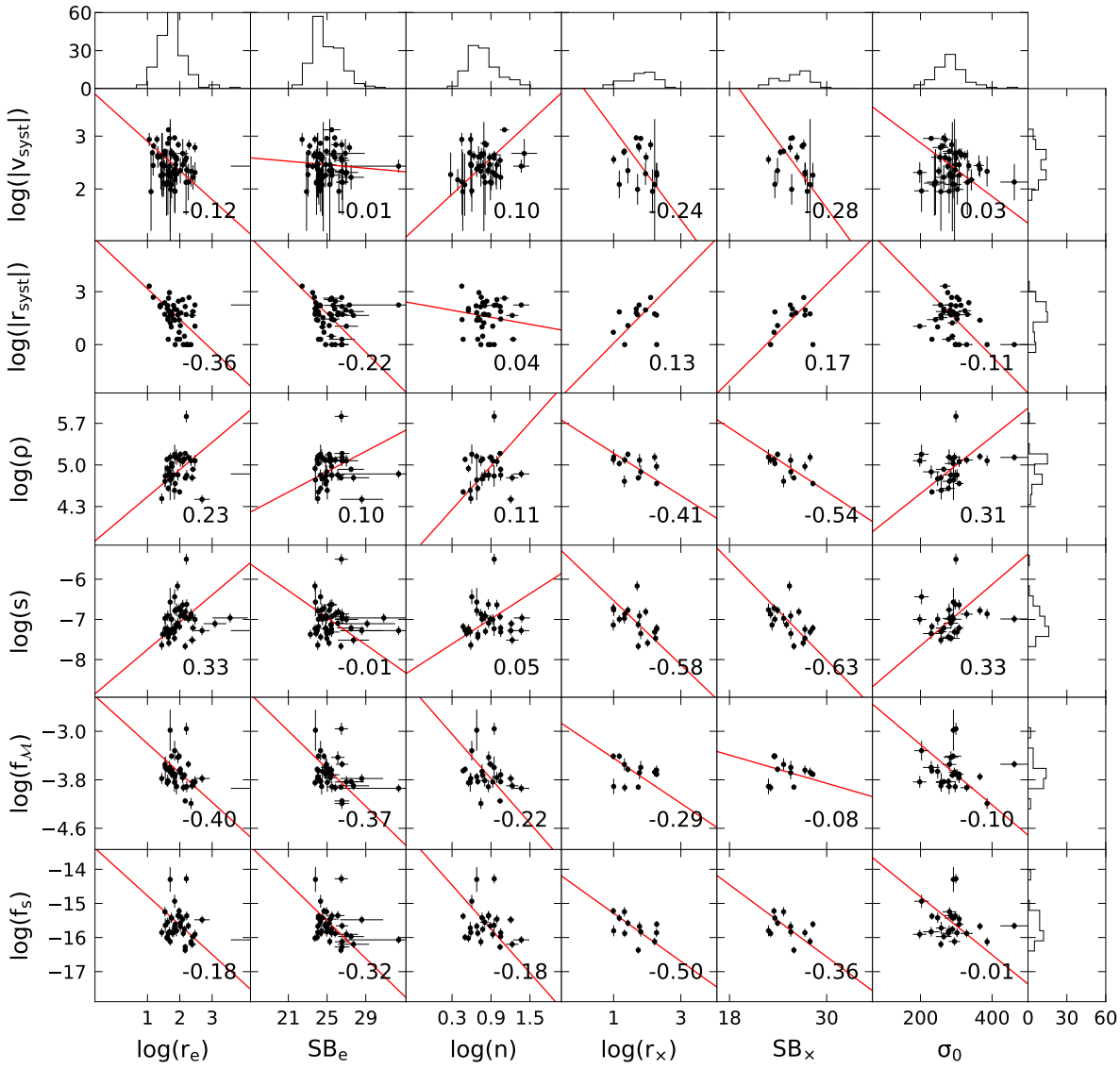

Figure 7.10: Correlations between BCG/ICL parameters (horizontal) and cluster parameters (vertical). The columns show (1) the effective radius r_e [kpc] along the major axis and (2) corresponding effective surface brightnesses SB_e [g' mag arcsec^{-2}], (3) Sérsic index n of the SS BCGs, (4) transition radius $r_\times$ [kpc] and (5) transition surface brightnesses $SB_\times$ [g' mag arcsec^{-2}] between the two Sérsic profiles of the DS BCGs, and (6) central velocity dispersion (data taken from Lauer et al. 2014). The rows show (1) the absolute systemic velocity offset $v_{|\mathrm{syst}|}$ (data taken from Lauer et al. 2014), (2) radial X-ray emission peak offset $r_{|\mathrm{syst}|}$ (data also taken from Lauer et al. 2014), (3) mass density ρ [$M_\odot$ kpc^{-3}], (4) number density of satellite galaxies s [kpc^{-3}], (5) mass phase space density $f_\mathcal{M}$ [M$_\odot$ kpc^{-3} km^{-3} s^3], and (6) number phase space density of the satellite galaxies f_s [kpc^{-3} km^{-3} s^3] (6). The histograms show the number of data points in each bin from the subplot containing either M_sat or $M_\mathrm{BCG+ICL}$ (cf. Fig. 7.7).

7.5.2 Alignment

Another quantity which is related to the connection between BCG/ICL and cluster formation/evolution is their alignment. Many studies have found strong correlations between the alignment of the BCG and the cluster galaxies distribution (Sastry, 1968; Dressler, 1978; Binggeli, 1982; Struble, 1990; Kim et al., 2002; Yang et al., 2006; Niederste-Ostholt et al., 2010; West et al., 2017). Our deep PA profiles allow us not only to investigate the alignment but also whether it improves with radius. Furthermore, we investigate whether the ICL is offset towards the cluster center. For these analyses, we consider only clusters where a center and position angle could be reliably determined from the satellite galaxy samples retrieved from the `SIMBAD` database. We have selected 50 out of the 170 clusters from our sample that fulfill these two criteria sufficiently well.

The results are shown in Fig. 7.11. We confirm that both, the BCG and the ICL are strongly aligned with the cluster orientation. Moreover, the ICL is aligned even better with the satellite galaxy distribution: the ICL is aligned $\Delta PA < 30°$ in $40/50 = 80\%$ clusters compared to the BCGs ($33/50 = 66\%$; compare West et al. (2017): $32/52 = 62\%$). The expected value for a random distribution would be 33%. Our results show an overall better alignment than the results from West et al. That might be an effect of relaxation over time. Their analyzed clusters are at significantly higher redshifts than ours and there is also an improvement in the alignment visible from their higher redshift sample to their lower redshift sample. The results from Huang et al. (2016) show a weaker alignment. A possible explanation is related to our visual optimization of the smoothing kernels for the galaxy density distributions: in case of isodensity contour twists (e.g., in A2029; possibly due to triaxiality of the Dark Matter halo) we favor the inner PA (i.e., closer to the radii where we measure the ICL PA) instead of the average PA of the galaxies density distribution. We expect the intrinsic alignment to be stronger where cluster- and ICL-radii are more similar.

Furthermore, the direction of the ICL offset compared to the direction of the cluster galaxies number density peak is aligned better than $< 60°$ in $33/46 = 72\%$ of the clusters. The expected value for a random distribution would be again 33%. Four outlier clusters are discarded from our subsample because the cluster offsets are > 400 kpc. Our measurements for the ICL offsets and the galaxy number density peak offsets are independent from each other and a strong correlation between them is unlikely to occur by chance. Contrary to our results, Gonzalez et al. (2005) found no significant ICL-to-BCG offsets (except in one case) for their sample of 24 BCGs.

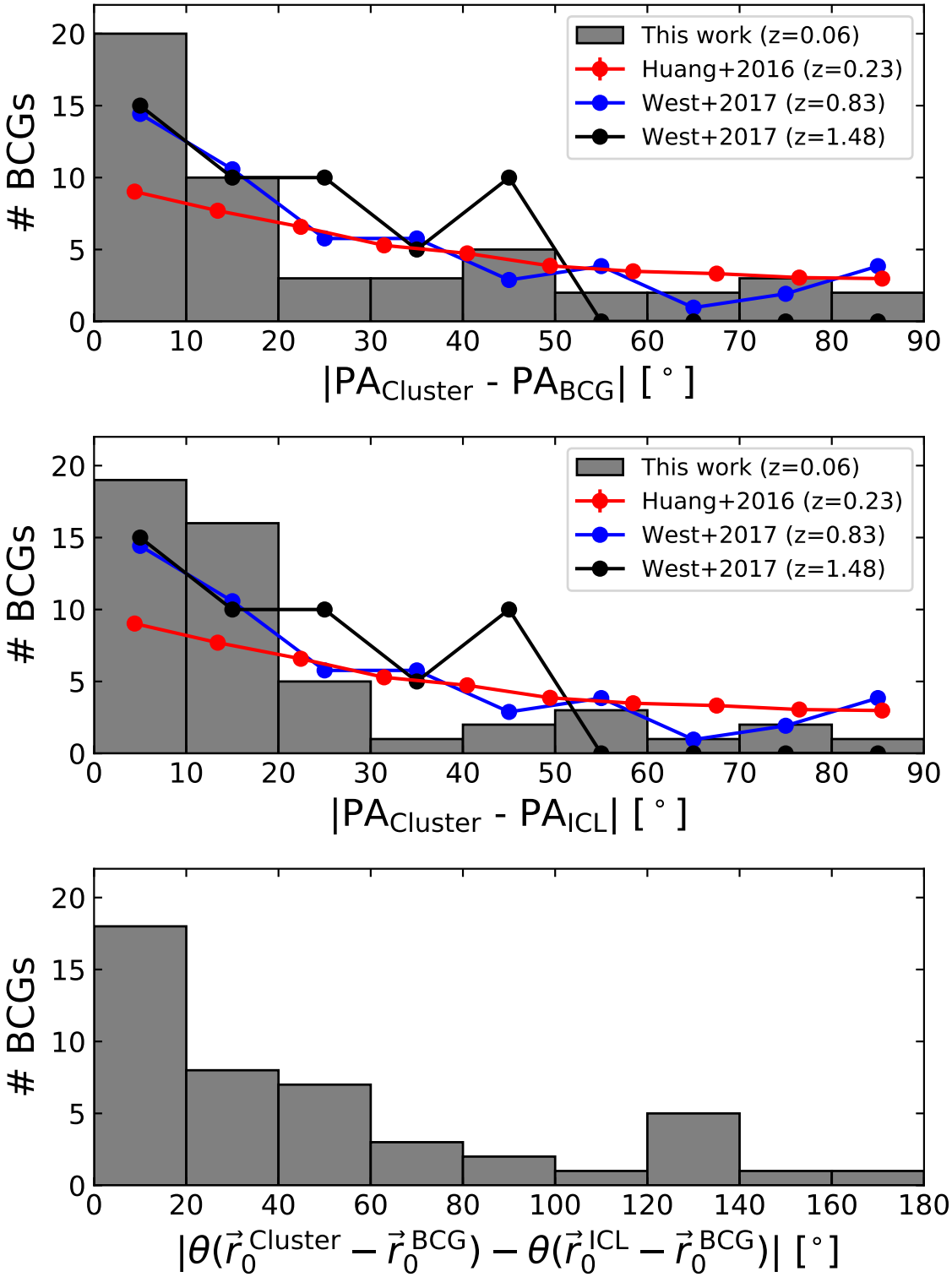

Figure 7.11: *Top and middle panels:* alignment between the BCG (top panel) or ICL (middle panel) with the cluster galaxies orientation. The data from Huang et al. (2016) and West et al. (2017) are renormalized and overplotted for comparison. *Bottom panel:* direction of the ICL offset compared to the direction of the cluster galaxies offset with respect to the BCG. A value of 0° means that the ICL and the cluster galaxies (on average) are offset towards the same direction.

7.5.3 Systemic velocity- and X-ray offsets

The discovery that DS BCGs show slightly more disturbed morphologies than SS BCGs lets us presume that this less relaxed state manifests further in higher systemic velocity offsets and larger X-ray offsets for DS BCGs. A systemic velocity offset is defined as the line of sight velocity difference between the average velocity of the cluster galaxies and the one of the BCG's core $|\bar{v}_{\mathrm{galaxies}} - v_{\mathrm{BCG}}|$ (Oegerle & Hill, 2001). The X-ray offset is the analogous measurement in the two other spatial dimensions. It is the projected radial distance between the peak of the X-ray emission which traces the cluster center and the center of the BCG. We use published data from Lauer et al. (2014) for this analysis.

Fig. 7.12 shows a double histogram of absolute systemic velocity offsets (top panel) and absolute X-ray offsets (bottom panel). The numbers for each Sérsic type add up to one. The normalization allows for a fair comparison since the two types of BCGs have different subsample sizes in this study (73 SS BCGs vs. 27 DS BCGs for the systemic velocity offsets and 39 SS BCGs vs. 14 DS BCGs for the X-ray offsets). The average error is 52 km s^{-1} for the systemic velocity offsets and on the order of a few tens of kpc for the X-ray offsets.

A Kolmogorov–Smirnov test gives a 43% probability that the SS and DS BCG samples are drawn from the same systemic velocity offset distribution. The test for the X-ray offsets gives 52% probability. These numbers do not allow us to draw any conclusion here.

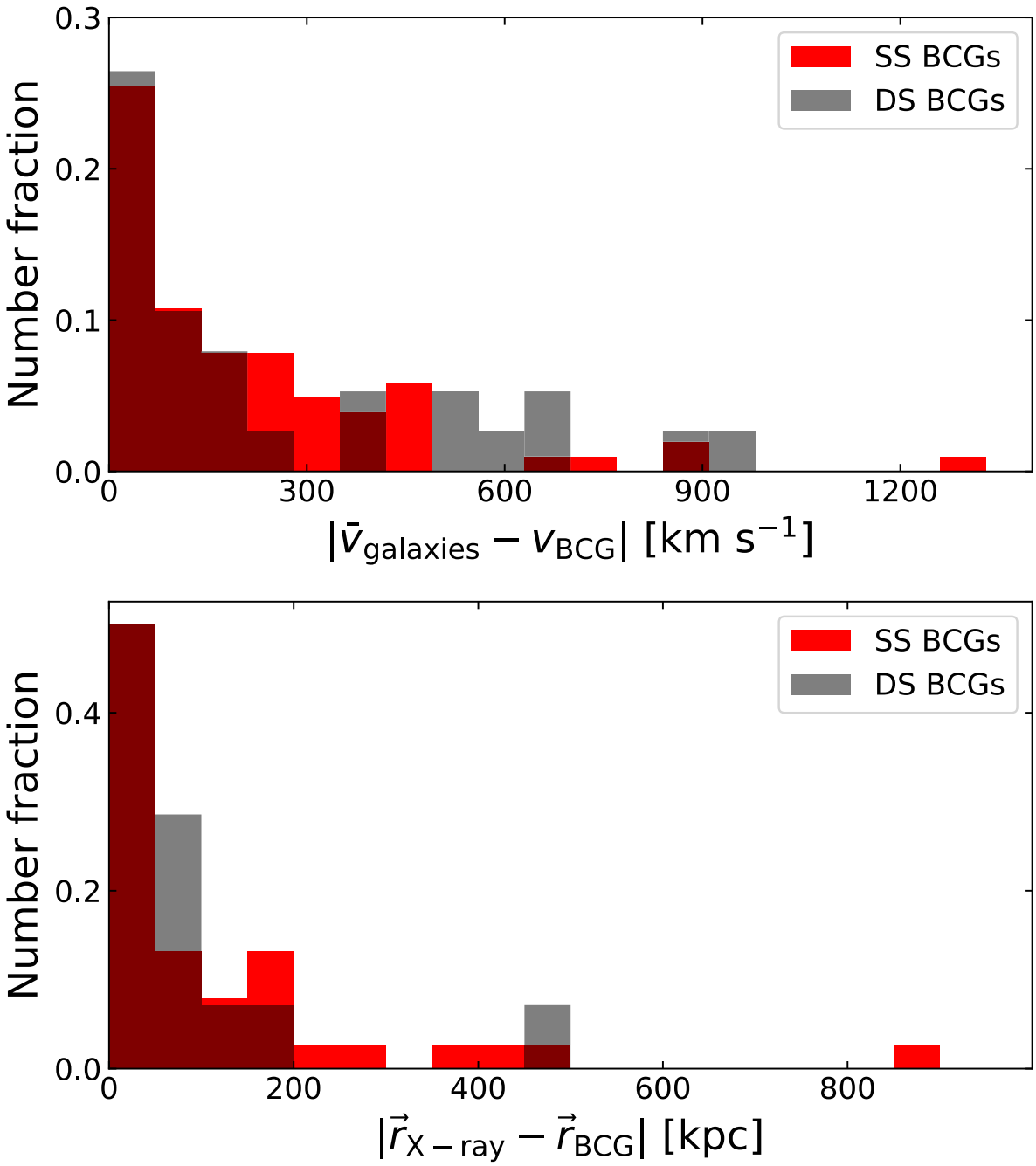

Figure 7.12: Normalized histograms of systemic velocity offsets (top panel) and X-ray offsets (bottom panel). Data are taken from Lauer et al. (2014). Only BCGs that overlap with the Lauer et al. sample were considered.

Chapter 8

Discussion

8.1 Do BCGs form a unique class of elliptical galaxies?

We compare the structural parameters of BCGs to those of regular ellipticals in Fig. 7.3. Spheroidals and ellipticals including classical bulges populate different areas in parameter space, which indicates that they are formed by different formation scenarios (Kormendy et al., 2009). BCGs also do not follow the correlations for regular ellipticals. The slopes are steeper. The downward trend of the Kormendy and $M_{\rm tot} \propto SB_{\rm e}$ relations in Fig. 7.3 illustrates the growing importance of the low-surface-brightness stellar halo and ICL contribution of ellipticals with increasing luminosity because half of the light is below the effective surface brightness. The broken slopes of these relations underline that the stellar halos and ICL are even more important for BCGs; that is, their growth is even more dominated by accretion in their low-SB outskirts (e.g., Oser et al. 2010). We emphasize that we do not try to dissect the ICL or stellar halos from the BCGs for deriving their structural parameters and instead consider their combined stellar light.

The effective radii are also larger than what would be expected from extrapolating the size-luminosity relation $M_{\rm tot} \propto \log(r_{\rm e})$ for regular ellipticals. All these findings confirm the picture that regular ellipticals and BCGs differ from each other in the importance of accretion in their formation history. BCGs reside near the center of their host cluster. Contrary to regular ellipticals, that enables them to accumulate enormous amounts of stellar material instead of being tidally stripped by the cluster potential.

8.2 Is the inner component of DS BCGs "Extra Light"?

An alternative explanation for the origin of DS profile shapes could be due to a central poststarburst stellar population as it is often seen in extra-light ellipticals (e.g., Faber et al. 1997; Kormendy 1999; Kormendy et al. 2009; Kormendy & Bender 2013). There are two families of ellipticals: boxy–core–nonrotating and disky–extralight–rotating (Bender 1988; Bender et al. 1988, 1989, 1991; Kormendy & Bender 1996; Kormendy et al. 2009). Most BCGs are categorized as boxy–core–nonrotating galaxies, which is further confirmed by the distribution of Sérsic indices (see Sec. 7.3). Those ellipticals are believed to have formed via dissipationless merging and subsequent violent relaxation. However, judging from the SB profiles in Appendix A, there are some BCGs that could potentially be categorized as

unusually massive extra-light ellipticals. Non-BCG extra-light ellipticals have small transition radii of $r_\times \lesssim 1$ kpc (Hopkins et al., 2009; Kormendy et al., 2009) or $r_\times < 0.04 r_\mathrm{e}$ (Mihos & Hernquist, 1994). A light excess above the inward extrapolation of the outer Sérsic profile is interpreted to arise from a poststarburst stellar population that was formed after a wet merger. The origin of the DS shape would then be unrelated to the ICL phenomenon. Those BCGs can bias the structural parameter relations and correlations with cluster properties.

By conservatively selecting only DS BCGs that have transition radii $r_\times \gtrsim 0.1 r_\mathrm{e}$ and transition surface brightness $SB_\times > 23$ g' mag arcsec^{-2}, we discard 49/98 BCGs from the DS sample that are potentially extra-light ellipticals and classify them as SS BCGs. The structural parameter relations between r_e, SB_e and M_tot for both split samples do not differ significantly from each other.

Furthermore, we inspect the isophotal distortions a_4 of the potential extra-light ellipticals. Extra light is frequently observed to have disky isophotes when viewed edge-on (e.g., Sec. 9.3 in Kormendy et al. 2009). At least some of the 49 potential extra-light BCGs in our sample should have high inclinations. Therefore, we expect the average a_4 to be higher in the inner regions for the potential extra-light BCG subsample than for the rest of the DS BCGs. We do not find that. The isophotes of the potential extra-light ellipticals are not diskier near the transition radii than those of the BCGs that have no potential extra light.

The abundance of multiple cores for potential extra-light ellipticals would increase if some of them are the remnants of the wet mergers. Contrary to that expectation, it is even less. Also, malicious handling of overlapping galaxies is thereby excluded as an artificial origin of small $r_\times$ DS profiles.

All 18 BCGs that overlap with the Lauer et al. (2007) sample (A76, A193, A260, A347, A376, A397, A634, A999, A1016, A1020, A1142, A1177, A1656, A1831, A2052, A2147, A2199, and A2589) are classified by the authors as cored ellipticals. The decisions were made based on high-resolution HST images. Six out of those BCGs are classified by our criteria as potential extra-light ellipticals: A193, A260, A397, A1020, A2147, and A2589. I.e., the SB profiles have a core inside a potential extra-light region. This will break the known dichotomy if the extra light will be confirmed to form in the same poststarburst scenario as it is the case for lower mass ellipticals.

8.3 Do DS BCGs differ from SS BCGs in their evolutionary state?

The members of both Sérsic types are, in general, very similar in their appearance. Both families follow the same structural parameter correlations (see Fig. 7.3 and Tab. 7.1). Any characteristic that qualifies each Sérsic type as distinct might be subtle. Nevertheless, there are differences beyond the simple number of analytic functions that are needed to fit their light profiles well.

First of all, we take a closer look at the average profiles presented in Fig. 7.2. The clearest discrepancy is found in the ellipticity ϵ profiles. DS BCGs are, on average, rounder at small radii $r = \sqrt{ab} < 16$ kpc and become more elliptical at larger radii. This is qualitatively consistent with the discovery by Donzelli et al. (2011). DS BCGs furthermore have lower scatter in position angle drifts $\Delta PA(r)$, that is, smaller isophote twists for individual galaxies.[1] And finally, DS BCGs have on average less boxy isophotes ($a_4^\mathrm{DS} > a_4^\mathrm{SS}$). We must

[1]The larger scatter at small radii can be attributed to the smaller ellipticities that increase the uncertainty

note here that boxy isophotes also result from shells (González-García & van Albada, 2005), which are actually marginally more common for SS BCGs (see Fig. 7.1). Nevertheless, all of these tendencies are identical with those of more rotationally supported and thus less evolved systems. The spatial offsets between the ICL and the BCG are on average larger for DS BCGs. This is related to the higher abundance of multiple nuclei (see Fig. 7.1) that drag the main nucleus along by their gravitational attraction. The analog to ICL offsets in velocity space is systemic velocity offsets, that is, the line-of-sight velocity difference between the BCG and the average cluster line-of-sight velocity. We have examined the distributions of systemic velocity- and X-ray gas peak offsets for SS and DS BCGs separately (see Fig. 7.12) using published data from Lauer et al. (2014). A Kolmogorov–Smirnov test showed that no conclusion can be drawn from those data.

The isophotal parameters that describe asymmetric distortions a_3, b_3, and b_4 are higher for DS BCGs (see Fig. 7.2). Such shapes are not stable and are therefore evidence for ongoing accretion. The larger abundance of signatures from these accretion processes is also documented in Fig. 7.1. These features are relatively short-lived because they are dynamically hot. They originate from collisions and stripping events with high relative velocities of order $\sim$1000 km s^{-1}. Because these remnants are visible today, DS BCGs must have undergone more of these events recently.

We mentioned before that any dichotomy between SS and DS BCGs is subtle. Most of our distinctions are not very significant, but they all point to the same conclusion. SS BCGs are currently in a more relaxed state because they have experienced fewer accretion events in the recent past. Either the earlier accreted stellar mass has already virialized by violent relaxation, or the events that would create a distinctly visible envelope have not yet taken place.

8.4 Does the outer Sérsic component trace the ICL?

This discussion was started around the pioneering work of Schombert (1986) and the thesis is supported by recent simulations (Cooper et al., 2015). First of all, we find that 121 (71%) out of our 170 observed BCGs are of SS type whereas 49 (29%) are of DS type. The bare existence of SS BCGs is problematic in this context. For these not uncommon cases, the transition between inner and outer Sérsic component is smooth so that any photometric decomposition is strongly degenerate (Bender et al., 2015). The number fraction of DS BCGs in this work is 19% points lower than the 48% found by Donzelli et al. (2011). One reason for that is the minimum transition radius that we require for a potential DS BCG to be classified as such. The number fraction in the Magneticum simulation is with 58% (Remus et al., 2017) also higher than ours. If we included the potential DS BCGs with very small transition radii, then our DS number fraction would increase to 58%, which would agree perfectly with the results of Remus et al. That agreement strengthens the conclusions drawn from this simulation on the inner structure and dynamics of BCGs+ICL. By decomposing the stellar velocity distributions into two Maxwellians, they isolated the ICL as the dynamically hot component. This approach is motivated by the observed rises in velocity dispersion profiles towards the ICL (Ventimiglia et al. 2010; Toledo et al. 2011; Arnaboldi et al. 2012; Melnick et al. 2012; Murphy et al. 2014; Bender et al. 2015; Barbosa et al. 2018; Spiniello et al. 2018) and currently consensus for numerical simulation (Dolag et al. 2010; Puchwein et al. 2010;

of the PA measurement.

Rudick et al. 2011; Cui et al. 2014). In their publication, Remus et al. (2017) state that they find "no clear correlation between the presence of a second component in the velocity distribution and the presence of a second component in the radial density profile".

We now examine DS parameters that could possibly depend on the total integrated brightnesses $M_{\rm BCG+ICL}$ of the BCG+ICL systems. We use $M_{\rm BCG+ICL}$ as a proxy for the evolvedness of the system: more evolved BCGs have had more time to accrete stellar debris onto their ICL halos and have grown since in total brightness. If the hypothesis was correct that the outer photometric component traces the ICL, then at least one of the following four relations is necessary to emerge:

1. larger fraction of DS BCGs to all BCGs with increasing BCG+ICL luminosity ($R = 0.2$).
2. increasing light fraction $f_{\rm S2}$ encompassed in the outer Sérsic component with BCG+ICL luminosity if the BCG is unaffected by the accretion ($R = 0.2$),
3. larger transition radii $r_\times$ for higher luminosity if the components mix ($R = 0.26$),
4. a vertical size-luminosity relation if stars are accreted homogeneously over all radii.

In order to discuss option four, we refer to Tab. 7.1. The size-luminosity relation for DS BCGs is $\log(r_{\rm e}) \propto 1.41(\pm0.08)\log(L_{\rm BCG+ICL})$. That means fractional BCG growth is 41% larger in radius than in luminosity. That argument plus our finding that the light fraction at low SBs increases with BCG+ICL brightness (see Sec. 7.4, §2) disprove the fourth option in the list above. For the remaining options, we give the Spearman coefficients in the brackets. The absence of relations one and two are the strongest indicators that the two-component structure of the light profiles might be nothing more than a result of the recent accretion events and a photometric decomposition into two Sérsic functions is likely to be unphysical. Final conclusions can only be drawn from additional velocity information. We will explore whether the transition between the two components coincides with a distinct rise in velocity dispersion for a small subsample of BCGs in a subsequent paper.

8.5 ICL as a Dark Matter tracer

ICL is the dynamically hot stellar component that was assembled by tidally stripping stars from cluster galaxies. These stars move freely in the cluster potential and, when virialized, should trace the overall mass distribution. This expectation was recently confirmed for six clusters from the Hubble Frontier Fields (Montes & Trujillo, 2019). The ICL in these clusters traces the overall Dark Matter distribution including substructure better than the hot X-ray gas, because it is less perturbed by mergers than the dissipative gas.

We examine four criteria that potentially qualify ICL as a good Dark Matter tracer: (1) the ICL PA alignment with the cluster PA, (2) the offset from the BCG towards the cluster center, (3) the ellipticity, and (4) the line-of-sight velocity. We have selected a subset of 50 clusters from our dataset with the most reliable cluster PA and cluster center measurements. The satellite galaxies are used as test particles for the underlying Dark Matter distribution (e.g., Shin et al. 2018).

(1) We begin our discussion with the PA alignment between the BCG, ICL and their host clusters.

It is well known that BCGs are well aligned with their host clusters (see Sec. 7.5.2). Our results show that the alignment is even better for the ICL. The difference in PA is $\Delta PA < 30°$ in 80% of the clusters whereas that is only the case for 66% of the BCGs (see Fig. 7.11). The expectation value for a random distribution is only 33%.

(2) Criterion two is the offset between BCG, ICL and their host clusters. We begin with the direction of the offsets and then discuss their amplitudes.

The direction of the ICL offset from the BCG coincides in 72% of the cases to better than 60° with the direction of the cluster offset from the BCG. A random distribution would have only 33% matches. We conclude that the ICL is generally more at rest in the cluster potential than the BCG.

The amplitude of the ICL offset radially increases (see Fig. 7.2, central panel). At 200 kpc circular radius, the isophotes are shifted on average by 17%, i.e., 37 kpc with 34 kpc intrinsic scatter. For a subsample of 31 clusters, in which the cluster and ICL offset directions agree by $< 60°$, and the cluster offset is less than < 400 kpc, we find an amplitude of 93 ± 62 kpc of the cluster offsets, compared to 9.3 ± 9.7 kpc for the ICL offsets.

We now compare our results to ICL offsets, X-ray gas offsets and Dark Matter centroid offsets with respect to the BCGs which have been published in the literature.

Similar to our results, ICL-to-BCG offsets exist in Hydra (12 kpc, Arnaboldi et al. 2012) and A1651 (15 kpc, Gonzalez et al. 2005). However, 23/24 BCGs are consistent with having no ICL offsets in the study by Gonzalez et al. (2005). By comparing the projected center of the satellite galaxy distribution with the projected location of BCGs, Zitrin et al. (2012) found typical BCG offsets of around 12 kpc in 10 000 SDSS clusters. Oguri et al. (2010) determined mass profiles of 25 clusters using weak lensing methods from high-quality Subaru/Suprime-Cam imaging data. They find that most of the centroids coincide with the location of the BCG within their measurement uncertainty of 35 kpc. However, a non-negligible number of clusters shows large offsets of up to 500 kpc. The intracluster medium (hot, X-ray emitting gas) is a good tracer for the total mass distribution because it can be assumed to be in hydrostatic equilibrium. Umetsu et al. (2014) found for 20 CLASH clusters a median offset between the BCG and the X-ray peak of 7 kpc with 21 kpc intrinsic scatter. Using high-resolution Chandra data, Lauer et al. (2014) found a median offset of 10 kpc but $\sim 15\%$ of the BCGs have offsets larger than 100 kpc (see also Fig. 7.12, bottom panel).

We conclude that the average amplitude our measured BCG-to-ICL offsets is consistent with the BCG-to-Dark Matter offsets measured by other authors.

(3) A third quality, that is required for ICL to be a good Dark Matter tracer, is that its average ellipticity ϵ must be similar to the average ellipticity of Dark Matter halos. For the ICL, we have measured an axis ratio $(b/a)_{\rm ICL} = 1 - \epsilon \approx 0.5 - 0.6$ at the largest circular radius $r = \sqrt{ab} \approx 200$ kpc. The average ellipticity of Dark Matter halos can be measured by using satellite galaxies as test particles or using stacked weak lensing measurements. Both methods have been applied by Shin et al. (2018) for 10,428 SDSS clusters. They found an average axis ratio $(b/a)_{\rm DM} = 0.573 \pm 0.002({\rm stat}) \pm 0.039({\rm sys})$ using the satellite galaxy method or $(b/a)_{\rm DM} = 0.56 \pm 0.09({\rm stat}) \pm 0.03({\rm sys})$ using the stacked weak lensing method. The results agree with the average ICL ellipticity.

(4) By measuring line-of-sight velocities, Bender et al. (2015) found the mean ICL line-of-sight velocity around the BCG NGC 6166 to be shifted toward the mean line-of-sight velocity of the cluster galaxies. Therefore, the ICL is more at rest with respect to the cluster as a whole, and subsequently, also with the Dark Matter.

From all of the considerations above, we conclude that the ICL is better aligned than the

BCG in position, velocity, ellipticity and position angle with respect to the cluster galaxies and consequently, with respect to the Dark Matter distribution.

Chapter 9

Summary and Conclusions

We have obtained optical g'-band observations of 170 galaxy clusters with the Wendelstein Wide Field Imager. The data reduction pipeline was developed and assembled specifically for that instrument and optimized for low-surface-brightness photometry. We have measured semimajor axis surface brightness (SB) profiles of the BCGs down to a limiting SB of $SB_{\rm lim} = 30\ g'$ mag arcsec^{-2}, which is an unprecedented depth for a large samplesize.
Our results for the structure of BCGs, including their ICL envelopes, are summarized as follows:

A1 BCGs have larger effective radii, dimmer effective surface brightnesses, and brighter absolute magnitudes than expected for an extrapolation of the parameter correlations for regular ellipticals. The Kormendy, the size–luminosity and the $M_{\rm tot}$–$SB_{\rm e}$ relations have broken slopes at least in part because of the presence of ICL around the BCGs.

A2 By fitting Sérsic functions to the semimajor axis SB profiles, we find that 71% of the observed BCGs are well described by a single Sérsic function (SS BCGs). The remaining 29% of BCGs have variations in the slope of their SB profiles that require using two Sérsic functions to obtain a good fit (DS BCGs). DS BCGs with transition radii $r_\times < 0.1 r_{\rm e}$ and transition surface brightnesses $SB_\times < 23\ g'$ mag arcsec^{-2} were fitted with a single Sérsic function excluding the inner excess light. The DS profile shape is more likely to arise in those cases because of a poststarburst stellar population following a wet merger than because of the ICL phenomenon.

A3 SS and DS BCGs do not deviate significantly from each other in their parameter correlations between effective radii $a_{\rm e}$ along the major axis, effective surface brightnesses $SB_{\rm e}$, and integrated absolute brightnesses $M_{\rm tot}$.

A4 SS BCGs are slightly more compact ($r_{\rm e}^{\rm SS} = 45 \pm 24$ kpc) than DS BCGs ($r_{\rm e}^{\rm DS} = 72 \pm 31$ kpc). In integrated brightnesses, SS BCGs are 14.8% fainter ($-23.68 \pm 0.53\ g'$ mag) than DS BCGs ($-23.83 \pm 0.41\ g'$ mag).

A5 The Sérsic indices of SS BCGs are significantly larger than $n \geq 4$ in 83% of the cases. That value approximately separates the two classes of disky–coreless–rotating ellipticals and boxy–core–nonrotating ellipticals.

A6 The radial profiles of their structural parameters show that SS BCGs have on average

(a) shallower ellipticity profiles,

(b) stronger individual isophote twists,

(c) smaller ICL offsets,

(d) boxier isophotes,

(e) less pronounced asymmetric isophotal distortions, and

(f) fewer accretion signatures

than DS BCGs. We deduce from these results that SS BCGs are on average marginally more relaxed because they have encountered fewer accretion events in the recent past. The tendencies are identical to those of more triaxial and dispersion supported, that is, more evolved systems.

A7 The average isophote twists, i.e., position angle variations with radius, are $\Delta PA/\Delta r \sim 10^{\circ}/100$ kpc.

A8 The average ellipticity increases with radius and reaches $\epsilon = 0.4$–0.5 at a circular radius of $r \approx 200$ kpc.

A9 The isophotal offset with respect to the nucleus increases with radius. At 200 kpc circular galactocentric radius from the nucleus, the average offset is 37 kpc with 34 kpc intrinsic scatter.

Our results for the approaches to separate the ICL from the BCGs photometrically are summarized as follows:

B1 For DS BCGs, the luminosity fraction of the outer Sérsic component $S2$ relative to the total BCG+ICL luminosity is 52±21%. The abundance of DS BCGs relative to SS BCGs and the large intrinsic scatter of $S2$ are well reproduced by the Magneticum simulation (if we would include the extra-light BCGs in our DS BCG subsample) where Remus et al. (2017) found no correlation between the existence of a two-component nature of the stellar velocities which represent the BCG and dynamically hot ICL and the existence of a two-component nature of the SB profiles. In our observational data, the BCG+ICL brightness correlates only weakly with $S2$, the transition radius $r_{\times}$ between the two Sérsic components and with the transition surface brightness $SB_{\times}$. Both results suggest that the separation between BCG and dynamically hot ICL is not possible based on photometric decompositions of their light profiles. That is in agreement with the photometric and kinematic results of a case study of NGC 6166 (Bender et al., 2015).

B2 The fiducial ICL/BCG luminosity fraction above an integrated brightness of $M > -21.85$ g' mag is $71 \pm 22\%$. The corresponding ICL/Cluster luminosity fraction is $20\% \pm 12\%$.

B3 The fiducial ICL/BCG luminosity fraction below $SB > 27$ g' mag arcsec^{-2} is 34%±19%. It increases with total BCG+ICL brightness, indicating that BCGs grow predominantly by accretion in their low-SB outskirts. The corresponding ICL/Cluster luminosity fraction is $10\% \pm 12\%$.

B4 The fiducial ICL/BCG luminosity fraction above an inner de Vaucouleurs function is $42\% \pm 33\%$. The corresponding ICL/Cluster luminosity fraction is $12\% \pm 8\%$.

B5 The fiducial ICL/BCG luminosity fraction inferred via the DS profile decomposition method is 52%±21%. The corresponding ICL/Cluster luminosity fraction is 18%±17%.

B6 The (BCG+ICL)/Cluster luminosity fraction is 28% ± 17%.

Our results for the correlations of BCG/ICLs with their host cluster properties are summarized as follows:

C1 We find positive correlations between BCG+ICL brightness and cluster mass, cluster radius, cluster richness and integrated satellite brightness. That confirms that the growth of BCGs is connected to the growth of their host clusters.

C2 The BCG position angles (PAs) are aligned to better than $\Delta PA < 30°$ in $33/50 = 66\%$ with the PAs of their host clusters. The alignment between the ICL and their host clusters is even stronger: $41/50 = 82\%$ are better aligned than $\Delta PA < 30°$.

C3 The ICL offset with respect to the BCG at 200 kpc circular radius is 37 kpc with 34 kpc intrinsic scatter. That is consistent with the offsets between the BCG and X-ray gas centroids or Dark Matter mass centroids.

C4 The direction of the ICL offsets agrees to better than 60° with the direction of the cluster galaxies number density peak offset in $33/46 = 72\%$ of the clusters.

C5 The ICL ellipticity increases with radius and reaches $\epsilon = 0.4 - 0.5$ at a circular radius of $r \approx 200$ kpc. That is consistent with the ellipticity of cluster Dark Matter halos (Shin et al., 2018).

Results C2 – C5 qualify ICL as a potential Dark Matter tracer.

We conclude from our study that BCG+ICLs have scaling relations with steeper slopes than those for normal non-BCG ellipticals. That is likely because the faint ICL outskirts around BCGs have a significant influence on the structural parameters. We found that the light fraction at faint SB levels below $SB > 27$ g' mag arcsec^{-2} grows with total BCG+ICL brightness. That supports the idea that the role accretion becomes more and more important as BCG+ICLs grow – up to the point where the BCG+ICL sizes and luminosities become similar to those of whole galaxy clusters. Moverover, the correlations between BCG+ICL brightness and various host cluster parameters shows that BCG+ICL formation is tightly linked to the growth of their host clusters.

Our deep SB profiles enable us furthermore to decide more consistently whether a SB profile is well described by a SS or DS profile. The former case is more common (71%) at redshift $\bar{z} = 0.06$; that is, most of the BCG+ICLs have relatively smooth SB profiles. Whether the photometrically distinct stellar envelopes around the rarer DS BCGs trace the ICL is debated. We have shown that the isophotal shapes of DS BCGs are more disturbed and accretion signatures are more common inside them than in SS BCGs. Hence, it is possible that the envelopes are simply the result of unrelaxed, recently accreted material and not necessarily the signature of pure ICL. On the other hand, it could also be that SS BCGs have not yet accumulated sufficient stellar material to build up a distinct ICL envelope.

Nevertheless, we have compared fiducial ICL luminosity fractions $f_{\rm ICL}$, calculated with various methods of which (2), (3) and (4) are commonly applied in the literature: (1) a

constant brightness threshold of $M = -21.85$ g' mag, (2) constant SB threshold at $SB = 27$ g' mag arcsec^{-2}, (3) de Vaucouleurs fit to the inner SB profiles plus an outer light excess and (4) double Sérsic SB profile decomposition. The results range from $f_{\rm ICL} = 34\% - 71\%$ with large intrinsic scatter. The disagreement amongst the various methods underlines that the ICL dissection cannot be done unambiguously with photometric data alone. Future work based on color-information and kinematic data will help to gain more insight into the formation of BCGs and ICL.

Part II

WWFI data reduction pipeline

Chapter 10

Overview

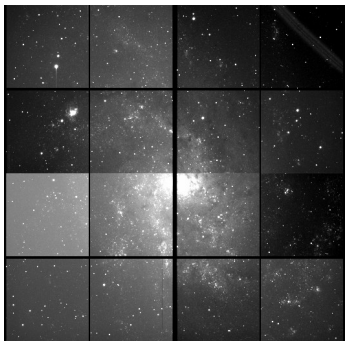

raw image of M33

autoreduce_V2.sh

stacked u'-g'-r' color image of M33

Example execution:

```
autoreduce_V2.sh -P=A1656 -rv=V191209 -p=abell1656 -fr=g -b -f
                 -cp=0.2 -sc -fs=g -ra=12:59:36 -dec=27:57:34
```

```
ds9 /data/wst/u/<USER>/WWFI/reduced/A1656/final/A1656_V191209_g_1.fits
```

This chapter is dedicated to assist users to work independently and efficiently with the WWFI data reduction pipeline `autoreduce_V2.sh`. It was developed and assembled to perform the basic reduction of WWFI raw data automatically and with minimal user input. One command line execution is sufficient to create a calibrated and stacked mosaic. More advanced options are available to perform background subtraction, removal of bright stars, satellite masking, and precise photometric zero-point calibration. These features require more user input and iteration but improve the results significantly.

The pipeline currently runs on the 2nd generation `EUCLID` computing cluster, which is operated by the Max Planck Institute for Extraterrestrial Physics (MPE) in Garching, Germany. At the time of writing this thesis (January 2020), it offers 8 computing nodes with 32 cores and 122.8 GB RAM each and 26 computing nodes with 40 cores and 377.4 GB RAM each. Users are allowed to utilize 256 cores simultaneously. That makes this setup ideal for parallelized WWFI data reduction.

10.1 Camera and Readout Modi

The WWFI camera is made of four 4096×4109 pixel sized e2v CCD detectors installed in a SI 900 camera system by Spectral Instruments. The detectors are aligned in a 2×2 mosaic (cf. Fig. 12.1). On the sky, the gaps between the CCDs are 98″ in the north–south direction and 22″ in the east–west direction for a position angle of 0°. The field of view of each CCD is 13.7′×13.7′, making the combined field of view extend over 27.6′ × 28.9′ with a pixel size of 0.2″/pixel. Finding charts for this setup can be created using the tool `finding_chart.sh`. Each quadrant of one CCD is readout at a different readout port, located at the nearest corner. This leads to the images being split into 16 squares, each with slightly different gain and bias offset level that both depend on the selected readout mode. These squared regions are referred to as "ports" in the following sections.

Two different fast readout modi with gains $g = 5.845\ e^-$/ADU (1) and $g = 2.26\ e^-$/ADU (6), respectively, as well as one slow readout modus with $g = 0.3739\ e^-$/ADU are available. Since both, the bias structure and the gain vary for different readout modi, masterbiasses and masterflats are created for each mode separately. Their date-folders have the assigned suffixes "", "ro6" and "slowro", respectively.

10.2 Work flow

The flow chart in Fig. 10.1 illustrates the sequences in which scripts are called.

Labels drawn alongside arrows show arguments that must be parsed to `autoreduce_V2.sh` in order to execute the script to which the arrows point. Manually executed scripts show examples of their available arguments if they are called without any arguments.

The script `autoreduce_V2.sh` is the user interface of the pipeline. It can be executed from any directory on the `EUCLID` cluster and the output files are always stored in the directories listed in Tab. 20.2. The arguments listed in Tab. 20.1 can be parsed to the script. They (de-)activate options and set parameter values, e.g., object names, filterbands, etc. An example call is

```
autoreduce_V2.sh -P=A1656 -rv=V191209 -p=abell1656 -fr=g -b -f
-cp=0.2 -sc -fs=g -ra=12:59:36 -dec=27:57:34
```

which reduces and stacks archival g'-band data of the Coma cluster. The project name is defined using `-P=<PROJECT>`. A version number for the reduction can be parsed using the argument `-rv=<VERSION>`, which must begin with the capital letter "V", e.g., `-rv=V191231`, marking the date of the execution. The raw-data file prefixes must be specified using `-p=<PREFIXES>`. If unknown, they can be looked up in the raw data directory (see Tab. 20.2). The remaining options and much more are described in the following chapters and can be looked up in the Table 20.1.

After execution, the input parameters are firstly checked for validity. If successful, raw- and calibration data are then collected by the script `prepare_V2.sh` by checking the filenames and header keywords. The observing log-files are not necessary here. After a final user confirmation, the script `script.autoreduce_V2` is executed in the background. From then on, the user can logout while the data reduction will continue until it has finished. Generally, no files are overwritten. The pipeline can be executed multiple times, e.g., when additional observations were taken afterwards and shall be reduced, too.

The creation of masterbias and/or masterflat images is activated by parsing the argument `-fr=<FILTERS>` in combination with the argument `-b` and/or `-f`, respectively. They are created only once. After they exist for a given date and readout mode (and filterbands `<FILTERS>` for masterflats), they are stored in the directories listed in Tab. 20.2 and will be reused in future `autoreduce_V2.sh` calls.

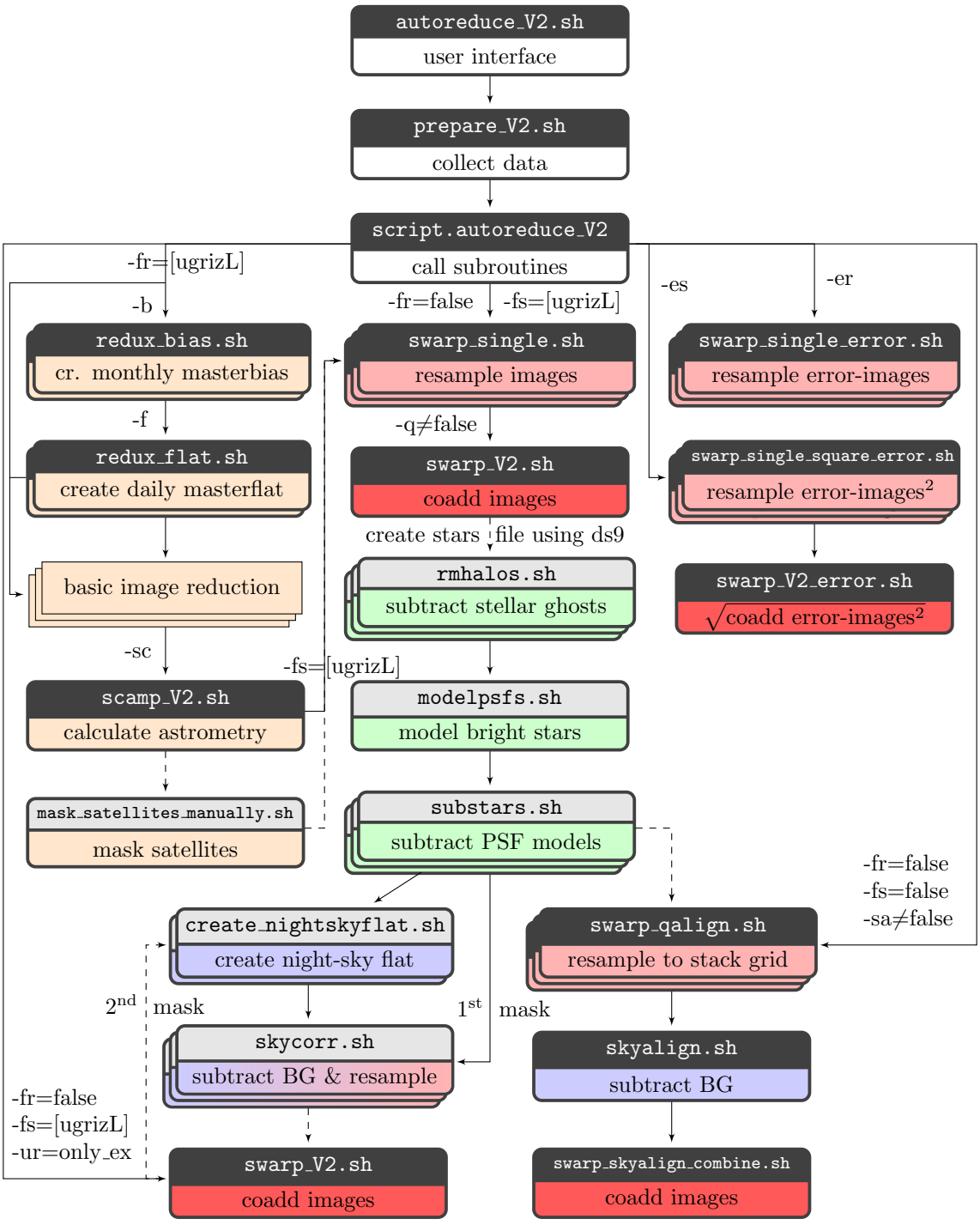

Figure 10.1: Flow chart of the WWFI data reduction pipeline. Black top-colored elements name scripts, which are executed automatically by the pipeline and gray top colored elements name manually executed, supplementary scripts. Bottom colors of the elements represent: white = organizing pipeline scripts, bright orange = standard reduction, bright red = resampling, red = coaddition, bright green = removal of bright stars, blue = background subtraction. Another flow chart just for the "basic image reduction" is shown in Fig. 10.2. One layer represents scripts, which are executed only once, whereas two (three) layers indicate that the script is executed in parallel for each night (image). Labels drawn alongside arrows show arguments that must be parsed to `autoreduce_V2.sh` in order to execute the script to which the arrows point. Dashed arrows point towards scripts, which needs to be executed manually.

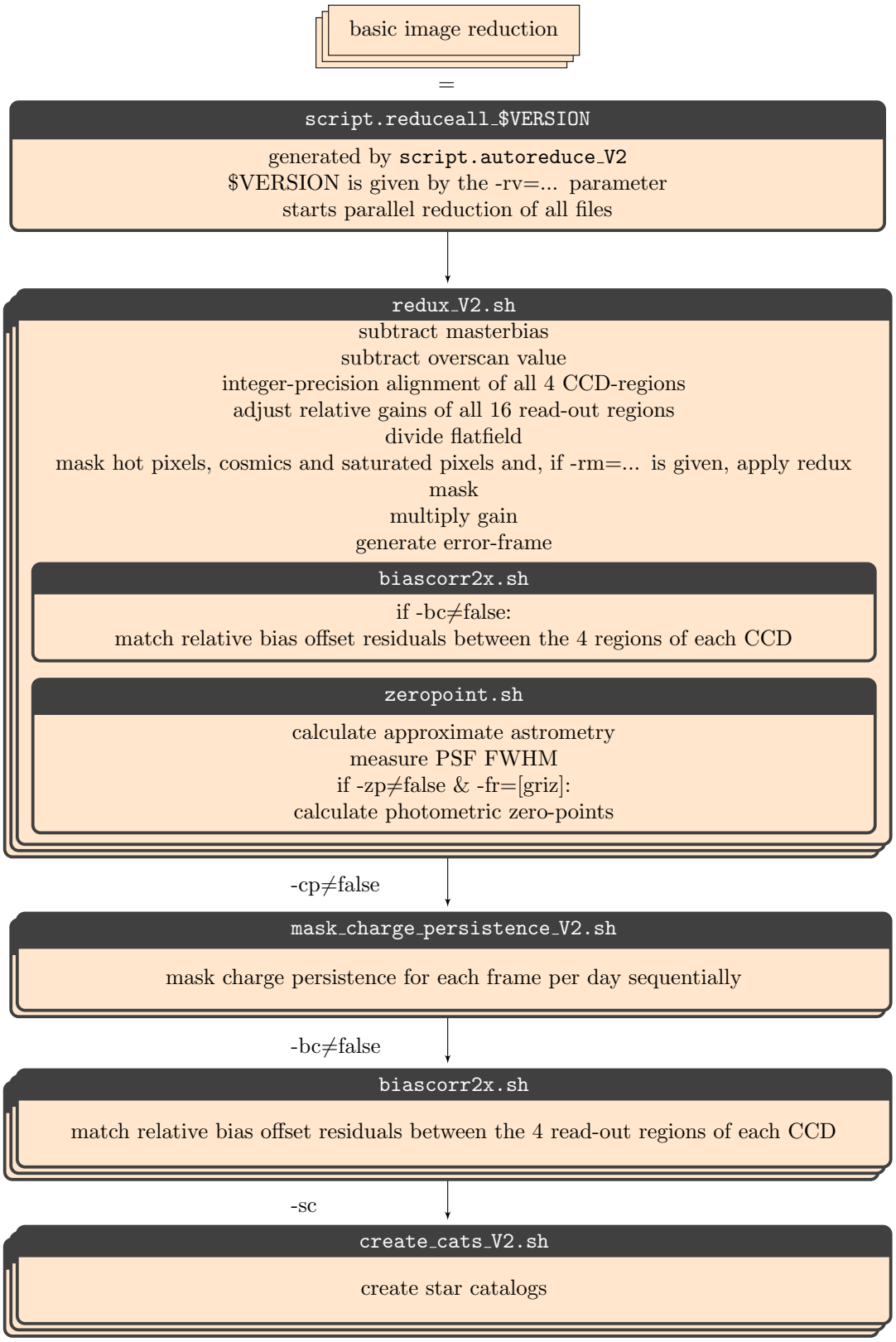

Figure 10.2: Flow chart of the basic image reduction. One layer represents scripts, which are executed only once whereas two (three) layers indicate that the script is executed in parallel for each night (image). Labels drawn alongside arrows show pipeline arguments, which are required to continue with the next step. If that argument is not given (for -sc) or set to false (for -cp or -bc), the step will be skipped.

Chapter 11

Calibration images

11.1 Masterbias

The currently recommended observing strategy is to take bias exposures, and subsequently create masterbiases, once every month. As the bias pattern and hot pixels are time-stable for at least a few years, this strategy has proven to be efficient and sufficiently precise. An option to create daily masterbiases is also available and can be activated by parsing the argument `-bd` for "bias daily" instead of `-b` for "bias (monthly)".

The masterbias routine is executed by the script `redux_bias.sh` and encompasses the following steps. First, for every bias image the average bias offset level is measured in each of the four ports of all the individual CCDs and subtracted using the script `zerobias.py`. Then the resulting images are averaged after clipping 3σ outliers with respect to the median, thus creating a masterbias including only the smaller scale pattern, but not the bias offset values. In the science images, this bias offset value will be measured and subtracted in/from the overscan regions.

11.2 Masterflat

Master-twilight-flats are recommended to be created daily. The pattern is sometimes more, sometimes less dominated by "measles". Those are bright or dark spots with sizes of a few to a few tens of pixels, varying in shape and number over time scales of one day. The pipeline argument activating the masterflat option is `-f`. If no twilight flats were observed at/in the required date, filter and readout-mode, then the masterflat from the closest date will be created or linked to the relevant date.

The masterflat routine is called by the script `script.masterflat_V2` and executed by the script `redux_flat.sh`. The procedure is the following. Firstly, the masterbias image is subtracted from all raw flat images. Then, the bias offset value is measured in the overscan region and subtracted from the corresponding ports using the script `zerobias.py`. After cropping the overscan regions, the CCD regions are approximately shifted with few-integer precision to the grid of their correct sky positions. The individual gains of the 16 ports are matched to a common value. A hot-pixel mask and the absolute gain are multiplied. An error image is created, which includes the photon noise of the sky. All flat images are then fitted by a 2D polynomial of fourth order, divided by it and multiplied with the polynomial of the reference image of that day. Thereby, the large-scale pattern is matched for all flat images before they are combined, so that no offsets remain around the masked stars.

Chapter 12

Basic data reduction

The basic data reduction is illustrated in the flow chart in Fig. 10.2. It is activated when the argument `-fr=<FILTERS>` is parsed. One or more filternames from the available set `<FILTERS>` = {u, g, r, i, z, L} can be given without spaces. Firstly, a script `script.reduceall_<VERSION>` is generated by `prepare_V2.sh` that contains the execution commands for `redux_V2.sh`. The latter contains the basic data reduction routines and is executed in parallel for each image.

The first part of the procedure is similar to the flat image reduction (see above). The masterbias is subtracted from the science image if the argument `-b` or `-bd` is parsed. An error image is created, consisting of the propagated statistical uncertainties, i.e., readout noise, overscan value uncertainty, flat fielding uncertainty as well as shot noise of the sky and celestial sources. These files have the prefix `e.`. In order to save disk space and increase performance speed, the generation of error images can be skipped by parsing the argument `-ne` to the pipeline.

After that follows the subtraction of the overscan values using `zerobias.py`. The program `wwfi_gaps` performs an approximate alignment of the CCD regions, relative gain correction and bleeding masking. Bleeding occurs when electrons leak out of saturated pixels onto their neighboring pixels. Those contaminated pixels are masked by setting all pixels with values larger than 20 000 ADU for readout mode 1, larger than 45 000 ADU for readout mode 6 and larger than 60 000 ADU for readout mode 3 to 0 in the science image and to -1 in the corresponding error image. A peculiar property of the WWFI is that only the boundaries of bleeding regions have high counts. The enclosed pixels can have very low or even negative counts. In order to mask the whole saturated region, the pixel coordinates farthest from the port border in readout direction is saved in a `*.cptab` table file, which is later used in the step of charge persistence masking to mask the full contaminated stripes (see Sec. 12.4). Another peculiarity occurs in the top right port of the bottom left CCD. When stars strongly saturate here, lines of negative pixel values extend towards the left, originating from all bleeding pixels. This effect is accounted for by masking all pixels with negative values.

The next step is the multiplication with both, the gain value and a hot pixel mask. Counts are now in units of photons per second times exposure time. Cosmics are masked using multiple methods implemented in `cosmicfits` (Gössl & Riffeser, 2002).

Furthermore, the science images are divided by a masterflat if the argument `-f` is parsed. A (redux-)mask with the filename `<FILENAME>.fits` can be multiplied to every (integer-

precision re-gridded) image, e.g., when an obscuration shadow dampens the flux in some parts of the images. The file must be located in the directory `/data/wst/u/<USER>/WWFI/reduced/<PROJECT>` and be parsed to the pipeline via the argument `-rm=<FILENAME>.fits`. The project name is specified using `-P=<PROJECT>`. It can be, e.g., the name of the observed target.

12.1 Bias level offset adjustments between ports

Each of the 16 ports has a different bias offset level added to the corresponding image region. An estimate of these offsets is calculated from the overscan regions in the science images and subtracted in a previous step. However, a small, time-variable offset between the overscan value and the zero-value of the exposed image region remains. A possible but unverified explanation is a heating up of the readout electronics when charges are read out and consequently an increase of dark current. Fig. 12.1, left panel, shows one reduced image where jumps are visible in the background values between the four ports in both of the top two CCD images. The script `biascorr2x.sh`, activated with the `-bc=<STRIPEWIDTH>` pipeline option, matches the background values along the borders between ports. The stripe in which the pixel values are measured has a thickness of `<STRIPEWIDTH>` on each side. The values are averaged in the width direction so that two one-dimensional vectors on each side of the border can be compared. The difference between these vectors $\mathbf{t}$ is then evaluated. In the first iteration, only differences lower than absolute $|\mathbf{t}| < 100$ counts are considered. The remaining values are averaged between the 30th and 70th percentiles. In the second iteration, only differences lower than absolute $|\mathbf{t}| < 2$ counts are considered. The remaining values are more or less clean background difference values, which are then averaged to obtain one offset value O for each border. The clockwise offsets along the four borders in each CCD image are labeled as the hours of a clock $O3, O6, O9$ and $O12$, where $O3$ is the offset from the bottom right port minus the top right port, $O6$ is bottom left minus bottom right, $O9$ is top left minus bottom left and $O12$ is top right minus top left.

The top left and bottom right ports levels are matched to the level of the bottom left port. For the top right port, the two possible offset-pathways are averaged. All ports levels are now matched to the bottom left port level, whose own bias offset level also fluctuates. The weighted average of all offsets is then added to all four ports to reduce the overall fluctuation. The quantitative description for this level matching is

$$\begin{aligned} F_{\mathrm{new}}(P2) &= F_{\mathrm{old}}(P2) - O9, \\ F_{\mathrm{new}}(P3) &= F_{\mathrm{old}}(P3) - [(O9 + O12) + (-O3 - O6)]/2, \\ F_{\mathrm{new}}(P4) &= F_{\mathrm{old}}(P4) + O6, \\ F_{\mathrm{new}}(P1234) &= F_{\mathrm{old}}(P1234) + (O9 - O6 + [(O9 + O12) + (-O6 - O3)]/2)/4, \end{aligned} \tag{12.1}$$

where $F_{\mathrm{new}}(Pi)$ and $F_{\mathrm{old}}(Pi)$ are the fluxes in the full port region i after and before bias level offset correction.

This procedure works well as long as there are no saturation stripes or charge persistence stripes present in the offset measuring regions. Unfortunately, these occur not infrequently and then in multiple subsequent exposures. Therefore, the script `biascorr2x.sh` is executed again after those stripes had been masked by `mask_charge_persistence_V2.sh` (activated

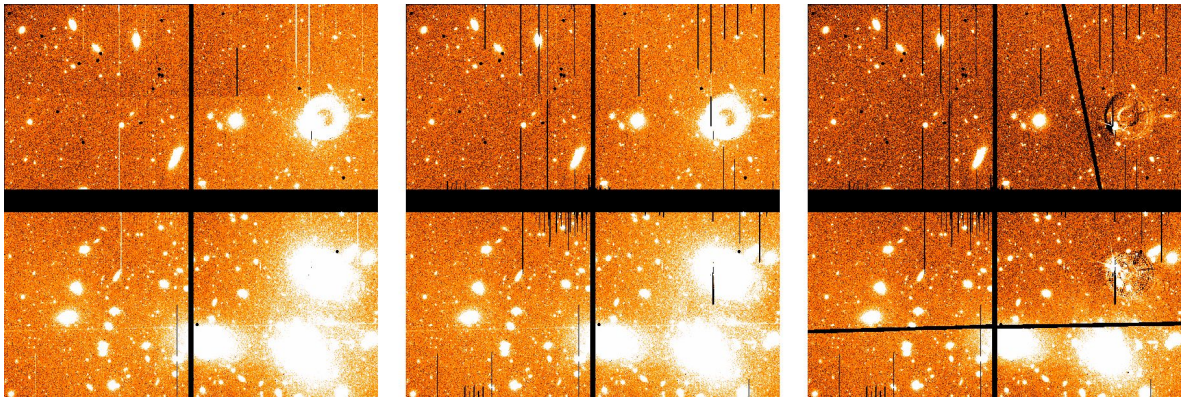

Figure 12.1: Bias level offset adjustments between ports in a single exposure of the coma cluster A1656. The background values of the four quadrants in each CCD are matched to each other. *Left:* after bias level adjustment but before charge persistence masking. Offsets remain in the top two CCDs. *Middle:* after another bias level adjustment iteration succeeding charge persistence masking. The offsets in the top two CCDs are removed but a new one is introduced in the bottom right CCD due to a bright star close to a port border. *Right:* after bias level adjustment on the residuals after subtracting a stack using `substack.sh` and `postbiascorr.sh`. Bright stars are also removed at this stage and two satellites trails are masked.

via `-cp=<THRESHOLD>` in the pipeline). The improvement can be seen in Fig. 12.1, from left to middle panel.

In some cases, the offset measurements are biased by extended galaxies and bright stars with relatively sharp edges, which fall close to the port borders. An example is shown in Fig. 12.1, middle panel, bottom right CCD. An enlarged version of the image is shown in Fig. 14.1. In that image area, a jump of the background value is visible between the top left and the top right port. It is caused by a bright star. These residual offsets can be removed at a later stage by manually calling the script `postbiascorr.sh`. It matches the offsets by running `biascorr2x.sh` on the residuals after a coadded image was subtracted from the single images using `substack.sh`. The executing commands are:

```
cd /data/wst/u/<USER>/WWFI/reduced/<PROJECT>/<REDUXVERS>/stacks/
substack.sh  auto  g  ../../final/<STACK>  ../../final/<POSTMASK>
postbiascorr.sh  auto  <FILTER>
```

The resampled files `stacks/swarp_<FILTER>/q*.resamp.fits` must already exist beforehand, e.g., from a previous `autoreduce_V2.sh ... -fs=<FILTERS>` execution. The reason is that the `FLASCALE` header keyword from those files is used by `substack.sh` to undo the flux scaling.

The last argument for `substack.sh` is optional. It parses a mask file, letting `postbiascorr.sh` ignore the thereby masked regions. Such a mask file can be created as follows (see also Sec. 19):

```
cd /data/wst/u/<USER>/WWFI/<PROJECT>/final/
create_maks.sh <STACK> <MASKNAME>
               # recommended masking parameters: 25smag 1 0 5 n
```

12.2 Preliminary astrometric solution

So far, the CCD regions had been only approximately shifted to their real positions on the sky, and no rotation and stretching had been performed, yet. Therefore, only an approximation to the true astrometric solution can be calculated at this stage of the data reduction. This is automatically done with the script `script.astrometry.sh`. The main purpose of this step is to identify known point sources in order to calculate the photometric zero-point of each image.

Source catalogs are created using the script `script.sex`, which makes a `SExtractor` (Bertin & Arnouts, 1996) call. These catalogs are then filtered with three different conditions:

1. `FLAGS=0 & FWHM>0.6″ & FWHM<10″`
   (common case),
2. `FWHM>0.6″ & (XY_IMAGE<-7 | XY_IMAGE>7) & X2_IMAGE<70 & Y2_IMAGE<70`
   (suitable for comet data where stars are strongly elongated),
3. `FLAGS<8 & ERRAWIN_IMAGE<0.1 & FWHM_IMAGE>0.4″ & FWHM_IMAGE<30`
   (suited for low signal-to-noise data).

The astrometric solution is calculated for each of the three differently filtered source catalogs using `SCAMP` (Bertin, 2006). The search parameters are constrained inside a maximum position error of $5'$ and a maximum position angle error of $5°$ is assumed. If the calculation fails, the constraints are softened to allow for $40'$ position error and $180°$ position angle error. That is necessary for data taken before the beginning of 2014, when no initial world coordinate system was provided yet, and for the rare cases when image headers are corrupt.

The "cont." value is a measure for the accuracy of the astrometric solution. It is provided in the last column of the `SCAMP` output for the given file. They are compared for all three results and the best solution is stored in the header of the image. Resulting world coordinate systems are precise only to a few pixels. However, this is sufficient to calculate the photometric zero-point in the next step.

Furthermore, two header keywords `BG` and `BGRMS` are stored. They are the median value of the background checkimage and the median value of the background root-mean-square noise checkimage, respectively. Both are provided by `SExtractor`.

12.3 Photometric zero-points

Photometric zero-points are calculated for each image using the tool `calib_ZP`, by comparing the `SExtractor` source catalog, created in the previous step, to the Pan-STARRS DVO PV3 catalog (Flewelling et al., 2016). This feature is only implemented for the g'-, r'-, i'-, and z'-bands as no Pan-STARRS catalogs exist for the u'- and L-bands. It can be deactivated with the option `-zp=false`.

In WWFI data, source fluxes are measured in circular $5'' = 25$ px diameter apertures, using the `SExtractor` parameters for background modeling `BACK_SIZE=64` and `BACK_FILTERSIZE=3`[1]. The calculated zero-point is stored in the header keywords `ZP` and `ZP25`. Unfortunately, the

[1]For details about the background modeling by `SExtractor`, see the manual at `https://www.astromatic.net/pubsvn/software/sextractor/trunk/doc/sextractor.pdf`.

calculated zero-point depends on the aperture size since light leaks out of the apertures, especially when the seeing is larger than FWHM $\gtrsim 2''$. Therefore, the final coadded image should be re-calibrated (see Sec. 16).

A second zero-point is calculated for fluxes measured inside $10'' = 50$ px diameter apertures but blending makes the fit highly unstable (cf. Fig. 16.1). This value is stored in the header keyword `ZP50`.

Two more keywords are stored: `SEEING`, which approximates the seeing by the median FWHM value of all detected sources, and `TRANSPAR`. Latter is an estimate for the sky transparency during the observation but it is also sensitive to the long-term degradation of mirror reflectivity due to dust (cf. Fig. 20.1, top panel).

$$\texttt{TRANSPAR} = \texttt{dex}(0.4(ZP25 - 2.5\log(\texttt{EXPTIME}) - ZP_{\rm best})), \tag{12.2}$$

where `EXPTIME` is the exposure time and

$$ZP_{\rm best}(g') = 25.240, \tag{12.3}$$
$$ZP_{\rm best}(r') = 25.155, \tag{12.4}$$
$$ZP_{\rm best}(i') = 24.640, \tag{12.5}$$
$$ZP_{\rm best}(z') = 23.907. \tag{12.6}$$

These values are approximately the modes of the distribution zero-points, calculated for a large number of exposures. They depend on the seeing and mirror reflectivity (see long-term evolution in Fig. 20.1, top panel).

The zero-point script can also be called manually using

```
qsub $SCRIPTS/zeropoint.sh ‘pwd‘ <FILENAME>.fits true 50 1 N AUTO
```

12.4 Charge persistence masking

Here we briefly describe the options. For a detailed analysis of this phenomenon, see the chapter 2.2.4 of the Master's thesis by Matthias Kluge (LMU, 2015).

Bright sources saturate the potential wells of the pixels with electrons. Some electrons get trapped in lattice defects and are released on thermal time scales. During readout, these released electrons are deposited in the pixels opposite of the readout direction. The resulting bright stripes are referred to as saturation stripes. Furthermore, electrons get trapped in all pixels along the readout direction. These become visible as fainter charge persistence stripes in subsequent images. An example is shown in Fig. 12.2. Heavy contamination by charge persistence stripes is visible throughout the whole image. This illustrates that charge persistence stripes can remain significant for many hours, depending on the severity of saturation and background brightness in the subsequent images.

The pixel positions of saturated stars and times of saturation are stored by the program `wwfi_gaps` in the files `*.cptab` in the `.../redux/` directory. They are used by the program `mask_charge_persistence_V2.sh` to identify and mask saturation- and charge persistence stripes if the 2σ clipped average flux in an affected column exceeds the 2σ clipped average flux in the darkest of the ± 15 surrounding columns by `<THRESHOLD>` times the standard deviation σ in the affected column. The value for `<THRESHOLD>` is parsed by `-cp=<THRESHOLD>` to the pipeline. A well tested, good value is 0.2.

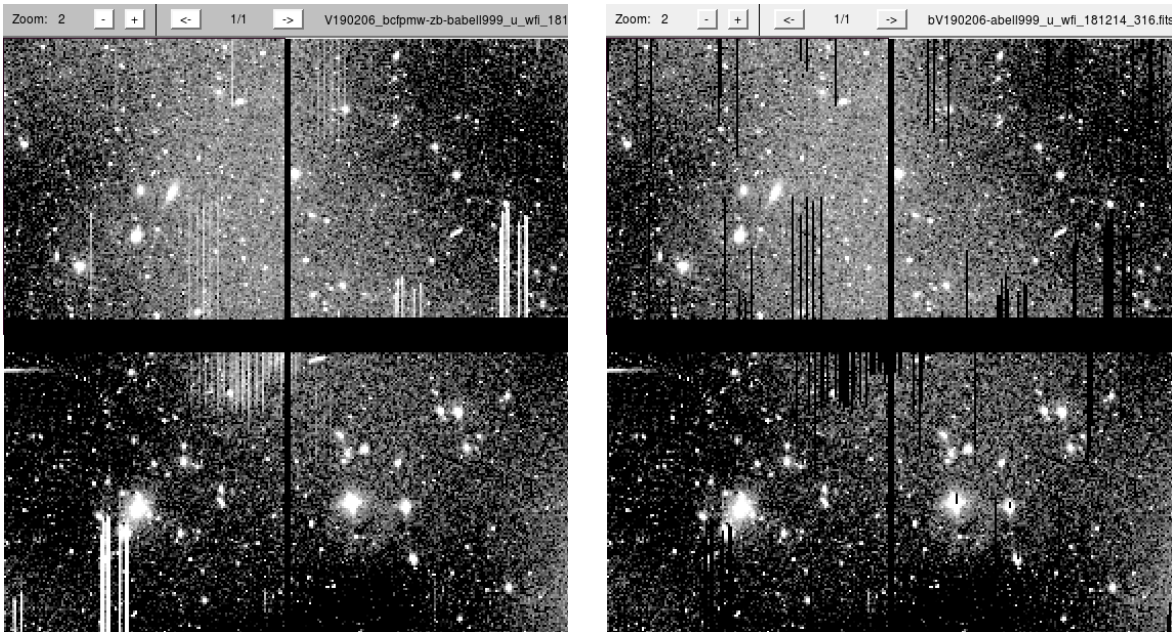

Figure 12.2: Example of charge persistence stripes in a 10 min u'-band exposure of A999 before masking (left) and after masking (right). The Trapezium star cluster in M42 was observed until three hours before this observation. The faint sky in the u'-band makes the stripes stand out.

There are cases when stars had saturated strongly in previous observations, e.g., when M42 was observed prior to an Abell cluster (see Fig. 12.2). In order to mask them, all pixel positions of saturated stars must be remembered and then checked for residual stripes in the first Abell cluster exposure. This can be done by reducing the M42 observations along with the Abell observations in a dedicated pipeline run and by parsing the argument `-cp=1000min`. All saturated pixels positions will then be stored for 1000 minutes after saturation occurred. The work-flow is demonstrated below.

```
autoreduce_V2.sh -P=A1656 -rv=V191209 -p="abell1656 abell1656_sky"
                 -ra=12:59:36 -dec=27:57:34 -fr=g     -b -f -d=20170125
autoreduce_V2.sh -P=A1656 -p="abell1656 abell1656_sky m42 foc bestfoc"
                 -rv=V191209cp -ra=12:59:36 -dec=27:57:34 -fr=ugriz
                 -b -f -d=20170125 -cp=1000min
cd /data/wst/u/mkluge/WWFI/reduced/A1656/V191209/redux/
cp ../../V191209cp/redux/V180719cp-abell1656_sky_g_wfi_170125_
   379.fits.cptab.date.new
   V180719-abell1656_sky_g_wfi_170125_379.fits.cptab.usethis
autoreduce_V2.sh -P=A1656 -p="abell1656 abell1656_sky" -rv=V191209
                 -ra=12:59:36 -dec=27:57:34 -fr=g
                 -b -f -d=20170125 -cp=0.2
```

The informations of all previously saturated pixels is stored in the table file of the last M42 observation `V180719cp-abell1656_sky_g_wfi_170125_379.fits.cptab.date.new`. By copying it to the location of the main data reduction directory, it will be used instead of the local `*.cptab` file. The copied table file must end with the name `*.usethis`.

Chapter 13

Precise astrometric solution

Astrometric solutions are calculated for all images when the argument `-sc` is parsed to the pipeline. The procedure involves three steps: 1) file splitting, 2) creation of source catalogs and 3) calculation of the astrometric solutions. The resulting world coordinate systems, i.e., astrometric solutions, are stored in the `stacks/*.scamp.head` files.

13.1 File splitting

Each file `V*.fits` in the `redux/` directory contains all four CCD images at fixed pixel positions. Relative or absolute rotations, as well as stretches and sub-pixel shifts between the CCDs are not corrected, yet. However, they are crucial for the astrometric precision. Therefore, the files firstly need to be split into four single images. This is done by the script `create_cats_V2.sh`. The split images are then stored in the `stacks/` directory with the prefixes `q?wc-` where `?` is an integer ranging from $1 <= Q <= 4$. CCDs are numbered clockwise: $Q = 1$ is bottom left, $Q = 2$ is top left, $Q = 3$ is top right and $Q = 4$ is bottom right.

13.2 Source catalogs

Source catalogs are necessary to compare the positions of sources in WWFI images to their expected R.A. and Dec. positions. They are created for each split CCD image individually using `SExtractor` and then merged to one catalog using the script `create_cats_V2.sh`. Faint sources with $S/N < 10$ are discarded.

13.3 Astrometry

Astrometric solutions are calculated for all images in the `stacks/` directory in parallel. The program `SCAMP` matches the source positions in the WWFI catalogs to those of the reference sources in the 2-MASS J-band catalog. Only shift, rotation and stretching is considered. No higher order distortions are necessary because the corrector optics flatten the field of view sufficiently well. Global astrometric solutions are calculated for all four CCDs simultaneously, i.e., relative astrometric solutions for all four CCDs are fixed to increase the stability. They had been determined for one representative image and are since then hard-wired into the

pipeline. The file `/data/wst/u/wst/WWFI/SCRIPTS/wwfi.ahead` contains the relative shifts, stretches and rotations of the CCDs: 0.30° (bottom left), 0.14° (top left), 0.18° (top right) and 0.32° (bottom right) in clockwise direction. No evolution is expected to occur over time.

Several quality checks are implemented to discard files with erroneous solutions. Files with less than six detected sources are discarded by moving them to the directory `stacks/not_enough_stars`. Files, for which the astrometric matching did not converge are marked with the word `RED` in the logfile `stacks/log.scamp`. They are discarded by moving them into the directory `stacks/bad_astrometry`. Moreover, files with a pixel scale ≤ 0.1991 or ≥ 0.1994 are also discarded (cf. Fig. 20.1). In addition to that, the photometric solutions (for the u'- and L-bands or for all bands if `-zp=false` is parsed to the pipeline) are erroneous for all files if the astrometric solution is wrong for at least one of them. If at least one file is discarded, another iteration of `SCAMP` is executed for the remaining files.

The overall pixel scale depends slightly on the observed filterband (see Fig. 20.1, second panel from the bottom). For instance, it is $\sim 0.05\%$ larger for the u'-band compared to the i'-band. The reason is currently unknown and unexplored, but probably related to the filter-glasses. Atmospheric diffraction would lead to a continuous increase with wavelength but the z'-band pixel scale is more consistent with the r'- than with the i'-band pixel scale. However, this has no important consequence because the global pixel scale is calculated for each image independently.

Chapter 14

Satellite trails masking

Satellite- or air plane trails appear in $\sim 3\%$ of all 60 s exposures. An automatic masking procedure using a Hough transform was implemented in a previous version of the pipeline by Annalisa Mana. It could in principle be re-activated in the current version, too. However, even after optimizing the parameters, a significant fraction of false positive and false negative detections remain. Manual masking is a much more reliable strategy, although it requires some user interaction. Moreover, by visually inspecting each image, other contaminations are easily identified. Affected images can be discarded by moving them to the directory `stacks/bad/`. Examples for contaminations are shown in Fig. 14.3. Once identified, the file names, e.g., "`abell1656_g_wfi_170125_360`" can be appended to the file `/data/wst/u/<USER>/WWFI/bad.tab`, to prevent the script `prepare_V2.sh` from collecting them in future reductions.

An efficient tool to inspect the images quickly and to mask satellite trails manually is the program `fitsedit` by Johannes Koppenhöfer. Firstly, the user quickly scans through all binned images in the folder

```
cd /data/wst/u/<USER>/WWFI/reduced/<PROJECT>/<REDUXVERS>/
   biascorr_binned_after_cpcorr/
fitsedit -z 2 *
```

or, if charge persistence masking was deactivated, in the folder

```
cd /data/wst/u/<USER>/WWFI/reduced/<PROJECT>/<REDUXVERS>/
   biascorr_binned/
fitsedit -z 2 *
```

A right mouse click forwards to the next image. When identifying a satellite trail, the user writes down the date, file count number (last three digits in the filename) and optionally the quadrant (CCD) number of the image. The quadrant numbers are 1: bottom left, 2: top left, 3: top right and 4: bottom right. After that, the script `mask_satellites_manually.sh` has to be executed from the `stacks/` folder.

```
cd /data/wst/u/<USER>/WWFI/reduced/<PROJECT>/<REDUXVERS>/stacks/
mask_satellites_manually.sh <FILELIST>
```

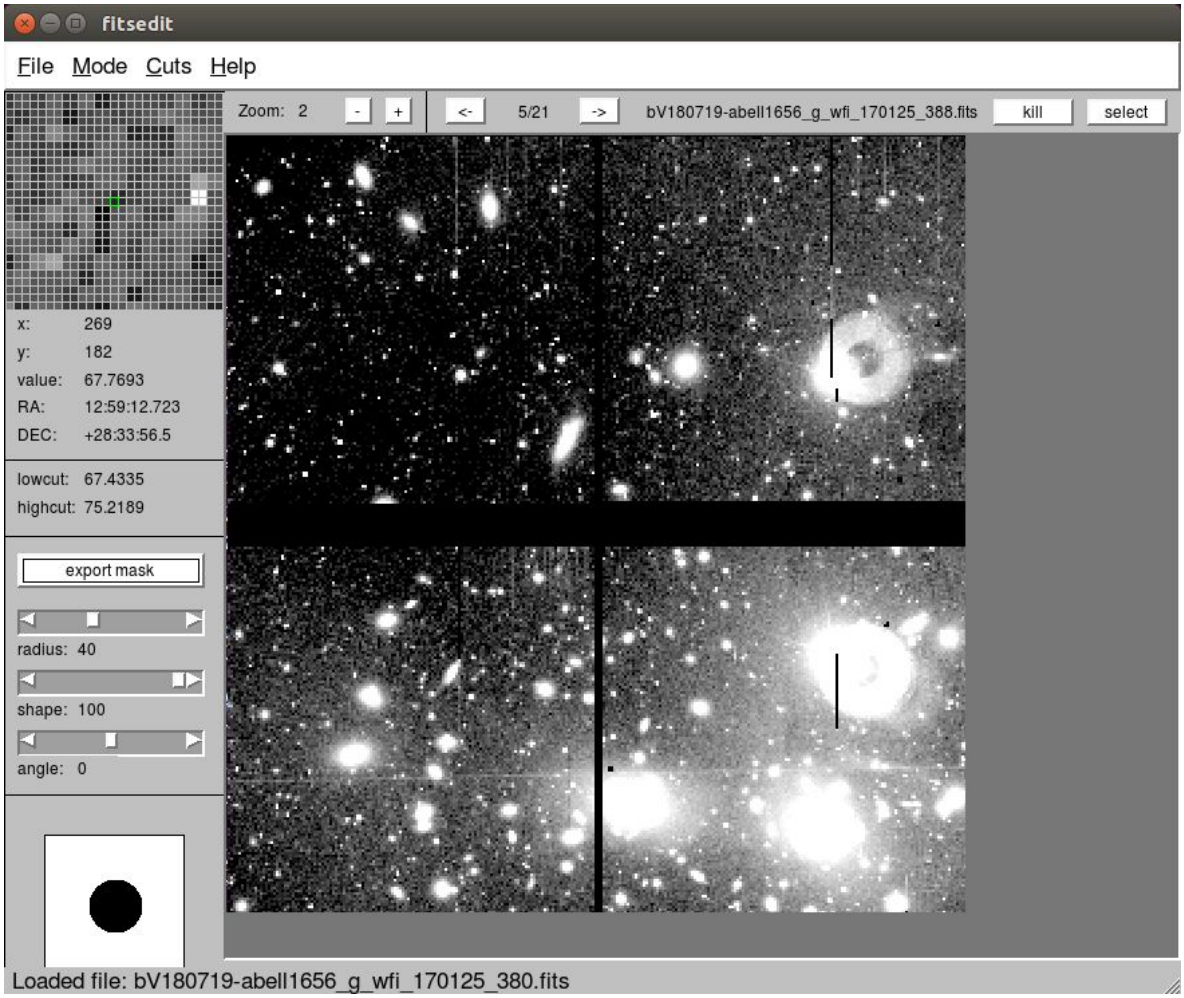

Figure 14.1: Identification of a satellite trail. One horizontal trail is visible in the bottom two quadrants (CCDs). The CCD IDs are 1: bottom left, 2: top left, 3: top right and 4: bottom right. The files are located in the directory `/data/wst/u/<USER>/WWFI/reduced/<PROJECT>/<REDUXVERS>/biascorr_binned/` or `/data/wst/u/<USER>/WWFI/reduced/<PROJECT>/<REDUXVERS>/biascorr_binned_after_cpcorr/`.

where `<FILELIST>` has the syntax `q[1234]*<DATE>_<FILECOUNT>` or `<DATE>_<FILECOUNT>`, e.g.:

```
mask_satellites_manually.sh q[14]*170125_388 q2*170125_389 170125_390
```

Another instance of `fitsedit` opens up and the user can mask the satellite trails by clicking once at the beginning of the trail and a second time at the end of the trail. The line width can be adjusted using the scaling bar on the left. It is useful to experiment with the options `halfline` and `line`. Mistakes can be undone once by pressing key 2 on the keyboard. Having masked one image, the mask-file must be exported by clicking on the `export mask` button and pressing `OK` without changing the suggested filename. When all masks are saved, the user closes the `fitsedit` window and all masks will be multiplied to the images. This procedure can be repeated multiple times. It is best advised to perform satellite masking before the removal of bright stars (see Sec. 17).

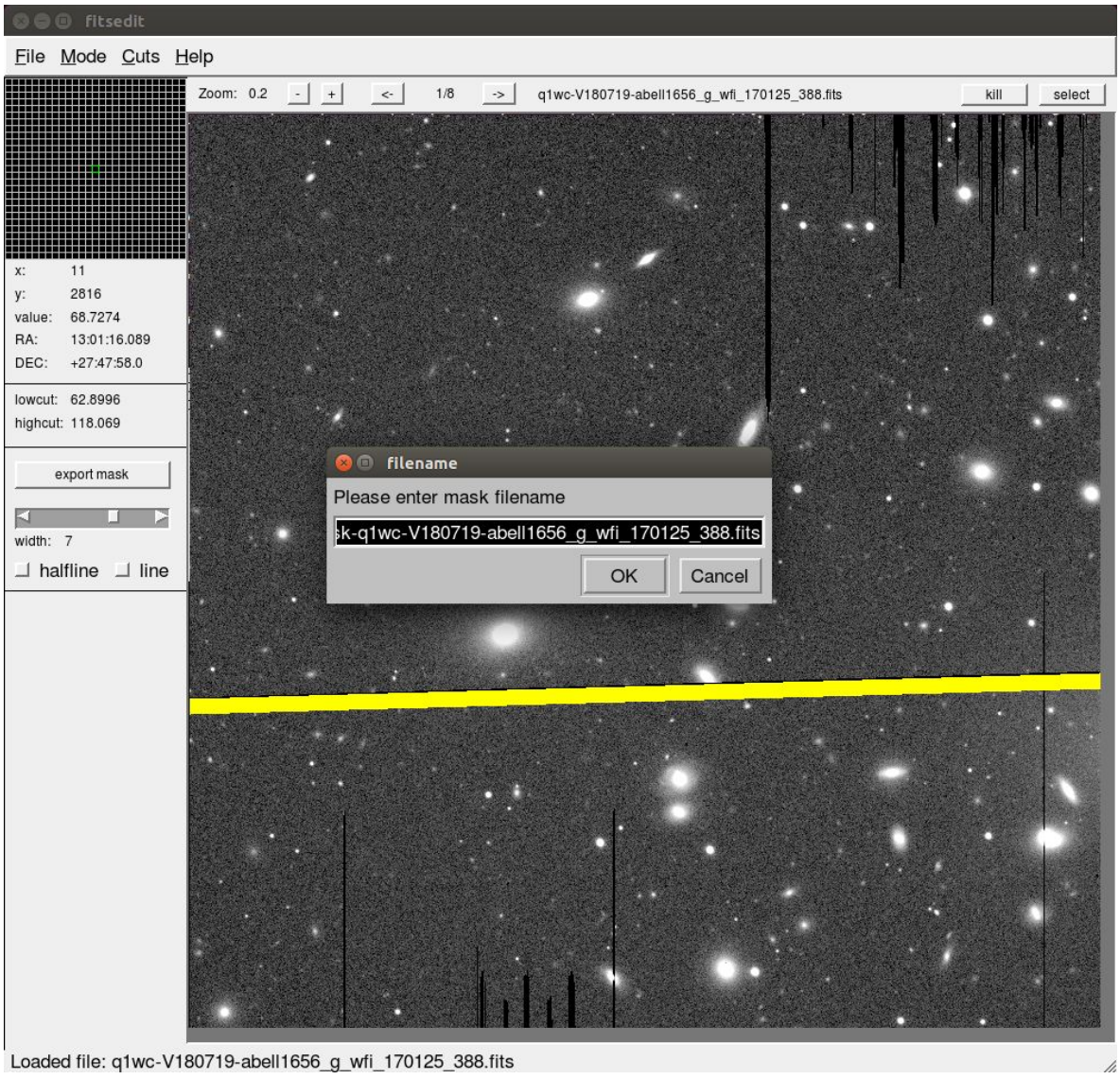

Figure 14.2: Masking of a satellite trail. By clicking once on the beginning of the trail and once at the end of the trail, a straight line (yellow) will be drawn on the image. The mask-file is saved by clicking on the `export mask` button and saving it with `OK`. The suggested filename must not be changed. The files are located in the directory `/data/wst/u/<USER>/WWFI/reduced/<PROJECT>/<REDUXVERS>/stacks/`.

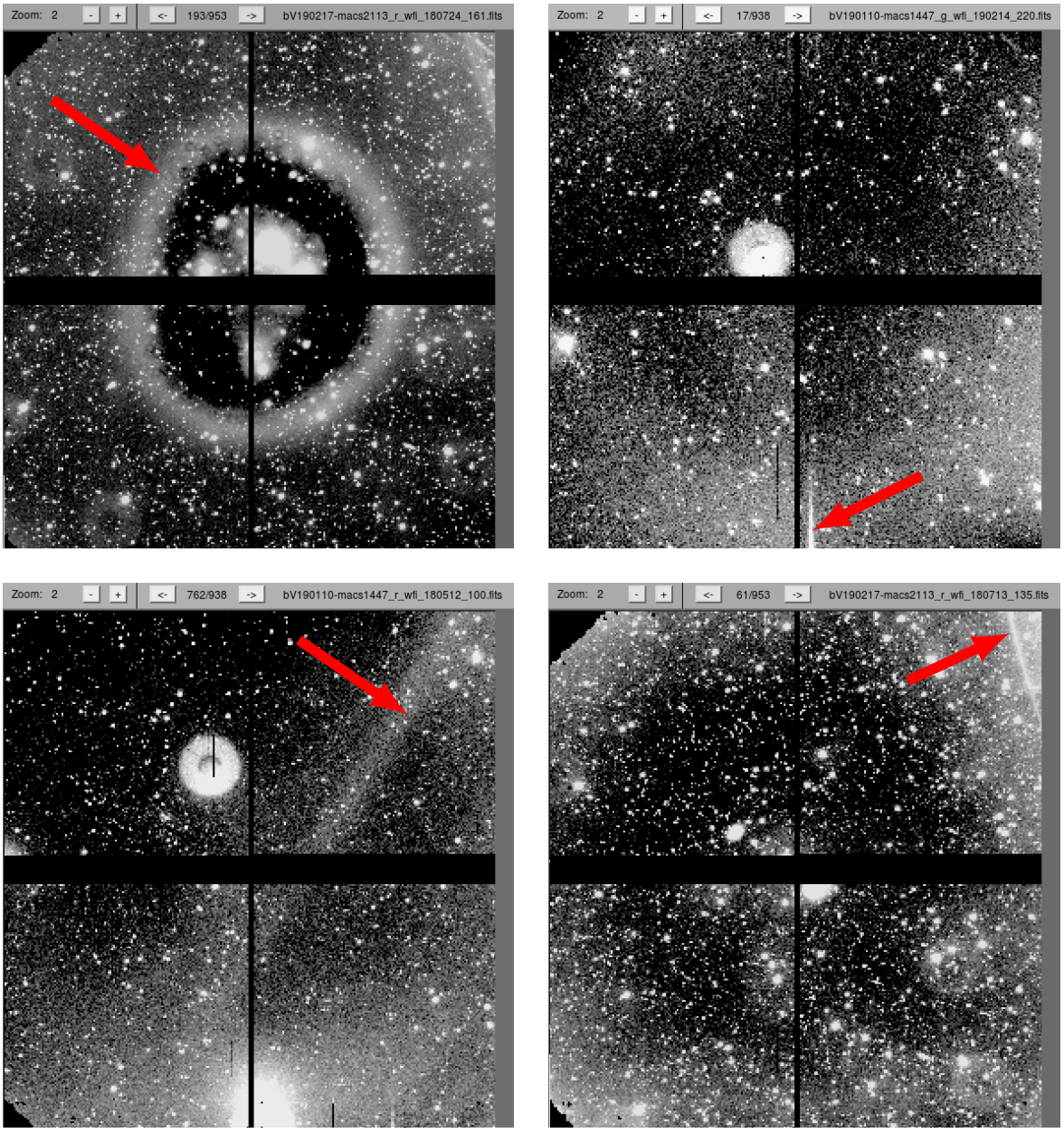

Figure 14.3: Examples of contamination are marked by red arrows. *Top left:* condensation on the CCDs, *top right:* stray-light at the bottom middle from a star just below the field of view, *bottom left:* diagonal stray-light from the top right to the bottom left and *bottom right:* stray-light at the top right corner.

Chapter 15

Resampling and stacking

15.1 Science images

The program `SWarp` (Bertin, 2010) is used to resample (i.e., regrid) and coadd the individual images using the astrometric solution calculated by `SCAMP`. These solutions are stored in the `stacks/*.scamp.head` files. They contain header keywords, that overwrite those in the `stacks/*.fits` files. Resampling and stacking is activated py parsing the argument `-fs=<FILTERS>` to the pipeline. If only resampling is required, stacking can be deactivated with the argument `-q=false`.

To ensure flux conservation when the pixel scale p is (slightly) changed, the header keyword `FLASCALE` $= (0.2''/\mathrm{px}/p)^2$ is multiplied to the images during the resampling process. While coadding, the header keyword `FLXSCALE` is multiplied to the images, thus scaling g'-, r'-, i'-, and z'-band images to the photometric zero-point, which is given by the pipeline argument `-zp=...`. The thereby applied photometric solutions were calculated either by comparison to Pan-STARRS catalogs (see Sec. 12.3) or by relative flux matching using `SCAMP` (see Sec. 13). The latter case is the only available option for the u'- and L-band images, which are scaled with `FLXSCALE` to a common zero-point. That unknown zero-point varies, depending on weather conditions and mirror reflectivity (cf. Fig. 20.1, top panel).

The resulting stacks will be centered at the R.A. and Dec. coordinates, as parsed to the pipeline via `-ra=...` and `-dec=...`. Both, sexagesimal (hh:mm:ss.ss for R.A. and dd:mm:ss.ss for Dec.) and degree (ddd.dddd) formats are accepted. The side length of the stack is given via the argument `-ss=...` in pixels. The coaddition method can either be weighted average (default) or median if the argument `-m` is parsed to the pipeline. In the former case, a weighting formula can be provided via `-w=...`. The weighted coaddition is then described by the following equation.

$$S(x,y) = \frac{\sum_i w_i^s(x,y) \cdot s_i(x,y) \cdot F_i}{\sum_i w_i^s(x,y)}, \tag{15.1}$$

where S is the coadded science stack, s_i are the single science images, w_i^s are their corresponding weight images, in which each pixel (x,y) is either the calculated weight number or zero if it is masked, and F_i is the `FLXSCALE` header keyword of the ith file.

Optimal signal to noise for extended sources is achieved with the default option `-w=1/BGRMS^2`. To optimize the S/N for point sources, the weighting formula must be changed

to `-w=1/(BGRMS^2*SEEING^2)`. Because the images are *not* normalized to one second exposure time, the background noise value `BGRMS` is automatically rescaled by multiplied it with the `FLXSCALE` value.

Another output of `SWarp` is a stacked weight map (see Fig. 3.1, left panel). It has the prefix `w.` and is equal to the sum of weights at each pixel position (see denominator in Eq. 15.1). This file is later used to estimate the spatially varying background noise during the creation of source masks (see Sec. 19).

If the coadding method is "weighted" (instead of median (`-m`) or clipping (`-k=...`); see Tab. 20.1), the process is accelerated significantly by splitting the stacking task into blocks, each coadding 52 quadrant images. Parallelization of the block stacking is responsible for the speedup. The resulting stacks are then coadded, while also considering the corresponding weight stacks, to create the final science stack. The result is mathematically equivalent to the much slower single-task stacking result.

15.2 Error images

Error images contain the flux uncertainties due to photon noise and calibration uncertainties that are propagated along the basic data reduction steps. These files have the prefix `e.`. No option to resample and stack error images is implemented in `SWarp` so far. As a workaround, the additional pipeline argument `-er` activates the resampling of error images e_i alongside with the science images. The option `-es` activates the quadratic resampling *and* stacking of the error images, i.e., they are multiplied with the weights, squared, resampled, and coadded. The resulting stack needs to be renormalized because `SWarp` automatically normalizes the stack by the sum of the squared weights. The automatic normalization is undone by multiplying the stack with the coadded error weight file, then taking the square root, and finally, dividing it by the coadded science weight file.

$$E(x,y) = \frac{\sqrt{\sum_i (w_i(x,y) \cdot w_i^s(x,y) \cdot e_i(x,y) \cdot F_i)^2}}{\sum_i w_i(x,y)} \tag{15.2}$$

$$= \sqrt{\frac{\sum_i (w_i(x,y) \cdot w_i^s(x,y) \cdot e_i(x,y) \cdot F_i)^2}{\sum_i w_i(x,y)^2}} \cdot \frac{\sqrt{\sum_i w_i(x,y)^2}}{\sum_i w_i^s(x,y)}, \tag{15.3}$$

where E is the coadded error stack, e_i are the single error images, w_i are their corresponding weight images, and F_i is the `FLXSCALE` header keyword of the ith file. The weights of the science images w_i^s (see Eq. 15.1) are also multiplied to scale the errors.

The term under the first square root in Eq. 15.3 is the error-stack output of `SWarp`, $\sqrt{\sum_i w_i^2}$ is the corresponding weight file, and $\sum_i w_i^s$ is the weight file of the science stack.

Chapter 16

Photometric zero-point recalibration

16.1 General remarks

The zero-points for the g'-, r'-, i'-, and z'-bands are calibrated to the Pan-STARRS DVO PV3 catalog (Flewelling et al., 2016). The zero-points for the u'- and L-bands are highly variable for different stacks since they are determined using the relative photometric solutions provided by `SCAMP`. In this section, implications of light leaking out of apertures are discussed mainly for the g'-band. The derived corrections can be applied analogously to the r'-, i'-, and z'-bands after the extended PSF SB profiles are measured for these bands, too.

As mentioned in Sec. 12.3, the extended PSF wings are relevant for the zero-point calibration. In principle, the whole integrated fluxes of selected stars in WWFI images must be matched to the whole integrated (calibrated) literature fluxes of the same stars. By neglecting the PSF wings, errors on the order of $\sim 10\%$ can be made since the WWFI PSF curve of growth in Fig. 16.2 shows that $\sim 10\%$ of the PSF's light is distributed beyond commonly used apertures.

This is less of an important issue for point source photometry, as long as fluxes are always measured in the same aperture sizes within which they were measured for the zero-point calibration.

However, the implications of neglected PSF wings are important for surface photometry of extended sources. If less than the full integrated fluxes of WWFI point sources is matched to the full integrated fluxes of the reference point sources, the image will be scaled too brightly. The opposite is the case when the reference stars' fluxes are measured in too small apertures.

The Pan-STARRS PSF magnitudes (to which the WWFI PSF magnitudes are calibrated) are calibrated to Calspec spectrophotometric standards from HST (Bohlin et al. 2001; Tonry et al. 2012). It is therefore not important how the Pan-STARRS PSF magnitudes were measured exactly if the PSF wings are always treated consistently.[1] The WWFI fluxes are therefore indirectly calibrated to HST Calspec fluxes. We assume the latter to include the PSF wings. It is therefore important to include the WWFI PSF wings into the flux measurements, too.

In order re-calibrate the zero-points correctly, it is inefficient and difficult to measure the

[1] The Pan-STARRS fluxes were measured using PSF models. The background was subtracted beforehand using a spline interpolation with a step size of 400 pixels ($= 100''$) (Magnier et al., 2016). Any PSF wings that extend beyond $50''$ radius are therefore removed before the flux is measured.

full PSF SB profile in every stacked observation. A simpler approach is to measure aperture fluxes in sufficiently large apertures ($\varnothing$ = 50 pixels = 10″), in which the enclosed flux is independent of the variable seeing. The outer PSF wings are assumed to be constant, since they are shaped by the static telescope optics. The re-calibration of the zero-point is then done by adding a number of constants to the magnitudes in order to correct for the missing flux leaking out of the finite apertures.

16.2 Increase of aperture size ⌀=25px → ⌀=50px

The calculated zero-points depend on the size of the chosen circular aperture. It must be sufficiently large so that the seeing-dependent inner part of the PSF is fully covered whereas blending influence is still minimal. Fig. 3.3, bottom panel, shows that the seeing-dependent Moffat term dominates the PSF surface brightness profile inside a circular radius of $r \gtrsim 3.84''$. That is equal to an aperture diameter of 38.4 pixels. A diameter of 50 pixels is therefore expected to be sufficiently stable towards seeing variability. However, blending is much more severe than in 25 pixels diameter apertures, as can be seen in Fig. 16.1: the calculated zero-points for faint stars are systematically too high because of a higher relative contribution from other sources leaking light into these apertures. This effect is stronger for larger apertures. It is negligible for the brightest sources for both aperture sizes because the calculated zero-points converge. The optimal brightness cut depends on the crowding in the field of view. Hence, it must be chosen by hand by optimizing the parameters `min` and `max` in the following command.

```
qsub $SCRIPTS/zeropoint.sh ‘pwd‘ A1656_V180719_5.fits
                           onlyzp 50 1 Y MANUAL
gnuplot -e "file=’A1656_V180719_g_5_50_good.tab’;min=14;max=16.5"
        $SCRIPTS/fitzp.gpl
```

The resulting zero-point is printed to the terminal. It is not consistent with the newly created header keyword `ZP50` value since that is determined from an unstable, automatic fit.

For the example of the g'-band stack of A1656, we get ZP25 = 29.9965 g' mag and ZP50 = 30.0449 g' mag (see Fig. 16.1). A consistency check using the g'-band PSF curve of growth in Fig. 16.2 shows that the quotient of the encircled intensities

$$I(r < 2.5'')/I(r < 5'') = 0.8925/0.9250 = 0.9649 \tag{16.1}$$

which corresponds to a zero-point shift of

$$(\mathrm{ZP50} - \mathrm{ZP25})_{\mathrm{COG}} = -2.5 \log(0.9649) = 0.0388\ g'\ \mathrm{mag}. \tag{16.2}$$

That result is close to the experimentally determined shift for the example of A1656

$$(\mathrm{ZP50} - \mathrm{ZP25})_{\mathrm{A1656}} = 0.0484 \pm 0.0055\ g'\ \mathrm{mag}. \tag{16.3}$$

The curve of growth in Fig. 16.2 shows that an aperture diameter of 10″ = 50 px is still too small to include the full fluxes. Therefore, the zero-points need further corrections for leaking light using the following steps.

16.3 Correction for aperture size ⌀=50px → ⌀=∞ using the curve of growth

The curve of growth of the circularly symmetric component of the g'-band PSF is shown in Fig. 16.2. The outermost radial point is at $r = 908''$ where the curve of growth has still not converged, yet. Even worse, the extrapolated curve of growth diverges. Since that cannot be true, the profile must be truncated at some larger radius beyond outermost measured data point. The best we can do is to assume that the full PSF's flux is encircled inside $r < 908''$. For this approximation, 7.5% of the PSF's light is distributed outside of a $10'' = 50$ pixels diameter aperture. Hence, the correction for the zero-point is

$$\Delta ZP_{\mathrm{COG:}10''\rightarrow 908''} = 2.5\log(1+0.075) \approx 0.0785\ g'\ \mathrm{mag}. \tag{16.4}$$

16.4 Ghosts

Out of focus reflections (i.e., Ghosts) were neglected so far. They further contribute to 1.78% of the sources' total light (see Sec. 3.1, §4). The correction for the zero-point is

$$\Delta ZP_{\mathrm{Ghosts}} = 2.5\log(1+0.0178) \approx 0.0192\ g'\ \mathrm{mag}. \tag{16.5}$$

16.5 Pan-STARRS offset

The currently used Pan-STARRS catalog is preliminary. The PSF magnitudes in a random sample of 10 Abell cluster pointings were examined for potential offsets between the preliminary Pan-STARRS catalog and the official Pan-STARRS data release 2 catalog. A systematic offset is measured, which has to be added to the so-far determined zero-points

$$\Delta ZP_{\mathrm{Pan-STARRS}} = 0.0178 \pm 0.0018\mathrm{mag}. \tag{16.6}$$

16.6 Summary and comparison to SDSS

In total, all correction terms that need to be applied to the zero-point, determined in a 50 pixels diameter aperture are

$$\begin{aligned} ZP &= ZP50 + \Delta ZP_{\mathrm{COG:}10''\rightarrow 908''} + \Delta ZP_{\mathrm{Ghosts}} + \Delta ZP_{\mathrm{Pan-STARRS}} && (16.7)\\ &= ZP50 + 0.0785\mathrm{mag} + 0.0192\mathrm{mag} + 0.0178\mathrm{mag} && (16.8)\\ &= 0.1155\mathrm{mag} && (16.9) \end{aligned}$$

A cross-check for a random sample of 10 BCG SB profiles measured on fully calibrated WWFI g'-band data and SDSS g-band data shows

$$\Delta ZP_{\mathrm{WWFI}\rightarrow\mathrm{SDSS}} = 0.023 \pm 0.019\mathrm{mag} \tag{16.10}$$

This is *inconsistent* with the correction for point sources: $g' - g = -0.012 - 0.139(g-r) = -0.12$ for $(g-r) = 0.78$ (Tojeiro et al., 2013).

SDSS magnitudes are calibrated using an aperture correction out to only $r = 7.4''$. Since we do not have the extended SDSS PSF SB profile at hand, we can make an order of magnitude approximation for the correction using our WWFI PSF SB profile. Outside of a circular aperture with that same radius of $r = 7.4''$ leaks 6.8% of the PSF's light. That corresponds to a brightness difference of 0.077 mag, which must be added to the SDSS SB profiles. Consequently, an error of only 0.02 mag arcsec^{-2} remains.

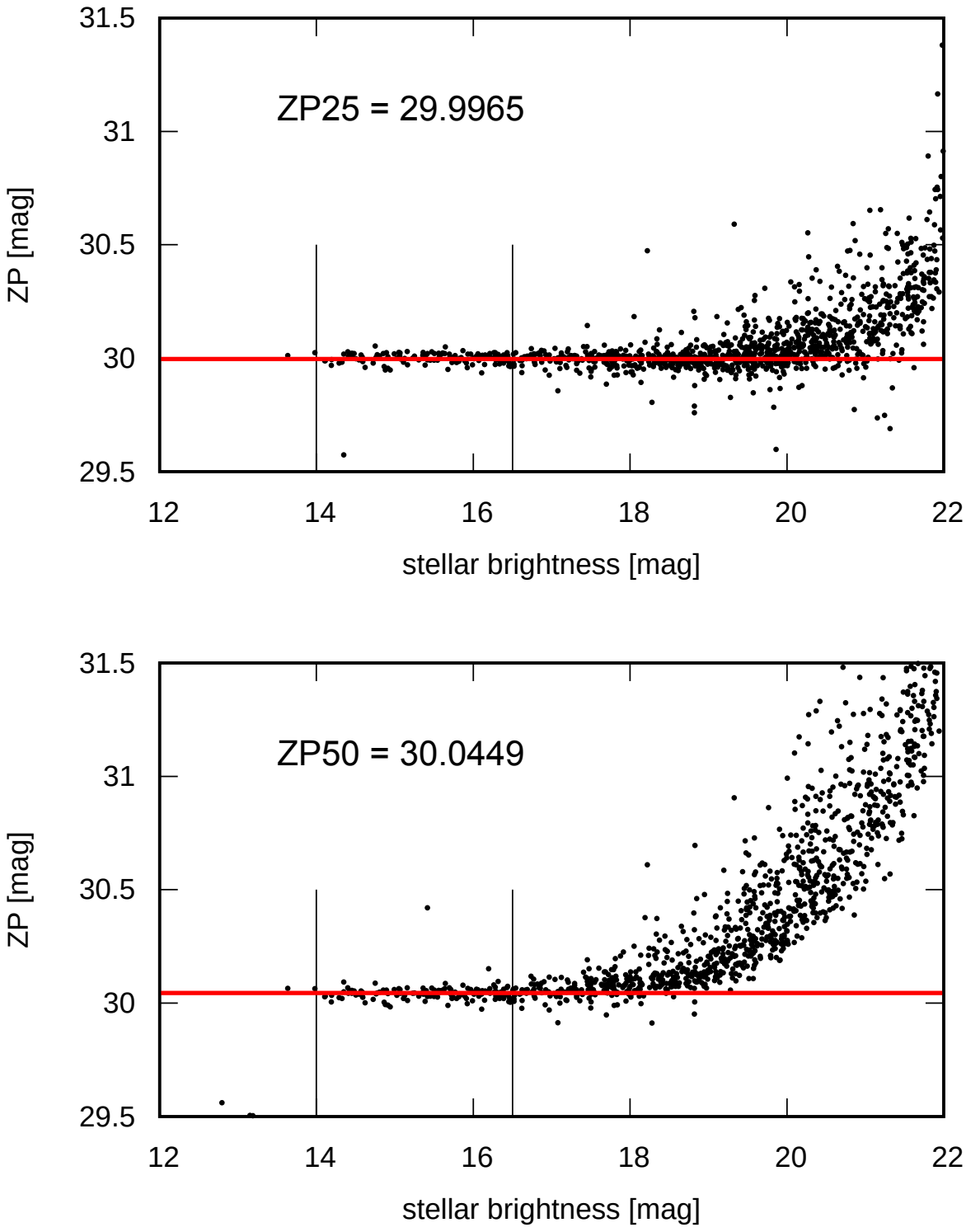

Figure 16.1: Examples for the determination of the zero-points in a stack. The aperture diameter is $5'' = 25px$ in the top panel and $10'' = 50px$ in the bottom panel. Black dots show the calculated zero-points for individual stars. The upward curvature for faint sources is due to blending. The red line indicates the best-fit value, which is also given in the label. The two vertical lines show the region in which the fit is performed.

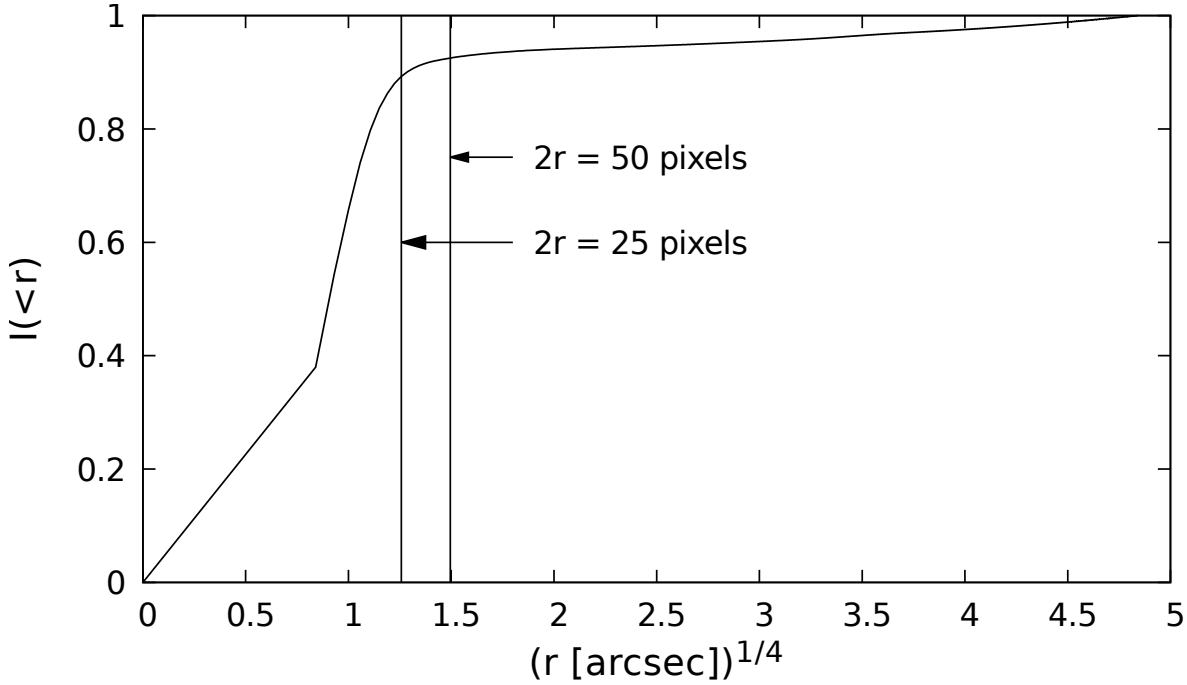

Figure 16.2: The curve of growth of a g'-band PSF. The integrated luminosity fraction at $I(r < 12.5px)/I_{\rm tot} = 0.8925$ and at $I(r < 25px)/I_{\rm tot} = 0.9250$).

Chapter 17

Removal of bright stars

The PSF wings of bright stars add a background pattern that is fixed in celestial coordinates. It can be subtracted from the single images before any of the background subtraction methods, described in Sec. 18, is applied. The procedure is split into three steps: 1) modeling/subtraction of ghosts using `rmhalos.sh`, 2) modeling of the circularly symmetric PSFs using `modelpsfs.sh` and 3) subtraction of those modeled PSFs using `substars.sh`.

Since bright stars often saturate in WWFI exposures, literature catalogs can be used to obtain the coordinates and brightnesses of the stars in consideration. A table file containing these information can easily be created using the program DS9 (`http://ds9.si.edu`):

```
cd /data/wst/u/mkluge/WWFI/reduced/A1656/final/
ds9 A1656_V191209_g_1.fits
# Analysis --> Catalogs --> Optical --> Tycho-2
# Copy the table to the clipboard by clicking on the dark gray table
  head row with the labels "_RAJ2000 _DEJ2000 recno ..."
# Paste the clipboard into a file called, e.g., stars_tycho.txt in the
  final/ folder
```

Since the TYCHO-2 catalog only contains B_T and V_T magnitudes, color transformations need to be applied in order to transform these magnitudes into Johnson B_J and V_J (ESA, 1997) and then into g and r magnitudes (Jester et al., 2005).

$$V_J = V_T - 0.09(B-V)_T, \tag{17.1}$$

$$(B-V)_J = 0.85(B-V)_T \tag{17.2}$$

$$g = V_J + 0.60(B-V)_J - 0.12 \tag{17.3}$$

$$r = V_J - 0.42(B-V)_J + 0.11. \tag{17.4}$$

Color transformations are not available for the u'-, i'-, z'-, and L-bands. Bright star modeling is therefore only implemented in the pipeline for the g'- and r'-bands.

Alternatively, or in combination with the TYCHO-2 catalog, the SDSS catalog can also be used to create such a table file for intermediately bright sources by choosing the catalog "SDSS Release 12" instead of "Tycho-2". Since there is some overlap between the two catalogs, it is possible to parse both tables to the scripts `rmhalos.sh` and `modelpsfs.sh`, which then

discard duplicates from the TYCHO-2 table if the separation to any star in the SDSS table is lower than $4''$. Contrary to TYCHO-2, SDSS covers only a part of the sky. In the lucky case that the field of view is covered by SDSS, it advised to filter the SDSS results in DS9 for only the brightest sources before copying the table. That can be done by typing e.g., $gmag<12 into the "Filter" field and pressing "Retrieve" to select only stars whose g-band brightness is brighter than 12 mag. The workflow is demonstrated by the following code:

```
cd /data/wst/u/mkluge/WWFI/reduced/A1656/final/

# create bright star tables stars_tycho.txt and/or stars_sdss.txt
modelpsfs.sh  auto  A1656_V191209_g_1.fits stars_tycho.txt  tycho
modelpsfs.sh  auto  A1656_V191209_g_1.fits stars_sdss.txt   sdss

# or
modelpsfs.sh  auto  A1656_V191209_g_1.fits
              stars_tycho.txt,stars_sdss.txt  tychosdss

cd /data/wst/u/mkluge/WWFI/reduced/A1656/V191209/stacks/

# subtract reflections
rmhalos.sh  auto  ../../final/stars_tycho.txt  1.0  tycho
rmhalos.sh  auto  ../../final/stars_sdss.txt   1.0  sdss
# or
rmhalos.sh  auto
            ../../final/stars_tycho.txt,../../final/stars_sdss.txt
            tychosdss

# subtract symmetric PSF
substars.sh  auto  ../../final/psf_A1656_V191209_g_1.fits  1.0
```

The resampled files `stacks/swarp_<FILTER>/q*.resamp.fits` must already exist beforehand, e.g., from a previous `autoreduce_V2.sh ... -fs=<FILTERS>` execution. The reason is that the `FLASCALE` header keyword from those files is used by `rmhalos.sh` and `substars.sh` to undo the flux scaling.

The scaling is not always optimal due to intrinsic stellar variability and systematic zero-point errors at this intermediate stage of the data reduction. Some iteration might be necessary to minimize the residuals. Latter are best checked in a newly created stack. Night-sky flat and/or background subtraction routines need to be run again (see Sec. 18). If the residuals are too strong, the backup files without removed stars can be restored.

```
cd /data/wst/u/mkluge/WWFI/reduced/A1656/V191209/stacks/
mv before_substars/* .
mv before_rmhalos/* .
```

The order is important. The scripts `rmhalos.sh` and `substars.sh` can then be executed again with a scaling factor chosen best somewhere between $0.85 \sim 1.15$ that substitutes the parameter 1.0 in the above examples.

Chapter 18

Background subtraction

Three different tools are available for background subtraction: `SWarp`, `skycorr`, which was developed during this PhD thesis project and `skyalign`, which was developed by Bianca Neureiter during her Bachelor's thesis project. Different methods qualify as optimal depending on the science case, observing strategy and observing conditions. The science case puts requirements on background flatness on certain spatial scales, e.g., for deep photometry, or it puts constraints on background similarity between exposures, e.g., for difference imaging. The observing strategy puts constraints on the achievable background flatness. For instance, the night-sky flat accuracy drops when the objects become too large compared to the dithersize. The observing conditions put constraints on the achievable background flatness or background similarity between images, e.g., passing clouds, moonlight or twilight.

In this chapter, all available methods are described in detail. Code examples for archival Coma cluster (A1656) data are provided to illustrate the how the methods are applied in practice. Moreover, a visual quality check tool for all single background-corrected images is described in Sec. 18.12.

The stacks that are created with the provided code examples are shown in Fig. 18.1 and 18.2. They illustrate the limits of each method and to give the reader an impression of the achievable background flatness quality. When the observations were taken during photometric and dark conditions, residual background inhomogeneities remain typically on a level of $\Delta SB \approx 30$ g' mag arcsec^{-2} (see Fig. 5.1 and Sec. 18.11). These residuals decrease when more exposures are combined.

18.1 Requirements

All following scenarios require that the basic data reduction is complete and a first stack is created. Moreover, it is advised that satellites are masked and bright stars are subtracted. The following code shows the necessary steps to reach this stage.

```
# basic reduction
autoreduce_V2.sh -P=A1656 -p=abell1656 -rv=V191209
                 -ra=12:59:36 -dec=27:57:34 -fr=g -b -f -cp=0.2 -sc
```

```
# mask satellites
cd /data/wst/u/mkluge/WWFI/reduced/A1656/V191209/stacks/
mask_satellites_manually.sh q[134]*170125_388

# create a stack
autoreduce_V2.sh -P=A1656 -p=abell1656 -rv=V191209
                 -ra=12:59:36 -dec=27:57:34 -fs=g -ur=redo_all -t=0.7

# model and subtract bright stars
cd /data/wst/u/mkluge/WWFI/reduced/A1656/final/
# create a bright star table stars.txt using DS9
modelpsfs.sh auto A1656_V191209_g_1.fits stars.txt
cd /data/wst/u/mkluge/WWFI/reduced/A1656/V191209/stacks/
rmhalos.sh  auto    ../../final/stars_obj.txt
substars.sh auto    ../../final/psf_A1656_V191209_g_1.fits
```

Or for the case that sky pointings were observed:

```
# basic reduction
autoreduce_V2.sh -P=A1656 -p="abell1656 abell1656_sky" -rv=V191209
                 -ra=12:59:36 -dec=27:57:34 -fr=g -b -f -cp=0.2 -sc

cd /data/wst/u/mkluge/WWFI/reduced/A1656/V191209/stacks/
mask_satellites_manually.sh q[134]*170125_388

# create a sky stack
autoreduce_V2.sh -P=A1656 -p=abell1656_sky -rv=V191209 -bs=400
                 -ra=12:56:39 -dec=28:08:37 -fs=g -ur=redo_all -t=0.7

# create a target stack
autoreduce_V2.sh -P=A1656 -p=abell1656 -rv=V191209
                 -ra=12:59:36 -dec=27:57:34 -fs=g -ur=redo_all -t=0.7

# model and subtract bright stars
cd /data/wst/u/mkluge/WWFI/reduced/A1656/final/
# create bright star tables stars_sky.txt stars_obj.txt
modelpsfs.sh auto A1656_V191209_g_1.fits stars_sky.txt
modelpsfs.sh auto A1656_V191209_g_2.fits stars_obj.txt
cd /data/wst/u/mkluge/WWFI/reduced/A1656/V191209/stacks/
rmhalos.sh  autosky ../../final/stars_sky.txt
rmhalos.sh  auto    ../../final/stars_obj.txt
substars.sh autosky ../../final/psf_A1656_V191209_g_1.fits
substars.sh auto    ../../final/psf_A1656_V191209_g_2.fits
```

18.2 No background subtraction

This option is recommended when the target extends over the whole field of view and is brighter than the sky. The pipeline argument `-bs=false` disables the background subtraction option of `SWarp`. All resampled files from a possible previous run are overwritten when the argument `-ur=redo_all` is parsed.

```
autoreduce_V2.sh -P=A1656 -p=abell1656 -rv=V191209 -ra=12:59:36
                 -dec=27:57:34 -fs=g -bs=false -ss=17500 -t=0.7
                 -ur=redo_all
```

The resulting stack made of 10 single exposures of A1656 is shown in Fig. 18.1, top left panel. Sharp edges around the single images are clearly visible. The sky brightness varies by $\sim 2\%$ between the 60 second exposures, even during the photometric and dark conditions. That motivates the various sky subtraction methods, which are described in the following subsections.

18.3 Unmasked spline interpolation or constant per CCD using `SWarp`

The spline interpolation method implemented in `SWarp`[1] is the fastest and simplest approach available. It does not require source-masking and therefore produces quick results without iterating. This option is suitable when quick results shall be obtained and/or when the target is small, e.g., a point source. The interpolation step size `BACK_SIZE` can be set to a value greater or equal to the CCD size (`-bs=4109`) to subtract a constant from each CCD image, i.e., from each quadrant in one WWFI exposure.

```
autoreduce_V2.sh -P=A1656 -p=abell1656 -rv=V191209 -ra=12:59:36
                 -dec=27:57:34 -fs=g -bs=4109 -ss=17500 -t=0.7
                 -ur=redo_all
```

The resulting stack can be seen in Fig. 18.1, top right panel. Faint and extended objects that cover a significant fraction of the CCD area are oversubtracted because the routine cannot distinguish between background inhomogeneities and faint galaxy outskirts or PSF wings. Nevertheless, the resulting stack is useful to create a first source mask, which can then be parsed to the more advanced methods implemented in `skycorr.sh`.

18.4 Polynomials with `skycorr`

This option is recommended when the sky varies strongly, e.g. due to clouds or twilight. It is also useful to generate a second, flat stack, which will act as a basis for a second, more complete source mask.

The script `skycorr.sh` allows to fit 2D polynomials to the unmasked pixels of either the full single exposures consisting of all four CCD images or the single CCD images separately.

[1] Details can be found in the on-line manual at
`https://www.astromatic.net/pubsvn/software/swarp/trunk/doc/swarp.pdf`

The fitting tool is named `getsky` and was written by Arno Riffeser and Johannes Koppenhöfer. The polynomials are evaluated on the pixel grid and subtracted from the images.

A source mask is required to get a clean estimate of the background pattern. It can be generated from the first stack (see Sec. 19) that was created in a previous step described in Sec. 18.3.

```
cd /data/wst/u/mkluge/WWFI/reduced/A1656/final/
create_mask.sh A1656_V191209_g_1.fits mask1_g.fits
               # recommended masking parameters: 26smag 1 0 11 n
```

The fit to the single CCD images is more stable when a polynomial is fitted and subtracted from the full image beforehand. That option is activated with the first comma separated parameter in the -o=2,n,n,n,n,2 argument for `skycorr.sh`. The number "2" is the order of the 2D polynomial. Firstly, the four CCD images are combined to one image on the final stack grid. The mask is then multiplied to that image and the remaining unmasked pixels are fitted by a 2D polynomial of second order. That polynomial is evaluated on the pixel grid of the stack, resulting in a background model for one full image. The background model image is then cropped to the grid of each single resampled image and subtracted from them.

After that follows the fitting of a 2D polynomial to each masked CCD image separately. That option is activated with the last parameter in the -o=2,n,n,n,n,2 argument for `skycorr.sh`. The mask is cropped to the grid of each single resampled image, multiplied to them and the remaining unmasked pixels are fitted again, by a polynomial of second order. This time, the fit is performed for each masked image individually. The resulting background model is then subtracted and the unmasked resampled files and the results are stored in the directory `stacks/swarp_<FILTER>`.

```
# create a mask
cd /data/wst/u/mkluge/WWFI/reduced/A1656/final/
create_mask.sh A1656_V191209_g_1.fits mask1_g.fits
               # recommended masking parameters: 26smag 1 0 11 n

# fit polynomials to the unmasked pixels and subtract them
skycorr.sh -f=g -rv=V191209 -o=2,n,n,n,n,2 -mf=mask1_g.fits
           -ss=17500 -del

# stack the results
autoreduce_V2.sh -P=A1656 -p=abell1656 -rv=V191209 -ra=12:59:36
                 -dec=27:57:34 -fs=g -ss=17500 -t=0.7 -ur=only_ex
```

The resulting stack can be seen in Fig. 18.1, bottom left panel. The background appears fairly flat but faint outskirts of large objects are oversubtracted due to masking incompletenesses (see Sec. 19). Moreover, the bright pattern in the top right corner illustrates the danger of leaving the polynomial fit unconstrained in largely masked corners.

18.5 Night-sky flats with skycorr

This method is suitable when the dither pattern is larger than the target. Hence, sufficient sky coverage is available to model the average background pattern. In the first step an intermediate stack is created using the polynomial approach described in the previous subsection. This intermediate stack is the basis for a second, more complete source mask. It is necessary to model the background more accurately. That second mask is multiplied to all un-resampled individual images, which are then normalized by one constant per WWFI exposure and averaged for each observation night. The result is one normalized night-sky flat per night. Each quadrant (CCD area) of the night-sky flat is then fitted with 2D polynomials of fourth order to smear out residual charge persistence stripes and extrapolate into possible regions without sky coverage. That night-sky flat is then flux and background level scaled to the unmasked pixels of the individual images and subtracted from them. Finally, these background-subtracted images are resampled and coadded to create the final stack. A simulation of this procedure is shown and explained in Sec. 18.11.

```
# create a first mask
cd /data/wst/u/mkluge/WWFI/reduced/A1656/final/
create_mask.sh A1656_V191209_g_1.fits mask1_g.fits
               # recommended masking parameters: 26smag 1 0 11 n

# fit polynomials to the unmasked pixels and subtract them
skycorr.sh -f=g -rv=V191209 -o=2,n,n,n,n,2 -mf=mask1_g.fits
                -ss=17500 -del

# stack the intermediate results
autoreduce_V2.sh -P=A1656 -p=abell1656 -rv=V191209 -ra=12:59:36
                 -dec=27:57:34 -fs=g -ss=17500 -t=0.7 -ur=only_ex

# create a second, more complete mask
create_mask.sh A1656_V191209_g_2.fits mask2_g.fits
               # recommended masking parameters: 27.5smag 1 0 11 n

# create night-sky flats
create_nightskyflat.sh -f=g -rv=V191209 -mf=mask2_g.fits -t=0.7

# scale the night-sky flats to the single images and subtract them
skycorr.sh -f=g -rv=V191209 -o=n,n,sd,n,n,n -mf=mask2_g.fits
           -ss=17500 -del

# stack the results
autoreduce_V2.sh -P=A1656 -p=abell1656 -rv=V191209 -ra=12:59:36
                 -dec=27:57:34 -fs=g -ss=17500 -t=0.7 -ur=only_ex
```

The result can be seen in Fig. 18.1, bottom right panel. The outskirts around the two central BCGs are much better preserved than by the previous method. However, this method still leads to oversubtraction for very extended objects whose sizes are comparable to the size of the dither pattern.

18.6 Night-sky flats from sky pointings

Sky pointings are observations taken in a relatively empty sky region $1 \sim 2°$ offset from the target. They are necessary when the target is larger than the dither pattern or comparable to the WWFI field of view. Ideally, sky pointings are observed in an alternating sequence: object – sky – object – sky etc. Those are referred to as bracketing sky pointings. A night-sky flat can be created for each night from the sky exposures. Ideally, bright stars and ghosts were also subtracted from them (see Sec. 18.1). This night-sky flat is then scaled to each of the two masked, bracketing sky exposures and the average of them is subtracted from the target exposure.

A mask is here necessary for the sky pointings instead of the target pointings. The sky stack that acts as the basis for this mask, can be created following the instructions in Sec. 18.1. After that stack was created, the procedure is the following:

```
cd /data/wst/u/mkluge/WWFI/reduced/A1656/final/

# create a mask for the sky stack
create_mask.sh A1656_V191209_g_1.fits mask1_g_sky.fits
               # recommended masking parameters: 0.15s 1 0 11 n

# create night-sky flats from the sky pointings
create_nightskyflat.sh -f=g -rv=V191209 -mf=mask1_g_sky.fits
                       -t=0.7 -p=abell1656_sky

# scale the night-sky flats to the bracketing sky exposures
# and subtract them from the target exposures
cd /data/wst/u/mkluge/WWFI/reduced/A1656/V191209/stacks/
fit_to_bracketing_sky.sh auto g

# resample and stack the corrected images
autoreduce_V2.sh -P=A1656 -p=abell1656 -rv=V191209 -ra=12:59:36
                 -dec=27:57:34 -fs=g -bs=false -ur=redo_all

# or alternatively: resample the corrected images,
# match the residual background constants for the full images
# and then stack them
autoreduce_V2.sh -P=A1656 -p=abell1656 -rv=V191209 -ra=12:59:36
                  -dec=27:57:34 -sa=g,10,0,0 -ss=17500 -t=0.7
```

The resulting stack can be seen in Fig. 18.2, top left panel. Residuals remain due to the varying sky background between object and sky exposures and due to the different sky gradients at the object and sky positions. The offsets can be reduced by using `skyalign` (last call in the script above) by matching the residual background levels of all single exposures. However, the gradient remains. The resulting stack is shown in Fig. 18.2, top right panel.

18.7 Night-sky flats from the residuals of a subtracted reference stack

This strategy is useful when the ditherpattern is smaller than the target and when sky pointings were not taken every night. Thereby, the required telescope time can be significantly reduced. However, the quality degrades when the target SB becomes brighter than the night-sky due to flat-fielding and zero-point uncertainties. For instance, it is not optimal for M31.

The method in the previous section can be used to create a well flattened reference stack. That stack is then subtracted from the observations taken at different dates and a night-sky flat is created from the residuals for each night. These normalized night-sky flats are then scaled to the residuals, again after subtracting the reference stack from the single images. Finally, the rescaled night-sky flats are subtracted from the single exposures. Uncertainties in zero-point and flatfielding require to mask the regions that are brighter than ~ 25 g' mag arcsec^{-2}.

In the following example, sky pointings were made on 2017-01-25. The nights without sky pointings are 2017-01-24 and 2017-01-27.

```
# Create a reference stack. This is the result from the
# previous method but only files taken at 2017-01-25 are stacked.
autoreduce_V2.sh -P=A1656 -p=abell1656 -rv=V191209 -ra=12:59:36
                 -dec=27:57:34 -sa=g,10,0,0 -ss=17500 -t=0.7 -d=20170125

# create a mask of the brightest pixels
create_mask.sh A1656_V191209_skyalign_g_4.fits postmask_g.fits
               # recommended masking parameters: 25smag 1 0 5 n

# subtract the reference stack from single files and multiply the mask
cd /data/wst/u/mkluge/WWFI/reduced/A1656/V191209/stacks/
substack.sh auto g ../../final/A1656_V191209_skyalign_g_4.fits
            postmask_g.fits

# create night-sky flats from the residuals
cd nightskyflat_g
script.average_postnightskyflat.sh auto

# subtract the reference stack from the single images,
# multiply the mask and
# scale the night-sky flats to the residuals and subtract them
cd /data/wst/u/mkluge/WWFI/reduced/A1656/final
skycorr.sh -f=g -rv=V191209 -p=abell1656_sky -mf=mask1_g_sky.fits
           -ss=17500 -o n,sdp,n,n,n,n -del -d="2017012[47]"
           -ps=A1656_V191209_skyalign_g_4.fits -pm=postmask_g.fits

# stack the results
autoreduce_V2.sh -P=A1656 -p=abell1656 -rv=V191209 -ra=12:59:36
                 -dec=27:57:34 -sa=g,10,0,0 -ss=17500 -t=0.7 -ur=only_ex
```

The resulting stack is not shown but the quality is comparable to Fig. 18.2, top right panel.

18.8 Reference stack from SDSS data

Analogous to the previous method, the reference stack can also be data from other telescopes, e.g., archival SDSS data. To download a coadded SDSS image of the same object region as the Wendelstein data, go to the webpage `http://hachi.ipac.caltech.edu:8080/montage`, create an account or login and enter the following data into the form:

```
RA=12:59:48
Dec=27:58:48
Image Size (degrees) = 1
Pixel Scale = 0.2
```

Download the shell script and make it executable: `chmod 755 J125947.00+275848.0.sh`. Change the values of `IMAGE_SIZE` in the script to the WWFI stack size. Then execute it! Rename the resulting SDSS stack to a reasonable filename, e.g., `mv J125947.00+275848.0-g.fits A1656_SDSS_g.fits`. That stack can be seen in Fig. 18.1, bottom right panel. There are strong diagonal background inhomogeneities but the large-scale background pattern is flat (which is not always the case). Therefore, it is suited to act as a reference stack to create WWFI night-sky flats.

The SDSS photometric zero-point is 22.5 mag. The SDSS stack therefore needs to be rescaled in flux to the WWFI zero-point. The default value is 30 mag. Simply multiplying it by a factor of $dex(-0.4(22.5-30)) = 1000$ is not accurate enough for the reasons explained in Sec. 16 and especially 16.6.

```
# rescale the binned SDSS image
binnormfits -b 20 -n A1656_V191209_g_1.fits A1656_SDSS_g.fits
ds9 -title calsdss &
F=1000
while [ x"$F" != x ]; do
  multiplyfits.py -c $F bA1656_SDSS_g.fits
  subtractfits.py -n -f dbA1656_SDSS_g.fits bA1656_V180719_g_3.fits
  xpaset -p calsdss fits sbA1656_V180719_g_3.fits
  OLDF=$F
  read F
done
multiplyfits.py -c $OLDF A1656_SDSS_g.fits

# enter scaling factors (e.g. 1050) until the residuals become minimal
# and then press <ENTER>.

create_mask.sh A1656_V191209_g_4.fits postmask_g.fits
               # recommended masking parameters: 25smag 1 0 5 n
cd /data/wst/u/mkluge/WWFI/reduced/A1656/V191209/stacks/
substack.sh auto g ../../final/dA1656_SDSS_g.fits postmask_g.fits
```

```
cd nightskyflat_g
script.average_postnightskyflat.sh auto
cd /data/wst/u/mkluge/WWFI/reduced/A1656/final
skycorr.sh -f=g -rv=V191209 -p=abell1656_sky -mf=mask1_g_sky.fits
           -ss=17500 -o n,sdp,n,n,n,n -ps=A1656_V191209_g_4.fits
           -pm=postmask_g.fits -del -d="2019{1121,1122,1201}"
autoreduce_V2.sh -P=A1656 -p=abell1656 -rv=V191209 -ra=12:59:36
                 -dec=27:57:34 -sa=g,10,0,0 -ss=17500 -t=0.7 -ur=only_ex
```

The rest is analogous to the instruction in Sec. 18.8. Only the reference file `A1656_V191209_skyalign_g_4.fits` must be replaced by `dA1656_SDSS_g.fits` and the mask must be very conservative around bright stars since they are not removed from the SDSS stack (see Fig. 18.4).

The resulting WWFI stack can be seen in Fig. 18.1, bottom left panel. It is comparable to the top right stack but without the strong gradient.

18.9 Night-sky stacks: Fringes

Fringes are relatively time-stable interference patterns in the background. They arise from reflections of sky emission lines in the CCDs and are therefore only relevant in the i'- and z'-bands. They need to be subtracted in the i'-band only if the requirements on background flatness are relatively strict. Fringes in the z'-band need to be subtracted almost always because they are much brighter here. The procedure is almost identical to the one described in Sec. 18.5 but the last `skycorr.sh` command needs to be modified by replacing `-o=n,n,sd,n,n,n` with `-o=n,n,fd,n,n,n`. A nonsmoothed night-sky flat will be scaled to the individual images and subtracted.

```
...
skycorr.sh -f=g -rv=V191209 -o=n,n,fd,n,n,n -mf=mask2_g.fits
           -ss=17500 -del
autoreduce_V2.sh -P=A1656 -p=abell1656 -rv=V191209 -ra=12:59:36
           -dec=27:57:34 -fs=g -ss=17500 -t=0.7 -ur=only_ex
```

18.10 Relative background matching with polynomials using `skyalign`

In some science cases, e.g., for difference photometry, background homogeneity is less important than background similarity between images. The tool `skyalign` matches background patterns of all single exposures to each other using polynomials of order `<POLYORDER>`. It is described in detail in Bianca Neureiter's bachelor's thesis (LMU). No oversubtraction of extended sources occurs but a strongly inhomogeneous background pattern remains.

This method is activated by parsing the argument `-sa=<FILTERS>,<BINSIZE>, <POLYORDER>,<MINNUMBER>` to the pipeline.

```
autoreduce_V2.sh -P=A1656 -p=abell1656 -rv=V191209 -ra=12:59:36
                 -dec=27:57:34 -sa=g,10,2,1 -ss=17500 -t=0.7
```

The resulting single images will be stored in the directory `/data/wst/u/<USER>/WWFI/reduced/<PROJECT>/<REDUXVERS/stacks/qalign_<FILTER>/`. The parameter `<FILTERS>` is a list of filterbands. `<BINSIZE>` specifies the binning factor before the images are matched. `POLYORDER` is the order of the 2D polynomials, which are added to the backgrounds. `<MINNUMBER>` is the minimum number of images that must overlap for each pixel. Error images must be available for `skyalign`, i.e. the option `-ne` must *not* be activated in the pipeline.

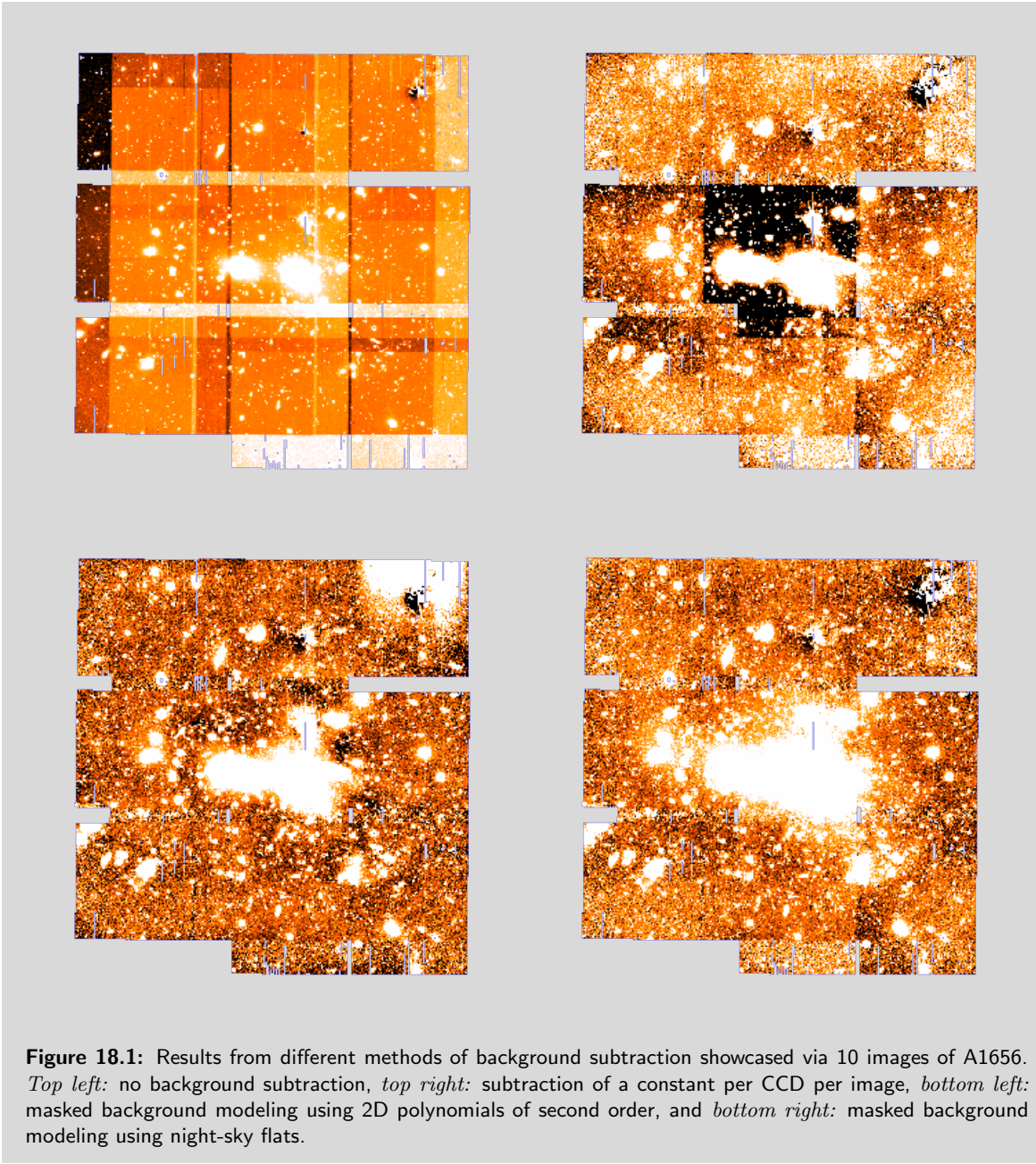

Figure 18.1: Results from different methods of background subtraction showcased via 10 images of A1656. *Top left:* no background subtraction, *top right:* subtraction of a constant per CCD per image, *bottom left:* masked background modeling using 2D polynomials of second order, and *bottom right:* masked background modeling using night-sky flats.

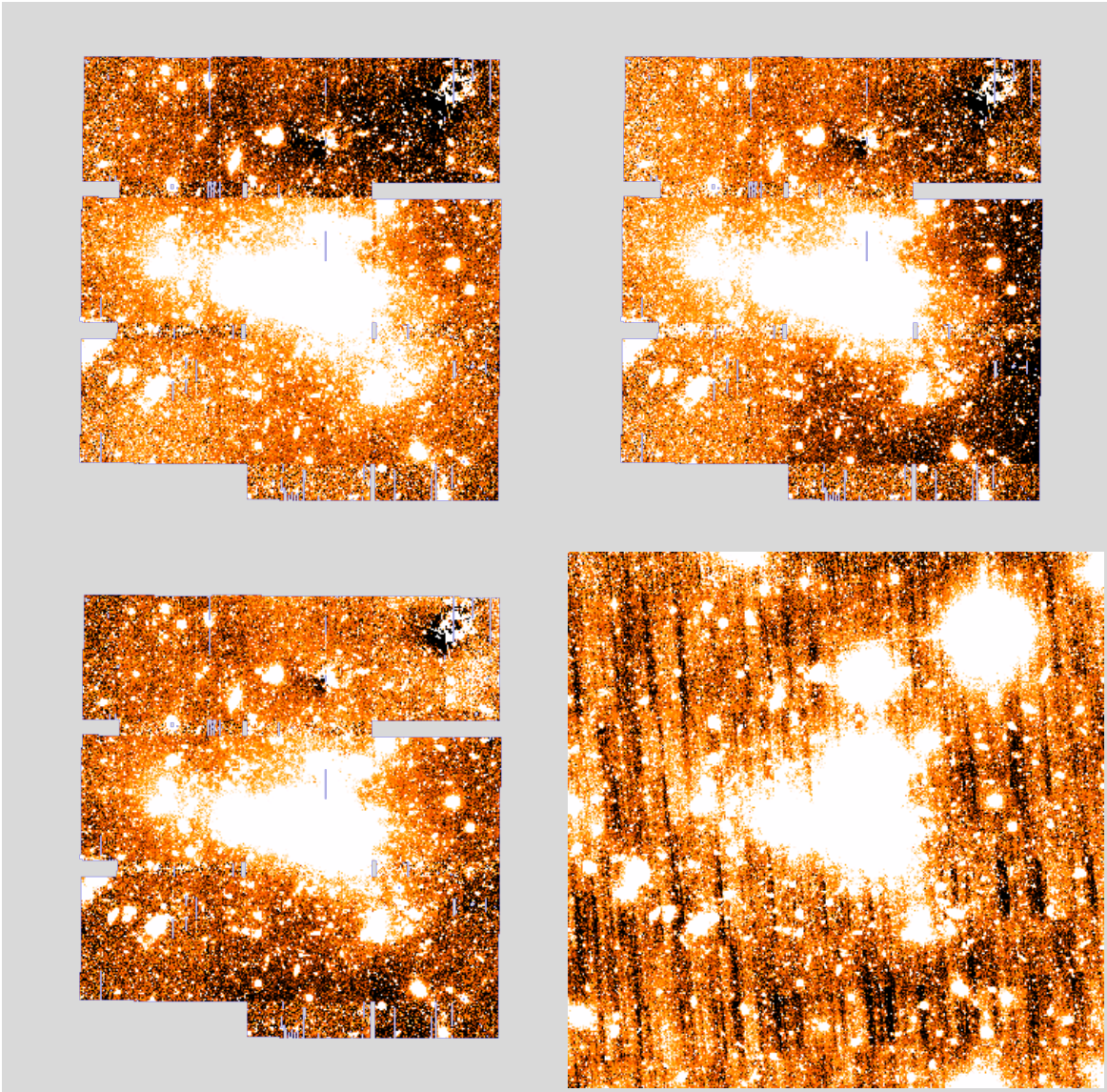

Figure 18.2: Results from different methods of background subtraction showcased via 10 exposures of A1656. *Top left:* background modeling using night-sky flats from sky pointings, *top right:* same as top left, but the residual background constants are matched using `skyalign`, *bottom left:* masked background modeling on residuals after subtracting an SDSS image (*bottom right*) from each WWFI exposure.

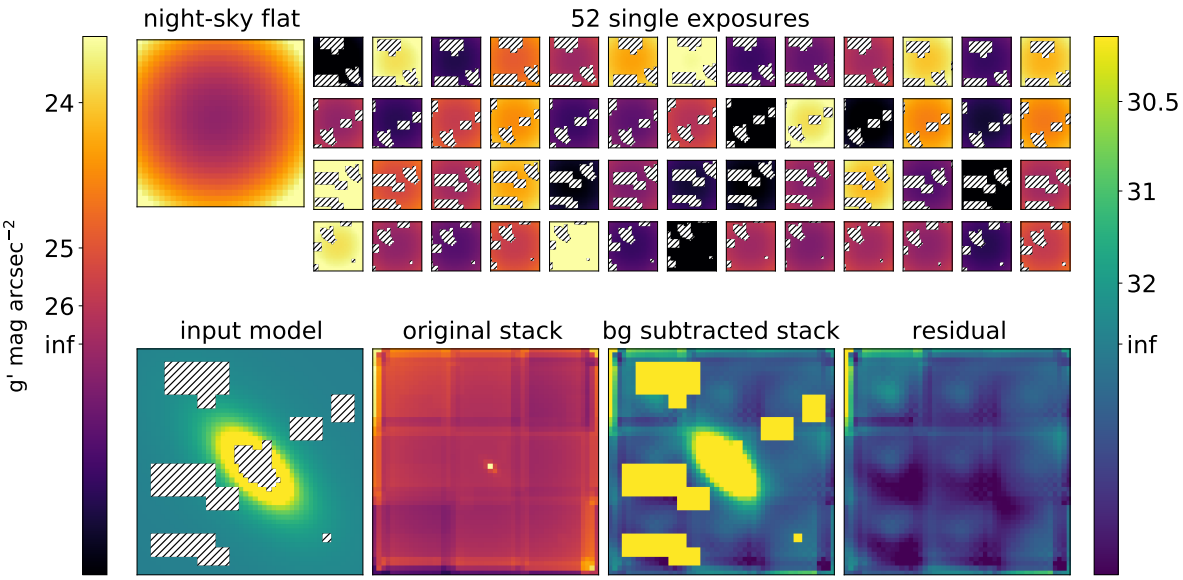

Figure 18.3: Simulation of the night-sky flat procedure. The top right rows contain 52 dithered, single exposures (not to scale). The night-sky flat, that is created by combining those single exposures, is shown in the top left panel. A constant is subtracted from the all of these images to enhance the visibility of background inhomogeneities. The single exposures and the night-sky flat are $30' \times 30'$ in size. The stacks in the bottom row are larger ($49' \times 49'$) because of the large dithering. They represent (from left to right): (1) input stack, consisting of a model BCG and masked (hatched) satellite galaxies; (2) stack including a sky background minus a global constant to enhance the visibility of background inhomogeneities; (3) stack after a scaled night-sky flat was subtracted from each single exposure, and (4) the residual of (1) minus (3). Two colorbars are given: black-red-yellow for images with large background inhomogeneities and black-green-yellow for images with small background inhomogeneities. The spatial resolution is $1'$/pixel.

18.11 Simulation of the night-sky flat procedure

To illustrate the procedure of the background subtraction method using night-sky flats, an idealized simulation is shown in Fig. 18.3. The bottom left image contains symbolic satellite galaxies and the input Sérsic model of a BCG+ICL (effective surface brightness $SB_\mathrm{e} = 26$ g' mag arcsec^{-2}, effective radius $r_\mathrm{e} = 100''$, Sérsic index $n = 9$, ellipticity $\epsilon = 0.5$ and position angle $PA = 45°$). Masks are illustrated by diagonal hatches. The masking threshold is set to $SB = 29$ g' mag arcsec^{-2}. Usually, ICL outskirts fainter than this threshold are invisible in reality due to the shot noise of the sky. Hence, they remain unmasked.

The 52 small images in the top rows represent the single exposures including statistically varying sky background. The background model consists of a constant surface brightness of $SB = 21.5$ g' mag arcsec^{-2} plus a second order polynomial representing the time-stable 2% spatial variation inside each image (cf. Fig. 3.2, right panel):

$$F_\mathrm{sky,i}(x,y) = A_i \times \left(\frac{(x-x_0)^2 + (y-y_0)^2}{5} + 10^{-0.4(21.5-30)} \right) + B_i, \qquad (18.1)$$

where $F_\mathrm{sky,i}$ is the sky flux at pixel position (x,y) in exposure i. A is a random scaling factor with mean $\bar{A}_i = 1$ and standard deviation of $\sigma(A_i) = 0.02$, representing the zero-point fluctuation of $\sim 2\%$ and B is a random offset with mean of $\bar{B}_i = 0$ and standard deviation of $\sigma(B_i) = 0.02 F_\mathrm{sky}$, representing the sky level fluctuation. The center coordinates in the single

images are $x_0 = 15'$ and $y_0 = 15'$. All values for x, y, x_0, y_0 are given in arcminutes. The zero-point is set to 30 g' mag with a fiducial pixel scale of $1''$/pixel. A diagonal sky gradient of 2% of the mean sky flux is added to the full, stacked image. The mask is created from the bottom left image and applied to the single, dithered images, indicated as hatched regions. These images are then normalized and averaged, resulting in the night-sky flat on the top left panel. That night-sky flat (NSF) is then rescaled by fitting its flux to the masked, single images using the formula (cf. Eq. 3.6)

$$\mathrm{NSF}_i(x, y) = \mathrm{NSF}(x, y) \times a_i + b_i. \tag{18.2}$$

After subtraction of the individually scaled night-sky flats from the single images, those images are then coadded to create the stack in the bottom panel, third column from the left in Fig. 18.3. The residuals of that stack minus the original stack in the bottom left is shown in the bottom right panel. The residual background constant is negative 31.3 g' mag arcsec^{-2} with a scatter of 31.75 g' mag arcsec^{-2}. That is in approximate agreement with the mock-BCG test described in Sec. 5.1. It confirms that the extended envelopes around the observed BCGs are preserved down to at least $SB = 30$ g' mag arcsec^{-2}, even if the mask is incomplete at levels fainter than $SB > 29$ g' mag arcsec^{-2}.

18.12 Quality check: background subtraction

Background subtraction accuracy is sensitive to a variety of unwanted effects. They include the scenarios shown in Fig. 14.3 and furthermore, passing clouds and beginning or ending twilight / moonlight. Files contaminated by the latter can be identified by a rapid increase/decrease of the background value:

```
cd /data/wst/u/mkluge/WWFI/reduced/A1656/V191209/redux
gethead BG V*.fits
```

or

```
cd /data/wst/u/mkluge/WWFI/reduced/A1656/V191209/stacks
gethead BG q1*.fits
```

Images contaminated by passing clouds are identified by image-to-image fluctuations of the sky transparency stored in the `TRANSPAR` header keyword. They can be examined by replacing the string `BG` by `TRANSPAR` in the upper example.

Visual inspection can be done for all images using the script `checkbg.sh`:

```
cd /data/wst/u/mkluge/WWFI/reduced/A1656/V191209/stacks/swarp_<FILTER>
checkbg.sh <METHOD>
```

where `<METHOD>` is an integer corresponding to the position of the applied `-o=?,?,?,?,?,?` argument value in `skycorr.sh`:

0: before background subtraction

1: polynomials fitted to the full images

2: night-sky flat scaled to the (masked) residuals after subtracting a reference stack

3: night-sky flat scaled to the masked full images

4: polynomials fitted to each CCDs

5: polynomials fitted to the full images

6: polynomials fitted to each CCDs

A 50×50 pixels binned jpeg image is created for each exposure (see Fig. 18.4). They can be quickly scanned by the user. The top left image shows the original image before background subtraction. The top right image is the background model. The bottom left image is the background subtracted image and the bottom right image is the residual after subtracting a reference stack (see Sec. 18.7 and 18.8) from the background subtracted image. Furthermore, the values of the header keywords `TRANSPAR` (sky transparency), `BG` (average background value) and `EXPTIME` (exposure time) are labeled at the top.

All contaminated files should either be masked (see Sec. 14) or discarded. Discarding can either be done by parsing the argument `-t=TRANSPAR_MIN` to `autoreduce_V2.sh` and `create_nightskyflat.sh` or by moving the affected files to a `bad/` folder:

```
cd /data/wst/u/mkluge/WWFI/reduced/A1656/V191209/stacks
mkdir bad
mv *180724_161* *180512_100* bad/
cd /data/wst/u/mkluge/WWFI/reduced/A1656/V191209/stacks/swarp_<FILTER>
mkdir bad
mv *180724_161* *180512_100* bad/
```

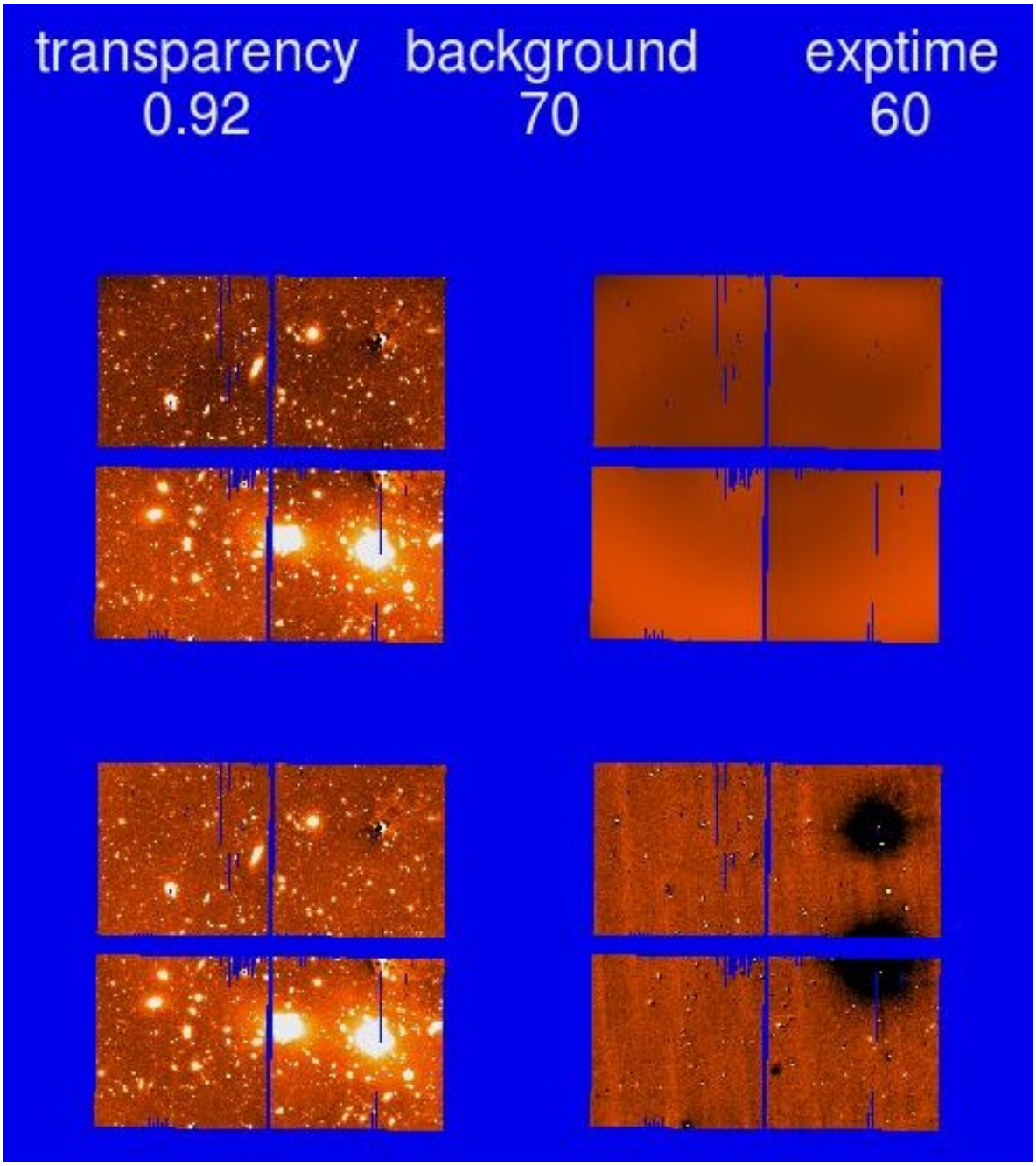

Figure 18.4: Background quality check image output by `checkbg.sh`. *Top left:* single image before background subtraction. *Top right:* background model. *Bottom left: single image after subtraction of the background model. Bottom right:* Residuals after subtraction of a reference stack from the background subtracted image. The two large black residuals arise from bright stars that were not subtracted from the SDSS reference image. The values of the header keywords `TRANSPAR` (sky transparency), `BG` (average background value) and `EXPTIME` (exposure time) are printed on the top.

Chapter 19

Source masking

Source-masks are essential for accurate background modeling. Extended and faint structures are easily oversubtracted because software routines cannot distinguish between background inhomogeneities and real extended low-surface-brightness features. This becomes important when the spatial scales and surface brightness levels of background inhomogeneities are comparable to those of the targets. In those cases, time-stable, i.e. dither position independent, background patterns can only be modeled when the sources are accurately masked.

Segmentation maps as check-image outputs of `SExtractor` are commonly used but allow only limited control of the masking parameters. That software only allows for a constant S/N masking threshold or a constant surface brightness masking threshold. The former option misses sources in the low-S/N corners of largely dithered, coadded images, which consequently leads to too high background estimations. The latter option leads to more frequent false positive detections of source mimicking positive noise peaks in the low-S/N corners of those stacks. There, it consequently results in too low background estimations. That is a severe problem when the S/N varies significantly across the field of view, e.g., because of largely dithered observations.

A compromise has to be found between the completeness of masks and a low number of false positives detections. This requirement initiated the development of the tool `create_mask.sh`. It enables the user to chose between a constant S/N threshold, a constant surface brightness threshold or an intermediate option that scales the threshold by the square root of the root-mean-square noise of the local background. The local noise $rms(x, y)$ is estimated by scaling the average rms noise of the whole stack $\overline{rms(x, y)}$ (determined using the standard deviation of the $\kappa - \sigma$ clipped (upper $\kappa = 3$, lower $\kappa = 4$) distribution of all pixel values in the stack) with the weight map $w(x, y)$ (see Sec. 15):

$$rms(x, y) = \frac{\overline{rms(x, y)}}{\sqrt{w(x, y)/\mathrm{median(w(x, y))}}}. \tag{19.1}$$

Examplaric masks created with for all three options are shown in Fig. 19.1. Fig. 19.2 shows the same masks multiplied to the WWFI stack of A1775. For the top left panel, a constant surface brightness threshold is applied. Too many false positive detections result in a darkening in the corners of both figures. For the top right panel, a constant S/N threshold is applied. Too few detections result in a brightening of the corners. Finally, for the bottom panel, the scaled threshold is applied. It provides the most homogeneous masks of all three

options. The more numerous masks near the center are at least in part owed to the overdensity of cluster galaxies.

The optimal scaling method depends on the average masking threshold. The behavior, which was explored by Bianca Neureiter during her Master's project. For the typical, recommended parameters (which are shown by the program on execution), the square root of the rms is sufficient. That is confirmed by the mock-BCG test described in Sec. 5.1.

The program allows to specify five masking parameters, which are described below.

1. threshold
2. expand diameter
3. border size
4. detection area
5. background box size.

The threshold (1) can be either given in units of S/N by entering a decimal number or given in units of surface brightness, e.g., `27.5mag`. The scaled option is activated by adding an "s" after the number, e.g. `0.15s` or `27.5smag`. All pixels in the smoothed image (see option 4) with values higher than this threshold will be masked.

The expand diameter (2) activates a fast Fourier transform convolution with a circular kernel where the given parameter is the radius of that kernel. Any masked pixel will thereby be replaced by that circular kernel, which expands the masks. A given radius ≤ 1 deactivates this option.

The border size (3) activates a cropping of the image in all directions by the given amount of pixels. That option is useful when the S/N and therefore mask homogeneity drops rapidly at the image borders. Columns or row consisting of only zeros or NaNs will be ignored.

The detection area (4) is the standard deviation of a circular Gaussian kernel, with which the (background subtracted; see option 5) image is convolved before sources are detected. The larger this parameter is chosen, the larger will the masked area be, but the more smaller sources will be missed.

The background box size (5) determines the background spline interpolation step size. Median background fluxes are measured inside square boxes with a side length of the given parameter. The pixel values inside these boxes are $\kappa - \sigma$ clipped where $\kappa = 3$ is the lower and $\kappa = 8$ is the upper clipping limit. The median of the remaining values is set as the grid-point value located at the center of each box. That grid is interpolated to form a full-sized background model, which is then subtracted. Further options are "n" for no background subtraction and "c", which activates that a constant is subtracted from the whole image. This constant is calculated as the median of the $\kappa - \sigma$ clipped distribution of all non-zero on non-NaN pixel values where $\kappa = 3$ is the lower and $\kappa = 4$ is the upper clipping limit. That option is useful when (1) the background varies on surface brightness levels comparable to the masking threshold and (2) extraordinarily extended objects like BCGs shall remain unmasked, i.e. their outskirts are thereby interpreted as background.

After the automatic masking is finished, the program offers to manually unmask regions and to improve the masks by manually adding masks of non-detected sources, e.g., extended PSF wings, extended galactic halos, galactic cirrus or smaller sources in the manually unmasked regions.

Zoomed images of masks created with different masking parameters are shown in Fig. 19.3 and 19.4.

The masking parameters that are appled to the top right image are recommended to use for the creation of night-sky flats (see Sec. 3.2 and 18.5) of polynomial background subtraction (see Sec. 18.4). The very small sources that remain in the top right panel are negligible for night-sky flat or polynomial background modeling. Their distribution is sufficiently homogeneous because they are mostly background sources and the night-sky flats are usually smoothed aggressively with 2D polynomials of fourth order (see Sec. 18.5). For the considered configuration, a homogeneous mask provides better results than a complete mask with an inhomogeneous distribution of false positives.

The bottom panels show the two masks that are applied before isophotal fluxes are measured (see Sec. 3.2 and 4.2). The bottom left panel contains the first mask and the bottom right panel contains both masks. They are more complete in the central regions for the price that the homogeneity degrades a bit towards the edges of the field of view. However that effect is negligible for the science case of this thesis (see Sec. 5.1).

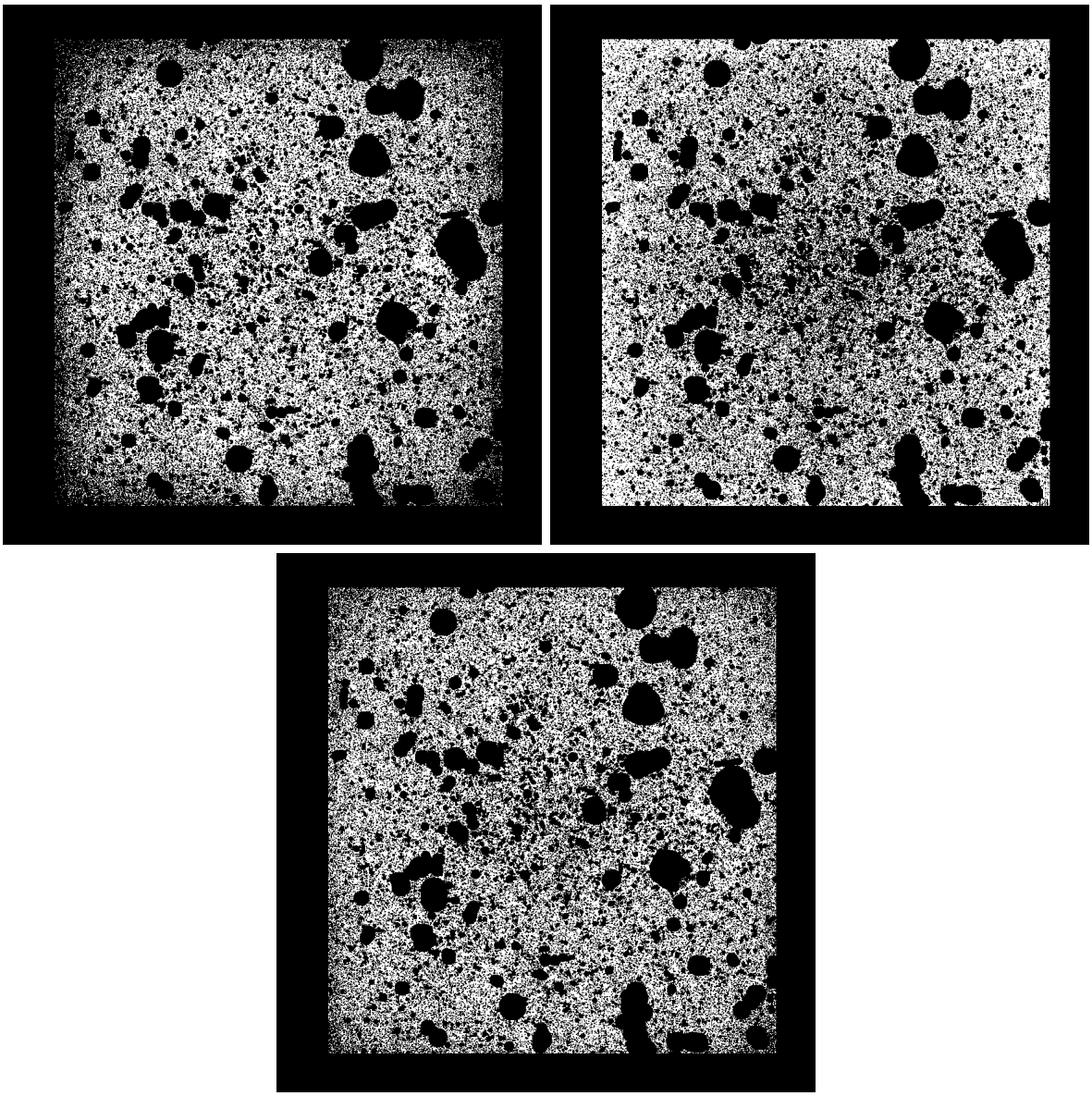

Figure 19.1: Masks created for the WWFI stack of A1775. *Top left:* constant surface brightness threshold. *Top right:* constant S/N threshold. *Bottom:* intermediate option using the scaled threshold. The large masks are added manually for very extended sources.

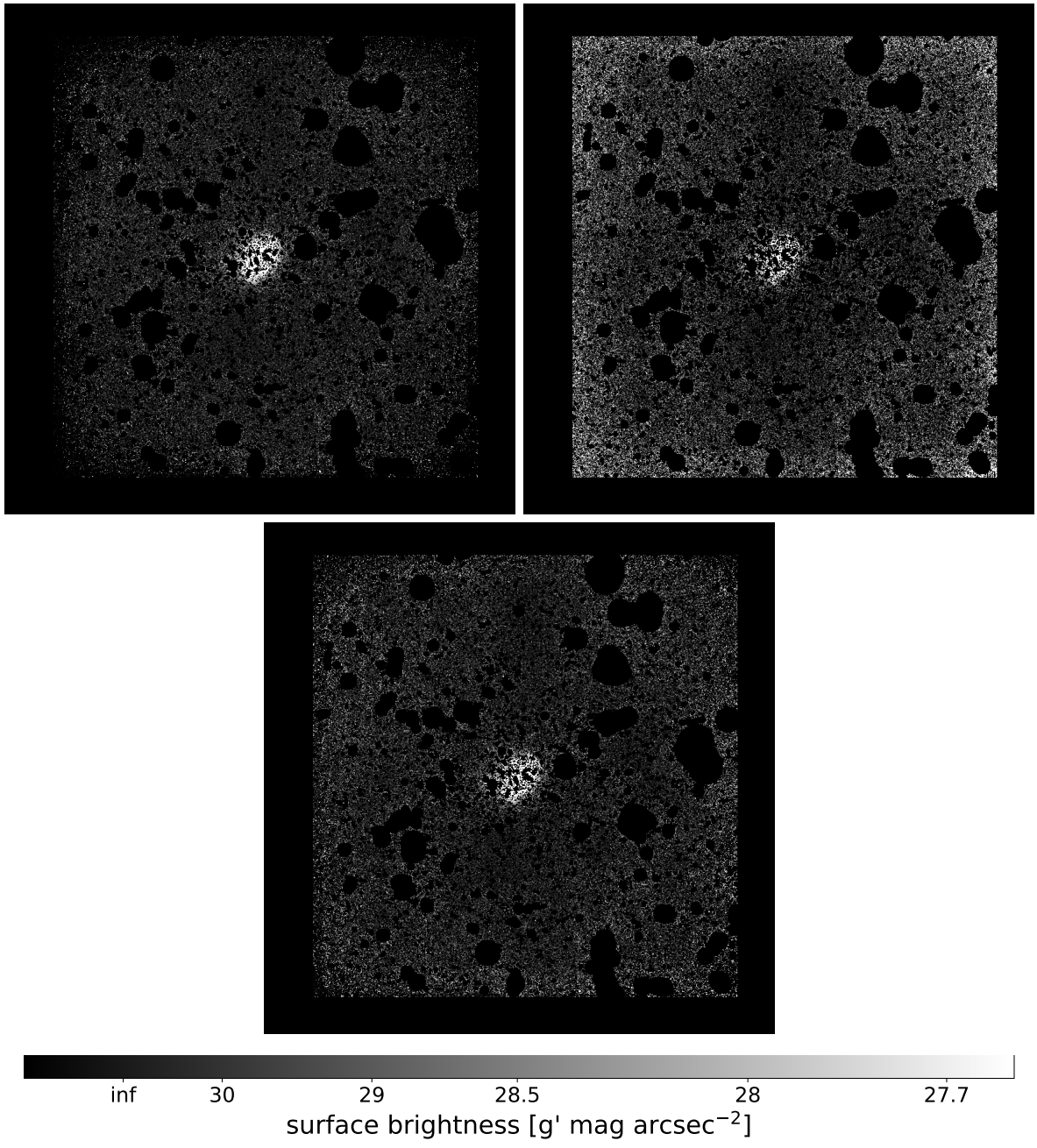

Figure 19.2: The same masks from Fig. 19.1 multiplied to the WWFI stack of A1775. *Top left:* constant surface brightness threshold. *Top right:* constant S/N threshold. *Bottom:* intermediate option using the scaled threshold. The BCG in the center remains purposely unmasked.

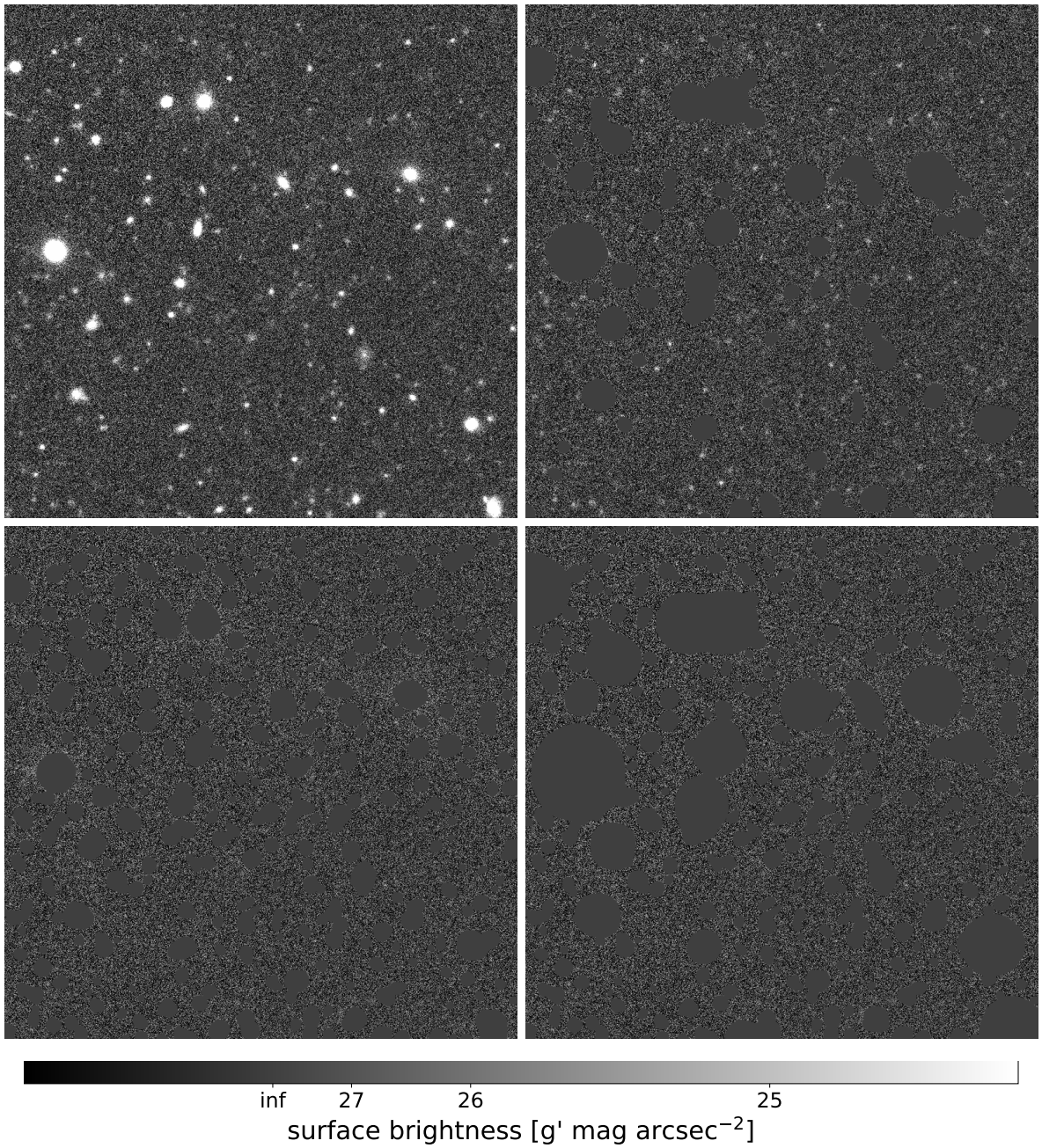

Figure 19.3: Masked zoom-in images. *Top left:* No masking. *Top right:* Mask for creation of night-sky flats. Masking parameters are: `27.5smag 1 0 11 n`. *Bottom left:* First mask of small sources for isophotal flux measurements. Masking parameters are: `0.15s 9 300 5 51`. *Bottom right:* Second mask of intermediate-sized sources for isophotal flux measurements, combined with the first mask. Masking parameters are: `0.15s 11 300 21 51`.

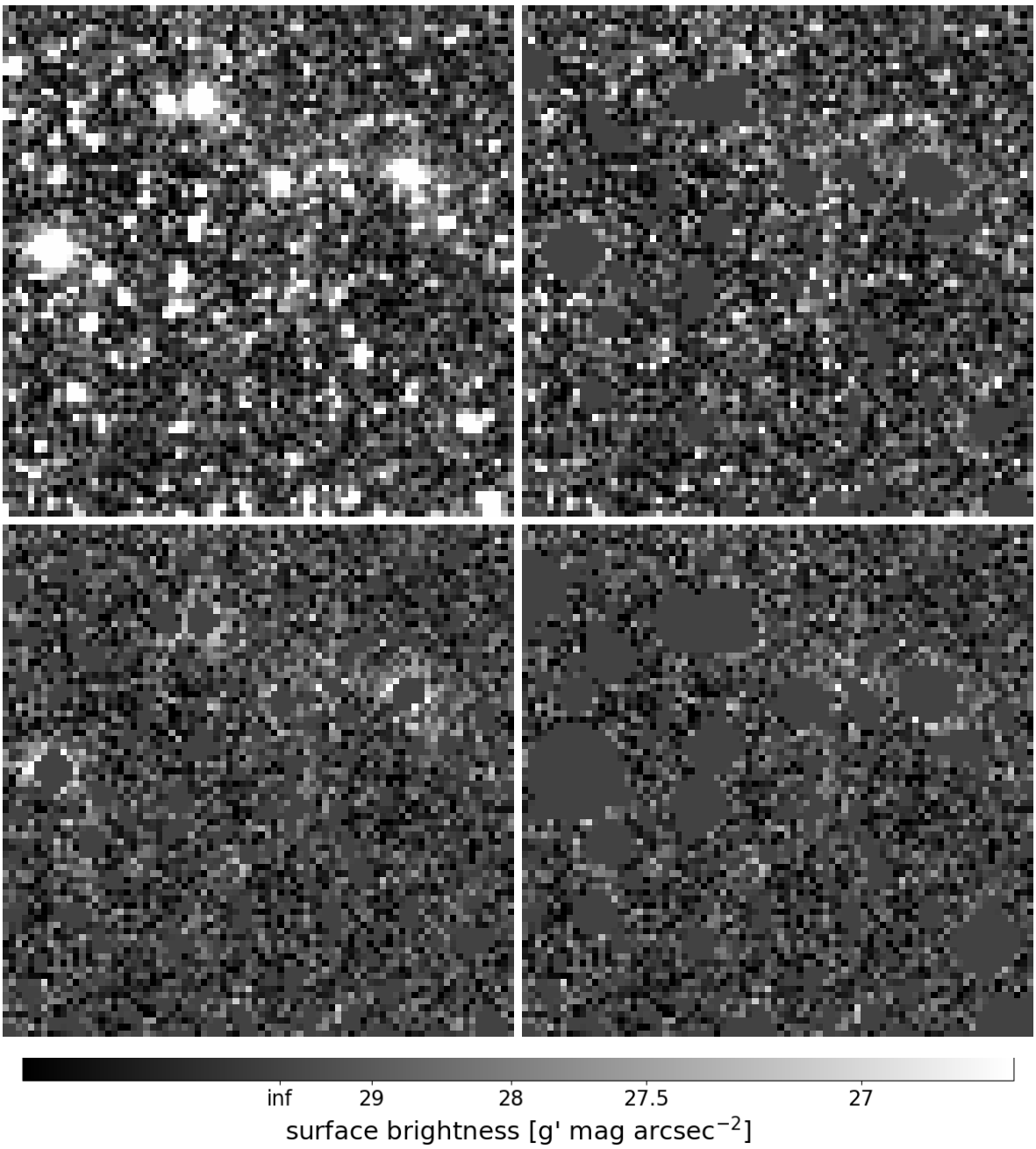

Figure 19.4: Same as Fig. 19.3 but 10×10 pixels binned to enhance the more extended and faint outskirts of the sources.

Chapter 20

Pipeline Appendices

short parameter	long parameter	default	alternative
-u=[...]	--user=<STRING>	[mkluge]	[wst]
-P=[...]	--project=<STRING>	[nA]	[M51]
-p=["..." "..."]	--prefixes=<STRINGS>	[nA]	["M51" "m51"],["*51"],["?51"],[m51]
-fr=[...]	--filtersredux=<STRING>	[false]	[ugriz],[gi]
-d=["..." "..."]	--dates=<STRINGS>	["201?????"]	[20151231],["20150101" "20151231"]
-ra=[...]	--ra=<STRING>	[0.0]	[120.50],[8:30:00.0]
-dec=[...]	--dec=<STRING>	[0.0]	[120.50],[120:30:00.0]
-ne	--noerror	[false]	[true]
-rm=[...]	--reduxmask=<STRING>	[false]	[reduxmask.fits]
-b	--masterbiascorr	[false]	[true]
-bd	--masterbiascorr_daily	[false]	[true]
-f	--masterflatcorr	[false]	[true]
-bc=[...]	--biascorr	[30]	[false],[8b]
-rv=[...]	--reduxvers=<STRING>	[V191203]	[V151231]
-cp=[...]	--chargepersistence=<STRING>	[false]	[0.2],[5min],[0.4,2min]
-st=[...]	--stardetectthresh=<INT>	[8]	[4]
-zp=[...]	--zeropoint=<INT>	[30]	[false]
-zpa=[...]	--zeropointaper=<INT>	[50]	[80]
-sc	--scamp	[false]	[true]
-pe	--position_error	[25.0]	[4.0]
-v=[...]	--vignette=<INT>	[false]	[400]
-fs=[...]	--filtersswarp=<STRING>	[false]	[gr],[ugriz]
-ur=[...]	--use_resampled=<STRING>	[use_ex]	[redo_all],[only_ex],[redo_w]
-s=[...]	--seeingmax=<STRING>	[100%]	[1.5],[20%]
-t=[...]	--transparencymin=<FLOAT>	[0]	[0.85],[1]
-q=[...]	--quadrants=<INT>	[1234]	[false],[1],[14],[1,4],[1234,1,4]
-m	--median	[false]	[true]
-ss=[...]	--stacksize=<INT>	[14000]	[17500],[70000,14000]
-bin=[...]	--bin=<INT>	[1]	[10]
-k=[...]	--kappa=<FLOAT>	[false]	[0.2],[3]
-bs=[...]	--backsize=<INT>	[4109]	[false],[256]
-bfs=[...]	--backfiltersize=<INT>	[1]	[false],[5]
-er	--errorresample	[false]	[true]
-es	--errorstack	[false]	[true]
-sa=[...]	--skyalign=<STRING>	[false]	[g,10,0,0],[ugriz,10,4,2,A1656_SDSS_g.fits]
-w=["..."]	--weighting=<STRING>	["1/BGRMS^2"]	[1/EXPTIME],["1/SEEING^2"]
			["1/(SEEING*BGRMS)^2"]

Table 20.1: Names and default values for the pipeline arguments. Either the short (column 1) or the long argument-name (column 2) can be parsed. Column (3) shows the default value, which is used when the argument in that row is not parsed. Alternative suggestions are listed in column (4), separated by commas. The values must be given without the rectangular brackets. This table is printed to the terminal when `autoreduce_V2.sh` is executed without any arguments. Detailed explanations for all arguments can be shown by executing `autoreduce_V2.sh --help`.

type of data	location	comments
scripts	/data/wst/u/wst/WWFI/SCRIPTS/	...
raw data, log files, comment files	/data/wst/u/wst/WWFI/rawdata/ <DATE>/	...
masterbias	/data/wst/u/wst/WWFI/masterbias/ <DATE>_<READOUT-MODE>/	format of raw data
masterflat	/data/wst/u/wst/WWFI/masterflat/ <DATE>_<READOUT-MODE>/ sky_<FILTER>/<VERSION>/	format of reduced data
reduced exposures (4 CCDs per image)	/data/wst/u/<USER>/WWFI/reduced/ <PROJECT>/<REDUXVERS>/redux/	approx. alignment, astrometry and zero-point
reduced quadrants (1 CCD) per image	/data/wst/u/<USER>/WWFI/reduced/ <PROJECT>/<REDUXVERS>/stacks/	precise astrometry stored in *.scamp.head files; quadrants extracted
resampled quadrants	/data/wst/u/<USER>/WWFI/reduced/ <PROJECT>/<REDUXVERS>/stacks/ swarp_<FILTER>/	precise astrometry approx. photometry in FLXSCALE header keyword
stacked image	/data/wst/u/<USER>/WWFI/reduced/ <PROJECT>/final/	precise astrometry; approx. zero-point
night-sky flats	/data/wst/u/<USER>/WWFI/reduced/ <PROJECT>/<REDUXVERS>/stacks/ stacks/nightskyflat_<FILTER>/	format of reduced quadrant

Table 20.2: Directories in which WWFI data is stored. <USER> is the user account name. <PROJECT> is the project name given with the autoreduce_V2.sh argument -P=<PROJECT>. <FILTER> is the filterband in which the observations were taken. <DATE> is the date (or month for masterbias) of observation. <RO-MODE> is the readout mode of the observations [*nothing* for mode 1 (fast), "ro6" for mode 6 (fast; optimized gain) and "slowro" for mode 3 (slow, low gain)].

Troubleshooting

Logfiles are created for every step of the data reduction to assist debugging. If the pipeline crashes, the experienced user can trace down the error source usually within one minute. From time to time, a small number of scripts can crash, especially after the system was updated. The pipeline checks in most cases whether all expected files exist and otherwise aborts the reduction. In that case, an error message can be found in the main logfile:

- /data/wst/u/<USER>/WWFI/reduced/<PROJECT>/log.autoreduce_V2_<TIMESTAMP>.

More detailed logfiles of the individual executed scripts are located in the following directories. They are usually identifiable by the fileprefix log.<SCRIPTNAME>.

- /data/wst/u/wst/WWFI/masterbias/
- /data/wst/u/wst/WWFI/masterbias/<DATE>_<READOUT-MODE>/
- /data/wst/u/wst/WWFI/masterflat/logs/
- /data/wst/u/wst/WWFI/masterflat/<DATE>_<READOUT-MODE>/sky_<FILTER>/<FLATVERS>/logs/
- /data/wst/u/<USER>/WWFI/reduced/<PROJECT>/logs/
- /data/wst/u/<USER>/WWFI/reduced/<PROJECT>/<DATE>/<FILTER>/<REDUXVERS>/redux_logs/
- /data/wst/u/<USER>/WWFI/reduced/<PROJECT>/<REDUXVERS/redux/logs/
- /data/wst/u/<USER>/WWFI/reduced/<PROJECT>/<REDUXVERS/stacks/
- /data/wst/u/<USER>/WWFI/reduced/<PROJECT>/<REDUXVERS/stacks/logs/
- /data/wst/u/<USER>/WWFI/reduced/<PROJECT>/<REDUXVERS/stacks/nightskyflat_<FILTER>/
- /data/wst/u/<USER>/WWFI/reduced/<PROJECT>/<REDUXVERS/stacks/swarp_<FILTER>/
- /data/wst/u/<USER>/WWFI/reduced/<PROJECT>/<REDUXVERS/stacks/qalign_<FILTER>/.

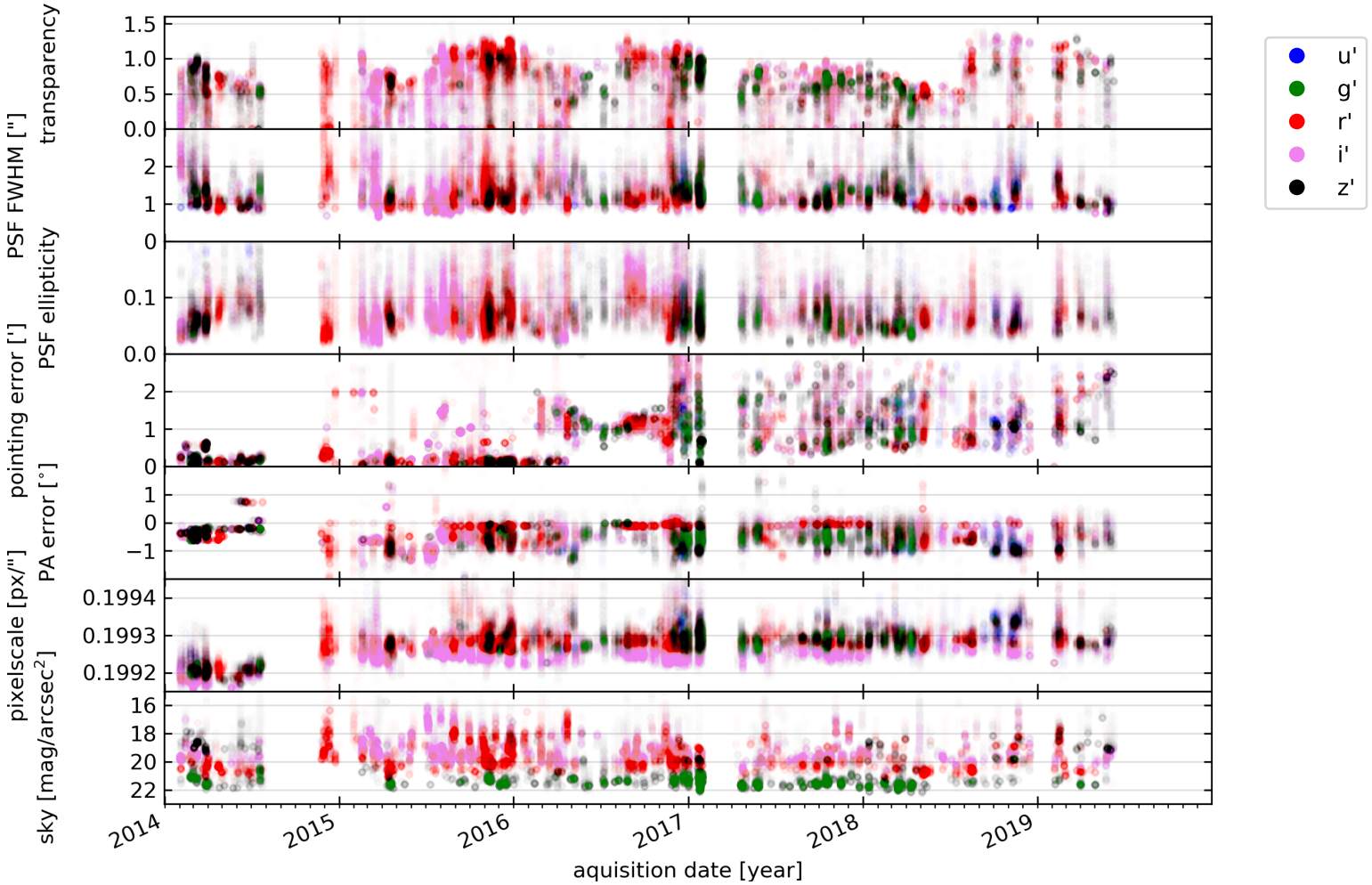

Figure 20.1: Overview of all reducible WWFI exposures (93793) taken between 2014 and 2019. The colors refer to the filterbands u': blue, g': green, r': red, i': pink and z': black. The data in the top panel is read from header keyword `TRANSPAR`, which is a combination of sky transparency and mirror reflectivity (see Sec. 12.3). Sharp increases in transparency are related to mirror cleaning events. The data in the second panel form the top is read from the header keyword `SEEING` (see also 12.3). The median PSF ellipticity $1 - b/a$ of each image is shown in the third panel, where a and b are semimajor and semiminor axis radii, respectively. Pointing errors, pointing position angle errors and the pixel scale are calculated from the preliminary astrometric solution (see Sec. 12.2). The lowest panel shows the sky brightness in the given filterband, calculated from the `BG` header keyword (see Sec. 12.2).

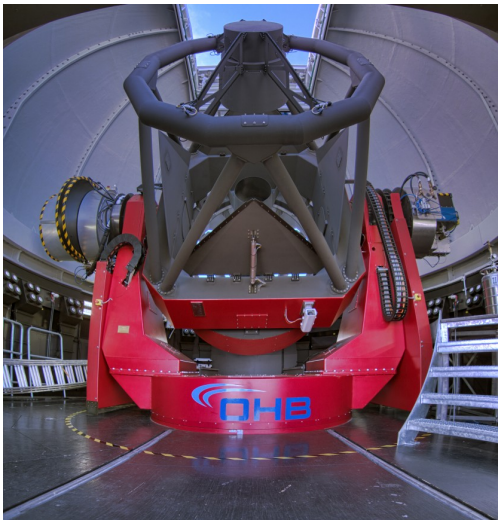

Figure 20.2: The 2m Fraunhofer telescope at the Wendelstein observatory. The WWFI is mounted on the left Nasmyth port.

Configuration	Nasmyth
Field of view	$26.6' \times 29.0'$
Gaps between CCDs	north–south: $22''$; east–west: $98''$ for $0°$ position angle
Focal length	15.6 m
F-ratio	7.4
Mirror diameter M1	2.1 m
Mirror diameter M2	0.71 m
Mirror diameter M3	0.71 m by 0.51 m
Central obscuration	12 %
Filters	Sloan u', g', r', i', z', L
Zero points	u' : 24.4, g' : 25.24, r' : 25.16, i' : 24.64, z' : 23.91
Auto guiding	2 off-axis 2000 px × 2000 px CCDs
Maximum field distortion	0.2 px (or 0.014 %)
Pixel scale	$0.1992'' \text{ px}^{-1}$
Pixel size	15 μm
Gain	$2.26 \text{ e}^- \text{ ADU}^{-1}$ in readout mode 6 (fast)
	$0.3739 \text{ e}^- \text{ ADU}^{-1}$ in readout mode 3 (slow)
Readout noise	1.94 ADU $\widehat{=}$ 4.38 e^- in readout mode 6 (fast)
	6.30 ADU $\widehat{=}$ 2.36 e^- in readout mode 3 (slow)
Dark current at −115°C	$0.07 \text{ e}^- \text{ min}^{-1}$
Dynamic Range	16 bit
Full well capacity (linear range)	$>200{,}000 \text{ e}^- \text{ px}^{-1}$
Peak quantum efficiency	0.9

Table 20.3: Technical details about the Wendelstein Telescope and WWFI. The values are in part collected from Hopp et al. (2010, 2014) and Kosyra et al. (2014). Gain, readout noise, dark current, and zero points (except u') have been newly measured. The primary aperture mask has been removed in August 2018, increasing the effective mirror size from 2.0 m to 2.1 m.

Bibliography

Abell, G. O., Corwin, Jr., H. G., & Olowin, R. P. 1989, ApJS, 70, 1, doi: 10.1086/191333

Albert, C. E., White, R. A., & Morgan, W. W. 1977, ApJ, 211, 309, doi: 10.1086/154935

Amorisco, N. C., Martinez-Delgado, D., & Schedler, J. 2015, ArXiv e-prints. https://arxiv.org/abs/1504.03697

Arnaboldi, M., Ventimiglia, G., Iodice, E., Gerhard, O., & Coccato, L. 2012, A&A, 545, A37, doi: 10.1051/0004-6361/201116752

Arp, H., & Bertola, F. 1969, Astrophys. Lett., 4, 23

—. 1971, ApJ, 163, 195, doi: 10.1086/150757

Atkinson, A. M., Abraham, R. G., & Ferguson, A. M. N. 2013, ApJ, 765, 28, doi: 10.1088/0004-637X/765/1/28

Barbosa, C. E., Arnaboldi, M., Coccato, L., et al. 2018, A&A, 609, A78, doi: 10.1051/0004-6361/201731834

Beers, T. C., & Tonry, J. L. 1986, ApJ, 300, 557, doi: 10.1086/163833

Bender, R. 1988, A&A, 193, L7

Bender, R., Burstein, D., & Faber, S. M. 1992, ApJ, 399, 462, doi: 10.1086/171940

Bender, R., Doebereiner, S., & Moellenhoff, C. 1988, A&AS, 74, 385

Bender, R., Kormendy, J., Cornell, M. E., & Fisher, D. B. 2015, ApJ, 807, 56, doi: 10.1088/0004-637X/807/1/56

Bender, R., & Moellenhoff, C. 1987, A&A, 177, 71

Bender, R., Paquet, A., & Nieto, J.-L. 1991, A&A, 246, 349

Bender, R., Surma, P., Doebereiner, S., Moellenhoff, C., & Madejsky, R. 1989, A&A, 217, 35

Bernardi, M., Hyde, J. B., Sheth, R. K., Miller, C. J., & Nichol, R. C. 2007, AJ, 133, 1741, doi: 10.1086/511783

Bertin, E. 2006, in Astronomical Society of the Pacific Conference Series, Vol. 351, Astronomical Data Analysis Software and Systems XV, ed. C. Gabriel, C. Arviset, D. Ponz, & S. Enrique, 112

Bertin, E. 2010, SWarp: Resampling and Co-adding FITS Images Together, Astrophysics Source Code Library. http://ascl.net/1010.068

Bertin, E., & Arnouts, S. 1996, A&AS, 117, 393, doi: 10.1051/aas:1996164

Besla, G., Martínez-Delgado, D., van der Marel, R. P., et al. 2016, ApJ, 825, 20, doi: 10.3847/0004-637X/825/1/20

Bílek, M., Cuillandre, J.-C., Gwyn, S., et al. 2016, A&A, 588, A77, doi: 10.1051/0004-6361/201526608

Bílek, M., Ebrová, I., Jungwiert, B., Jílková, L., & Bartošková, K. 2015, Canadian Journal of Physics, 93, 203, doi: 10.1139/cjp-2014-0170

Binggeli, B. 1982, A&A, 107, 338

Bohlin, R. C., Dickinson, M. E., & Calzetti, D. 2001, AJ, 122, 2118, doi: 10.1086/323137

Brough, S., Couch, W. J., Collins, C. A., et al. 2008, MNRAS, 385, L103, doi: 10.1111/j.1745-3933.2008.00442.x

Bullock, J. S., & Johnston, K. V. 2005, ApJ, 635, 931, doi: 10.1086/497422

Burke, C., Collins, C. A., Stott, J. P., & Hilton, M. 2012, MNRAS, 425, 2058, doi: 10.1111/j.1365-2966.2012.21555.x

Byrd, G., & Valtonen, M. 1990, ApJ, 350, 89, doi: 10.1086/168362

Calcáneo-Roldán, C., Moore, B., Bland-Hawthorn, J., Malin, D., & Sadler, E. M. 2000, MNRAS, 314, 324, doi: 10.1046/j.1365-8711.2000.03289.x

Capaccioli, M., Spavone, M., Grado, A., et al. 2015, A&A, 581, A10, doi: 10.1051/0004-6361/201526252

Carlin, J. L., Beaton, R. L., Martínez-Delgado, D., & Gabany, R. J. 2016, Astrophysics and Space Science Library, Vol. 420, Stellar Tidal Streams in External Galaxies (Springer, Cham), 219

Cattapan, A., Spavone, M., Iodice, E., et al. 2019, ApJ, 874, 130, doi: 10.3847/1538-4357/ab0b44

Chilingarian, I. V., Melchior, A.-L., & Zolotukhin, I. Y. 2010, MNRAS, 405, 1409, doi: 10.1111/j.1365-2966.2010.16506.x

Chilingarian, I. V., & Zolotukhin, I. Y. 2012, MNRAS, 419, 1727, doi: 10.1111/j.1365-2966.2011.19837.x

Chonis, T. S., Martinez-Delgado, D., Gabany, R. J., et al. 2011, in New Horizons in Astronomy, Proceedings of the Frank N. Bash Symposium 2011, held October 9-11, 2011. Austin, Texas, USA. Edited by S. Salviander, J. Green, and A. Pawlik. Published online at http://pos.sissa.it/cgi-bin/reader/conf.cgi?confid=149., id.23, 23

Contini, E., De Lucia, G., Villalobos, Á., & Borgani, S. 2014, MNRAS, 437, 3787, doi: 10.1093/mnras/stt2174

Contini, E., Yi, S. K., & Kang, X. 2018, MNRAS, 479, 932, doi: 10.1093/mnras/sty1518

Cooper, A. P., D'Souza, R., Kauffmann, G., et al. 2013, MNRAS, 434, 3348, doi: 10.1093/mnras/stt1245

Cooper, A. P., Gao, L., Guo, Q., et al. 2015, MNRAS, 451, 2703, doi: 10.1093/mnras/stv1042

Cooper, A. P., Cole, S., Frenk, C. S., et al. 2010, MNRAS, 406, 744, doi: 10.1111/j.1365-2966.2010.16740.x

Côté, P., McLaughlin, D. E., Hanes, D. A., et al. 2001, ApJ, 559, 828, doi: 10.1086/322347

Crnojević, D., Sand, D. J., Spekkens, K., et al. 2016, ApJ, 823, 19, doi: 10.3847/0004-637X/823/1/19

Cui, W., Murante, G., Monaco, P., et al. 2014, MNRAS, 437, 816, doi: 10.1093/mnras/stt1940

Da Rocha, C., & Mendes de Oliveira, C. 2005, MNRAS, 364, 1069, doi: 10.1111/j.1365-2966.2005.09641.x

Da Rocha, C., Ziegler, B. L., & Mendes de Oliveira, C. 2008, MNRAS, 388, 1433, doi: 10.1111/j.1365-2966.2008.13500.x

de Vaucouleurs, G. 1948, Annales d'Astrophysique, 11, 247

—. 1969, Astrophys. Lett., 4, 17

Dolag, K., Murante, G., & Borgani, S. 2010, MNRAS, 405, 1544, doi: 10.1111/j.1365-2966.2010.16583.x

Donzelli, C. J., Muriel, H., & Madrid, J. P. 2011, ApJS, 195, 15, doi: 10.1088/0067-0049/195/2/15

Dressler, A. 1978, ApJ, 226, 55, doi: 10.1086/156584

Duc, P.-A. 2017, in IAU Symposium, Vol. 321, Formation and Evolution of Galaxy Outskirts, ed. A. Gil de Paz, J. H. Knapen, & J. C. Lee, 180–182

Duc, P.-A., Cuillandre, J.-C., Karabal, E., et al. 2015, MNRAS, 446, 120, doi: 10.1093/mnras/stu2019

ESA, ed. 1997, ESA Special Publication, Vol. 1200, The HIPPARCOS and TYCHO catalogues. Astrometric and photometric star catalogues derived from the ESA HIPPARCOS Space Astrometry Mission

Faber, S. M., Tremaine, S., Ajhar, E. A., et al. 1997, AJ, 114, 1771, doi: 10.1086/118606

Feldmeier, J. J., Mihos, J. C., Morrison, H. L., et al. 2004, ApJ, 609, 617, doi: 10.1086/421313

Feldmeier, J. J., Mihos, J. C., Morrison, H. L., Rodney, S. A., & Harding, P. 2002, ApJ, 575, 779, doi: 10.1086/341472

Ferrarese, L., Côté, P., Cuilland re, J.-C., et al. 2012, ApJS, 200, 4, doi: 10.1088/0067-0049/200/1/4

Flewelling, H. A., Magnier, E. A., Chambers, K. C., et al. 2016, ArXiv e-prints. https://arxiv.org/abs/1612.05243

Foster, C., Lux, H., Romanowsky, A. J., et al. 2014, MNRAS, 442, 3544, doi: 10.1093/mnras/stu1074

Gnedin, O. Y. 2003, ApJ, 582, 141, doi: 10.1086/344636

Gonzalez, A. H., Zabludoff, A. I., & Zaritsky, D. 2005, ApJ, 618, 195, doi: 10.1086/425896

Gonzalez, A. H., Zaritsky, D., & Zabludoff, A. I. 2007, ApJ, 666, 147, doi: 10.1086/519729

González-García, A. C., & van Albada, T. S. 2005, MNRAS, 361, 1043, doi: 10.1111/j.1365-2966.2005.09243.x

Gössl, C. A., & Riffeser, A. 2002, A&A, 381, 1095, doi: 10.1051/0004-6361:20011522

Graham, A., Lauer, T. R., Colless, M., & Postman, M. 1996, ApJ, 465, 534, doi: 10.1086/177440

Gregg, M. D., & West, M. J. 1998, Nature, 396, 549, doi: 10.1038/25078

Hansen, S. M., Sheldon, E. S., Wechsler, R. H., & Koester, B. P. 2009, ApJ, 699, 1333, doi: 10.1088/0004-637X/699/2/1333

Harris, K. A., Debattista, V. P., Governato, F., et al. 2017, MNRAS, 467, 4501, doi: 10.1093/mnras/stx401

Hartke, J., Arnaboldi, M., Gerhard, O., et al. 2018, A&A, 616, A123, doi: 10.1051/0004-6361/201832711

Hernquist, L., & Quinn, P. J. 1988, ApJ, 331, 682, doi: 10.1086/166592

—. 1989, ApJ, 342, 1, doi: 10.1086/167571

Hoessel, J. G. 1980, ApJ, 241, 493, doi: 10.1086/158364

Høg, E., Fabricius, C., Makarov, V. V., et al. 2000, A&A, 355, L27

Hopkins, P. F., Cox, T. J., Dutta, S. N., et al. 2009, ApJS, 181, 135, doi: 10.1088/0067-0049/181/1/135

Hopp, U., Bender, R., Grupp, F., et al. 2014, in Proc. SPIE, Vol. 9145, Ground-based and Airborne Telescopes V, 91452D

Hopp, U., Bender, R., Goessl, C., et al. 2008, in Proc. SPIE, Vol. 7016, Observatory Operations: Strategies, Processes, and Systems II, 70161T

Hopp, U., Bender, R., Grupp, F., et al. 2010, Society of Photo-Optical Instrumentation Engineers (SPIE) Conference Series, Vol. 7733, The compact, low scattered-light 2m Wendelstein Fraunhofer Telescope, 773307

Hoshino, H., Leauthaud, A., Lackner, C., et al. 2015, MNRAS, 452, 998, doi: 10.1093/mnras/stv1271

Huang, H.-J., Mandelbaum, R., Freeman, P. E., et al. 2016, MNRAS, 463, 222, doi: 10.1093/mnras/stw1982

Huang, Z., Radovich, M., Grado, A., et al. 2011, A&A, 529, A93, doi: 10.1051/0004-6361/201015955

Ibata, R. A., Lewis, G. F., McConnachie, A. W., et al. 2014, ApJ, 780, 128, doi: 10.1088/0004-637X/780/2/128

Iodice, E., Capaccioli, M., Grado, A., et al. 2016, ApJ, 820, 42, doi: 10.3847/0004-637X/820/1/42

Iodice, E., Spavone, M., Capaccioli, M., et al. 2017, ApJ, 839, 21, doi: 10.3847/1538-4357/aa6846

—. 2019, A&A, 623, A1, doi: 10.1051/0004-6361/201833741

Jester, S., Schneider, D. P., Richards, G. T., et al. 2005, AJ, 130, 873, doi: 10.1086/432466

Johnston, K. V., Bullock, J. S., Sharma, S., et al. 2008, ApJ, 689, 936, doi: 10.1086/592228

Jorgensen, I., Franx, M., & Kjaergaard, P. 1992, A&AS, 95, 489

Karabal, E., Duc, P.-A., Kuntschner, H., et al. 2017, A&A, 601, A86, doi: 10.1051/0004-6361/201629974

Karademir, G. S., Remus, R.-S., Burkert, A., et al. 2019, MNRAS, 487, 318, doi: 10.1093/mnras/stz1251

Kellogg, E., Gursky, H., Leong, C., et al. 1971, ApJL, 165, L49, doi: 10.1086/180714

Kim, R. S. J., Annis, J., Strauss, M. A., & Lupton, R. H. 2002, in Astronomical Society of the Pacific Conference Series, Vol. 268, Tracing Cosmic Evolution with Galaxy Clusters, ed. S. Borgani, M. Mezzetti, & R. Valdarnini, 395

Kluge, M., Neureiter, B., Riffeser, A., et al. 2019, arXiv e-prints, arXiv:1908.08544. https://arxiv.org/abs/1908.08544

Kormendy, J. 1973, AJ, 78, 255, doi: 10.1086/111412

—. 1977, ApJ, 218, 333, doi: 10.1086/155687

Kormendy, J. 1999, in Astronomical Society of the Pacific Conference Series, Vol. 182, Galaxy Dynamics - A Rutgers Symposium, ed. D. R. Merritt, M. Valluri, & J. A. Sellwood

Kormendy, J., & Bahcall, J. N. 1974, AJ, 79, 671, doi: 10.1086/111595

Kormendy, J., & Bender, R. 1996, ApJL, 464, L119, doi: 10.1086/310095

—. 2012, ApJS, 198, 2, doi: 10.1088/0067-0049/198/1/2

—. 2013, ApJL, 769, L5, doi: 10.1088/2041-8205/769/1/L5

Kormendy, J., Fisher, D. B., Cornell, M. E., & Bender, R. 2009, ApJS, 182, 216, doi: 10.1088/0067-0049/182/1/216

Kosyra, R., Gössl, C., Hopp, U., et al. 2014, Experimental Astronomy, 38, 213, doi: 10.1007/s10686-014-9414-1

Krick, J. E., & Bernstein, R. A. 2005, in Bulletin of the American Astronomical Society, Vol. 37, American Astronomical Society Meeting Abstracts, 1452

Lauer, T. R. 1988, ApJ, 325, 49, doi: 10.1086/165982

Lauer, T. R., Postman, M., Strauss, M. A., Graves, G. J., & Chisari, N. E. 2014, ApJ, 797, 82, doi: 10.1088/0004-637X/797/2/82

Lauer, T. R., Gebhardt, K., Faber, S. M., et al. 2007, ApJ, 664, 226, doi: 10.1086/519229

Lin, Y.-T., Mohr, J. J., & Stanford, S. A. 2004, ApJ, 610, 745, doi: 10.1086/421714

Longobardi, A., Arnaboldi, M., Gerhard, O., Pulsoni, C., & Söldner-Rembold, I. 2018, A&A, 620, A111, doi: 10.1051/0004-6361/201832729

Lucy, L. B. 1974, AJ, 79, 745, doi: 10.1086/111605

Magnier, E. A., Sweeney, W. E., Chambers, K. C., et al. 2016, arXiv e-prints, arXiv:1612.05244. https://arxiv.org/abs/1612.05244

Malin, D. F., & Carter, D. 1980, Nature, 285, 643, doi: 10.1038/285643a0

—. 1983, ApJ, 274, 534, doi: 10.1086/161467

Mamon, G. A., Biviano, A., & Murante, G. 2010, A&A, 520, A30, doi: 10.1051/0004-6361/200913948

Mamon, G. A., & Łokas, E. L. 2005, MNRAS, 363, 705, doi: 10.1111/j.1365-2966.2005.09400.x

Mancillas, B., Duc, P.-A., Combes, F., et al. 2019, A&A, 632, A122, doi: 10.1051/0004-6361/201936320

Martínez-Delgado, D., Gabany, R. J., Crawford, K., et al. 2010, AJ, 140, 962, doi: 10.1088/0004-6256/140/4/962

Matthews, T. A., Morgan, W. W., & Schmidt, M. 1964, ApJ, 140, 35, doi: 10.1086/147890

Melnick, J., Giraud, E., Toledo, I., Selman, F., & Quintana, H. 2012, MNRAS, 427, 850, doi: 10.1111/j.1365-2966.2012.21924.x

Merritt, A., van Dokkum, P., Abraham, R., & Zhang, J. 2016, ApJ, 830, 62, doi: 10.3847/0004-637X/830/2/62

Merritt, D. 1984, ApJ, 276, 26, doi: 10.1086/161590

Mihos, J. C. 2004, Clusters of Galaxies: Probes of Cosmological Structure and Galaxy Evolution, 277

Mihos, J. C., Harding, P., Feldmeier, J., & Morrison, H. 2005, ApJL, 631, L41, doi: 10.1086/497030

Mihos, J. C., Harding, P., Feldmeier, J. J., et al. 2017, ApJ, 834, 16, doi: 10.3847/1538-4357/834/1/16

Mihos, J. C., & Hernquist, L. 1994, ApJL, 437, L47, doi: 10.1086/187679

Miville-Deschênes, M.-A., Duc, P.-A., Marleau, F., et al. 2016, A&A, 593, A4, doi: 10.1051/0004-6361/201628503

Moffat, A. F. J. 1969, A&A, 3, 455

Montes, M., & Trujillo, I. 2019, MNRAS, 482, 2838, doi: 10.1093/mnras/sty2858

Moore, B., Katz, N., Lake, G., Dressler, A., & Oemler, A. 1996, Nature, 379, 613, doi: 10.1038/379613a0

Morgan, W. W., Kayser, S., & White, R. A. 1975, ApJ, 199, 545, doi: 10.1086/153721

Morgan, W. W., & Lesh, J. R. 1965, ApJ, 142, 1364, doi: 10.1086/148422

Murphy, J. D., Gebhardt, K., & Cradit, M. 2014, ApJ, 785, 143, doi: 10.1088/0004-637X/785/2/143

Niederste-Ostholt, M., Strauss, M. A., Dong, F., Koester, B. P., & McKay, T. A. 2010, MNRAS, 405, 2023, doi: 10.1111/j.1365-2966.2010.16597.x

Oegerle, W. R., & Hill, J. M. 2001, AJ, 122, 2858, doi: 10.1086/323536

Oguri, M., Takada, M., Okabe, N., & Smith, G. P. 2010, MNRAS, 405, 2215, doi: 10.1111/j.1365-2966.2010.16622.x

Okamoto, S., Arimoto, N., Ferguson, A. M. N., et al. 2015, ApJL, 809, L1, doi: 10.1088/2041-8205/809/1/L1

Oser, L., Ostriker, J. P., Naab, T., Johansson, P. H., & Burkert, A. 2010, ApJ, 725, 2312, doi: 10.1088/0004-637X/725/2/2312

Patel, P., Maddox, S., Pearce, F. R., Aragón-Salamanca, A., & Conway, E. 2006, MNRAS, 370, 851, doi: 10.1111/j.1365-2966.2006.10510.x

Pillepich, A., Nelson, D., Hernquist, L., et al. 2018, MNRAS, 475, 648, doi: 10.1093/mnras/stx3112

Planck Collaboration, Ade, P. A. R., Aghanim, N., et al. 2014, A&A, 571, A1, doi: 10.1051/0004-6361/201321529

Pop, A.-R., Pillepich, A., Amorisco, N. C., & Hernquist, L. 2018, MNRAS, 480, 1715, doi: 10.1093/mnras/sty1932

Popesso, P., Biviano, A., Böhringer, H., & Romaniello, M. 2007, A&A, 464, 451, doi: 10.1051/0004-6361:20054708

Postman, M., & Lauer, T. R. 1995, ApJ, 440, 28, doi: 10.1086/175245

Puchwein, E., Springel, V., Sijacki, D., & Dolag, K. 2010, MNRAS, 406, 936, doi: 10.1111/j.1365-2966.2010.16786.x

Quinn, P. J. 1984, ApJ, 279, 596, doi: 10.1086/161924

Ragone-Figueroa, C., Granato, G. L., Murante, G., Borgani, S., & Cui, W. 2013, MNRAS, 436, 1750, doi: 10.1093/mnras/stt1693

Remus, R.-S., Dolag, K., & Hoffmann, T. 2017, Galaxies, 5, 49, doi: 10.3390/galaxies5030049

Rodriguez-Gomez, V., Pillepich, A., Sales, L. V., et al. 2016, MNRAS, 458, 2371, doi: 10.1093/mnras/stw456

Rudick, C. S., Mihos, J. C., Frey, L. H., & McBride, C. K. 2009, ApJ, 699, 1518, doi: 10.1088/0004-637X/699/2/1518

Rudick, C. S., Mihos, J. C., & McBride, C. 2006, ApJ, 648, 936, doi: 10.1086/506176

Rudick, C. S., Mihos, J. C., & McBride, C. K. 2011, ApJ, 732, 48, doi: 10.1088/0004-637X/732/1/48

Sastry, G. N. 1968, PASP, 80, 252, doi: 10.1086/128626

Schlafly, E. F., & Finkbeiner, D. P. 2011, ApJ, 737, 103, doi: 10.1088/0004-637X/737/2/103

Schneider, D. P., Gunn, J. E., & Hoessel, J. G. 1983, ApJ, 268, 476, doi: 10.1086/160973

Schombert, J. M. 1986, ApJS, 60, 603, doi: 10.1086/191100

Schweizer, F., & Seitzer, P. 1988, ApJ, 328, 88, doi: 10.1086/166270

Seigar, M. S., Graham, A. W., & Jerjen, H. 2007, MNRAS, 378, 1575, doi: 10.1111/j.1365-2966.2007.11899.x

Sérsic, J. L. 1968, Atlas de Galaxias Australes (Córdoba: Observatorio Astronomico, Univ. Córdoba)

Sharples, R. M., Zepf, S. E., Bridges, T. J., et al. 1998, AJ, 115, 2337, doi: 10.1086/300374

Shin, T.-h., Clampitt, J., Jain, B., et al. 2018, MNRAS, 475, 2421, doi: 10.1093/mnras/stx3366

Skibba, R. A., van den Bosch, F. C., Yang, X., et al. 2011, MNRAS, 410, 417, doi: 10.1111/j.1365-2966.2010.17452.x

Slater, C. T., Harding, P., & Mihos, J. C. 2009, PASP, 121, 1267, doi: 10.1086/648457

Spavone, M., Capaccioli, M., Napolitano, N., et al. 2017, Galaxies, 5, 31, doi: 10.3390/galaxies5030031

Spavone, M., Iodice, E., Capaccioli, M., et al. 2018, ApJ, 864, 149, doi: 10.3847/1538-4357/aad6e9

Spiniello, C., Napolitano, N. R., Arnaboldi, M., et al. 2018, MNRAS, 477, 1880, doi: 10.1093/mnras/sty663

Struble, M. F. 1990, AJ, 99, 743, doi: 10.1086/115370

Tal, T., van Dokkum, P. G., Nelan, J., & Bezanson, R. 2009, AJ, 138, 1417, doi: 10.1088/0004-6256/138/5/1417

Thuan, T. X., & Kormendy, J. 1977, PASP, 89, 466, doi: 10.1086/130146

Tojeiro, R., Masters, K. L., Richards, J., et al. 2013, MNRAS, 432, 359, doi: 10.1093/mnras/stt484

Toledo, I., Melnick, J., Selman, F., et al. 2011, MNRAS, 414, 602, doi: 10.1111/j.1365-2966.2011.18423.x

Tonry, J. L. 1985a, ApJ, 291, 45, doi: 10.1086/163039

—. 1985b, AJ, 90, 2431, doi: 10.1086/113948

Tonry, J. L., Stubbs, C. W., Lykke, K. R., et al. 2012, ApJ, 750, 99, doi: 10.1088/0004-637X/750/2/99

Trentham, N., & Mobasher, B. 1998, MNRAS, 293, 53, doi: 10.1046/j.1365-8711.1998.01114.x

Trujillo, I., & Fliri, J. 2016, ApJ, 823, 123, doi: 10.3847/0004-637X/823/2/123

Tully, R. B. 2015, AJ, 149, 54, doi: 10.1088/0004-6256/149/2/54

Umetsu, K., Medezinski, E., Nonino, M., et al. 2014, ApJ, 795, 163, doi: 10.1088/0004-637X/795/2/163

van der Marel, R. P., & Franx, M. 1993, ApJ, 407, 525, doi: 10.1086/172534

Veale, M., Ma, C.-P., Thomas, J., et al. 2017, MNRAS, 464, 356, doi: 10.1093/mnras/stw2330

Ventimiglia, G., Gerhard, O., Arnaboldi, M., & Coccato, L. 2010, A&A, 520, L9, doi: 10.1051/0004-6361/201015485

Von Der Linden, A., Best, P. N., Kauffmann, G., & White, S. D. M. 2007, MNRAS, 379, 867, doi: 10.1111/j.1365-2966.2007.11940.x

Watkins, A. E., Mihos, J. C., & Harding, P. 2015, ApJL, 800, L3, doi: 10.1088/2041-8205/800/1/L3

Watkins, A. E., Mihos, J. C., Harding, P., & Feldmeier, J. J. 2014, ApJ, 791, 38, doi: 10.1088/0004-637X/791/1/38

Welch, G. A., & Sastry, G. N. 1971, ApJL, 169, L3, doi: 10.1086/180801

West, M. J., de Propris, R., Bremer, M. N., & Phillipps, S. 2017, Nature Astronomy, 1, 0157, doi: 10.1038/s41550-017-0157

Willmer, C. N. A. 2018, ApJS, 236, 47, doi: 10.3847/1538-4365/aabfdf

Wright, E. L. 2006, PASP, 118, 1711, doi: 10.1086/510102

Yang, X., Mo, H. J., van den Bosch, F. C., et al. 2005, MNRAS, 362, 711, doi: 10.1111/j.1365-2966.2005.09351.x

Yang, X., van den Bosch, F. C., Mo, H. J., et al. 2006, MNRAS, 369, 1293, doi: 10.1111/j.1365-2966.2006.10373.x

Zhang, Y., Yanny, B., Palmese, A., et al. 2019, ApJ, 874, 165, doi: 10.3847/1538-4357/ab0dfd

Zheng, Z., Coil, A. L., & Zehavi, I. 2007, ApJ, 667, 760, doi: 10.1086/521074

Zibetti, S., White, S. D. M., Schneider, D. P., & Brinkmann, J. 2005, MNRAS, 358, 949, doi: 10.1111/j.1365-2966.2005.08817.x

Zitrin, A., Bartelmann, M., Umetsu, K., Oguri, M., & Broadhurst, T. 2012, MNRAS, 426, 2944, doi: 10.1111/j.1365-2966.2012.21886.x

Zwicky, F. 1951, PASP, 63, 61, doi: 10.1086/126318

Appendix A

Surface brightness profiles and Sérsic fits

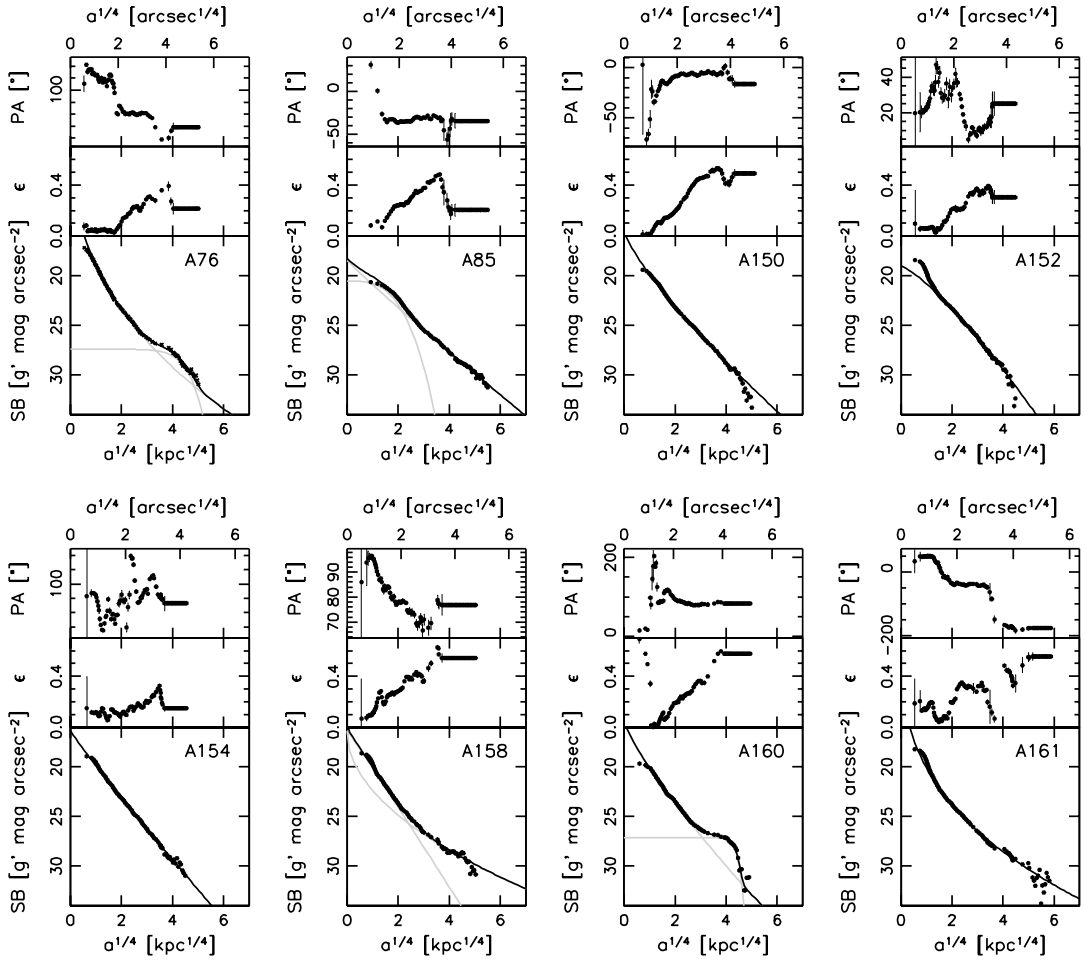

Figure A.1: The SB profiles are corrected for PSF broadening. No K-correction and no corrections for dust extinction and cosmic dimming are applied. If the SB profiles were fitted by a double Sérsic function, then the light gray lines show the contributions of each component. Ellipticity and position angle profiles are presented in the middle and top panels, respectively.

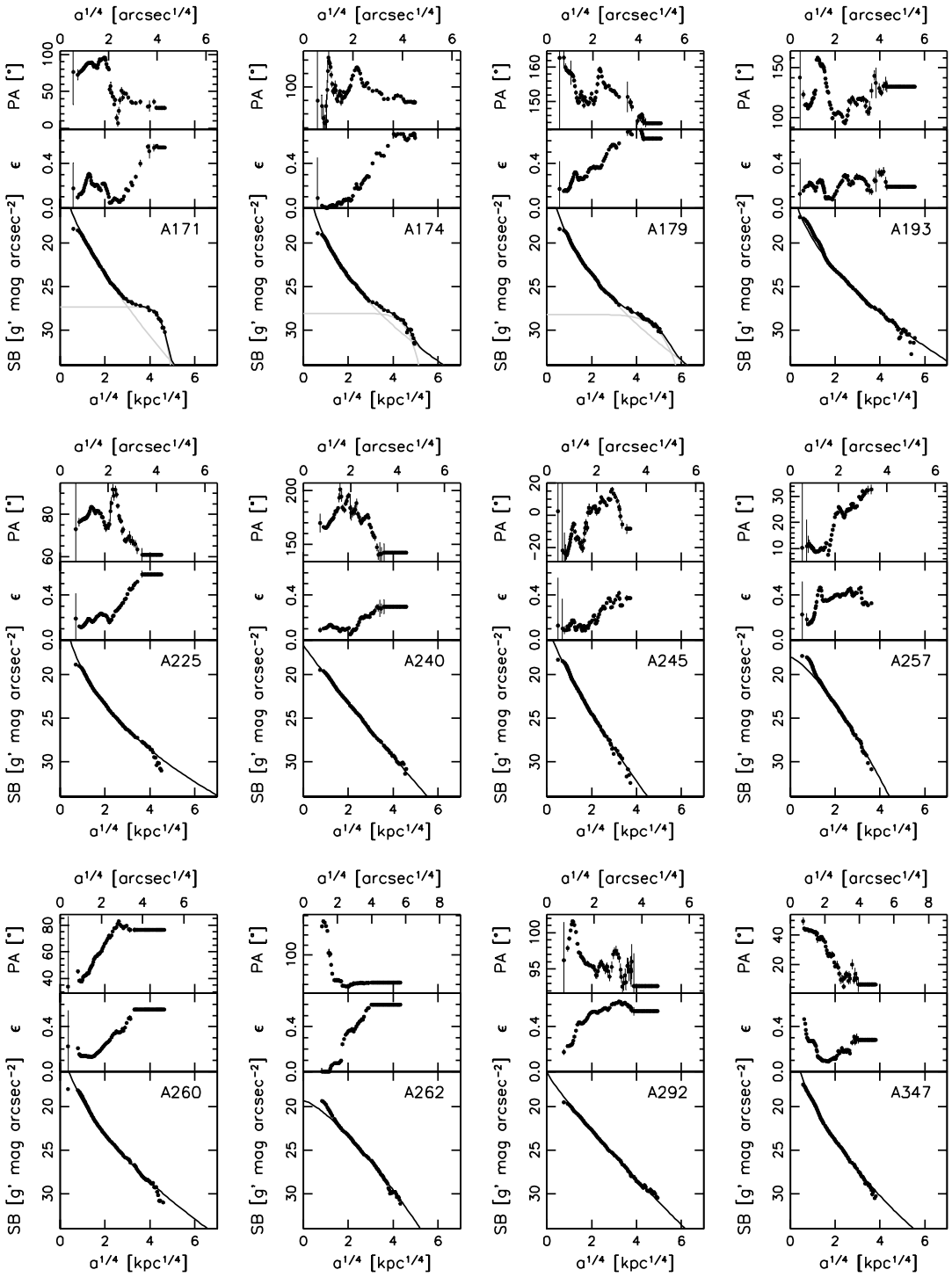

Figure A.1 *(continued)*

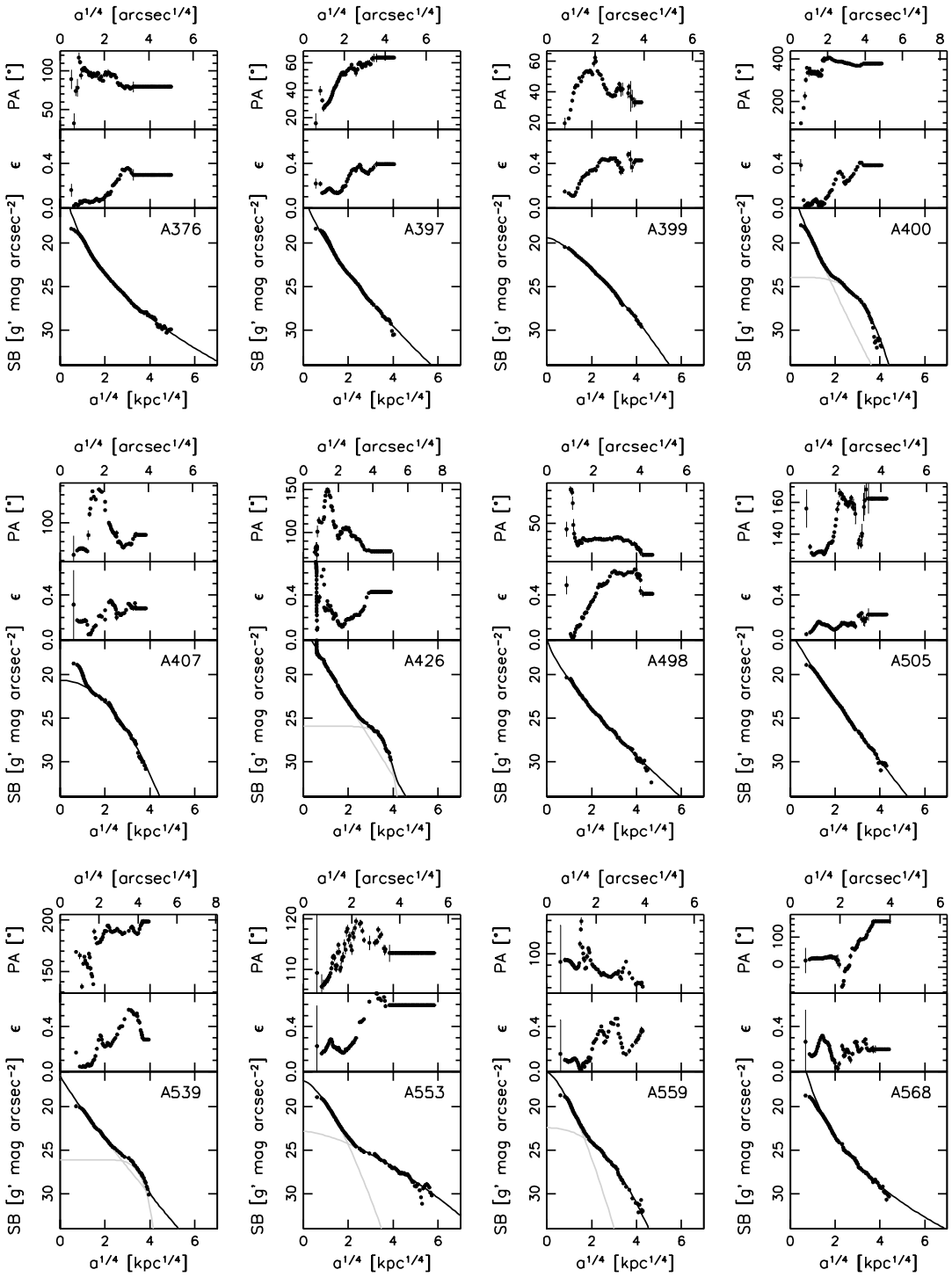

Figure A.1 *(continued)*

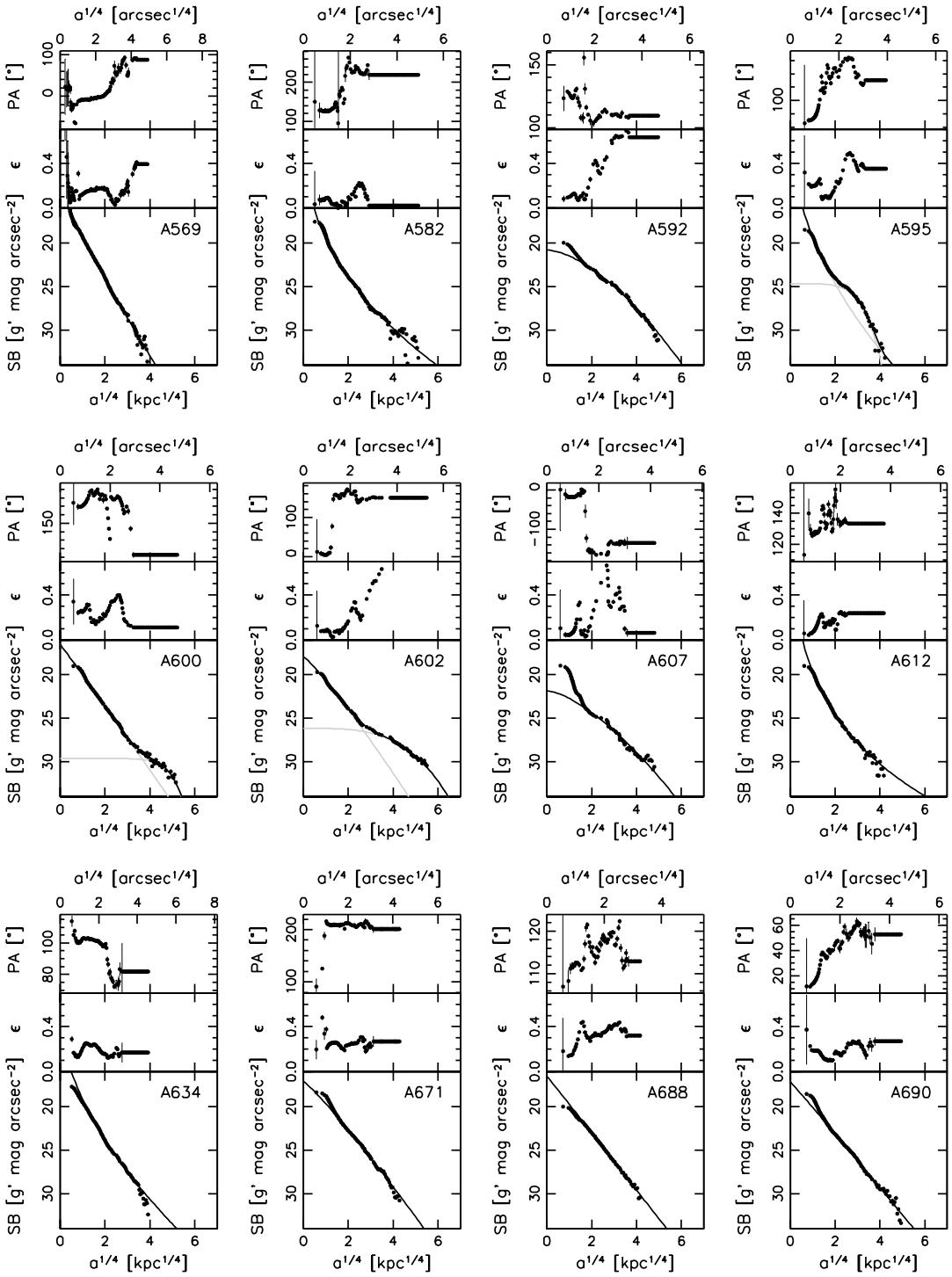

Figure A.1 *(continued)*

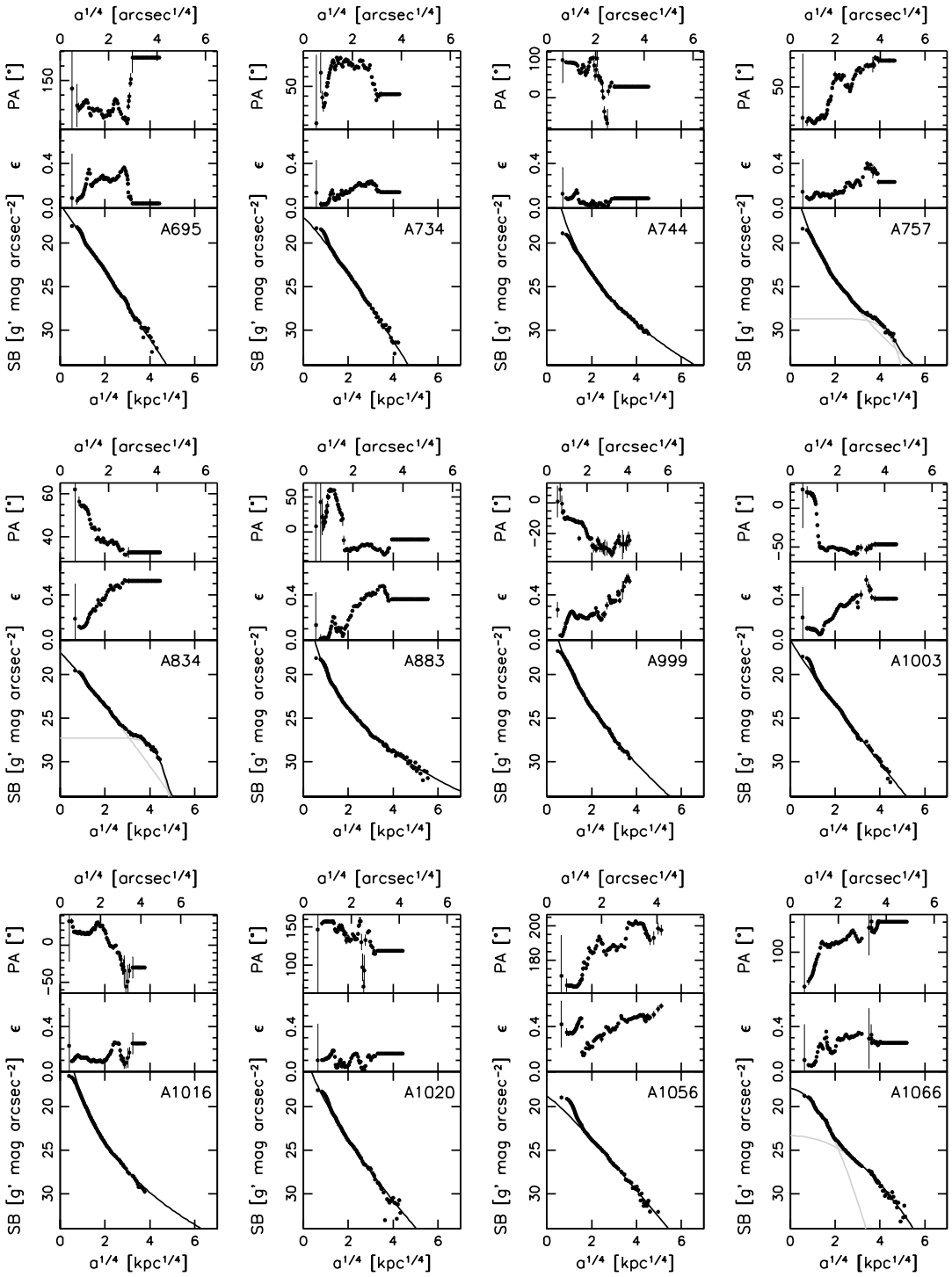

Figure A.1 *(continued)*

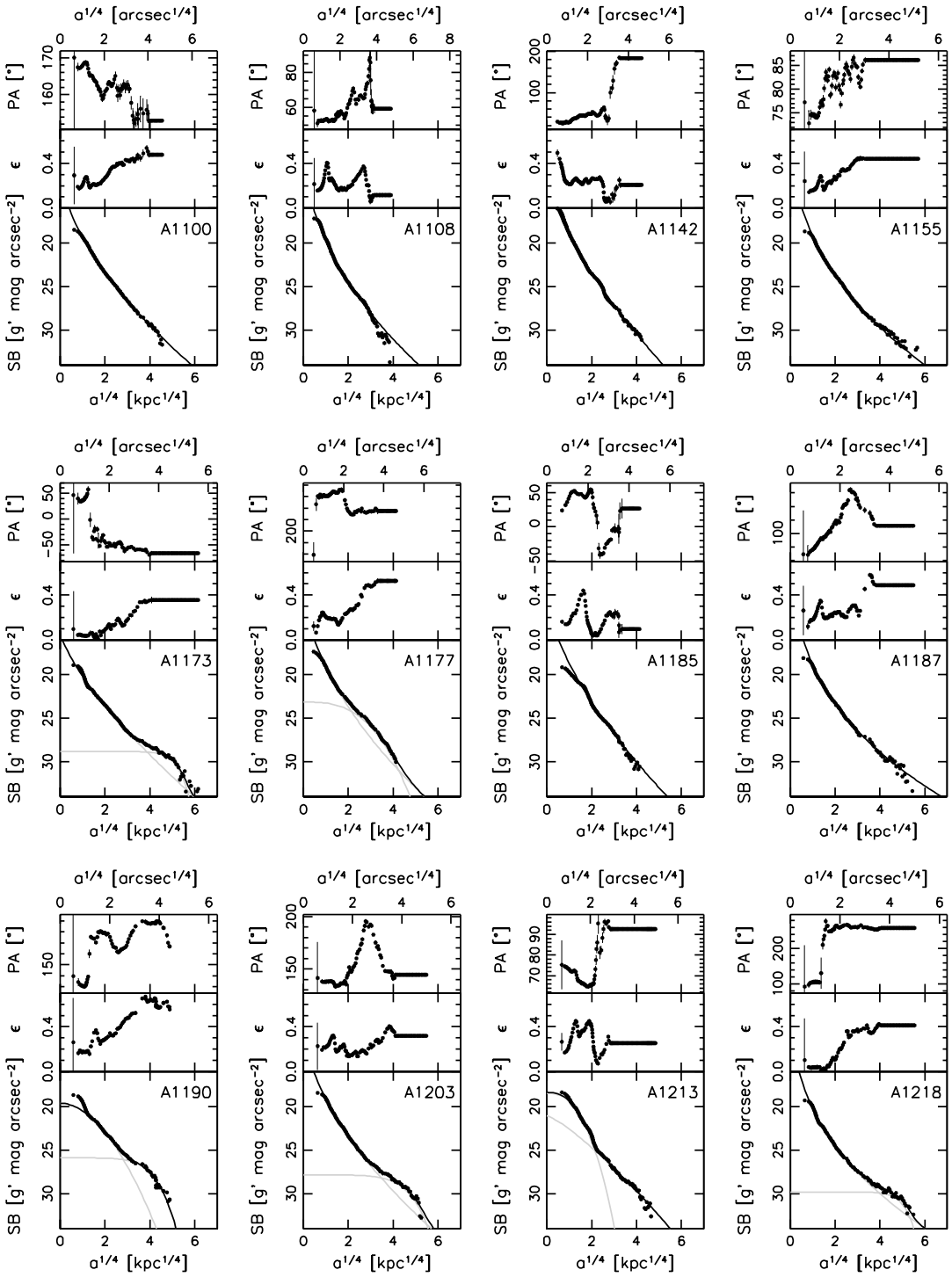

Figure A.1 *(continued)*

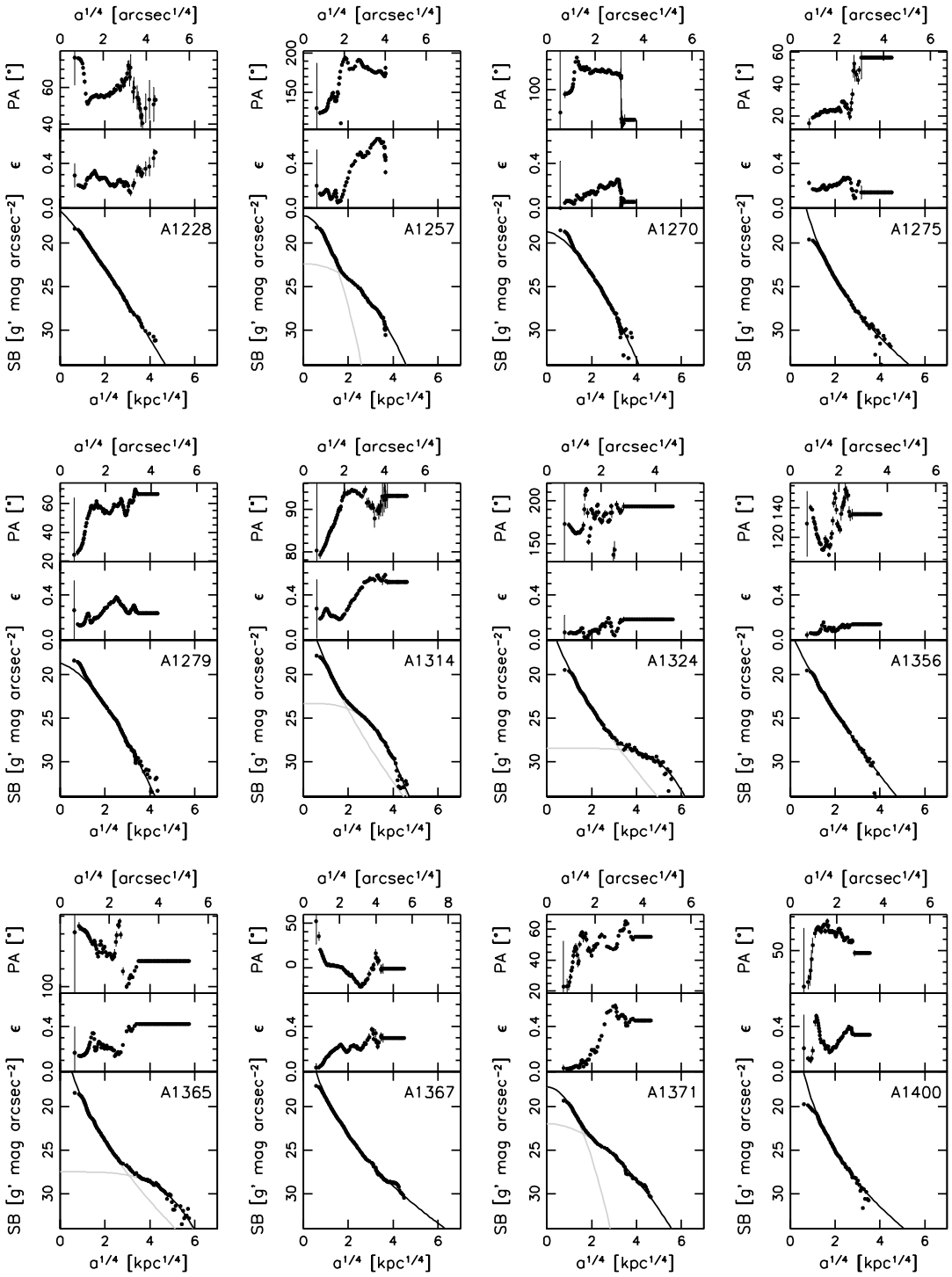

Figure A.1 *(continued)*

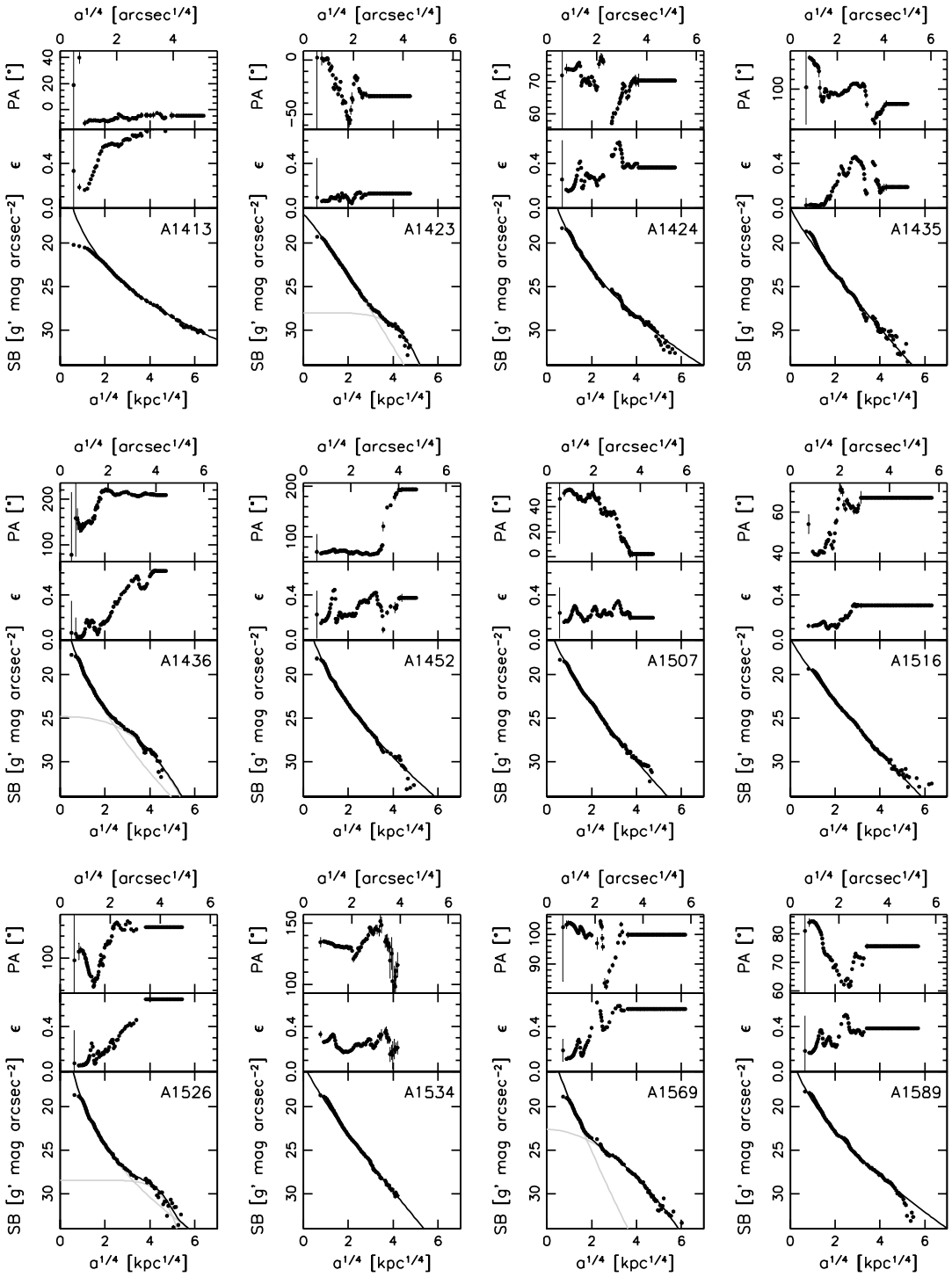

Figure A.1 *(continued)*

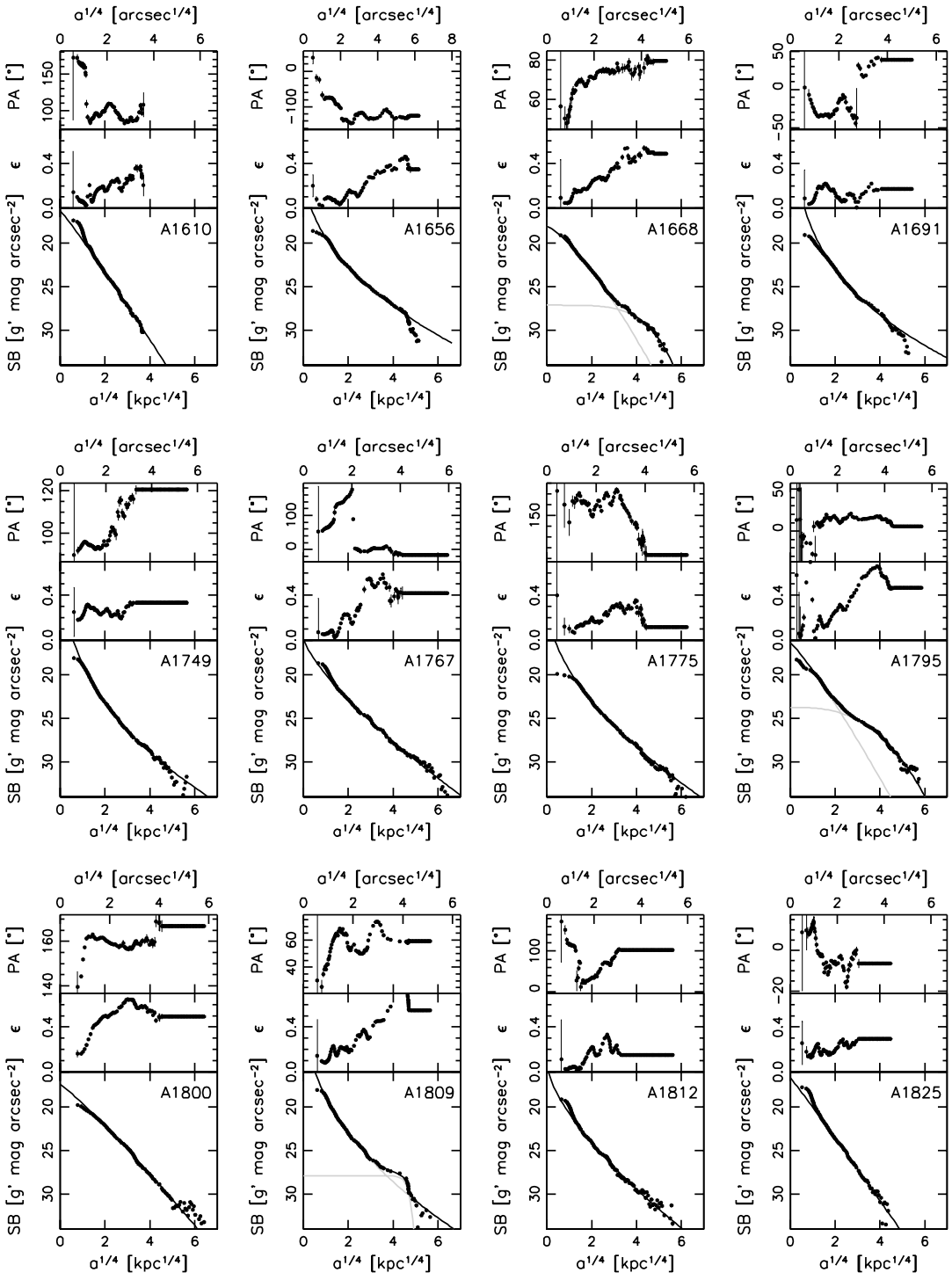

Figure A.1 *(continued)*

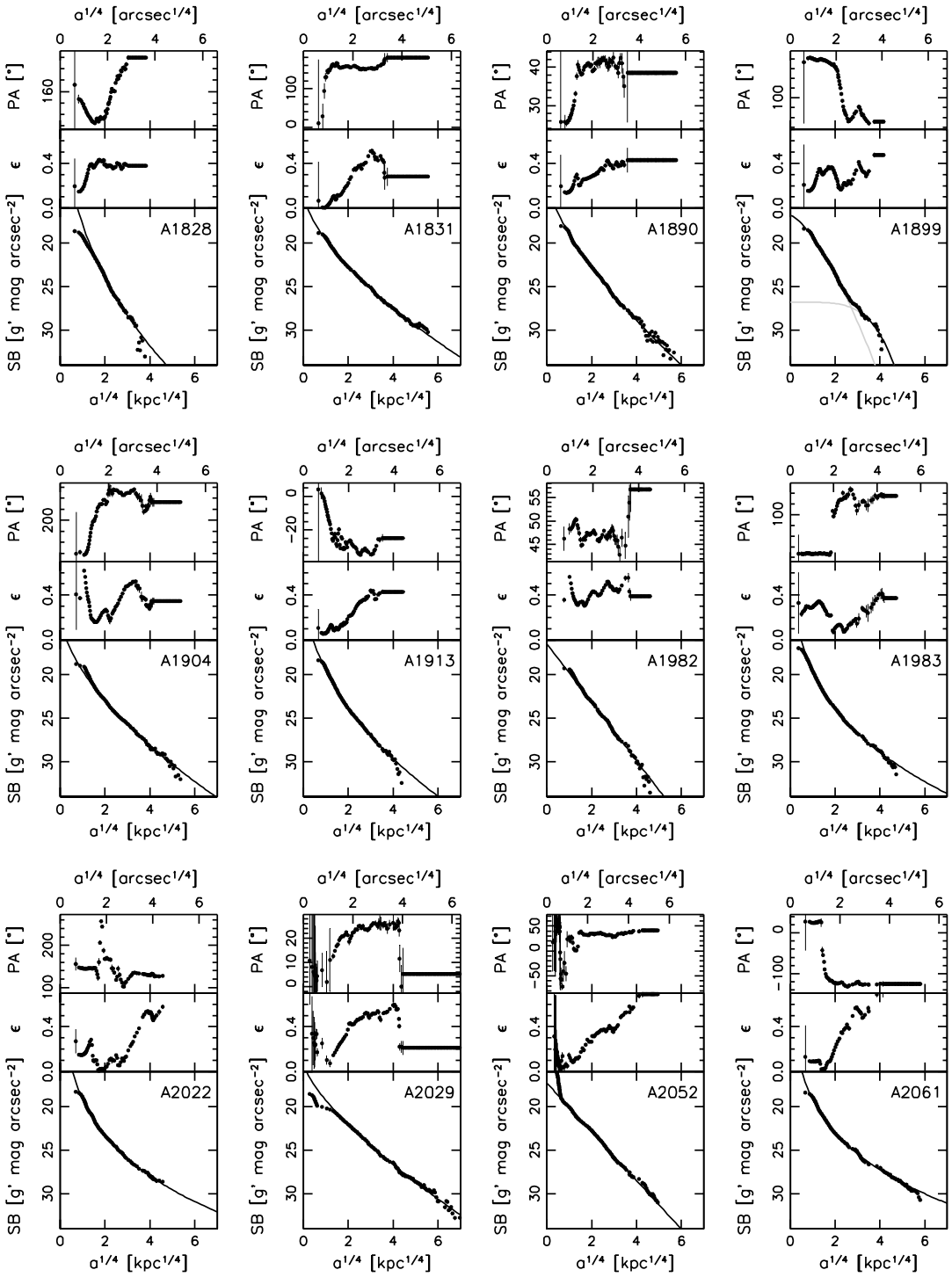

Figure A.1 *(continued)*

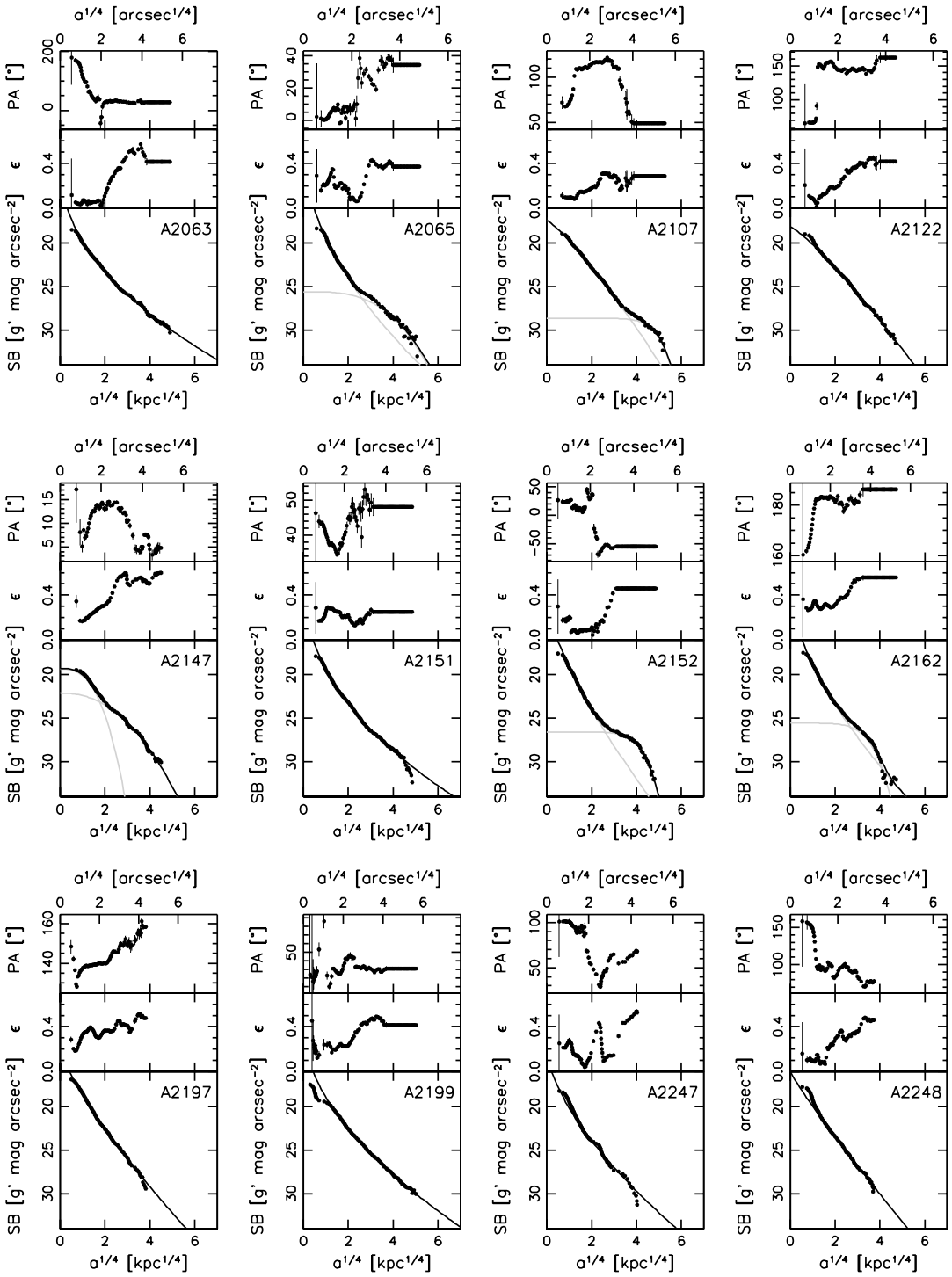

Figure A.1 *(continued)*

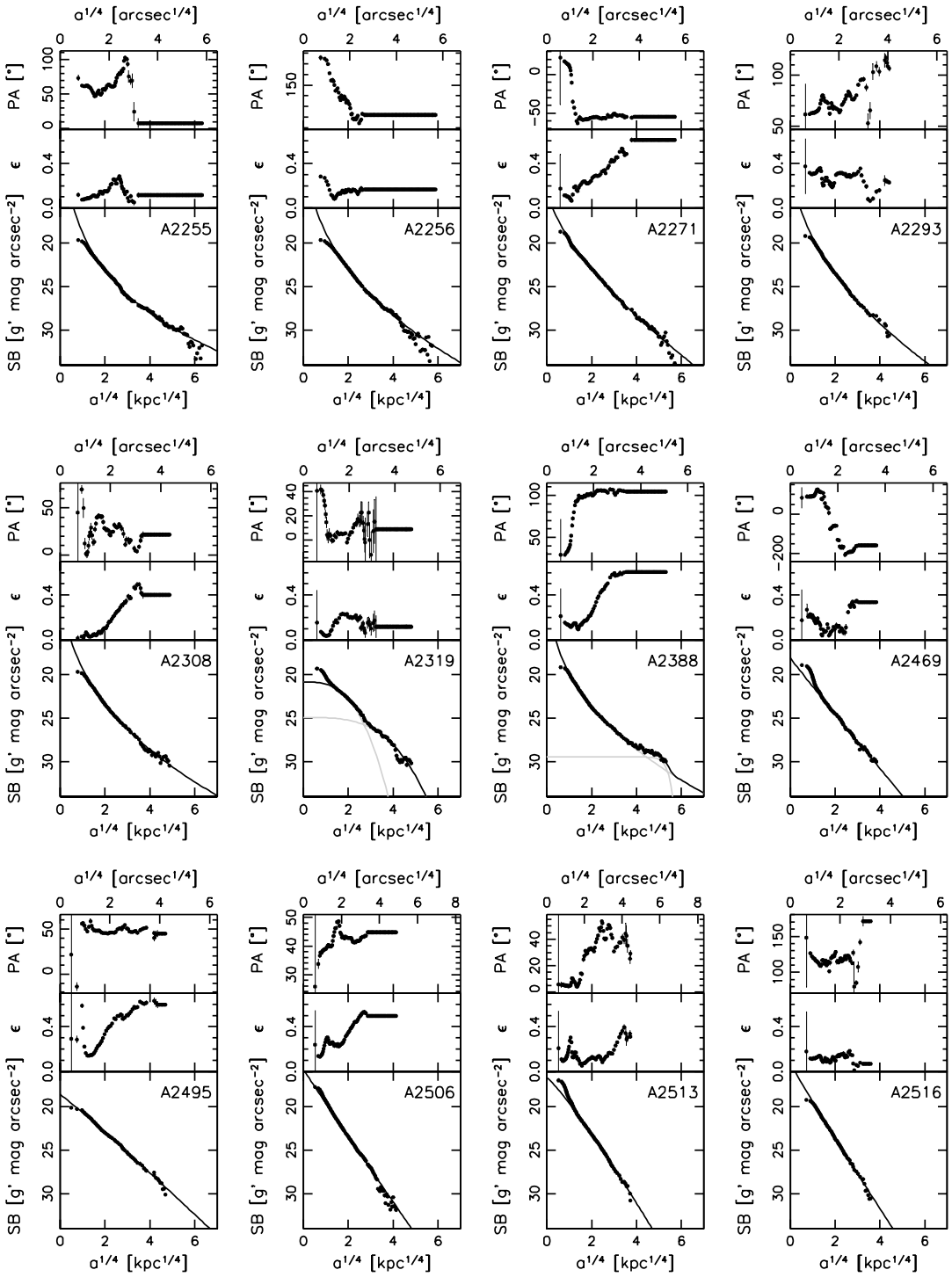

Figure A.1 *(continued)*

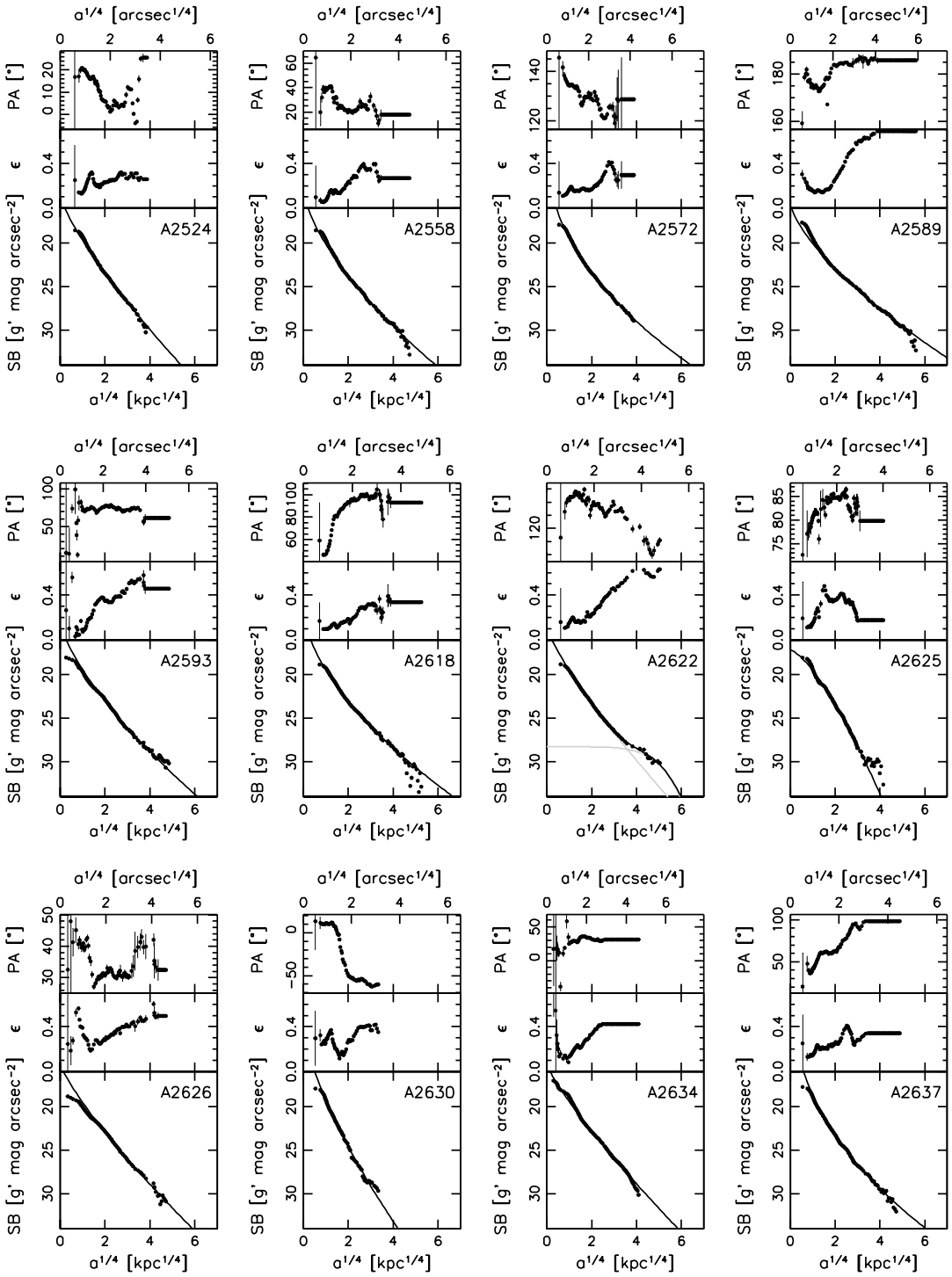

Figure A.1 *(continued)*

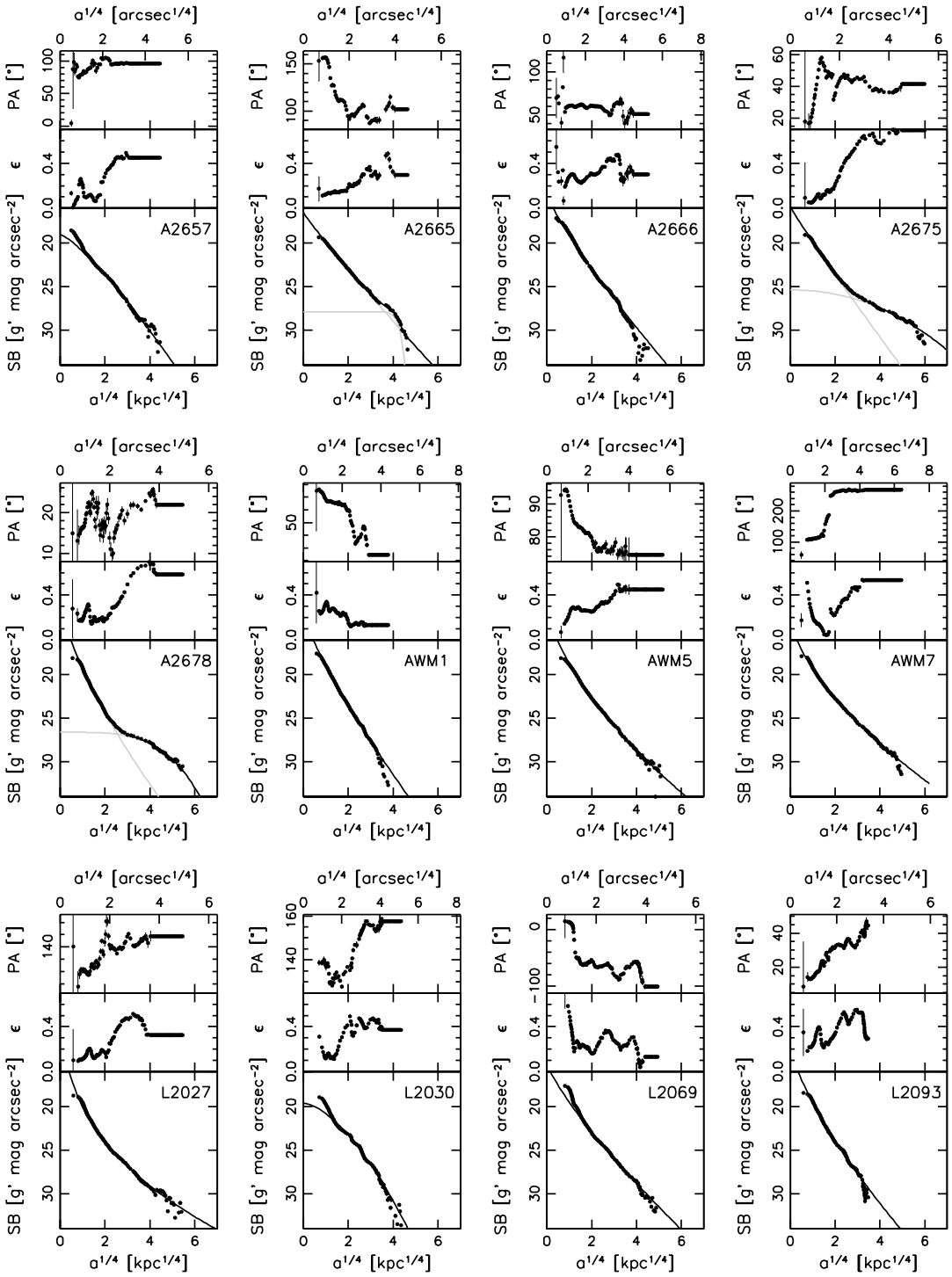

Figure A.1 *(continued)*

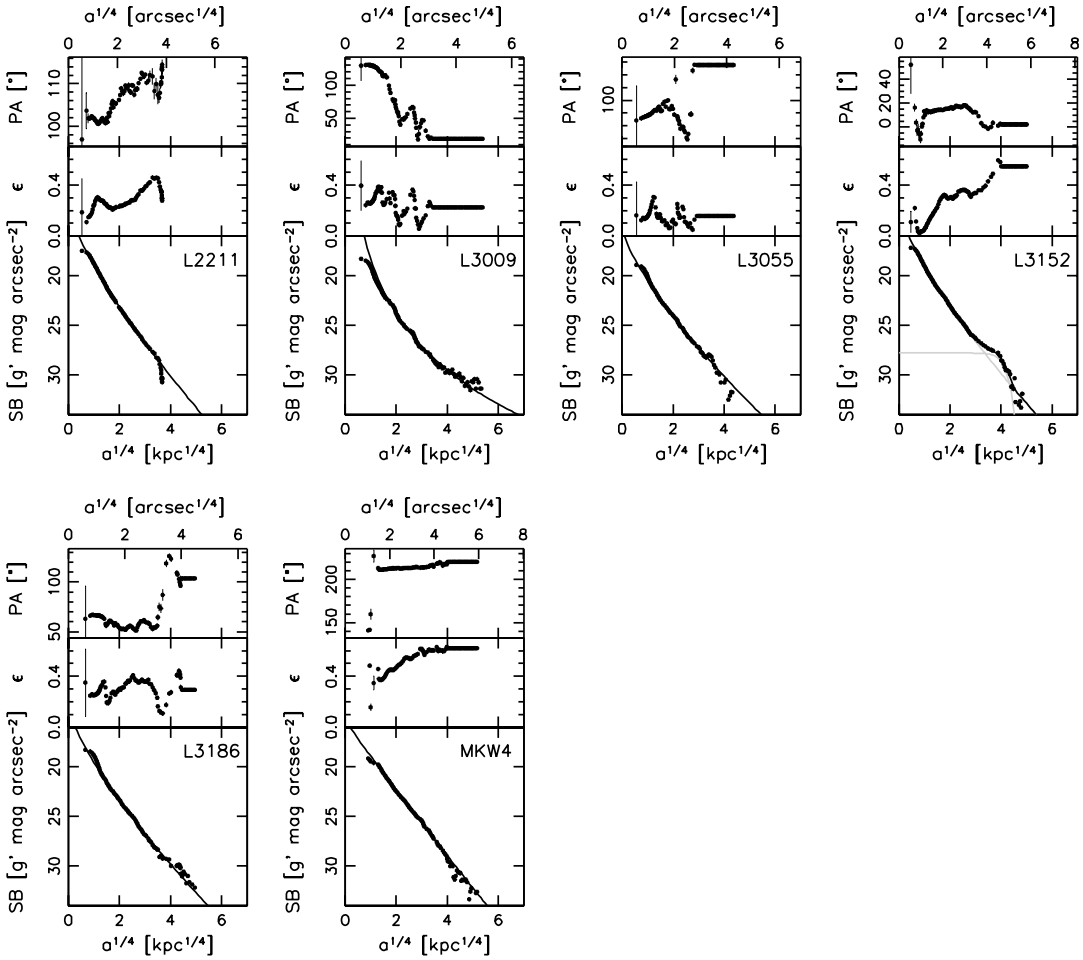

Figure A.1 *(continued)*

Appendix B

Image cutouts, centered on the BCGs

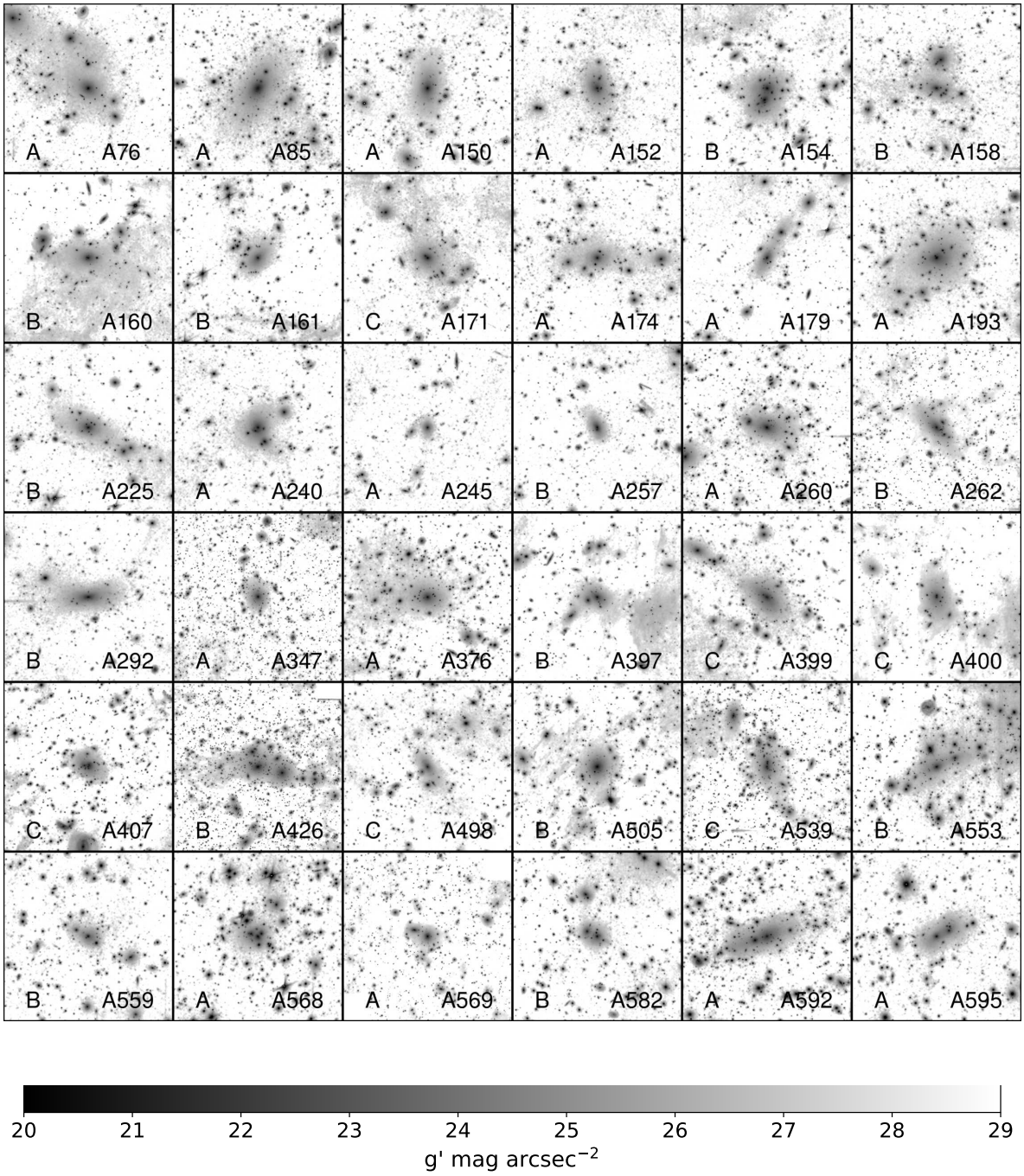

Figure B.1: Image cutouts, centered on all BCGs that are analyzed in this study. The side length of each box is 750 kpc. North is up and east is left.

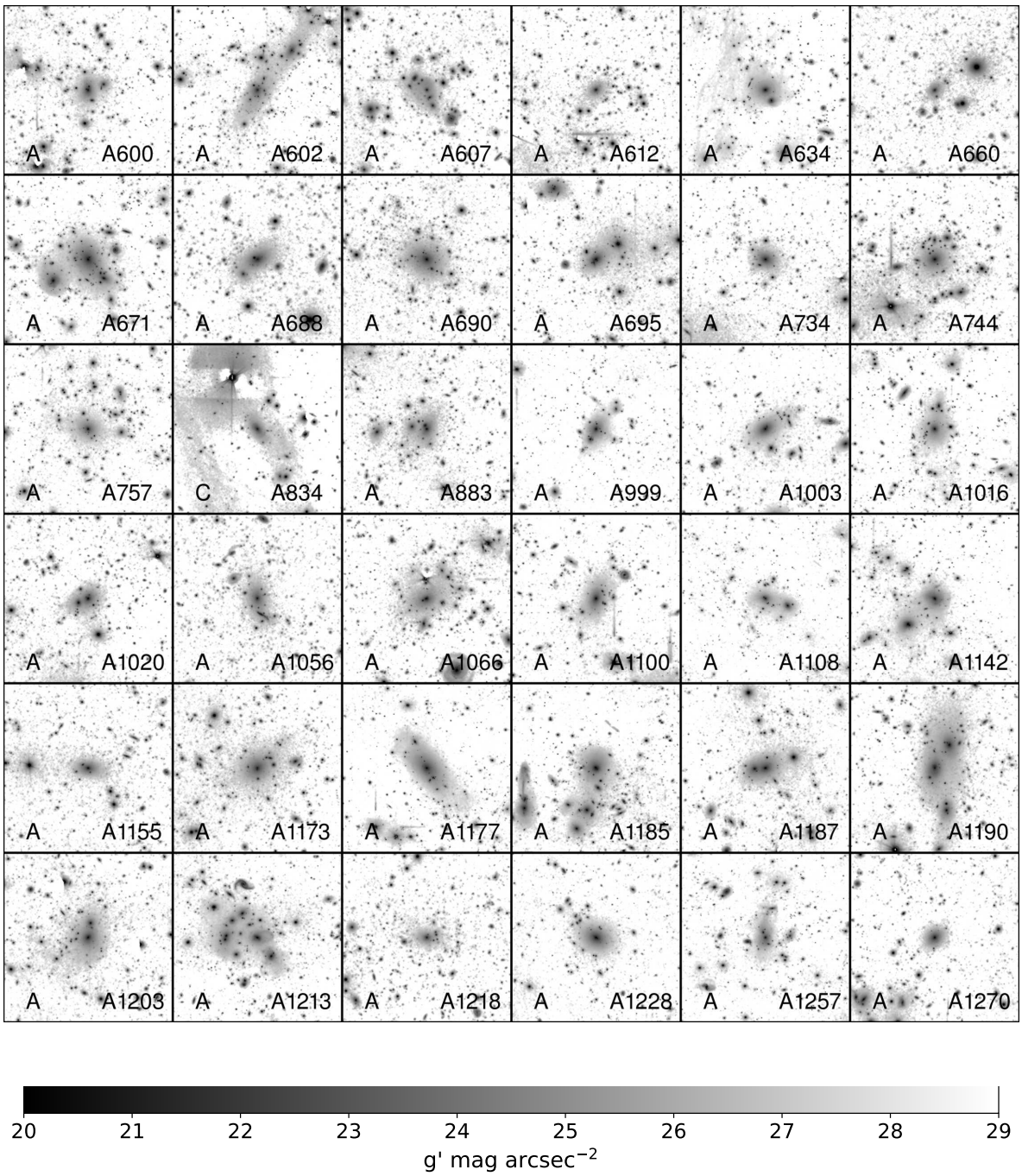

Figure B.1 *(continued)*

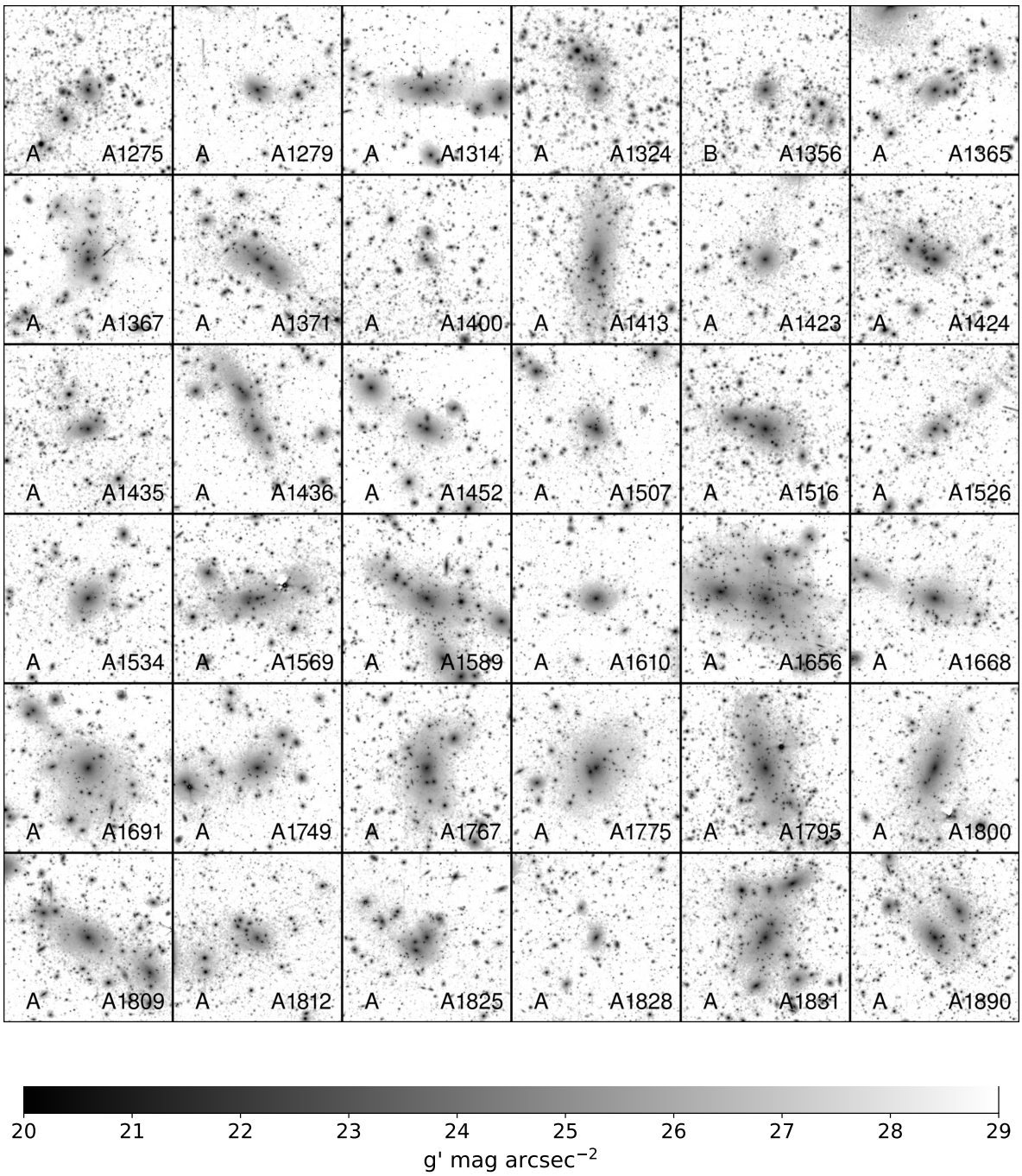

Figure B.1 *(continued)*

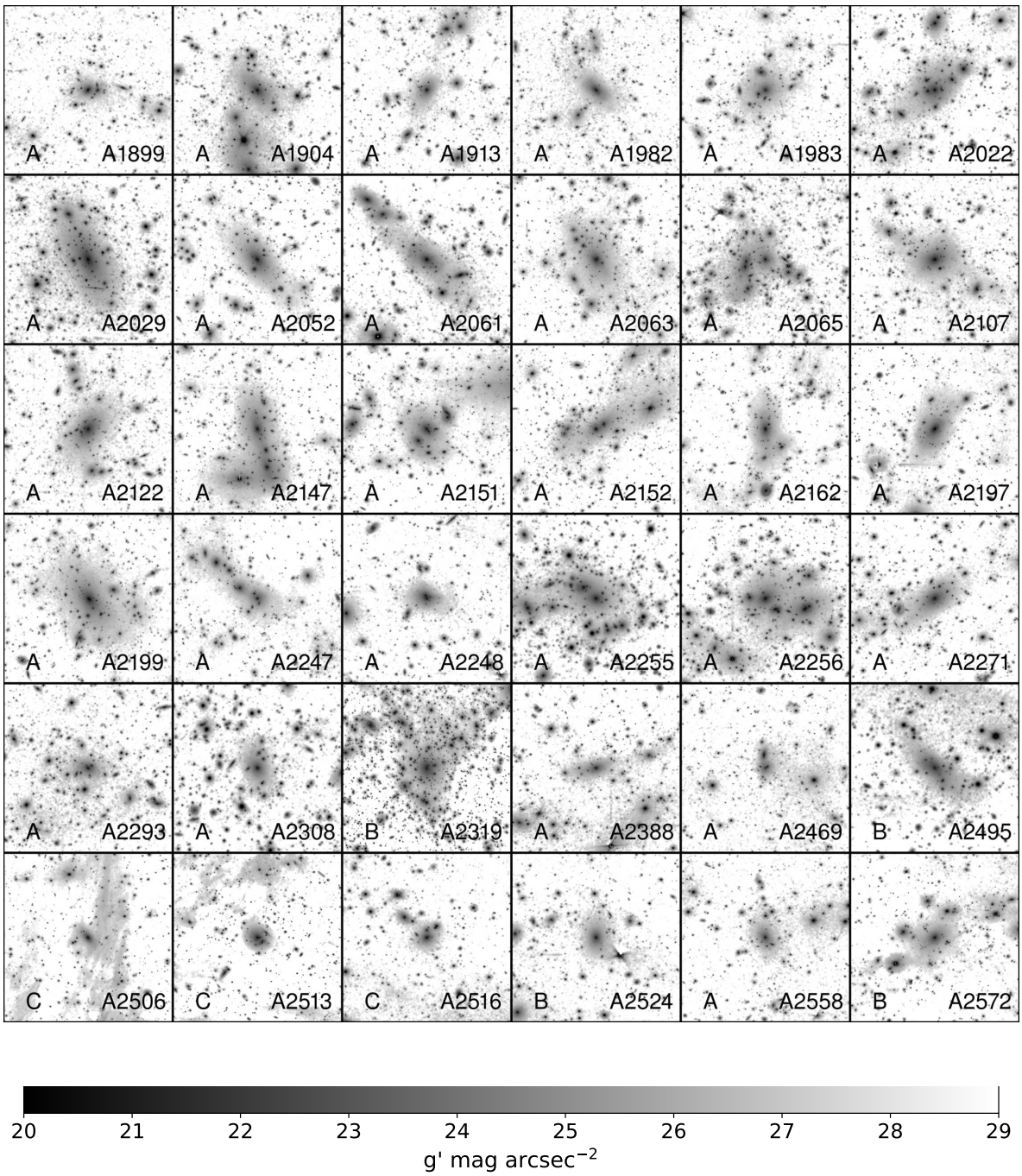

Figure B.1 *(continued)*

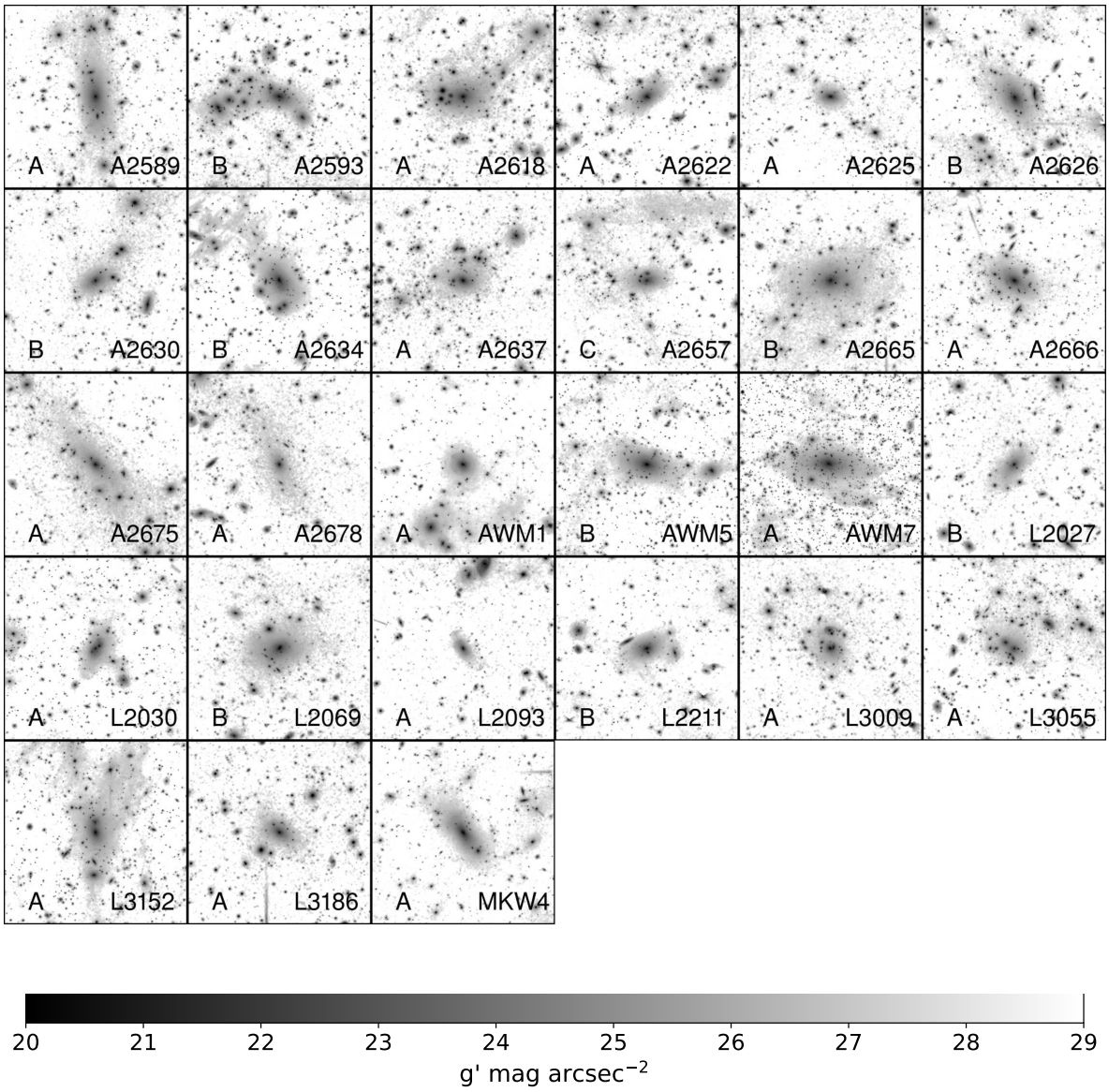

Figure B.1 *(continued)*

Appendix C

Full-sized images of the clusters

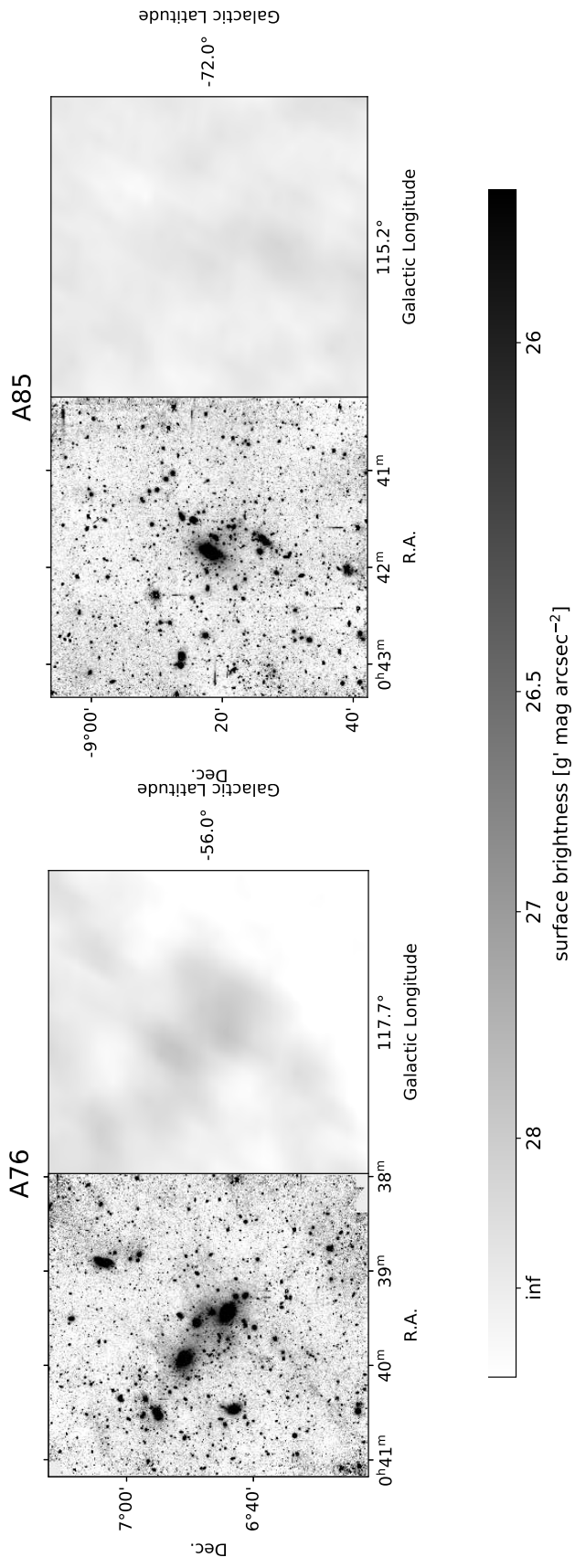

Figure C.1: Full-sized images of the observed galaxy clusters. The left panel of the subfigures is the WWFI g'-band stack and the right panel is the far-infrared 857 GHz Planck image of the same sky region. It is flux scaled using Eq. 5.1 and the median value is subtracted. Galactic coordinates are given for the image center.

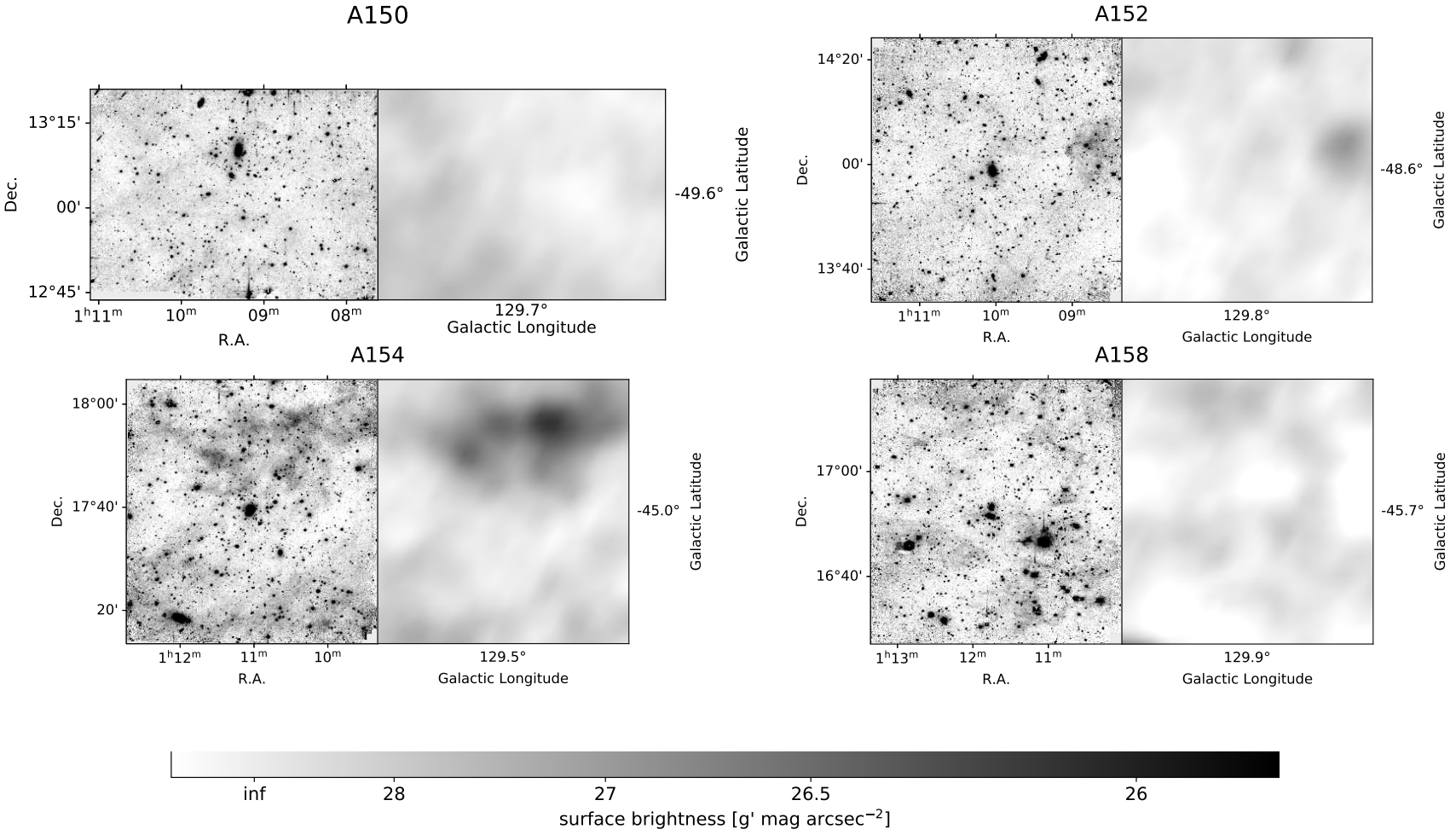

Figure C.1 *(continued)*

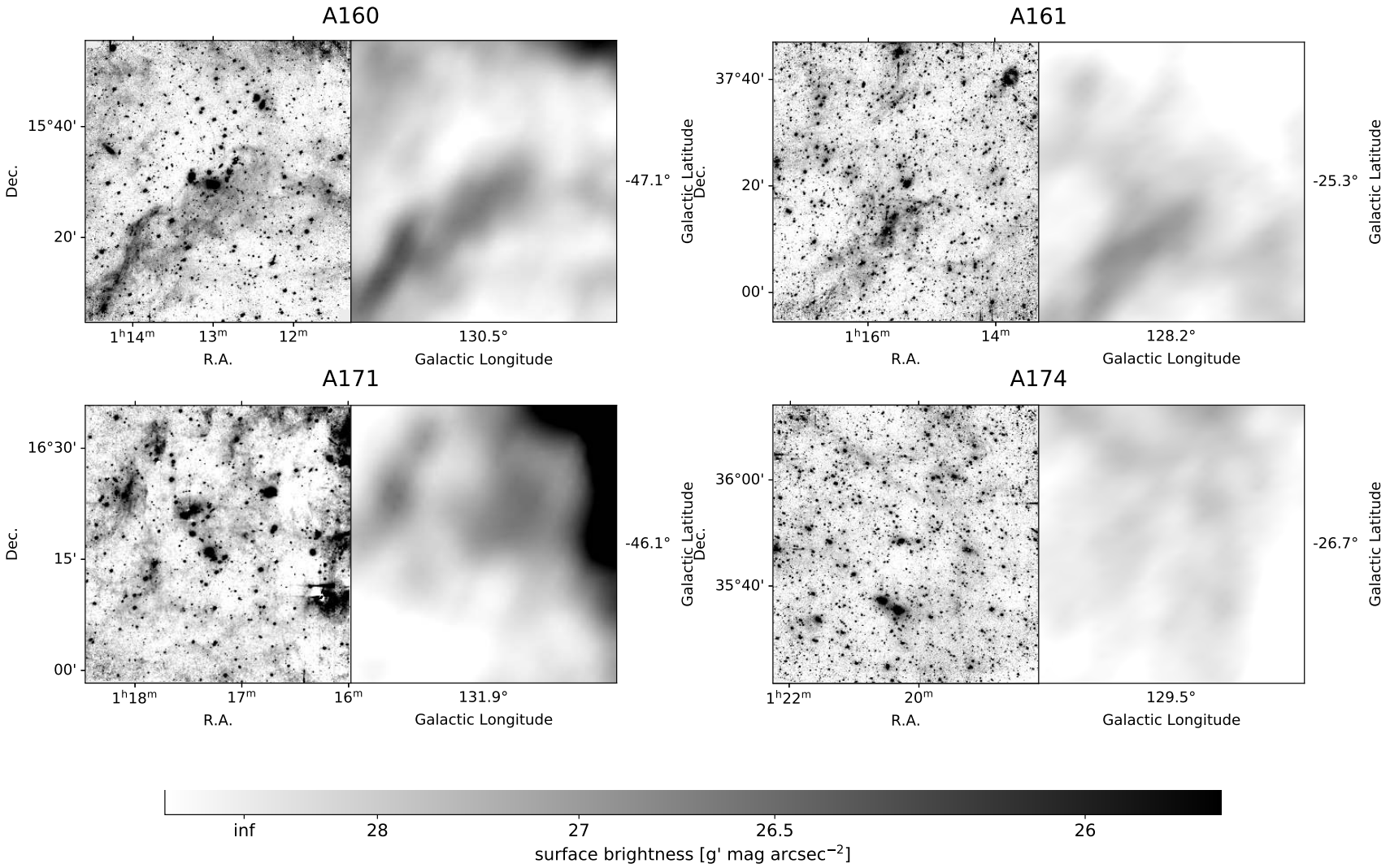

Figure C.1 *(continued)*

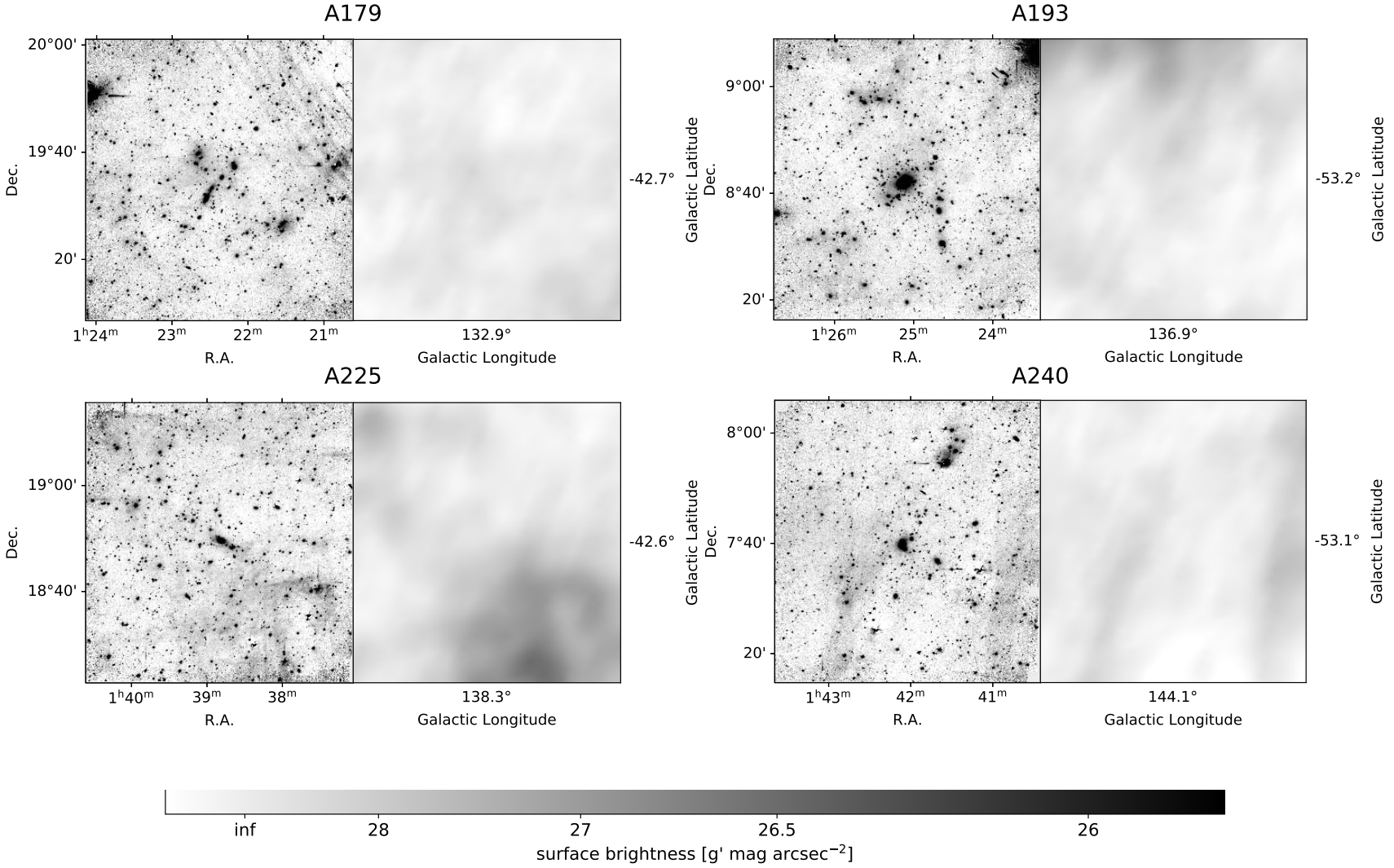

Figure C.1 *(continued)*

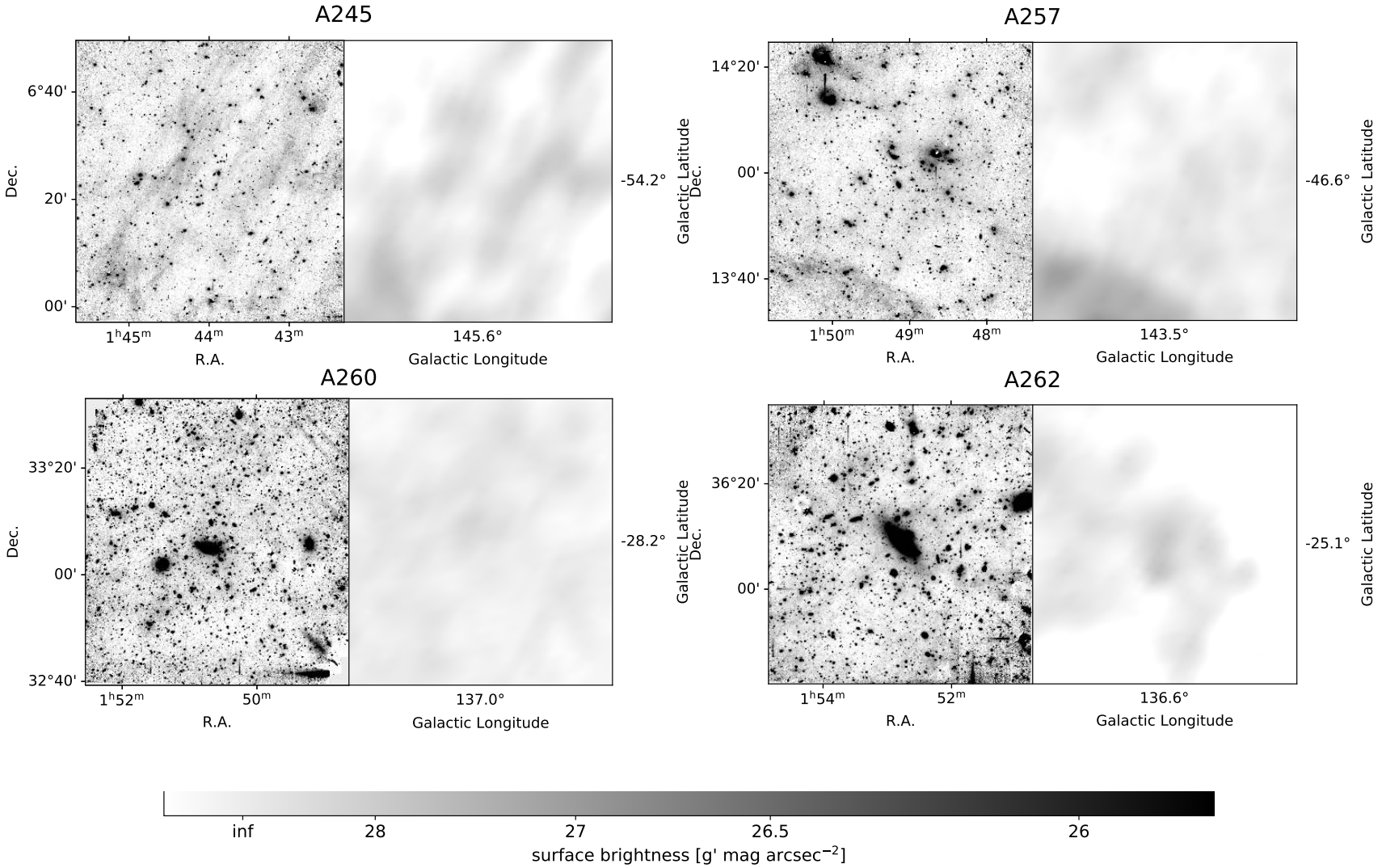

Figure C.1 *(continued)*

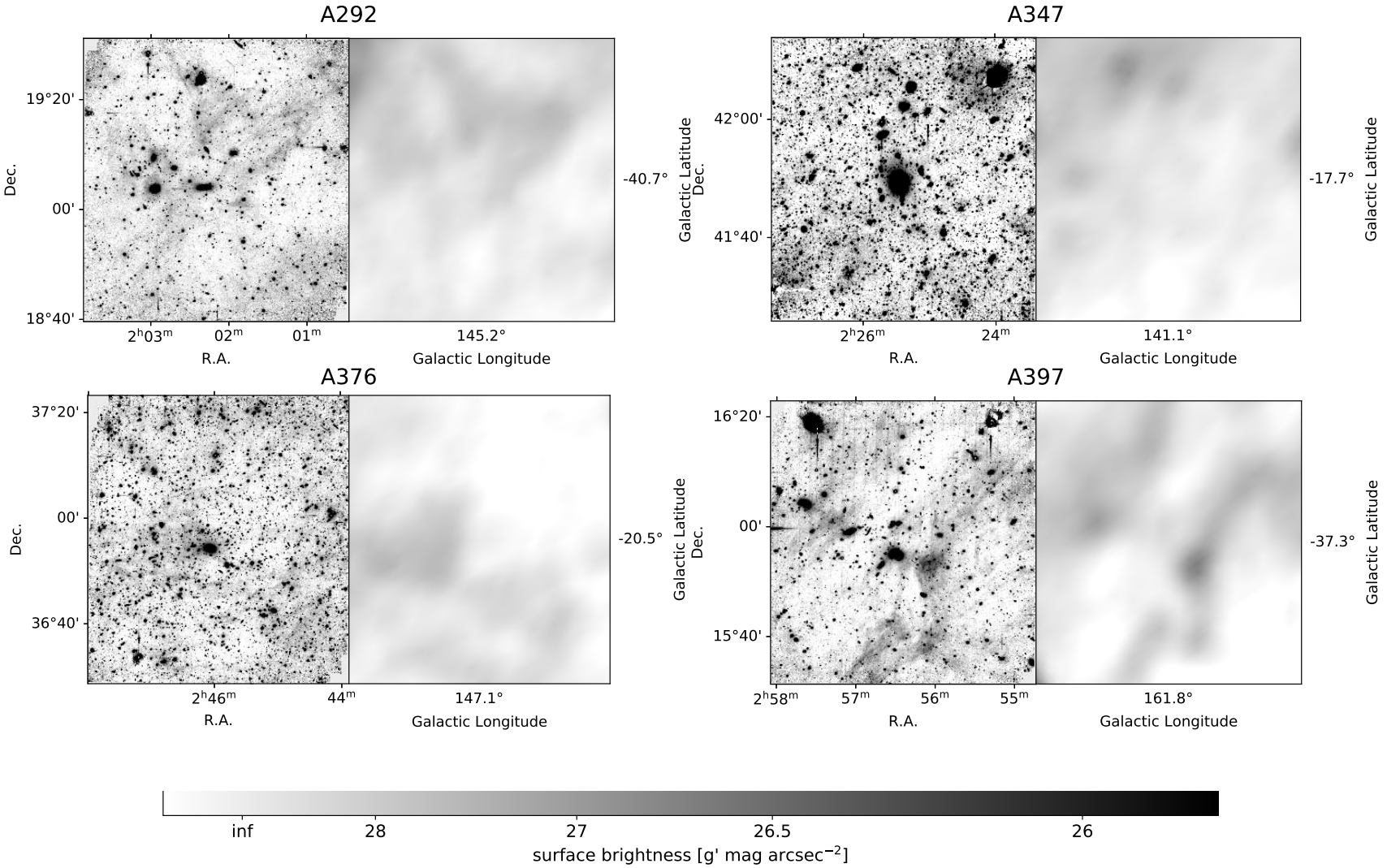

Figure C.1 *(continued)*

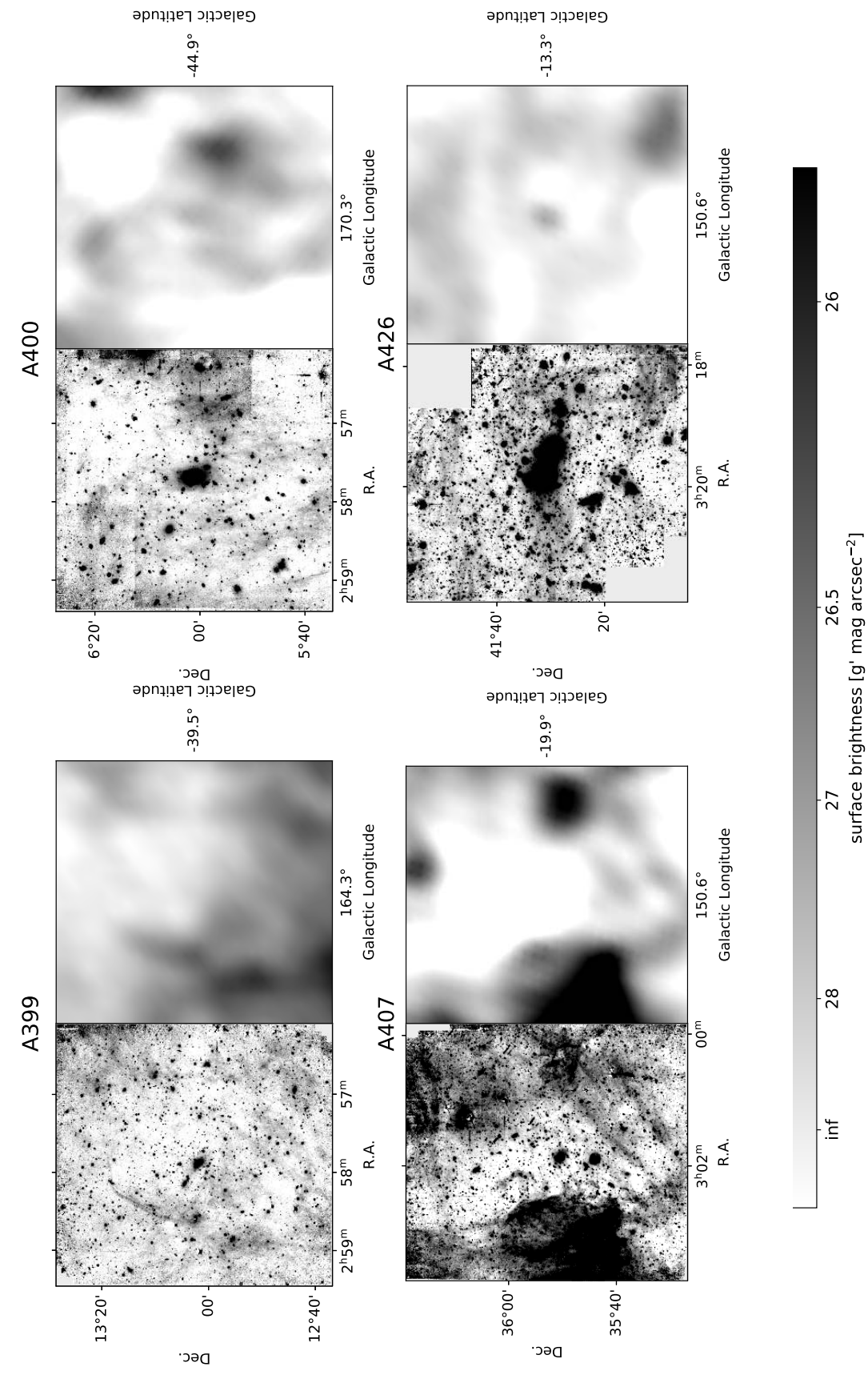

Figure C.1 *(continued)*

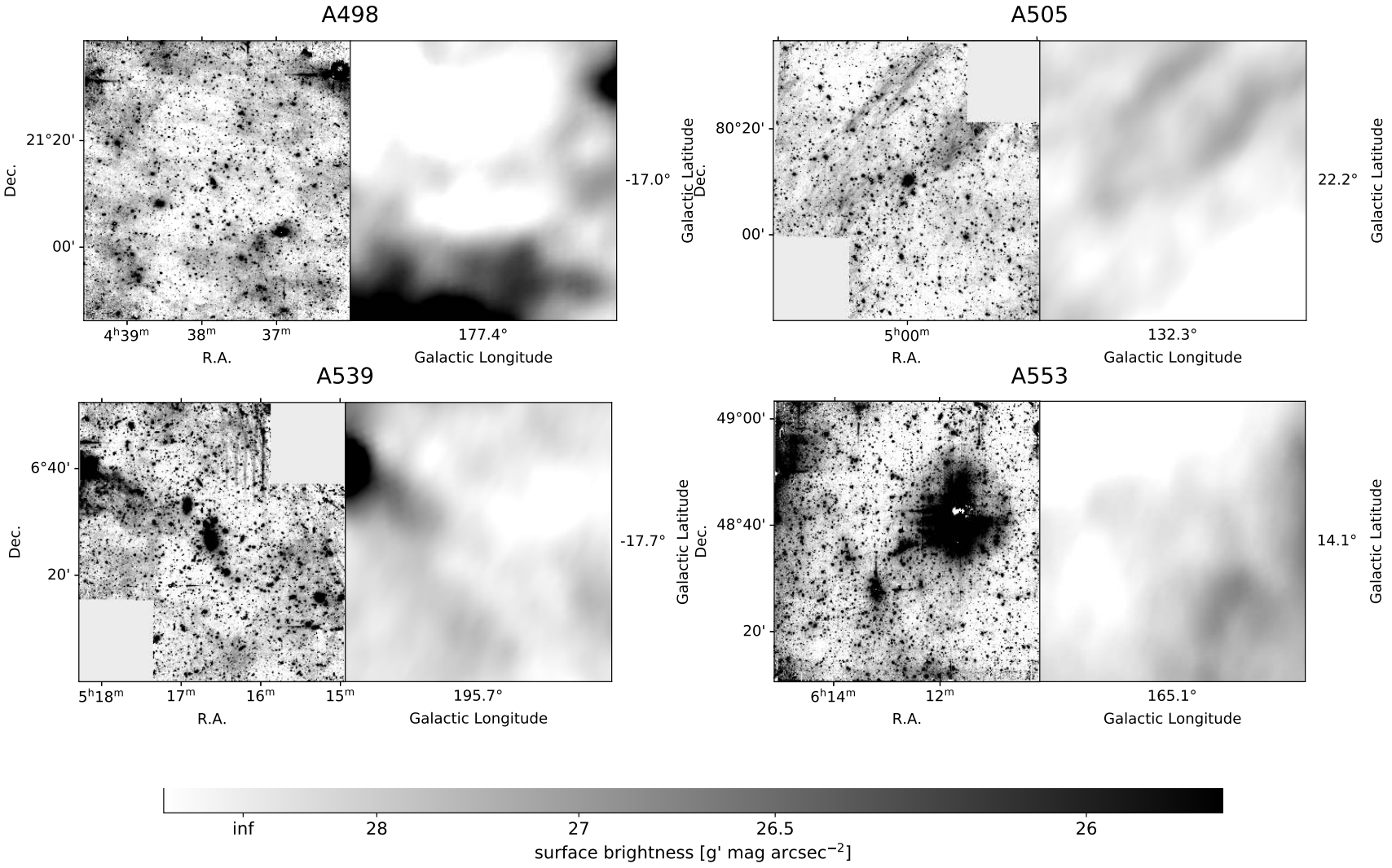

Figure C.1 *(continued)*

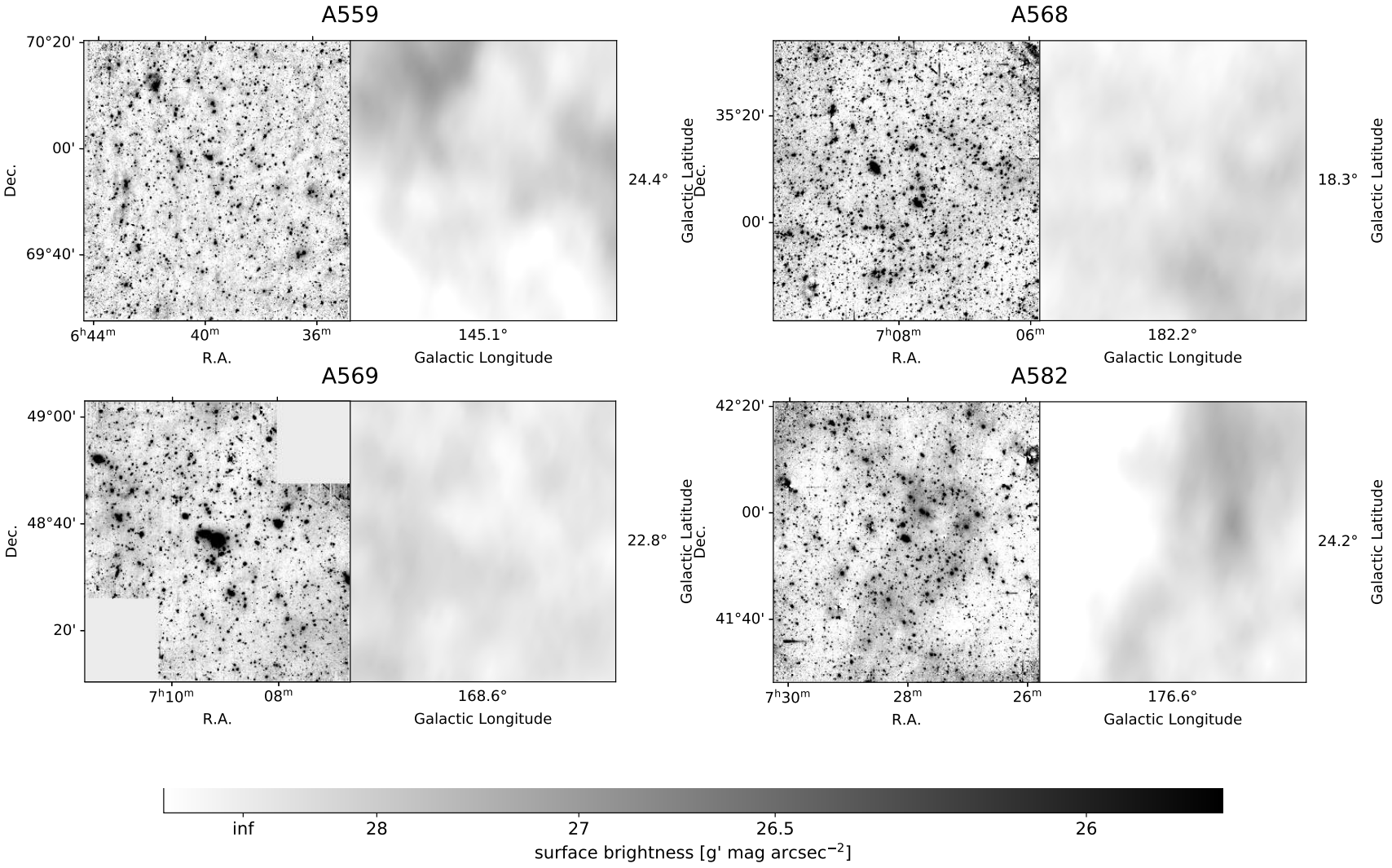

Figure C.1 *(continued)*

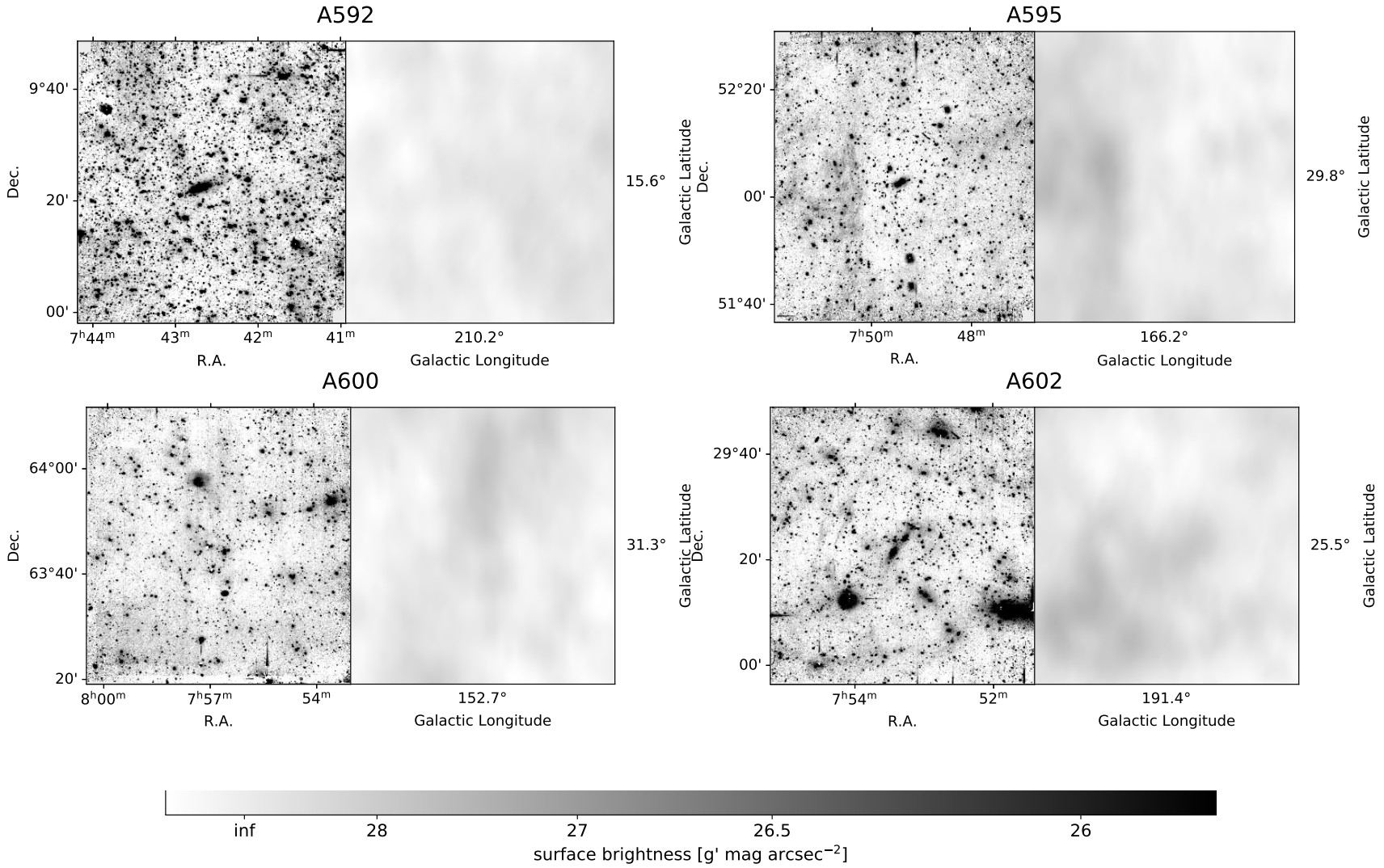

Figure C.1 *(continued)*

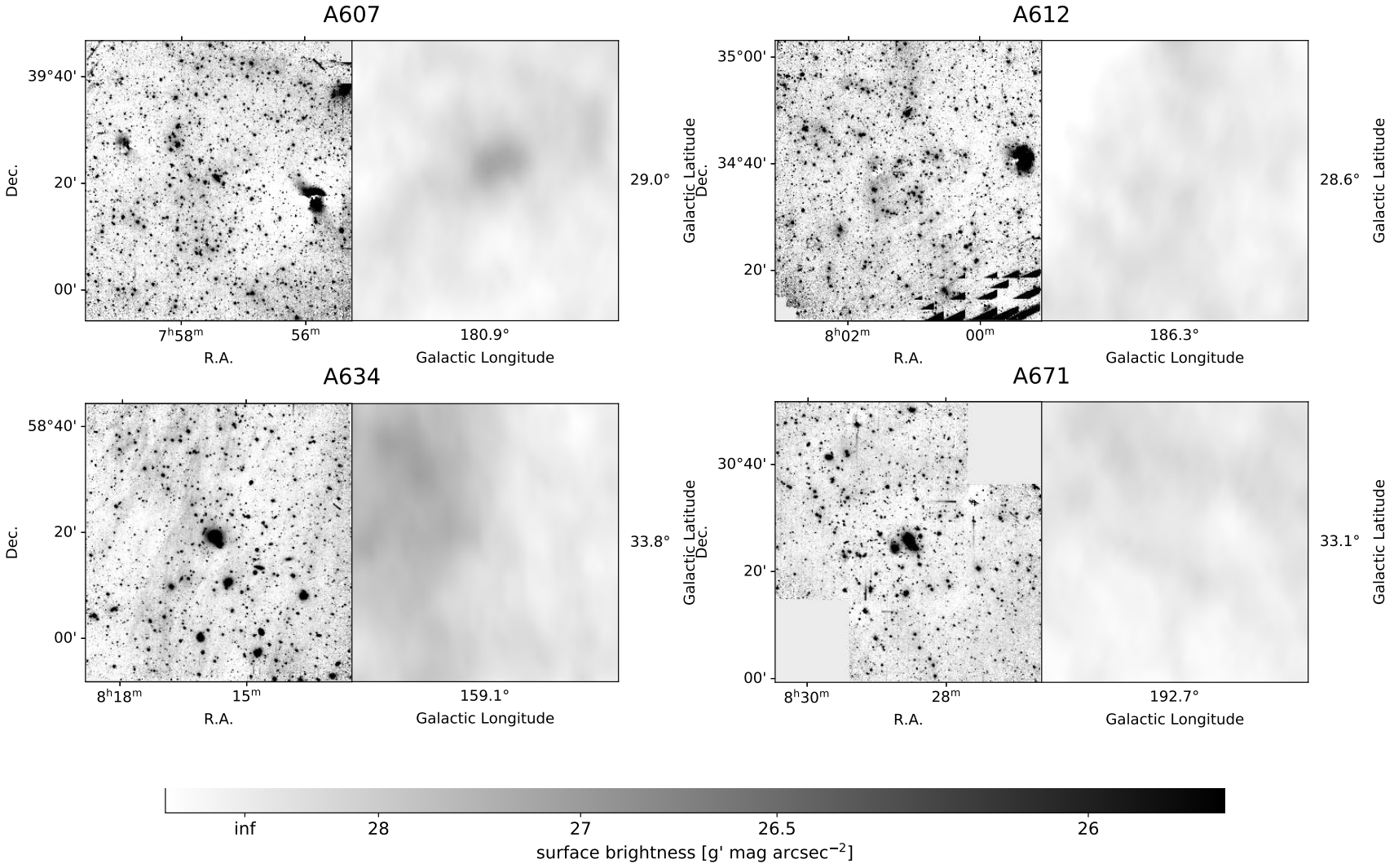

Figure C.1 *(continued)*

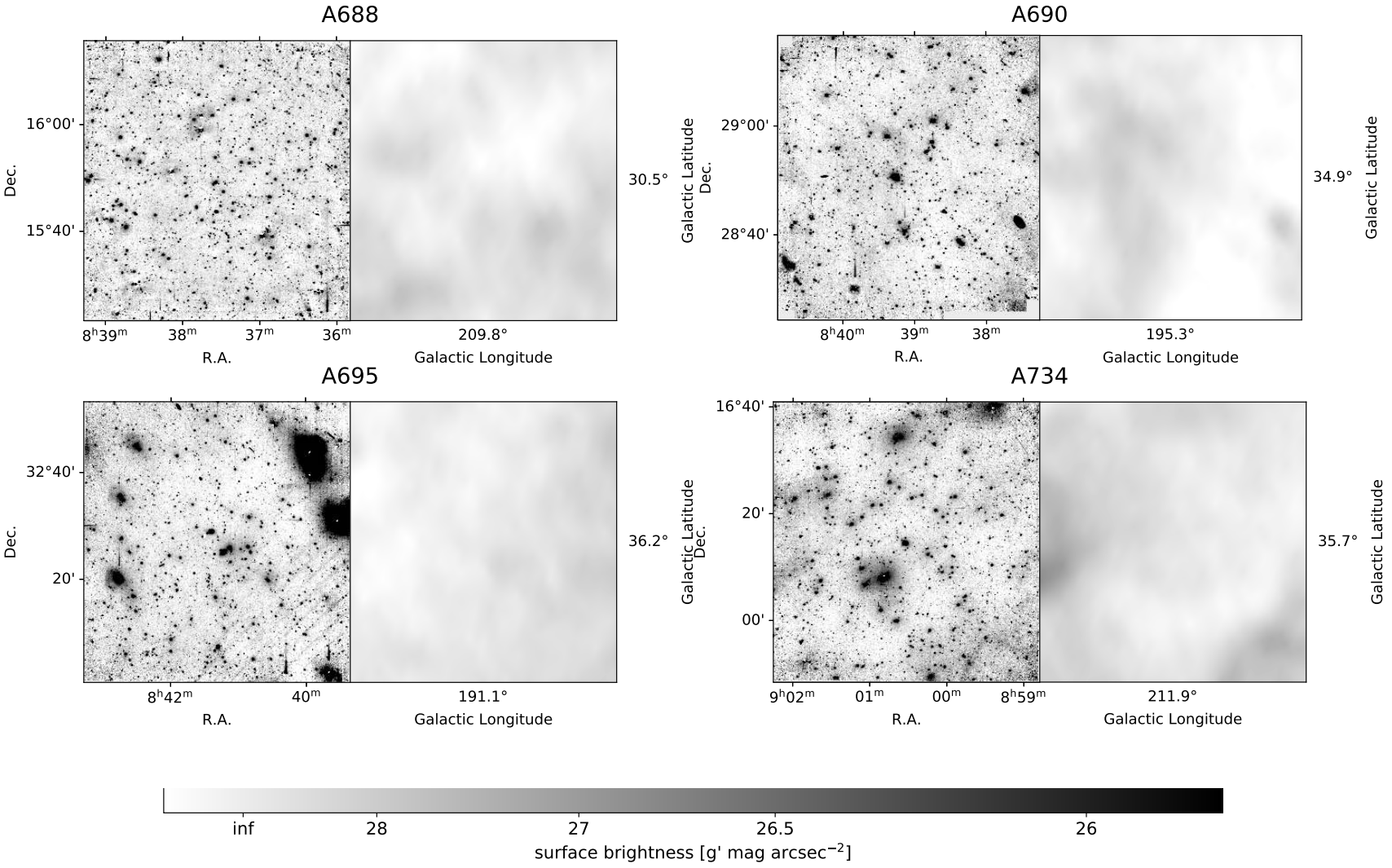

Figure C.1 *(continued)*

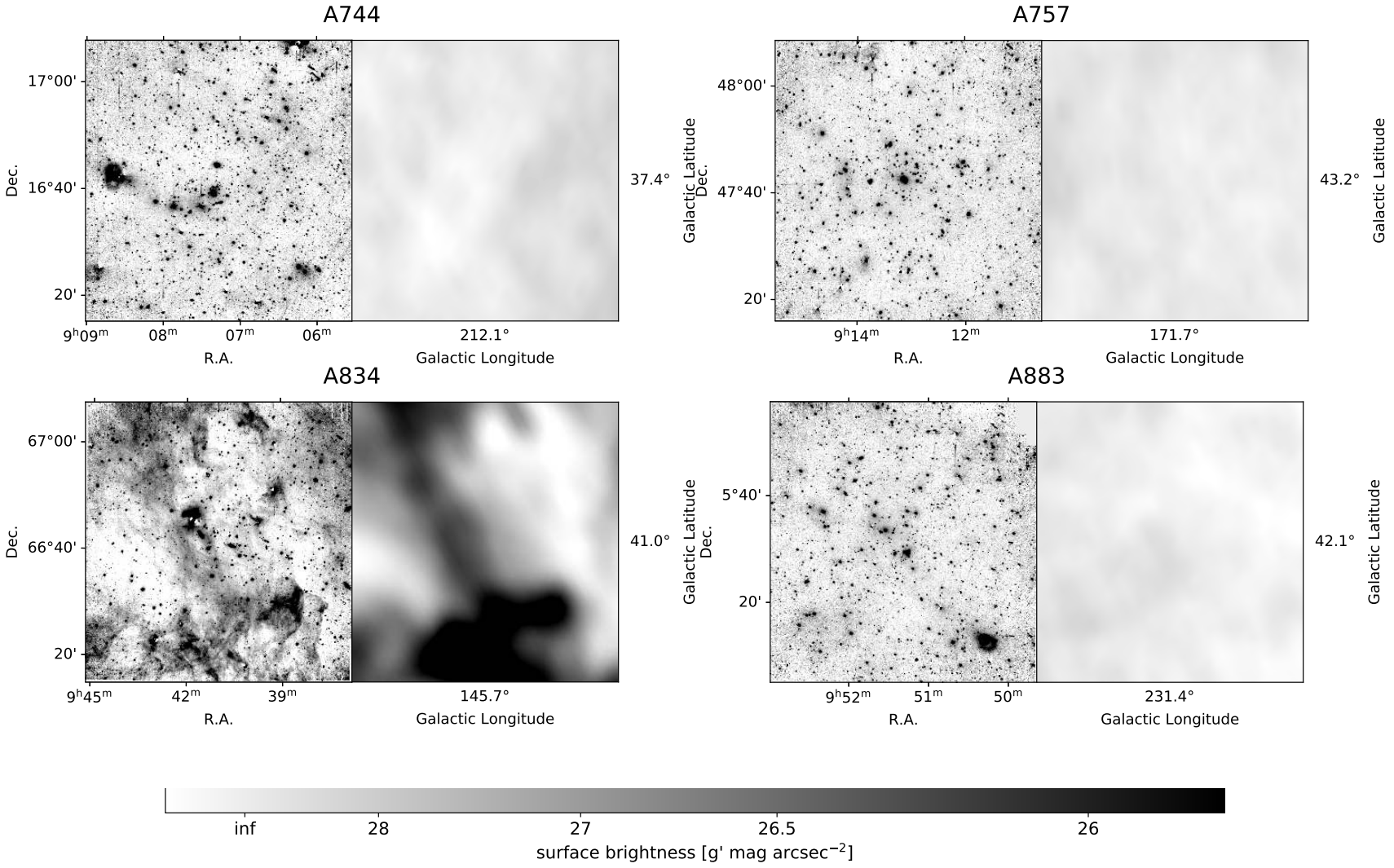

Figure C.1 *(continued)*

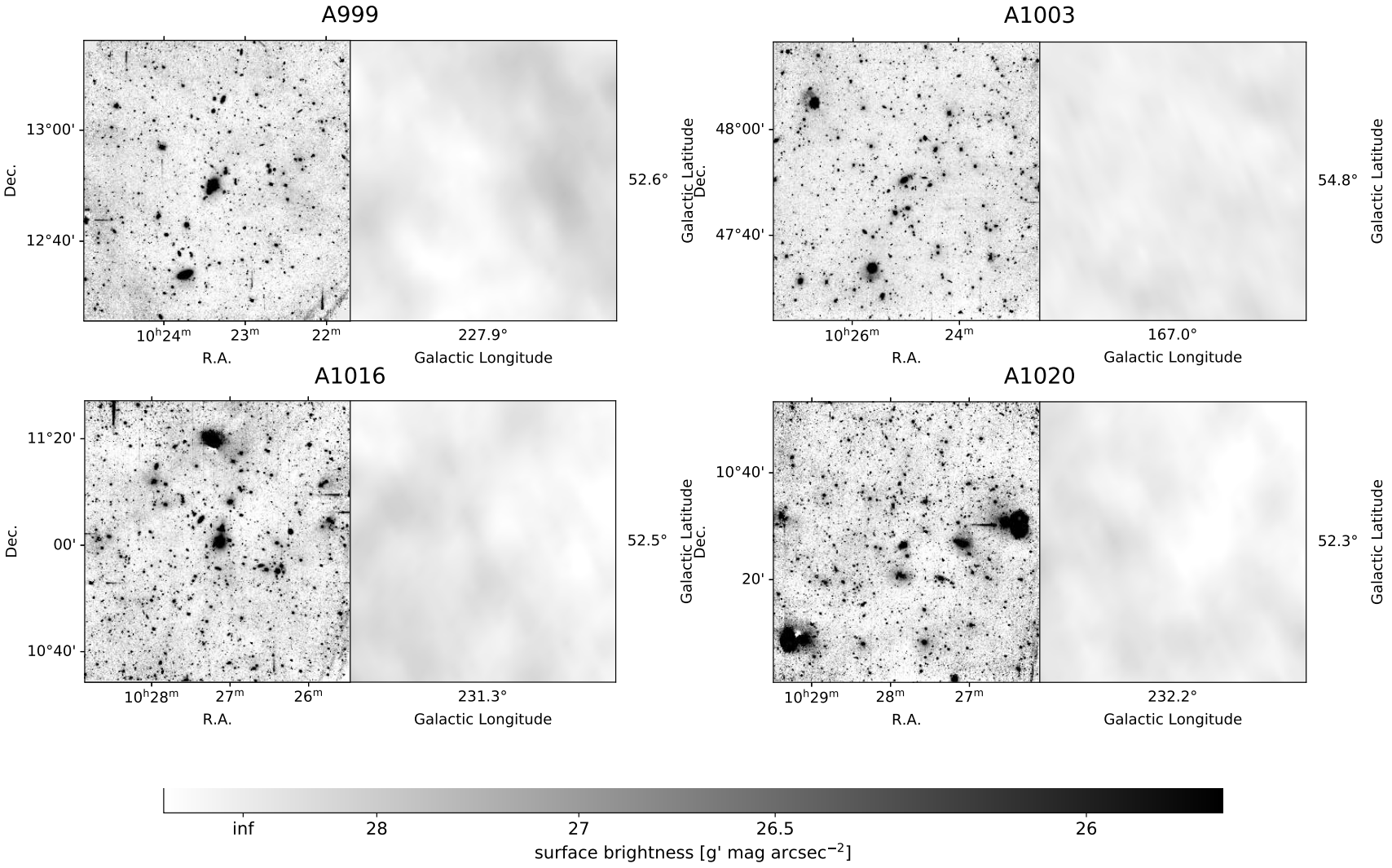

Figure C.1 *(continued)*

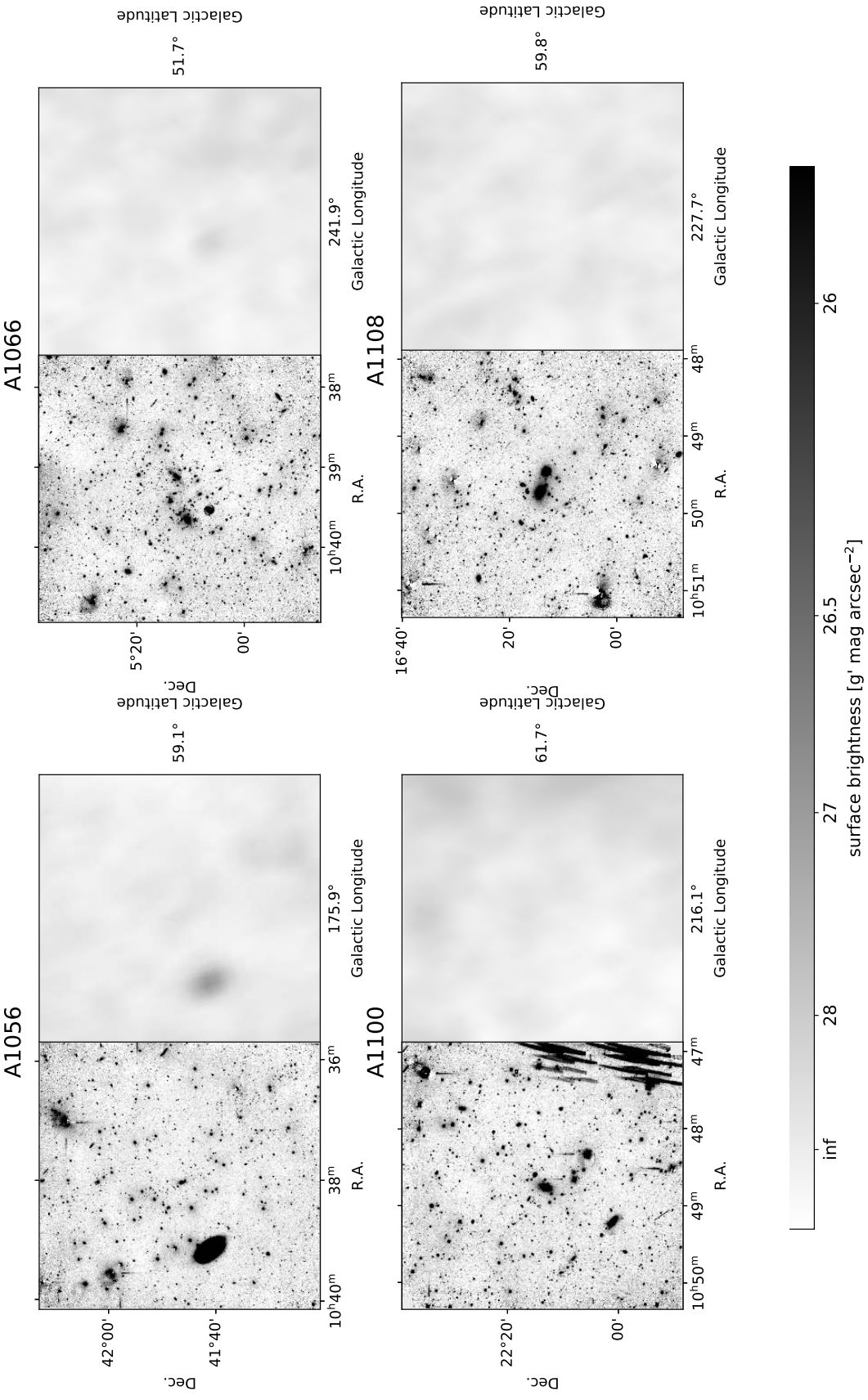

Figure C.1 *(continued)*

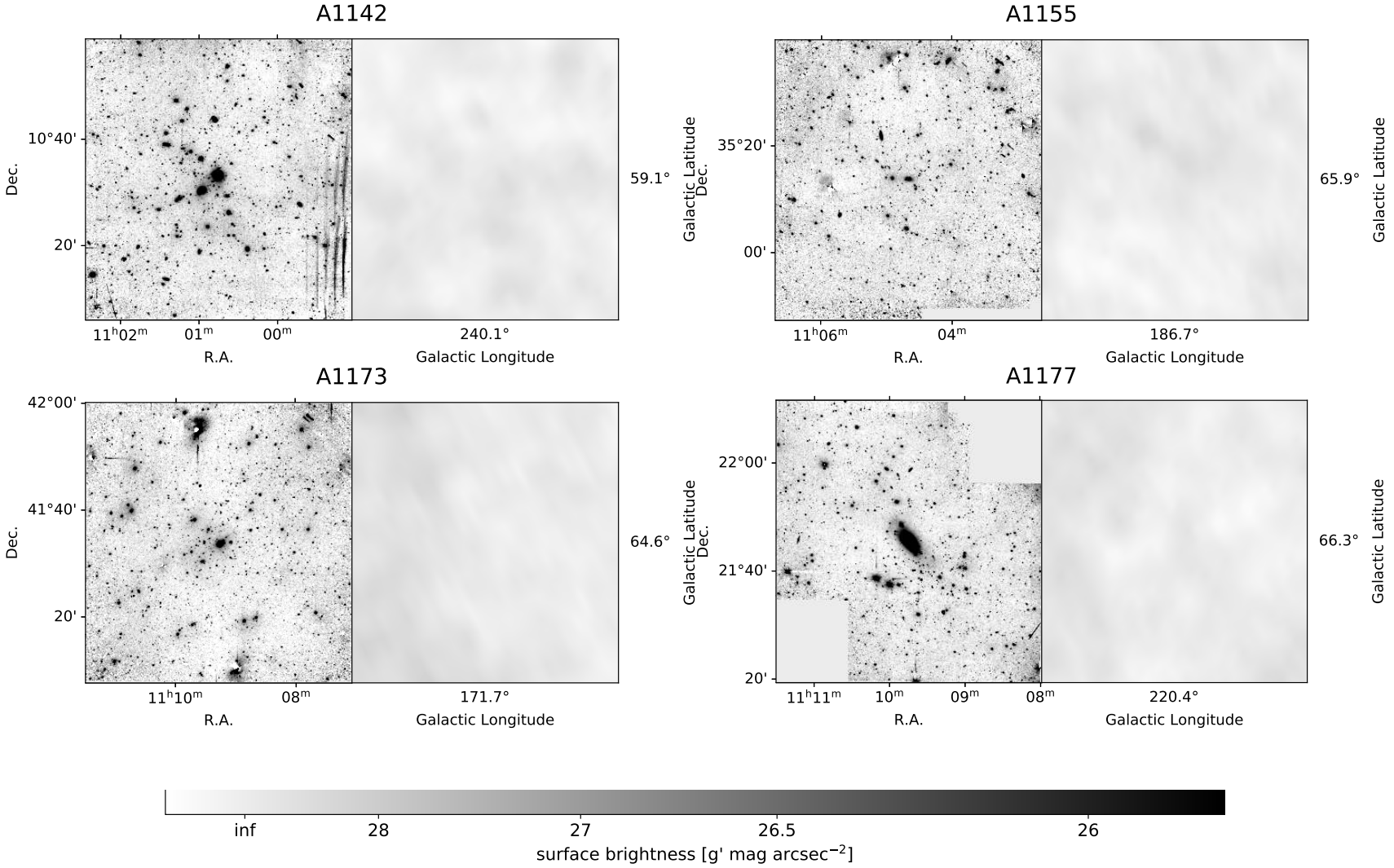

Figure C.1 *(continued)*

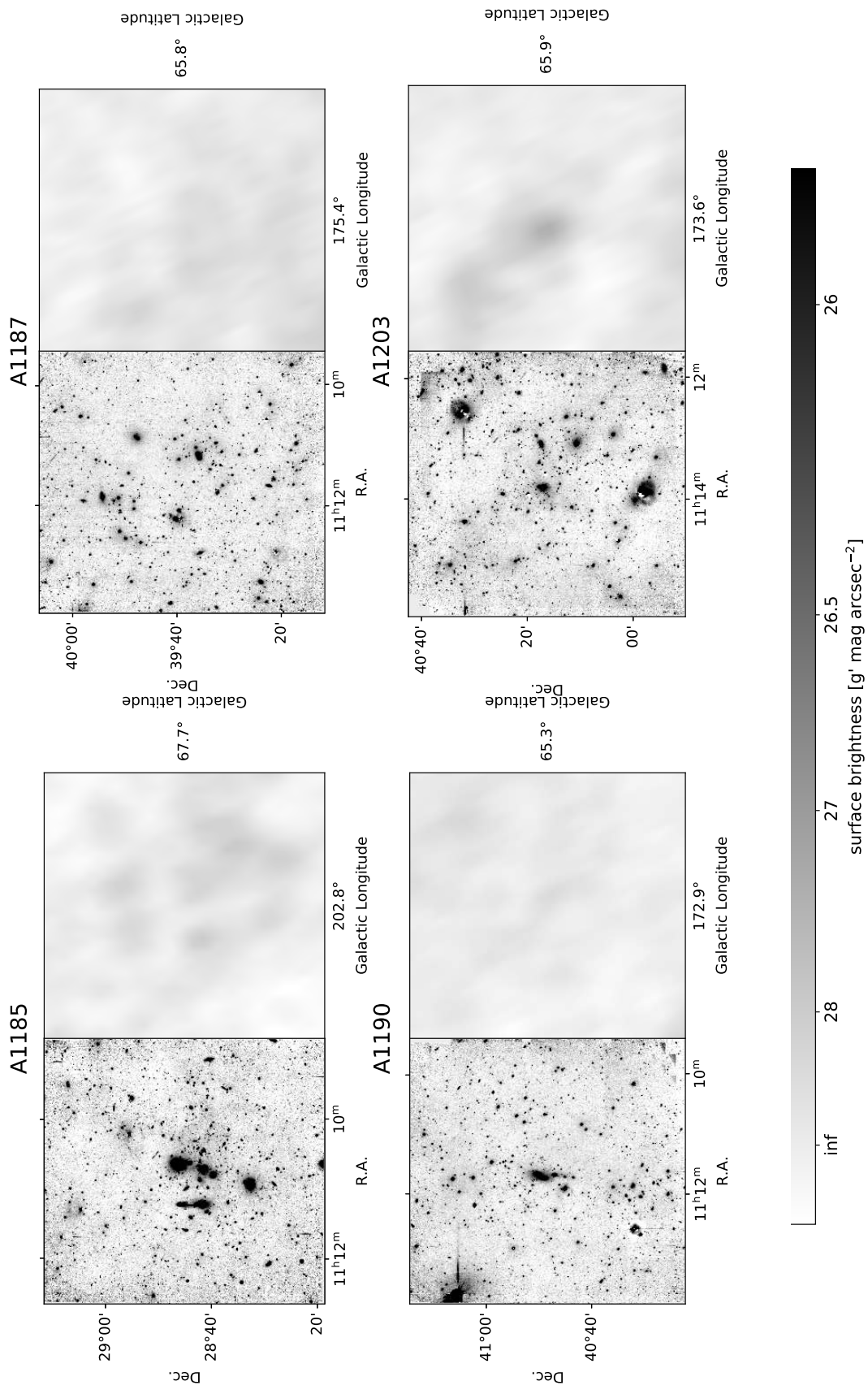

Figure C.1 *(continued)*

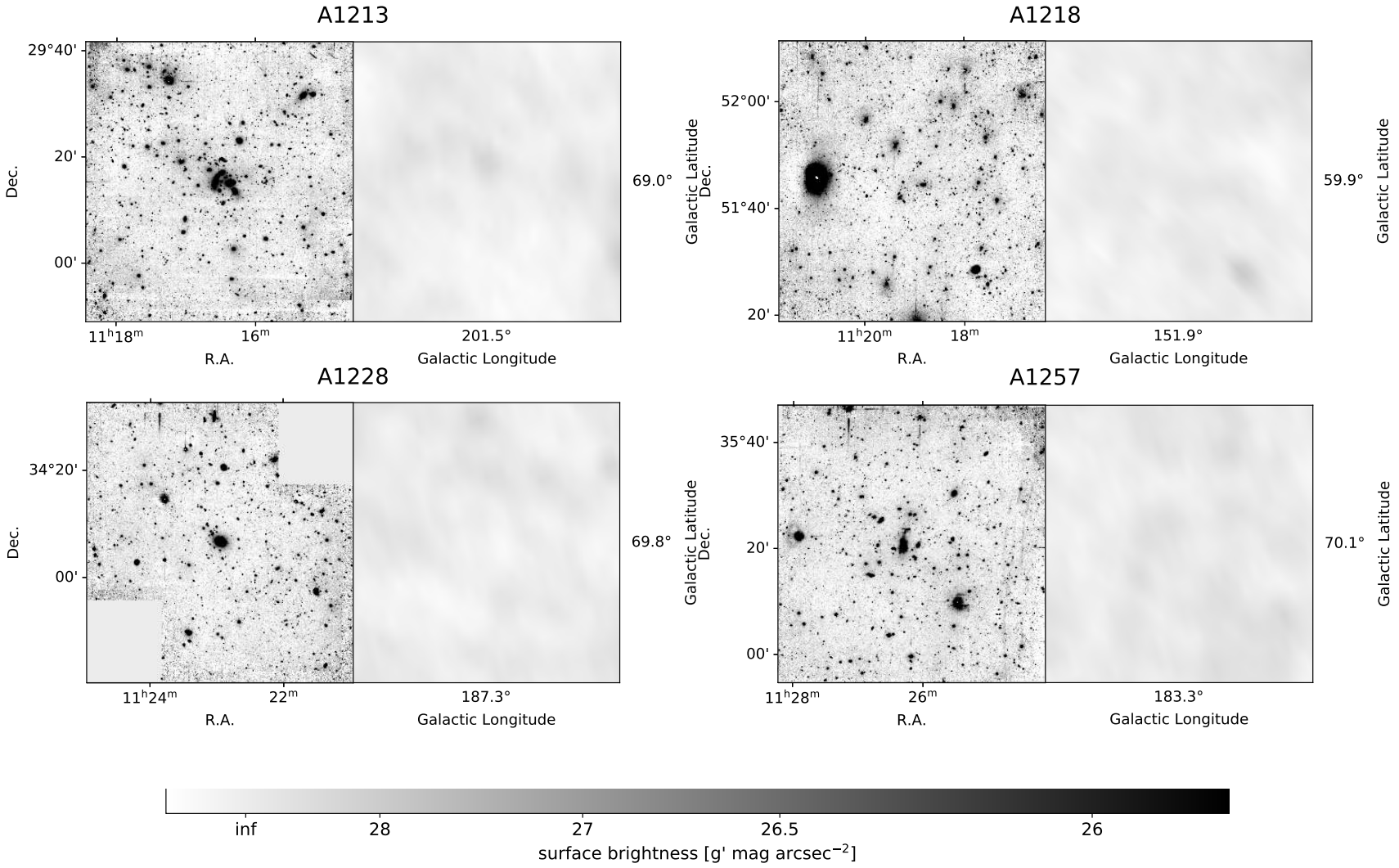

Figure C.1 *(continued)*

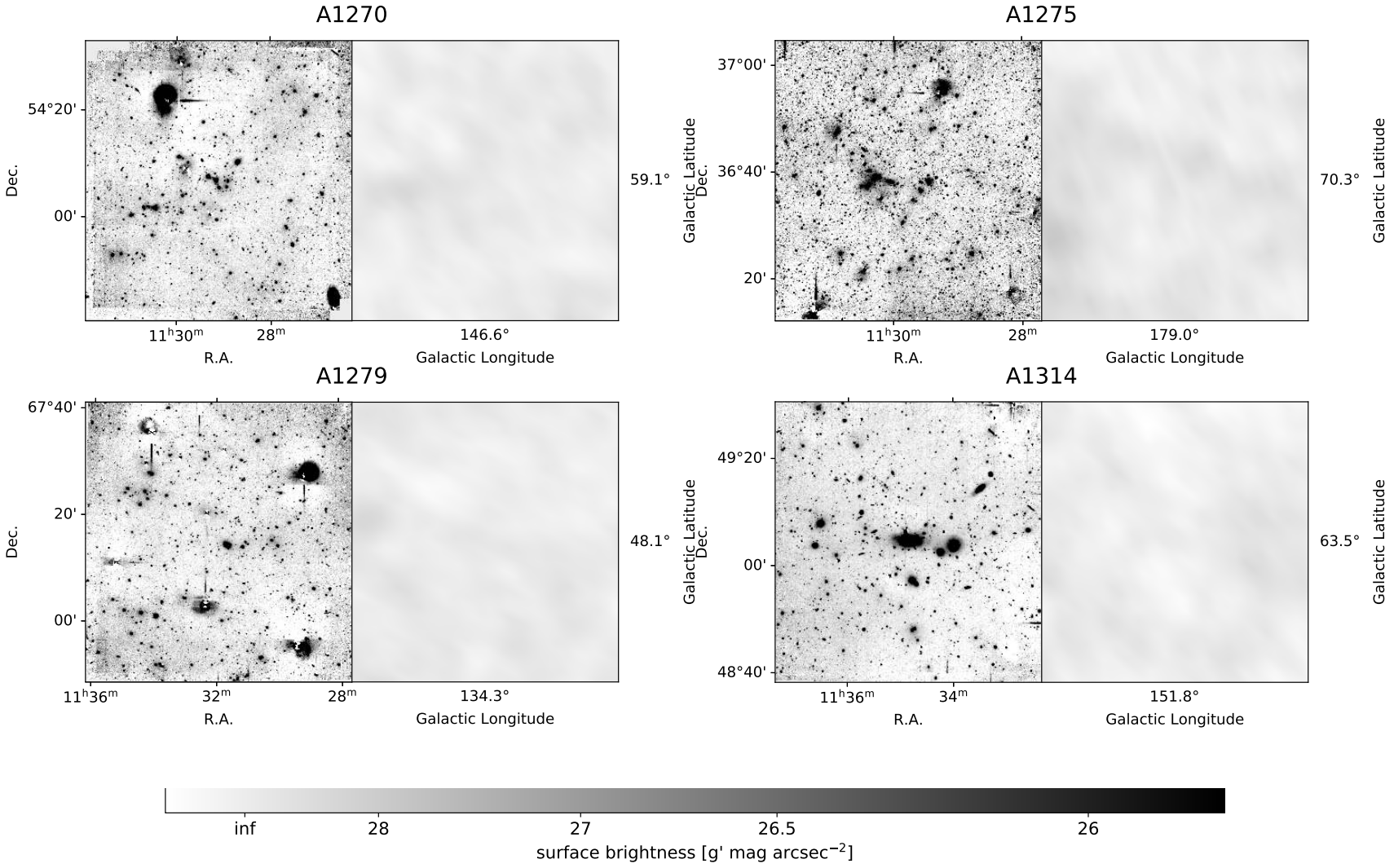

Figure C.1 *(continued)*

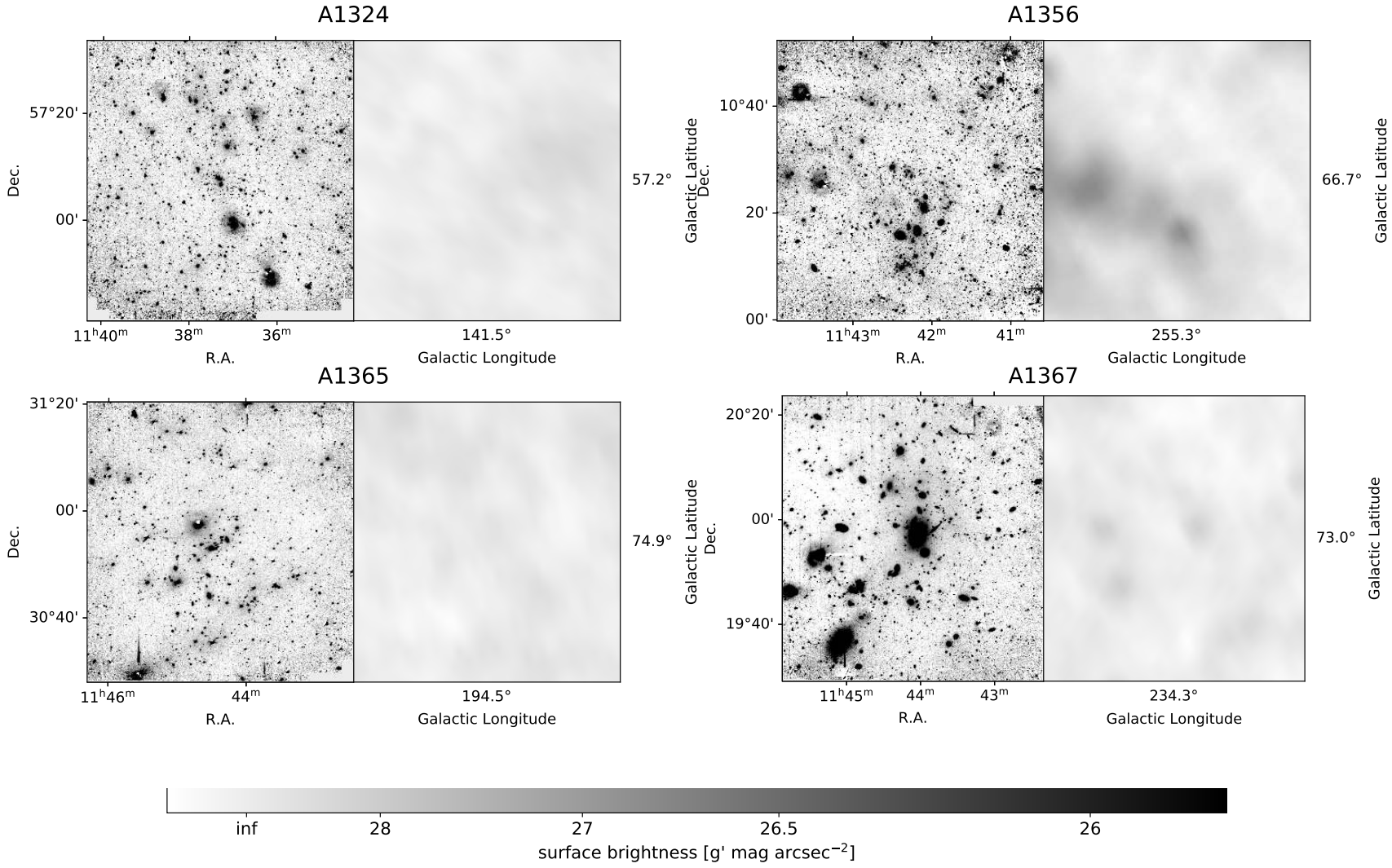

Figure C.1 *(continued)*

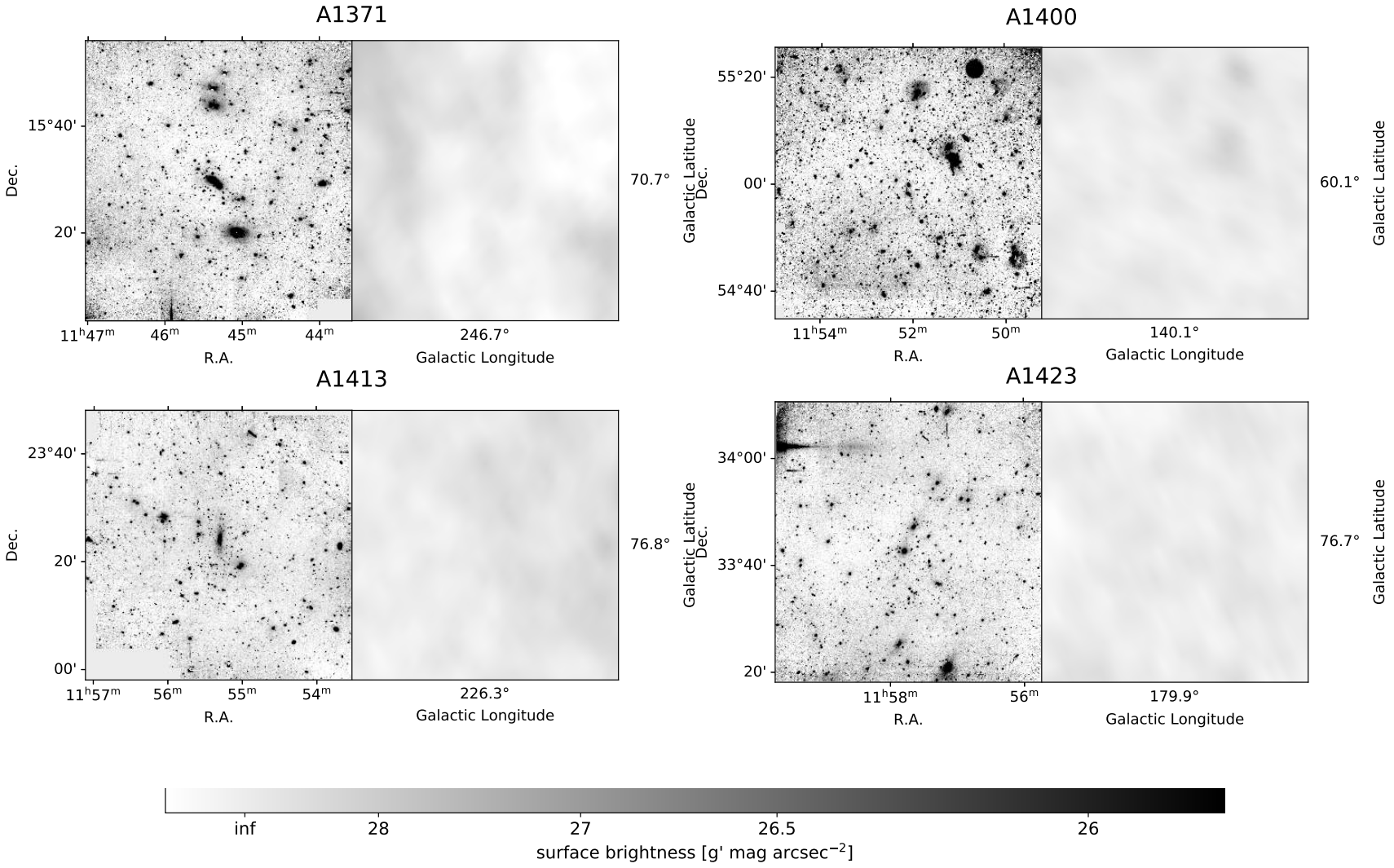

Figure C.1 *(continued)*

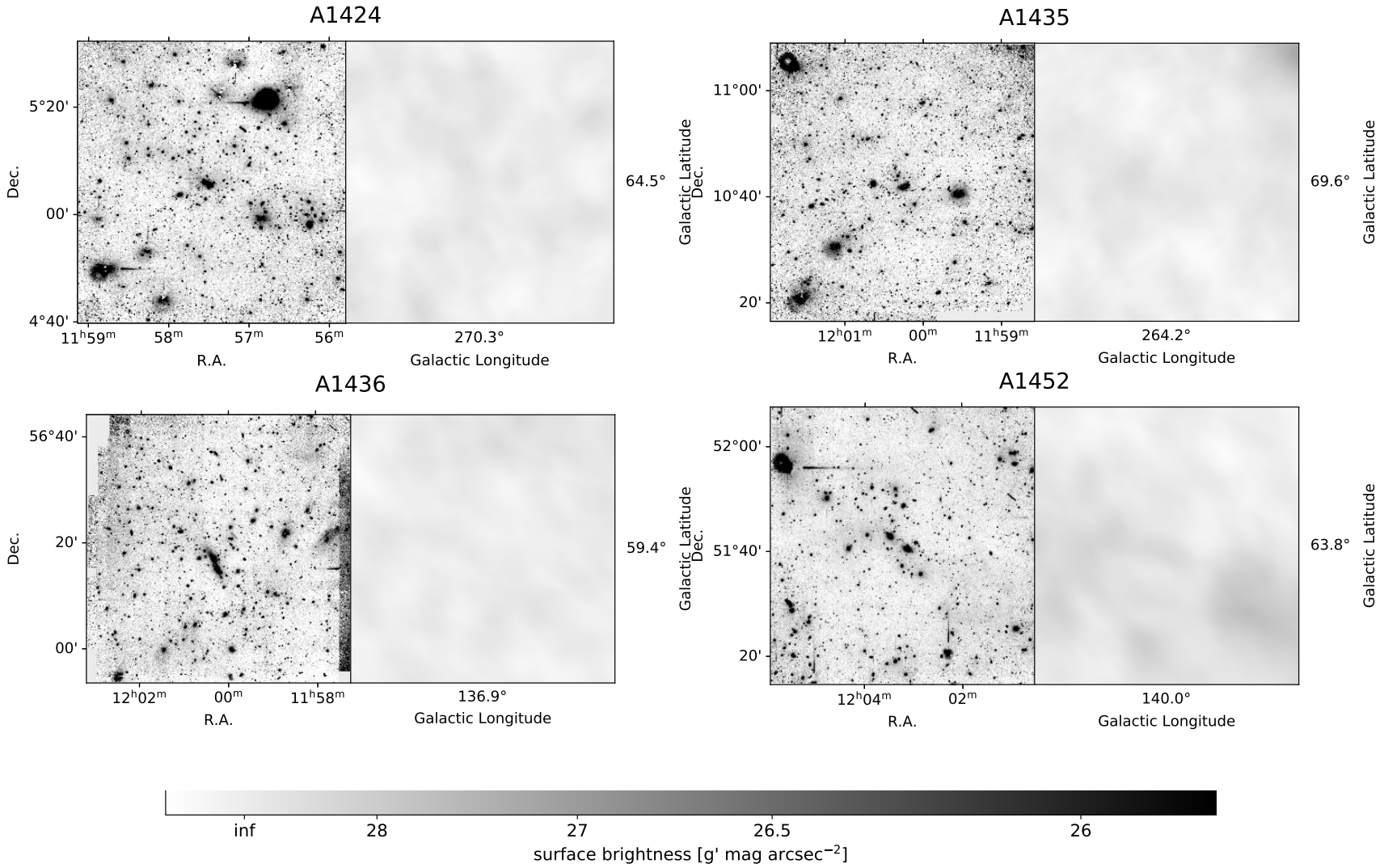

Figure C.1 *(continued)*

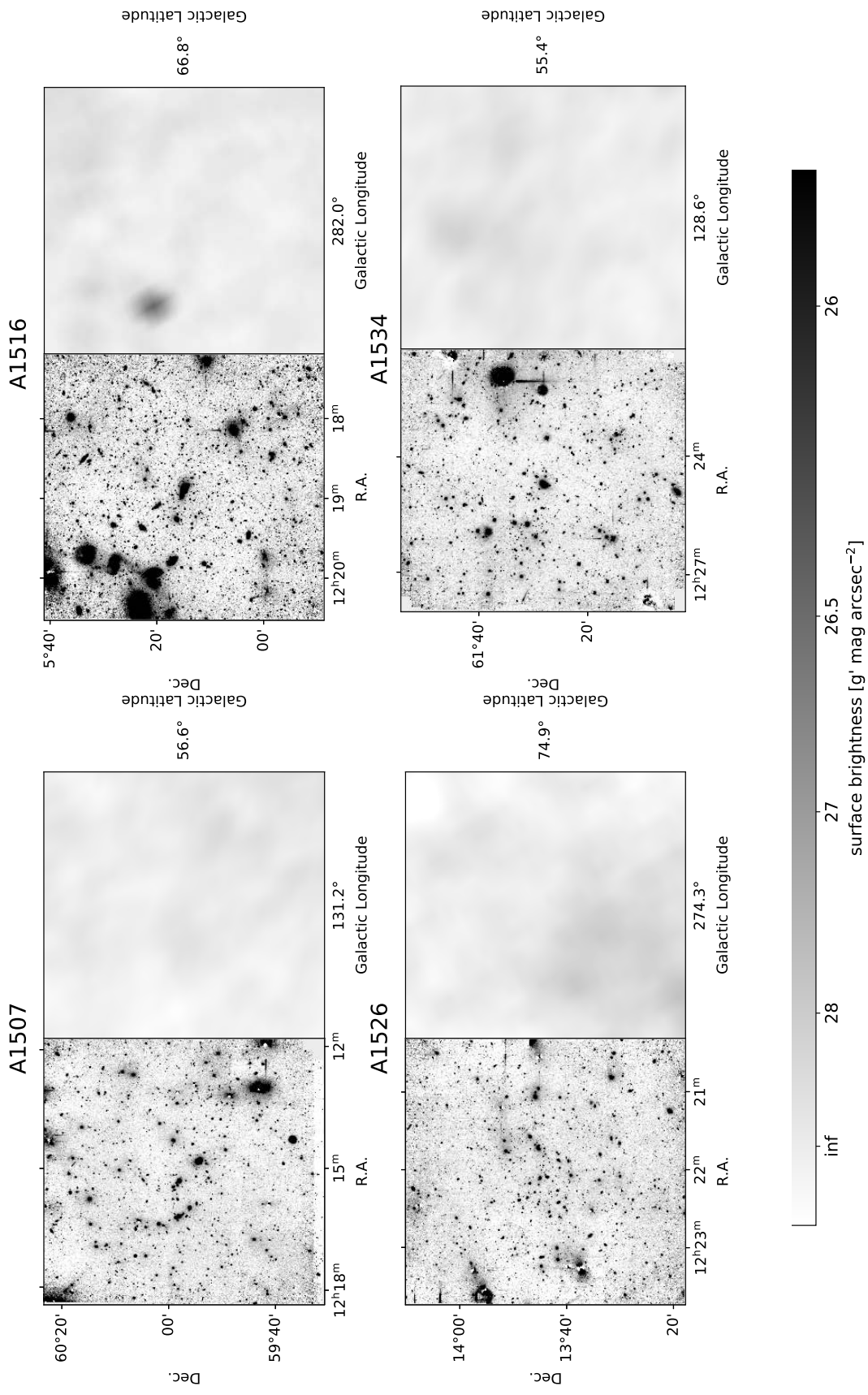

Figure C.1 *(continued)*

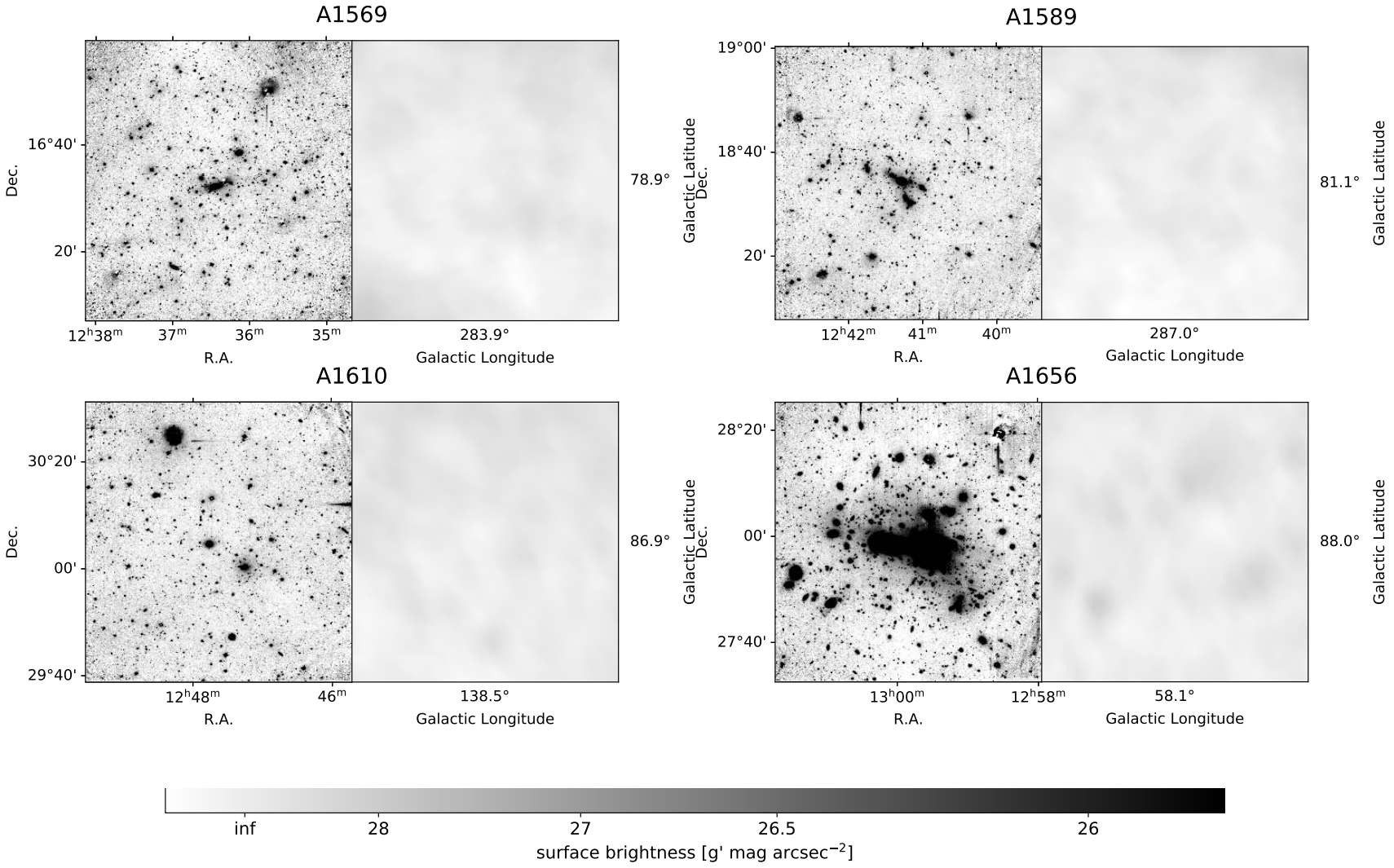

Figure C.1 *(continued)*

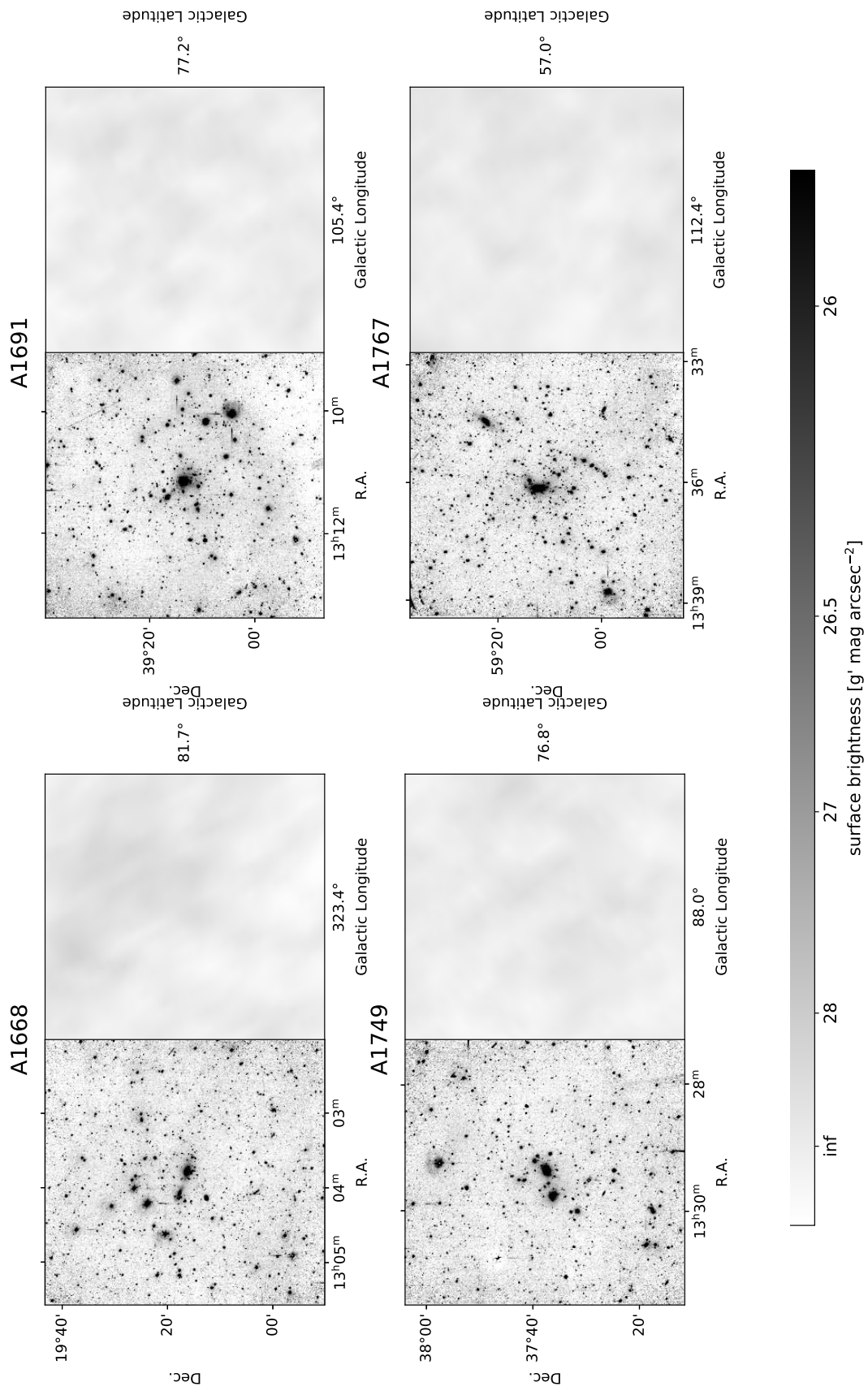

Figure C.1 *(continued)*

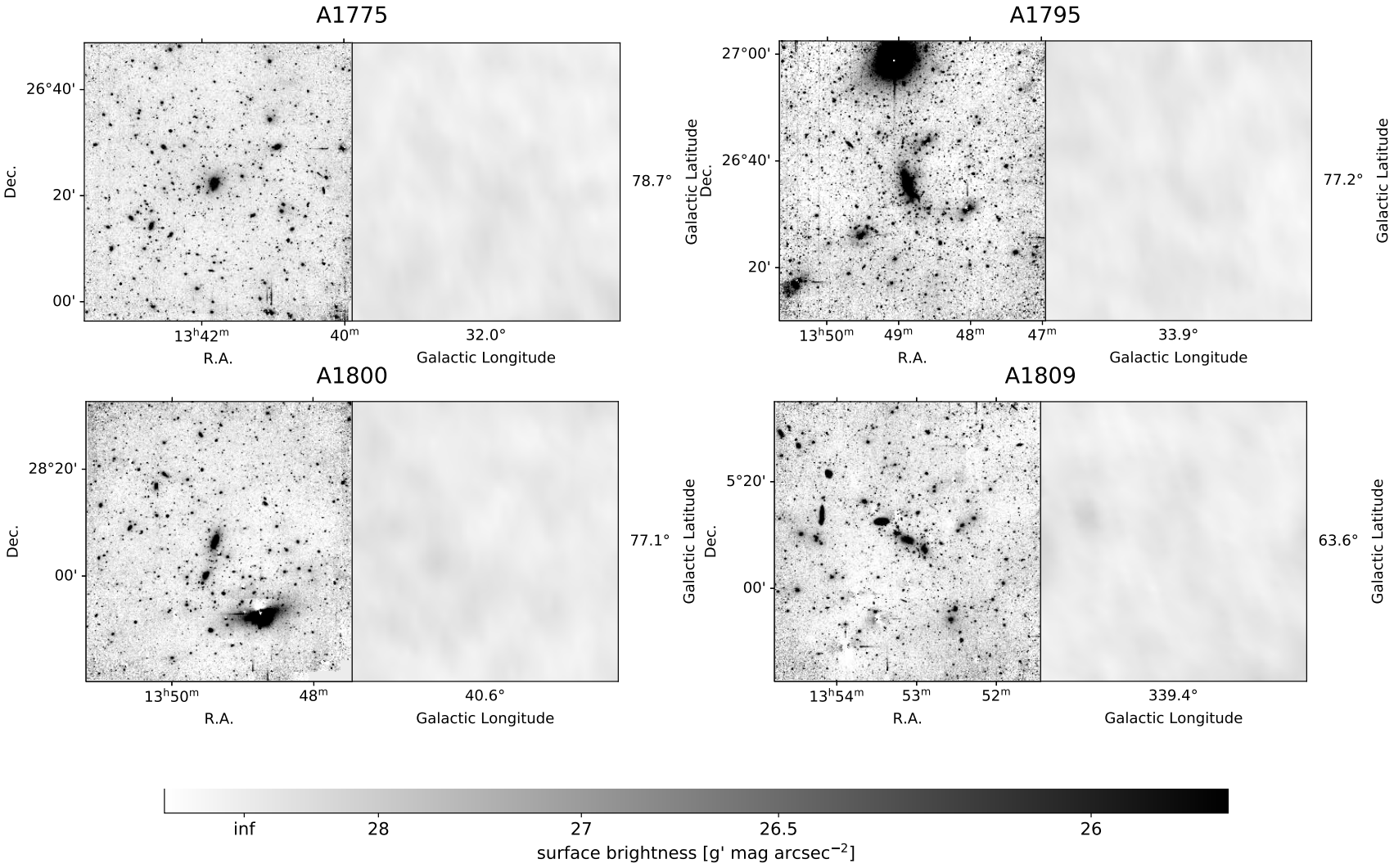

Figure C.1 *(continued)*

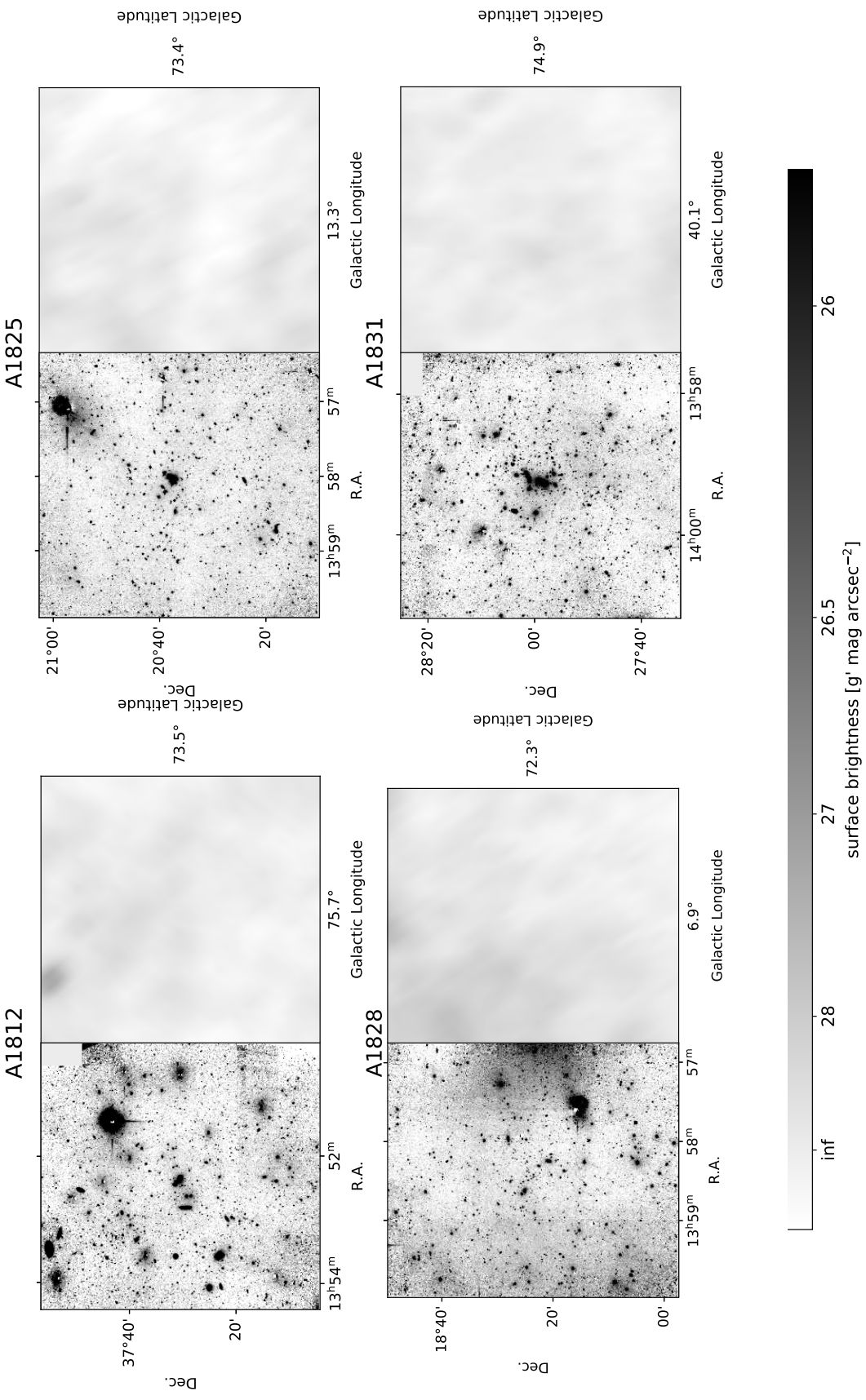

Figure C.1 *(continued)*

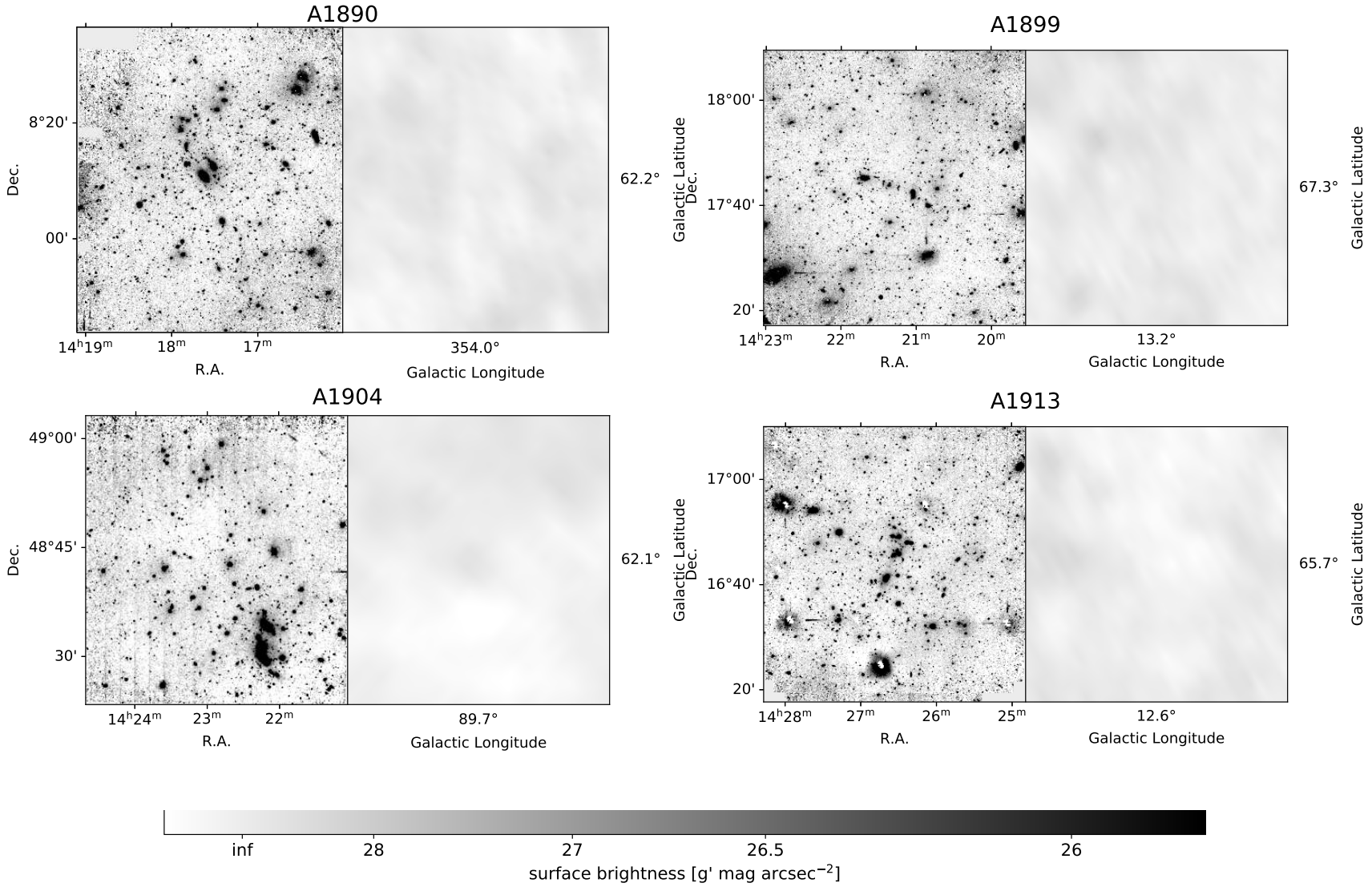

Figure C.1 *(continued)*

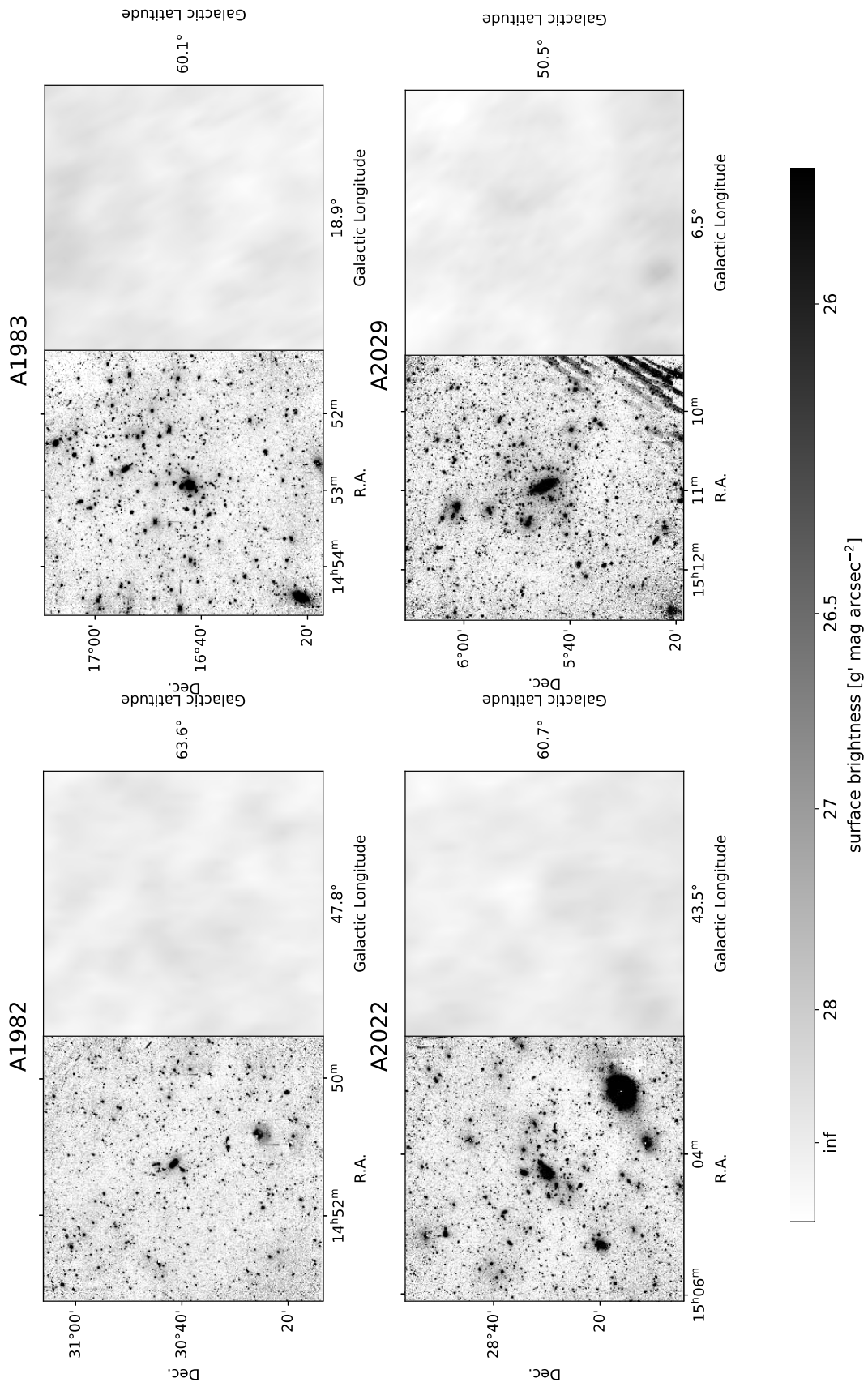

Figure C.1 *(continued)*

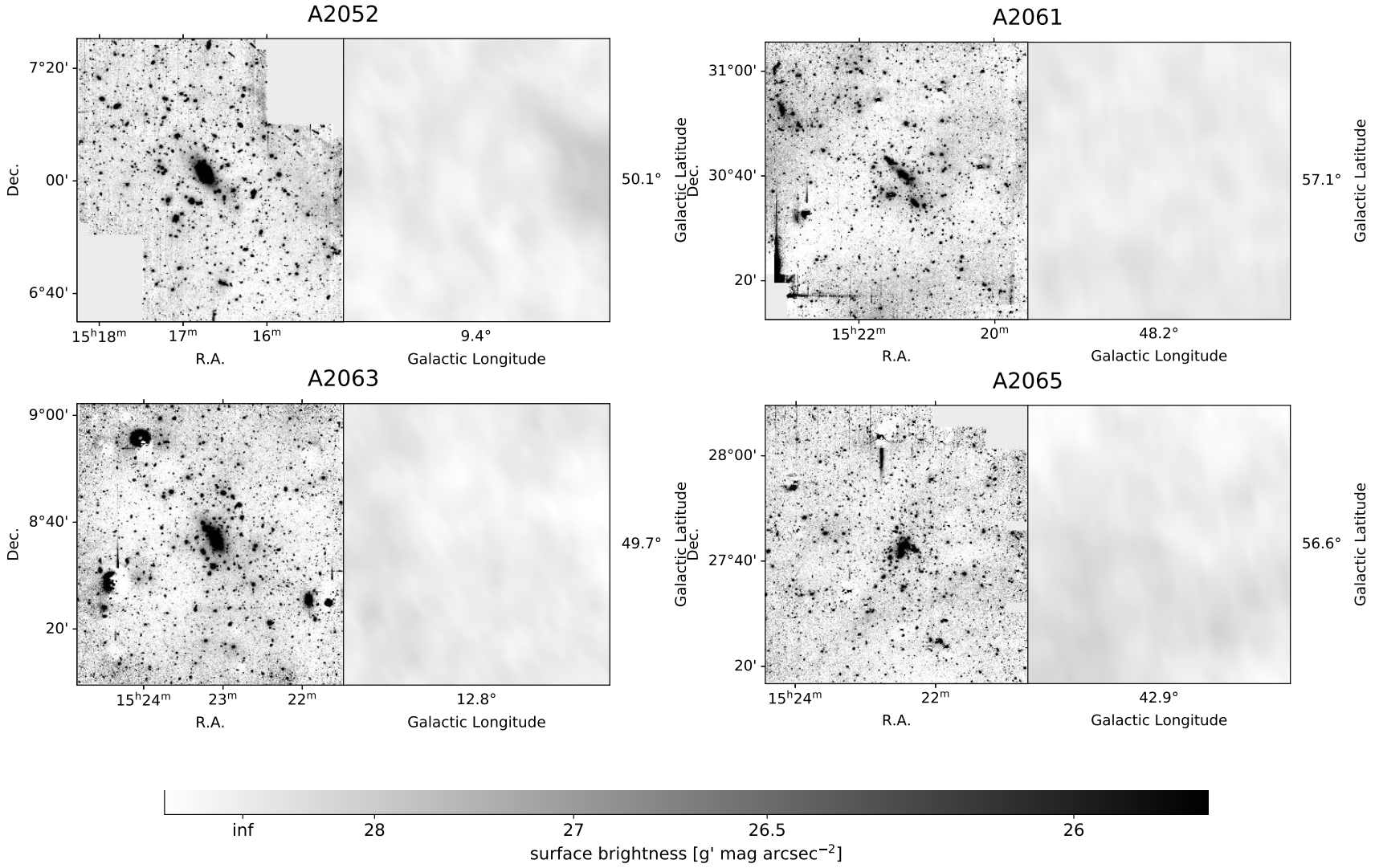

Figure C.1 *(continued)*

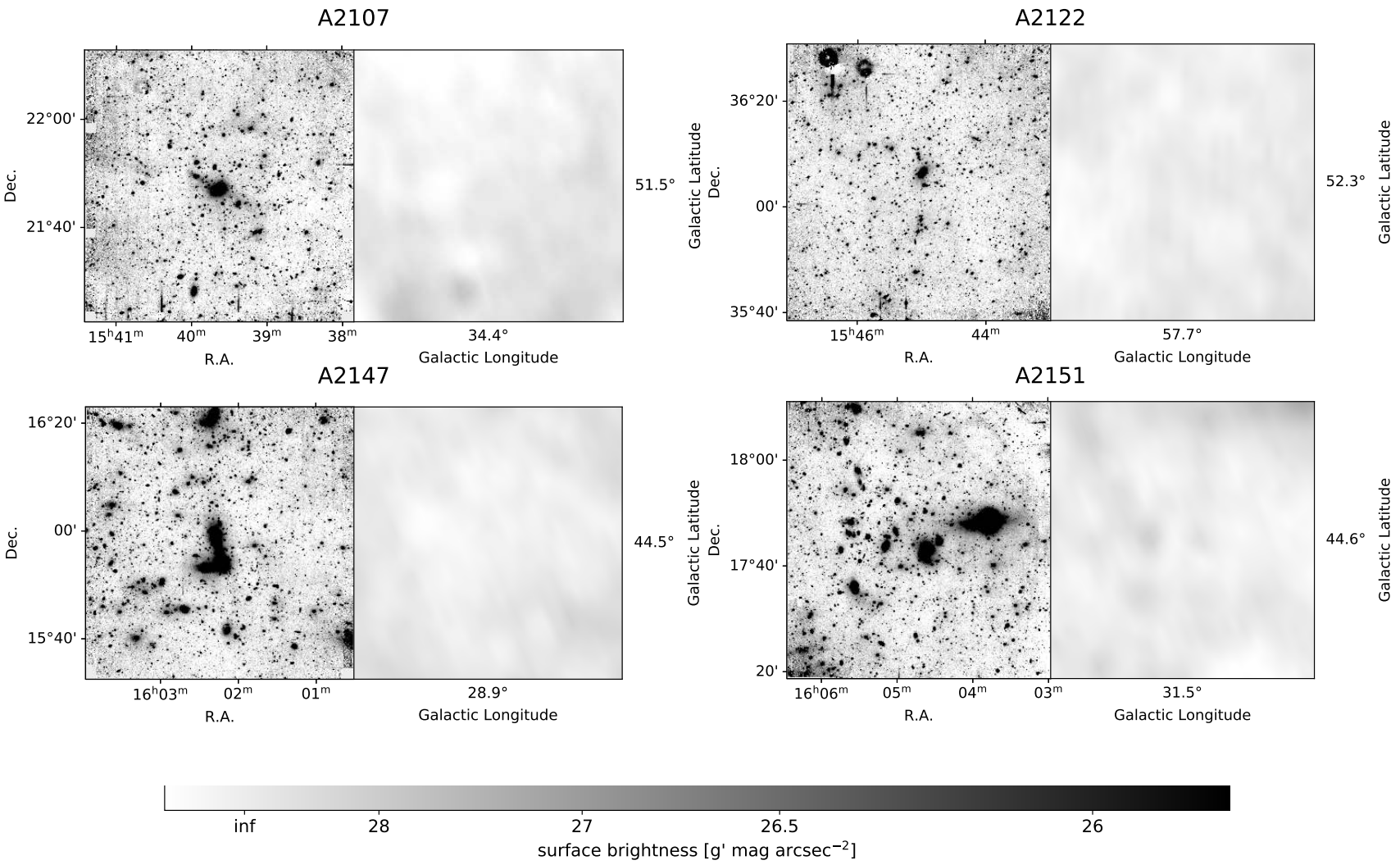

Figure C.1 *(continued)*

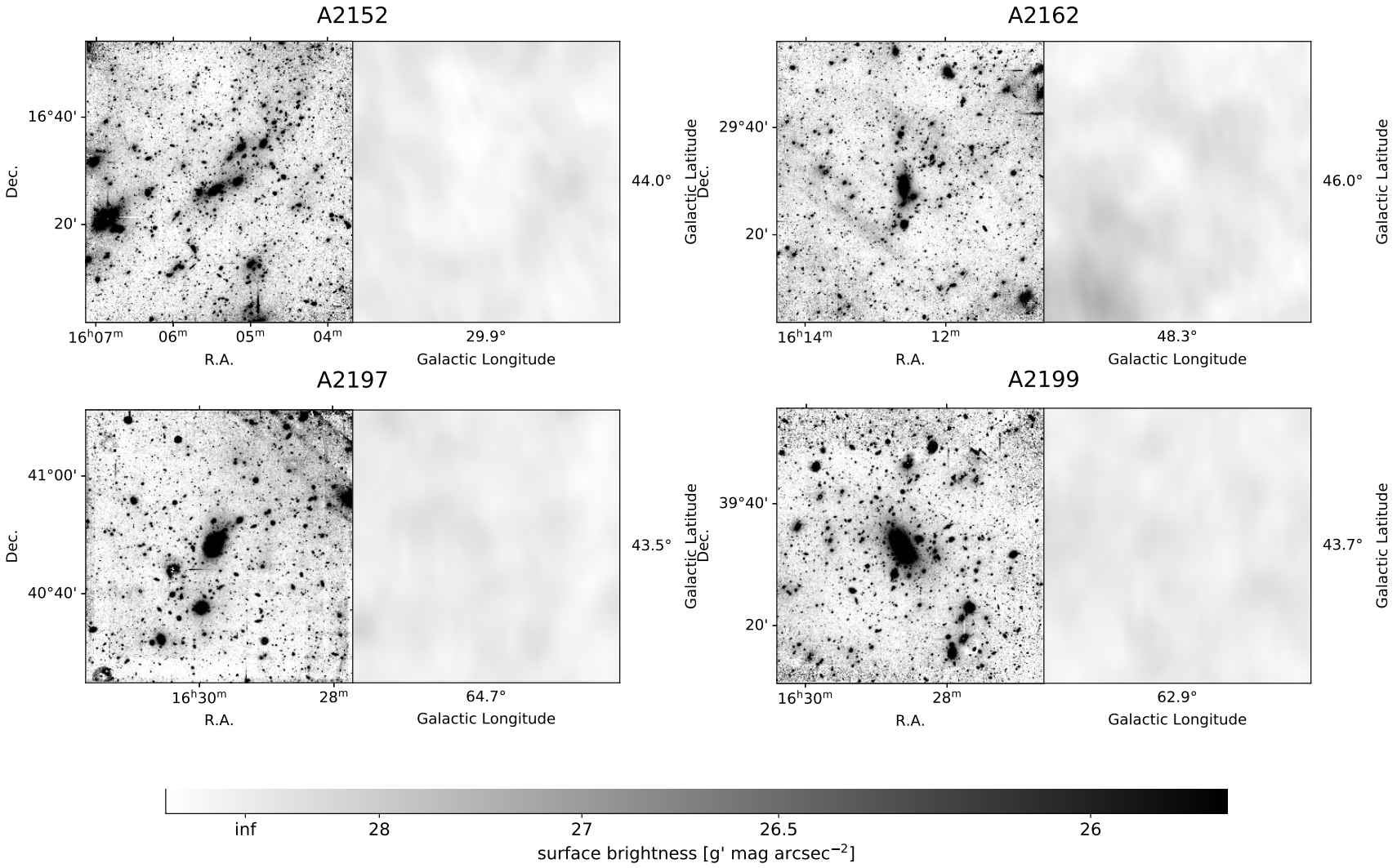

Figure C.1 *(continued)*

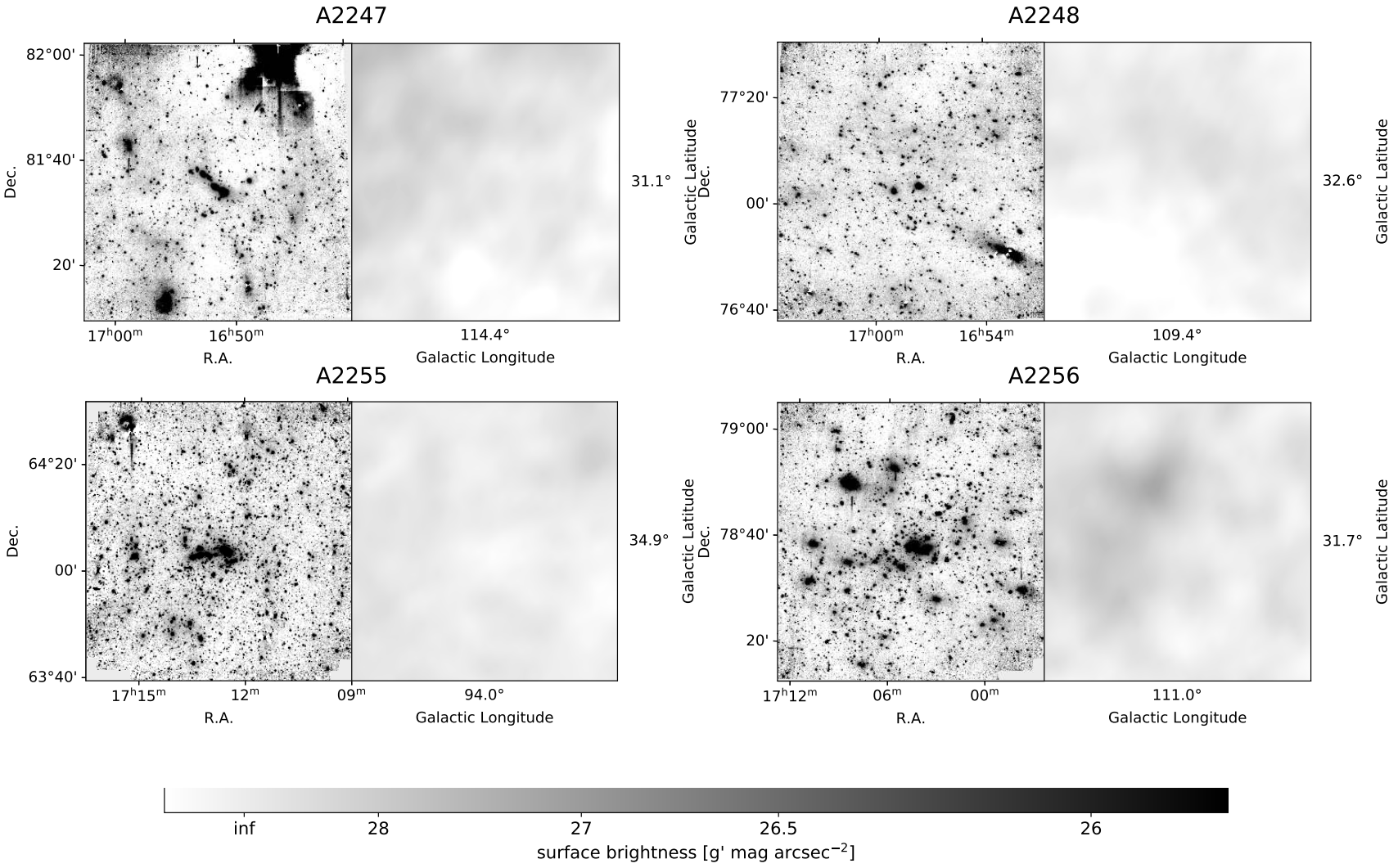

Figure C.1 *(continued)*

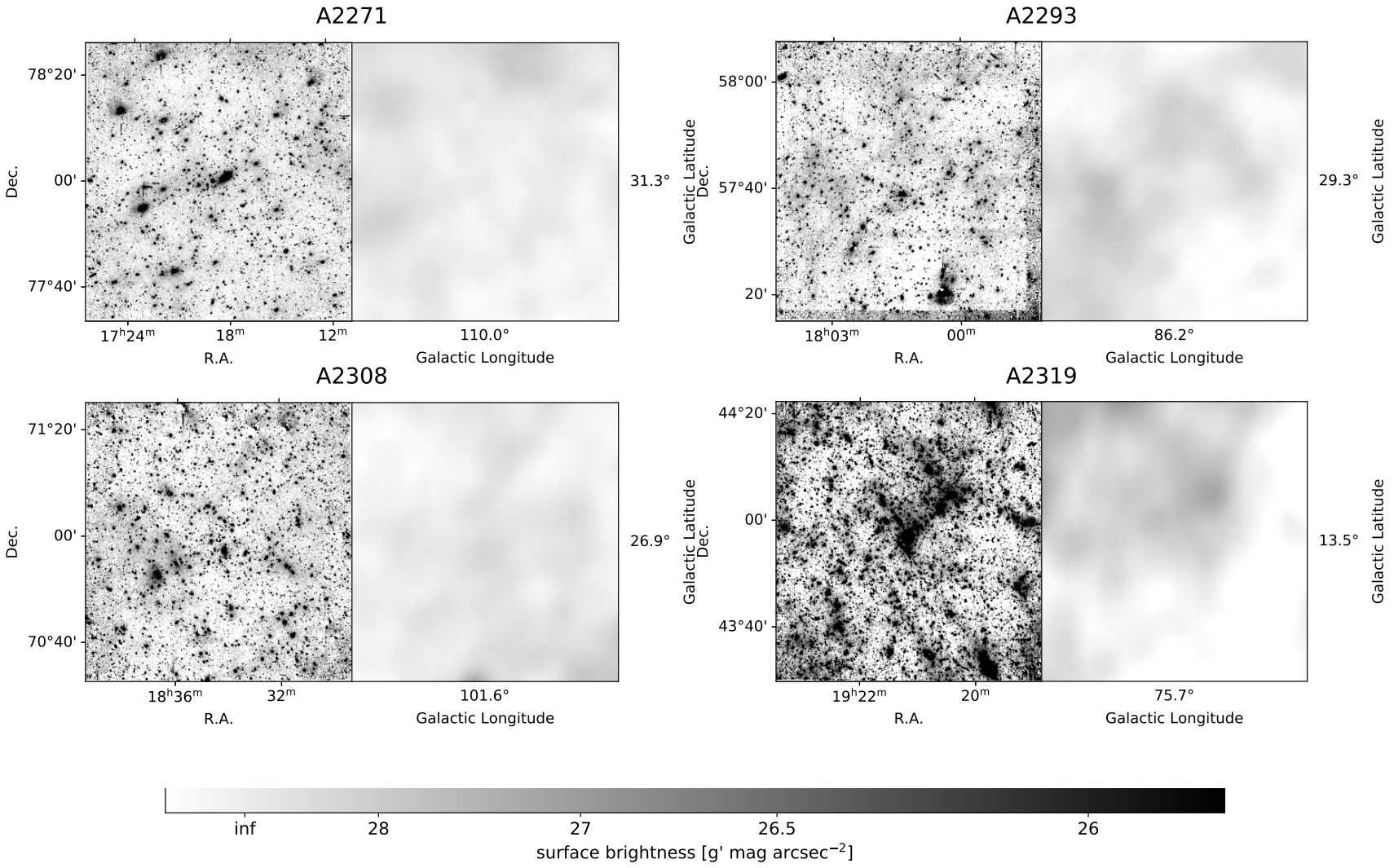

Figure C.1 *(continued)*

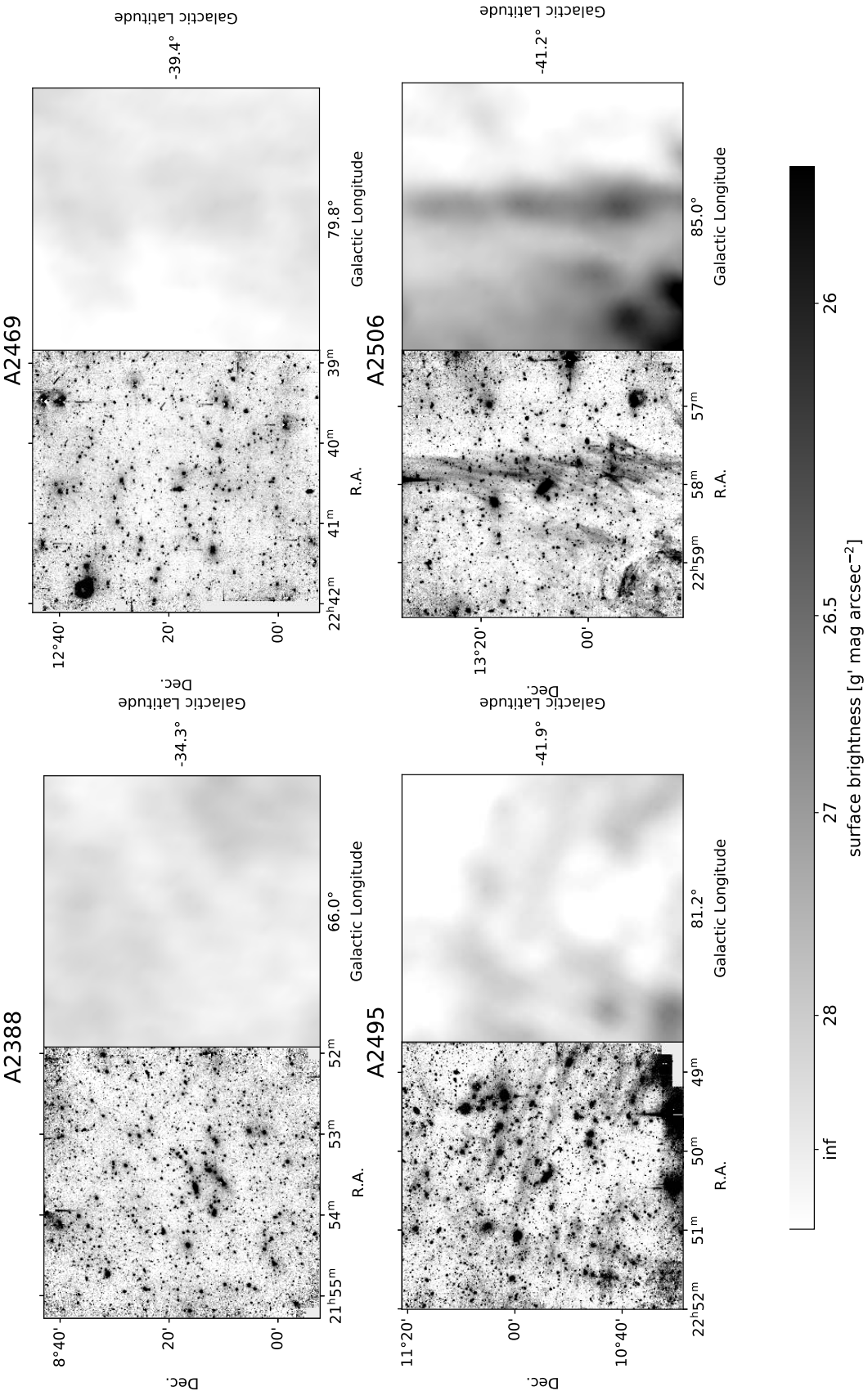

Figure C.1 *(continued)*

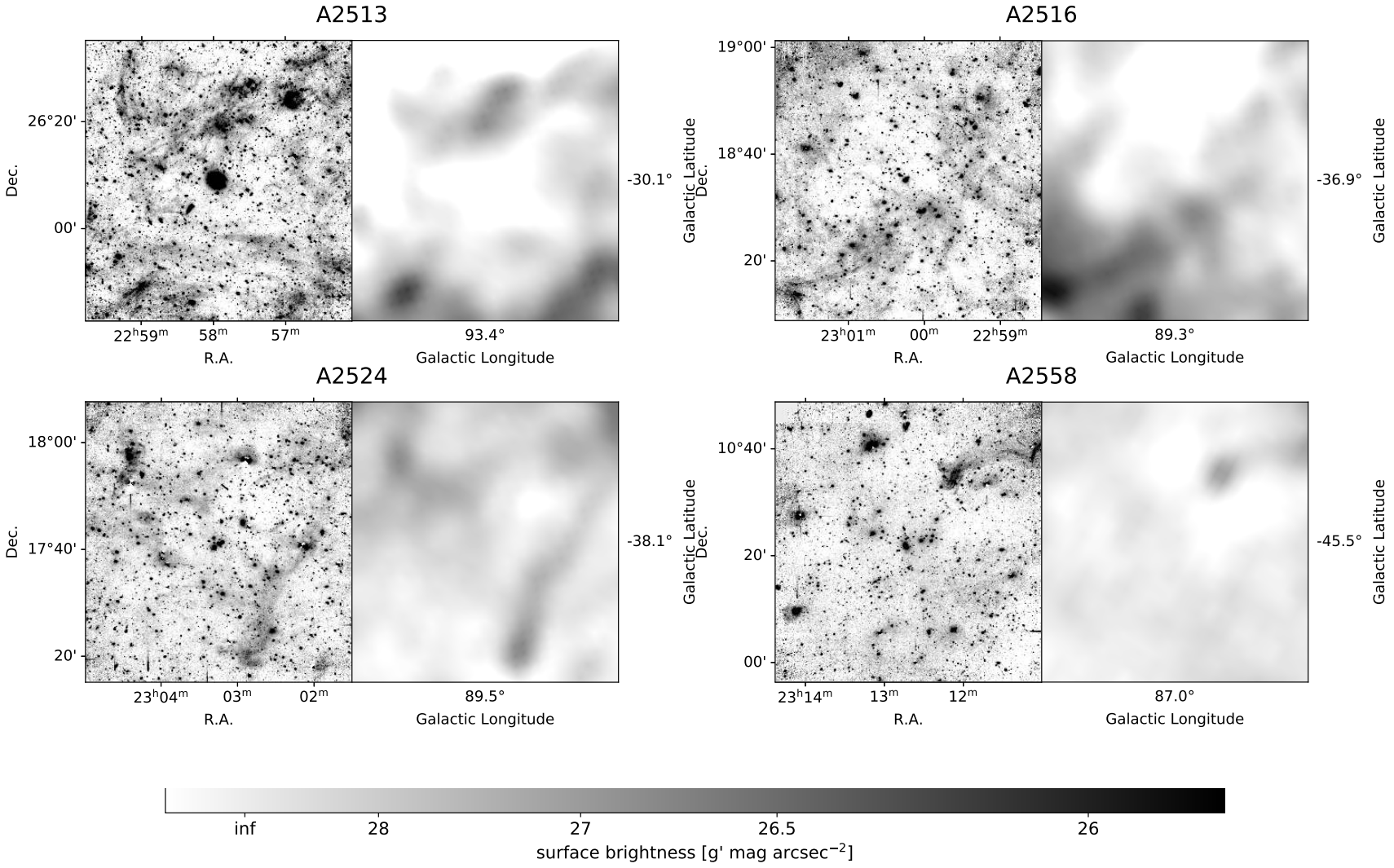

Figure C.1 *(continued)*

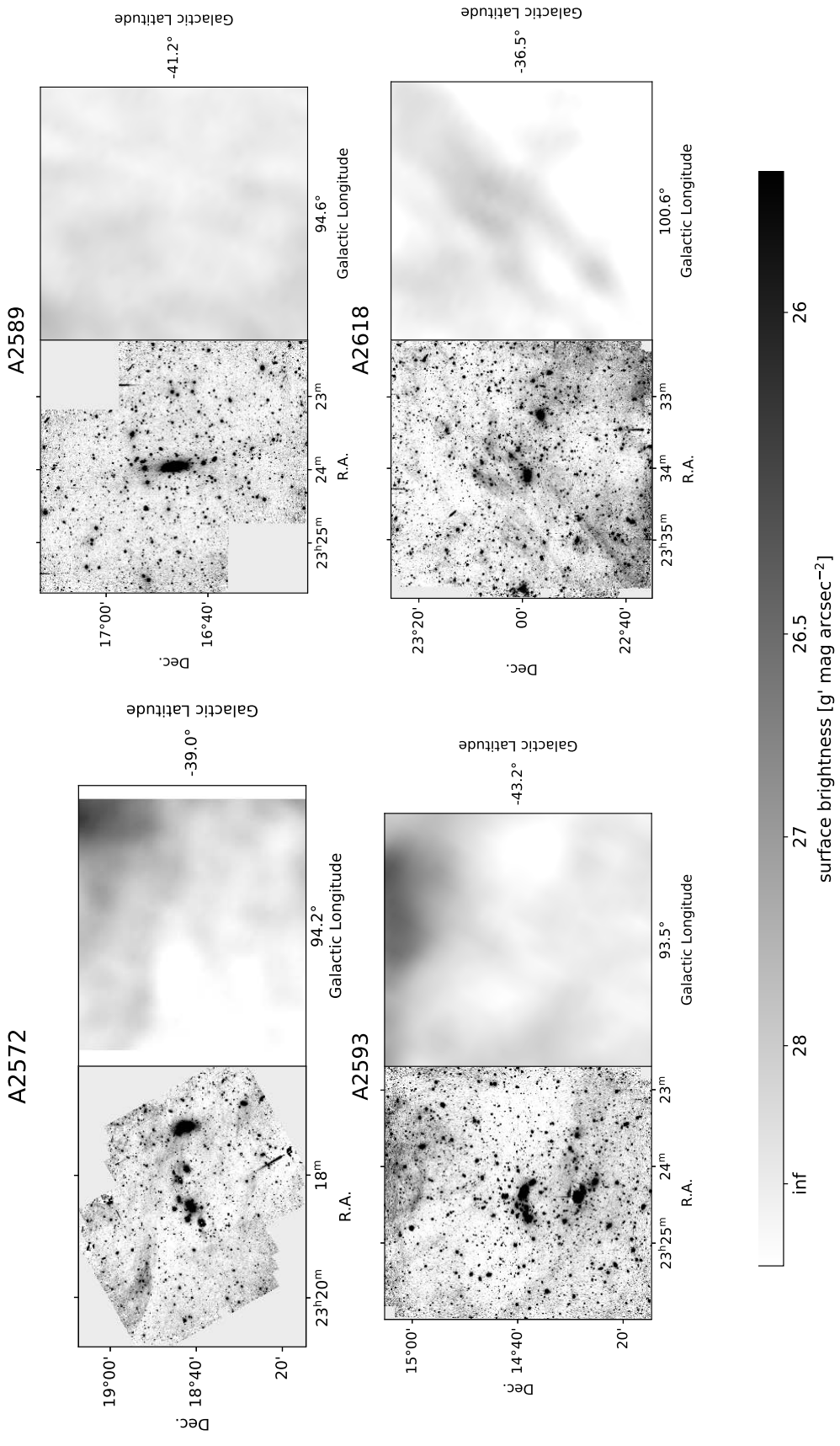

Figure C.1 *(continued)*

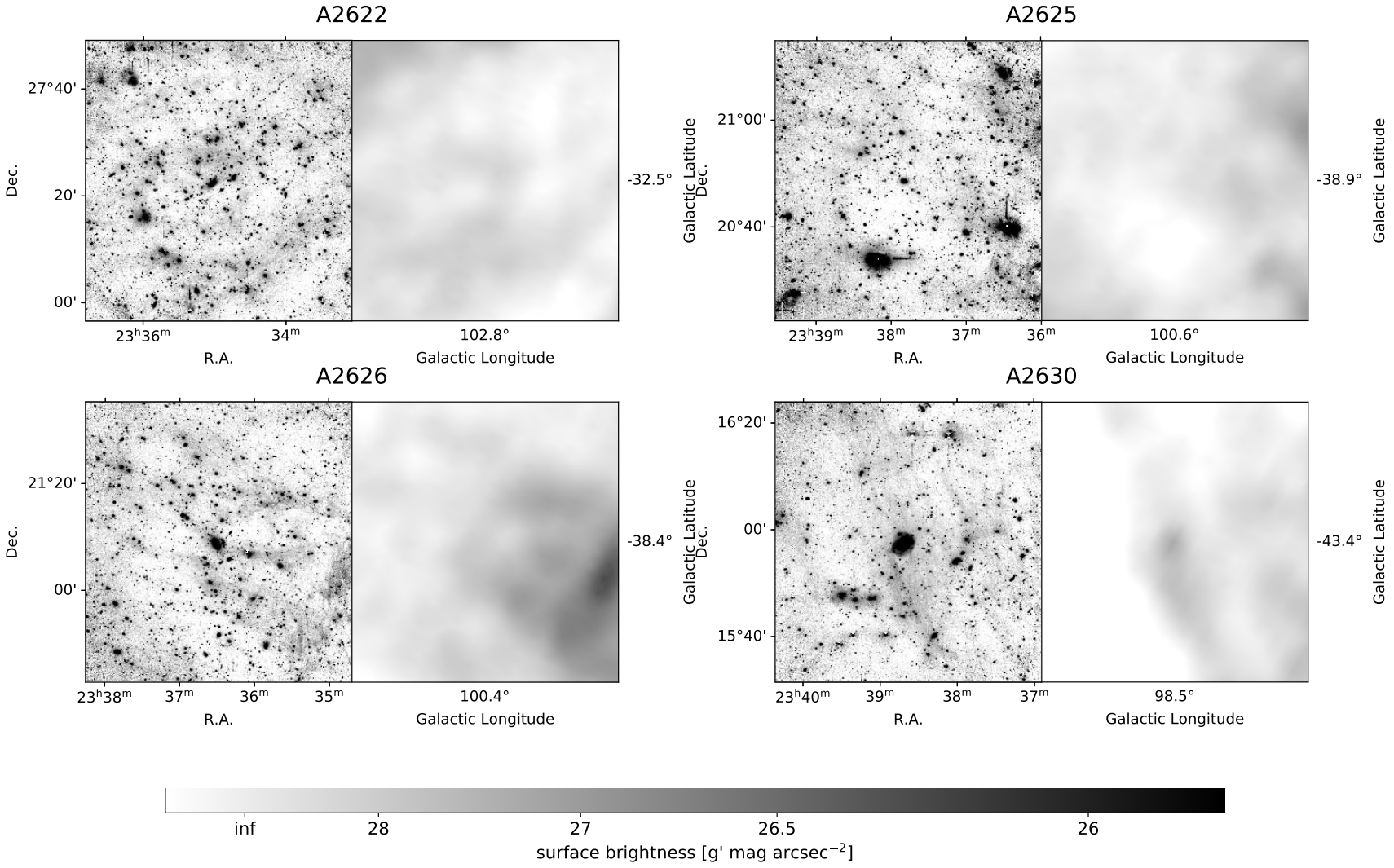

Figure C.1 *(continued)*

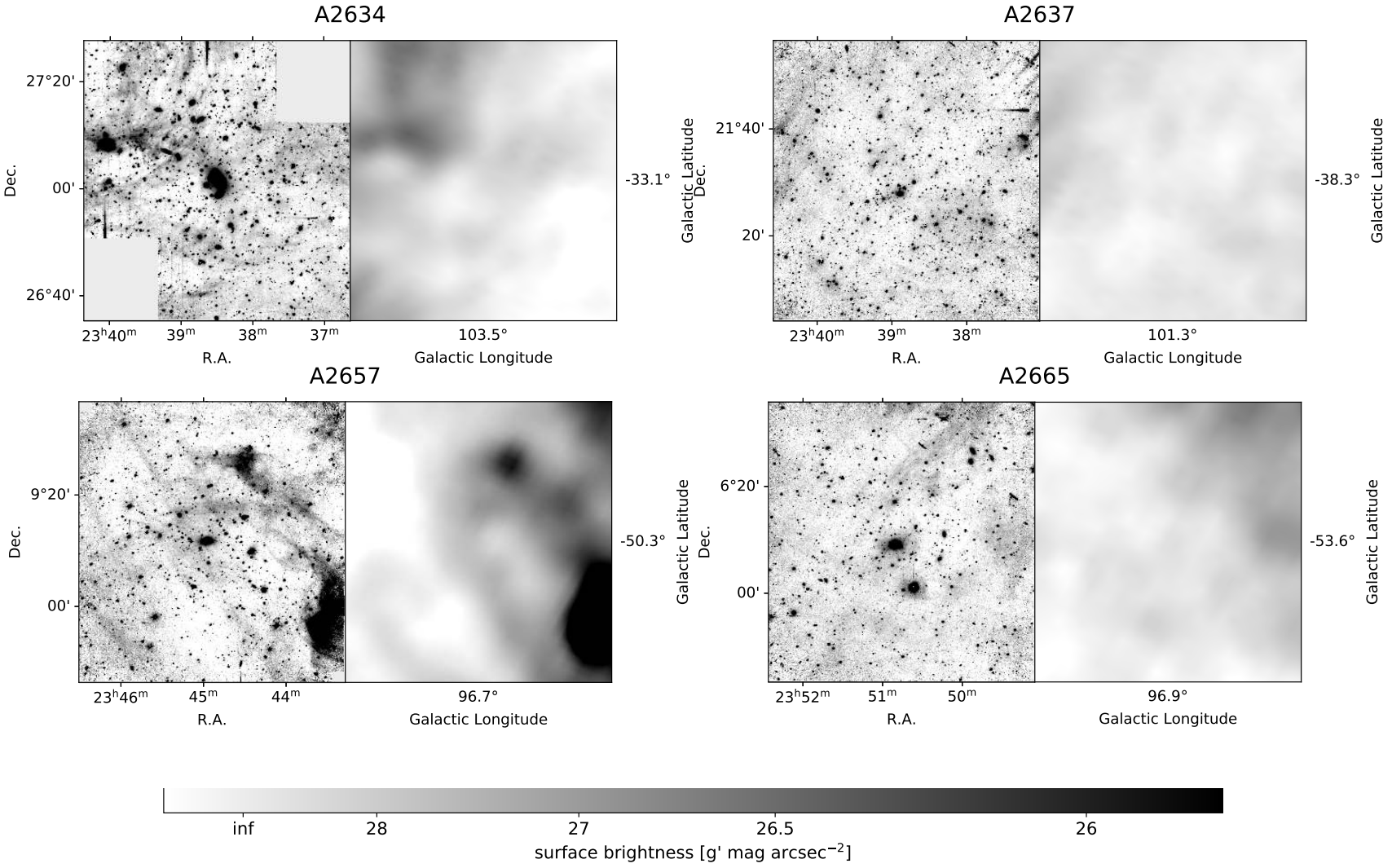

Figure C.1 *(continued)*

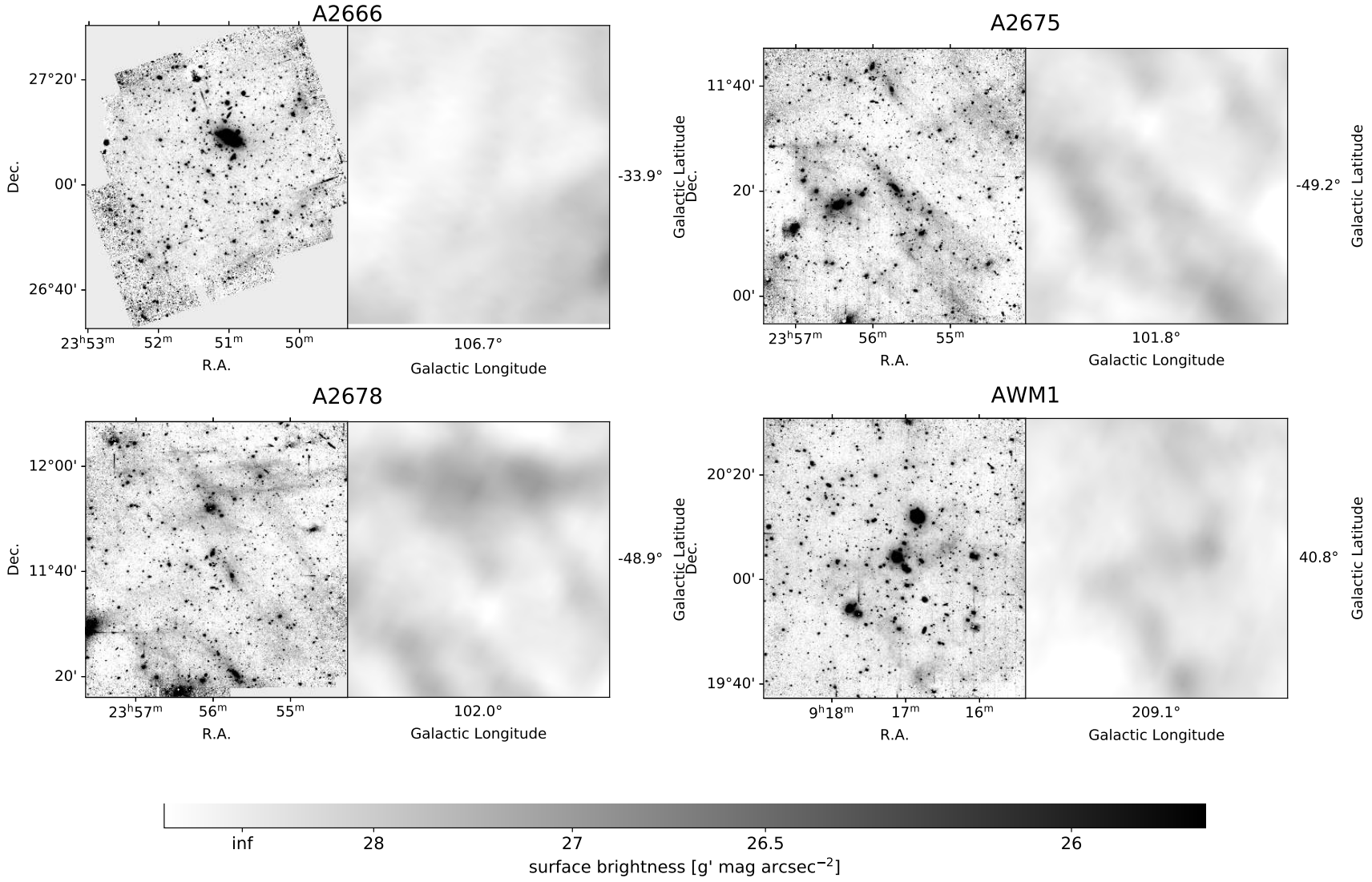

Figure C.1 *(continued)*

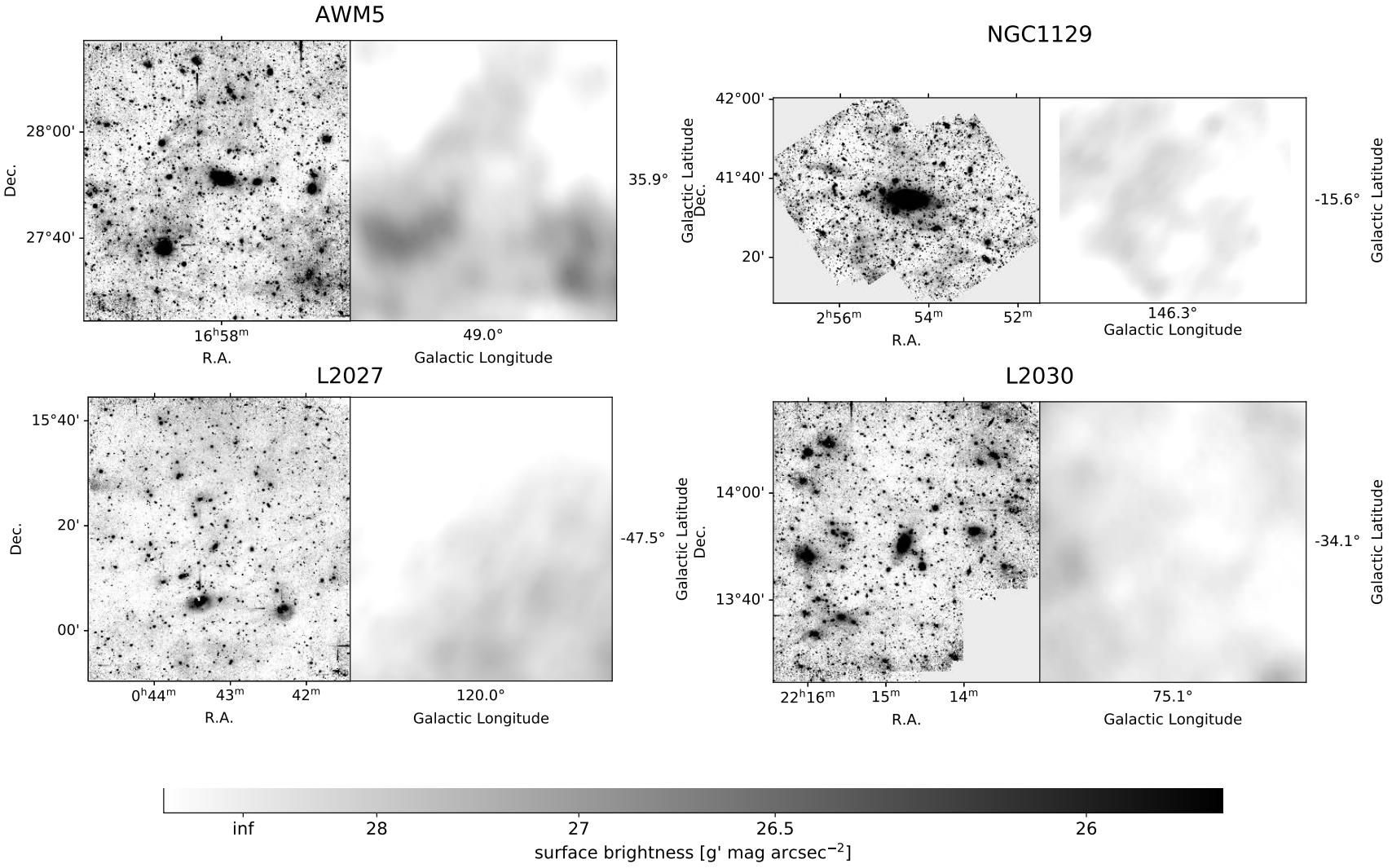

Figure C.1 *(continued)*

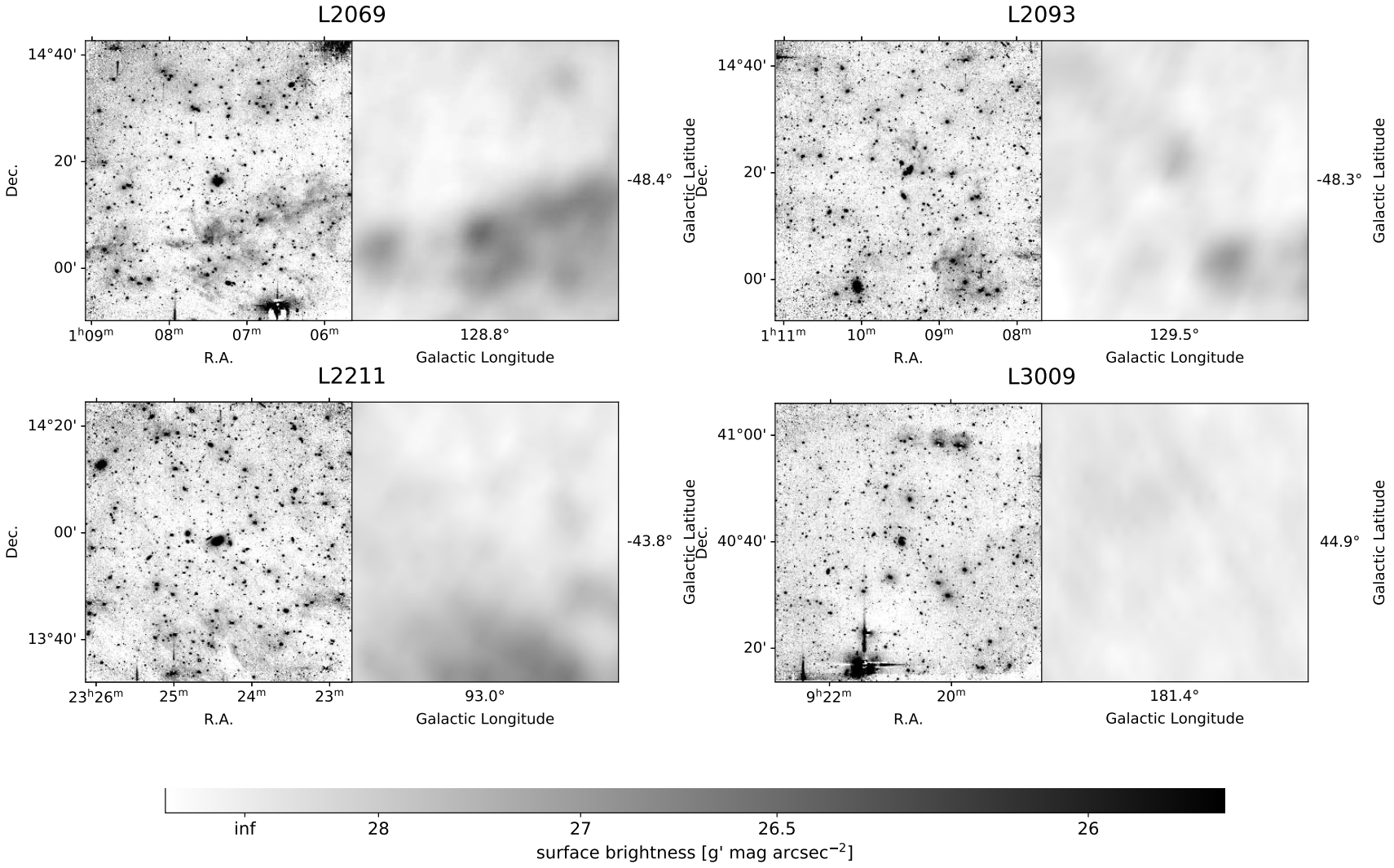

Figure C.1 *(continued)*

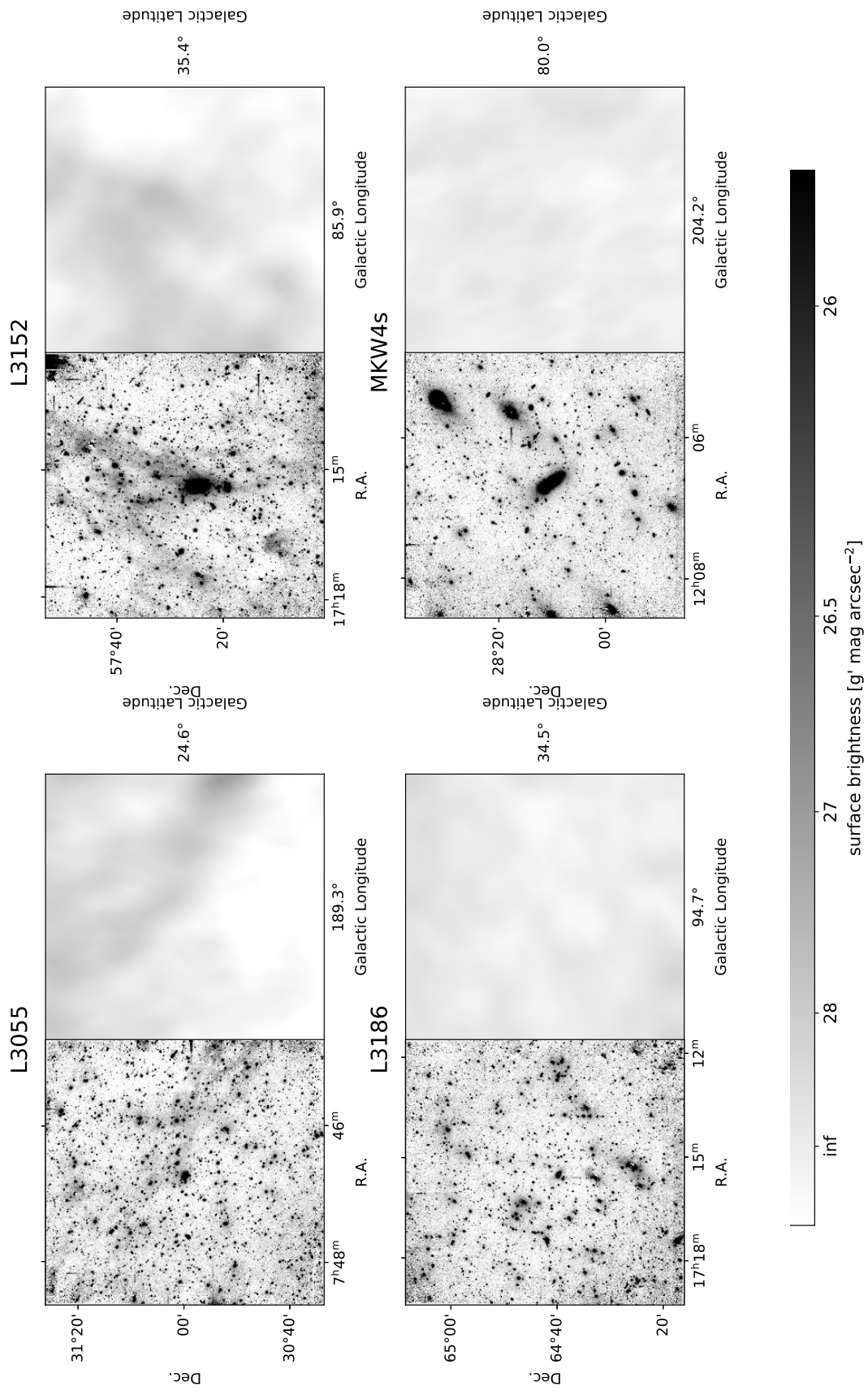

Figure C.1 *(continued)*

Appendix D

Structural Parameters of the BCG+ICLs

Table D.1: Structural Parameters of the BCG+ICLs.

	First Semimajor Axis Sérsic Component			Second Semimajor Axis Sérsic Component				Parameters from 2D Profile Integration			
Cluster	n_1	$r_{e,1}$ (kpc)	$SB_{e,1}$ (g' mag $''^{-2}$)	n_2	$r_{e,2}$ (kpc)	$SB_{e,2}$ (g' mag $''^{-2}$)	$S_2/(S_1+S_2)$	r_e (kpc)	SB_e (g' mag $''^{-2}$)	M_{tot} (g' mag)	Feature
(1)	(2)	(3)	(4)	(5)	(6)	(7)	(8)	(9)	(10)	(11)	(12)
A76	10.24 ± 1.14	$79.43^{+29.66}_{-23.16}$	26.15 ± 0.63	0.46 ± 0.08	$249.7^{+6.95}_{-6.81}$	27.66 ± 0.10	0.38 ± 0.06	147.0 ± 20.37	26.51 ± 0.06	-24.14 ± 0.07	d
A85	1.26 ± 0.29	$15.81^{+0.87}_{-0.84}$	22.43 ± 0.18	4.21 ± 0.70	$208.1^{+10.48}_{-10.10}$	26.74 ± 0.10	0.83 ± 0.04	139.1 ± 32.81	25.84 ± 0.40	-24.79 ± 0.10	...
A150	5.06 ± 0.25	$84.98^{+4.48}_{-4.31}$	25.61 ± 0.11	...	...	...	...	52.19 ± 5.66	24.57 ± 0.18	-23.81 ± 0.06	cd
A152	3.13 ± 0.09	$56.51^{+1.14}_{-1.13}$	24.97 ± 0.05	...	...	...	...	44.02 ± 2.15	24.50 ± 0.06	-23.55 ± 0.03	...
A154	4.28 ± 0.18	$51.08^{+1.38}_{-1.35}$	24.59 ± 0.06	...	...	...	...	43.09 ± 2.93	24.24 ± 0.10	-24.01 ± 0.04	ad
A158	3.90 ± 2.39	$19.24^{+44.43}_{-15.78}$	23.78 ± 1.10	7.95 ± 34.21	$3980^{+7.0E5}_{-2.9E4}$	32.65 ± 19.64	0.84 ± 0.26	1601 ± 1409	29.74 ± 2.32	-24.60 ± 0.60	...
A160	4.96 ± 0.31	$46.13^{+5.73}_{-5.24}$	25.08 ± 0.22	0.17 ± 0.02	$167.4^{+91.10}_{-64.60}$	26.58 ± 0.05	0.54 ± 0.08	130.4 ± 2.31	26.16 ± 0.01	-23.91 ± 0.01	d
A161	11.37 ± 1.55	$863.5^{+436.9}_{-316.3}$	30.28 ± 0.83	...	...	...	...	406.5 ± 277.3	28.25 ± 1.53	-24.43 ± 0.36	c
A171	5.98 ± 0.46	$21.39^{+1.64}_{-1.55}$	23.36 ± 0.15	0.27 ± 0.02	$236.3^{+3.06}_{-3.03}$	26.76 ± 0.04	0.52 ± 0.02	103.2 ± 1.33	26.01 ± 0.03	-24.27 ± 0.01	...
A174	9.89 ± 1.11	$113.9^{+45.75}_{-35.14}$	26.97 ± 0.66	0.38 ± 0.08	$264.6^{+8.22}_{-8.03}$	27.85 ± 0.11	0.30 ± 0.05	86.95 ± 13.94	26.06 ± 0.10	-23.85 ± 0.06	...
A179	8.66 ± 0.88	$100.9^{+34.47}_{-27.43}$	26.63 ± 0.57	0.53 ± 0.17	$382.3^{+28.75}_{-27.21}$	28.46 ± 0.13	0.37 ± 0.06	141.8 ± 26.63	26.77 ± 0.16	-23.64 ± 0.07	cd
A193	7.79 ± 0.98	$243.1^{+41.03}_{-36.42}$	27.38 ± 0.33	...	...	...	...	181.1 ± 67.92	26.55 ± 0.64	-24.67 ± 0.18	d
A225	10.54 ± 1.37	$284.1^{+91.64}_{-73.76}$	28.14 ± 0.58	...	...	...	...	98.82 ± 42.02	25.79 ± 0.79	-24.04 ± 0.18	...
A240	4.22 ± 0.16	$53.47^{+1.47}_{-1.44}$	24.89 ± 0.06	...	...	...	...	40.36 ± 2.35	24.21 ± 0.10	-23.74 ± 0.04	...
A245	5.05 ± 0.53	$16.09^{+0.81}_{-0.78}$	23.78 ± 0.10	...	...	...	...	11.61 ± 0.50	23.16 ± 0.09	-22.43 ± 0.02	...
A257	2.92 ± 0.16	$21.81^{+0.51}_{-0.50}$	23.33 ± 0.05	...	...	...	...	17.46 ± 0.33	22.88 ± 0.03	-23.02 ± 0.01	...
A260	7.58 ± 0.53	$115.0^{+13.55}_{-12.45}$	26.47 ± 0.23	...	...	...	...	53.07 ± 10.64	24.87 ± 0.42	-23.60 ± 0.10	...
A262	2.96 ± 0.11	$54.26^{+1.32}_{-1.29}$	25.02 ± 0.06	...	...	...	...	32.70 ± 1.18	24.11 ± 0.06	-22.89 ± 0.02	d
A292	4.57 ± 0.19	$81.07^{+2.85}_{-2.78}$	24.92 ± 0.08	...	...	...	...	66.02 ± 6.35	24.51 ± 0.13	-24.01 ± 0.05	...
A347	7.54 ± 0.54	$36.97^{+3.37}_{-3.15}$	25.26 ± 0.19	...	...	...	...	27.57 ± 3.94	24.51 ± 0.26	-22.60 ± 0.08	d
A376	11.17 ± 1.00	$446.3^{+116.5}_{-97.41}$	29.10 ± 0.47	...	...	...	...	244.3 ± 147.5	27.48 ± 1.34	-24.24 ± 0.29	...
A397	5.66 ± 0.35	$55.34^{+3.93}_{-3.74}$	25.14 ± 0.15	...	...	...	...	38.04 ± 4.09	24.23 ± 0.24	-23.42 ± 0.06	c
A399	2.85 ± 0.11	$65.11^{+1.72}_{-1.68}$	24.20 ± 0.06	...	...	...	...	58.36 ± 1.51	23.91 ± 0.05	-24.39 ± 0.02	c
A400	4.52 ± 0.90	$4.92^{+1.46}_{-1.20}$	21.94 ± 0.51	1.05 ± 0.09	$65.23^{+1.67}_{-1.64}$	25.10 ± 0.07	0.79 ± 0.02	46.56 ± 0.39	24.68 ± 0.01	-23.20 ± 0.01	d
A407	1.90 ± 0.14	$34.91^{+1.28}_{-1.25}$	23.45 ± 0.09	...	...	...	...	29.50 ± 0.22	23.03 ± 0.02	-23.77 ± 0.01	d
A426	4.25 ± 0.28	$14.55^{+1.32}_{-1.23}$	22.42 ± 0.17	0.44 ± 0.04	$97.04^{+1.42}_{-1.41}$	25.86 ± 0.07	0.37 ± 0.03	30.46 ± 0.30	23.75 ± 0.02	-23.64 ± 0.00	d
A498	5.38 ± 0.39	$98.41^{+9.35}_{-8.73}$	25.39 ± 0.19	...	...	...	...	55.21 ± 6.92	24.29 ± 0.21	-24.12 ± 0.06	b
A505	4.45 ± 0.17	$30.15^{+0.66}_{-0.65}$	23.43 ± 0.05	...	...	...	...	27.45 ± 0.90	23.12 ± 0.06	-24.00 ± 0.02	...
A539	4.44 ± 0.72	$45.65^{+21.11}_{-15.66}$	24.99 ± 0.66	0.42 ± 0.10	$97.99^{+2.44}_{-2.39}$	25.93 ± 0.16	0.37 ± 0.11	59.06 ± 3.11	24.85 ± 0.09	-23.49 ± 0.03	d
A553	2.66 ± 0.38	$7.14^{+1.19}_{-1.06}$	21.55 ± 0.27	2.62 ± 0.33	$505.6^{+64.47}_{-58.84}$	27.22 ± 0.23	0.93 ± 0.01	405.4 ± 47.01	26.73 ± 0.06	-25.35 ± 0.09	...

A559	2.73 ± 0.59	$3.34^{+0.57}_{-0.50}$	20.81 ± 0.28	1.75 ± 0.18	$51.18^{+2.53}_{-2.44}$	25.08 ± 0.11	0.75 ± 0.04	29.36 ± 0.80	24.02 ± 0.03	-23.25 ± 0.02	...
A568	25.83 ± 11.10	$228.5^{+284.6}_{-145.7}$	28.10 ± 1.88	...	...	...	...	191.4 ± 139.2	26.89 ± 2.01	-24.35 ± 0.32	...
A569	4.60 ± 0.21	$9.76^{+0.29}_{-0.29}$	22.59 ± 0.06	...	...	...	...	9.95 ± 0.20	22.49 ± 0.04	-22.26 ± 0.01	d
A582	9.41 ± 1.38	$69.87^{+12.36}_{-10.91}$	26.14 ± 0.35	...	...	...	...	52.96 ± 18.66	25.51 ± 1.02	-23.56 ± 0.14	...
A592	2.44 ± 0.13	$122.2^{+5.81}_{-5.61}$	25.21 ± 0.10	...	...	...	...	87.88 ± 2.98	24.40 ± 0.06	-24.31 ± 0.02	cd
A595	8.26 ± 1.46	$8.71^{+2.46}_{-2.03}$	22.68 ± 0.50	0.77 ± 0.07	$61.35^{+1.08}_{-1.07}$	25.34 ± 0.06	0.55 ± 0.04	34.36 ± 0.83	24.32 ± 0.02	-23.15 ± 0.01	a
A600	3.93 ± 0.20	$27.38^{+1.64}_{-1.57}$	23.97 ± 0.12	0.42 ± 0.18	$355.8^{+29.61}_{-27.87}$	29.48 ± 0.19	0.29 ± 0.04	59.45 ± 8.92	25.71 ± 0.53	-23.57 ± 0.06	d
A602	3.53 ± 0.31	$30.25^{+6.15}_{-5.34}$	24.66 ± 0.31	1.14 ± 0.16	$391.2^{+20.67}_{-19.88}$	27.70 ± 0.11	0.71 ± 0.03	172.0 ± 13.04	26.43 ± 0.04	-23.87 ± 0.04	c
A607	2.67 ± 0.28	$126.0^{+14.45}_{-13.30}$	26.43 ± 0.22	...	...	...	...	121.7 ± 16.37	26.41 ± 0.45	-23.86 ± 0.08	...
A612	20.24 ± 14.22	$199.4^{+389.8}_{-154.5}$	28.98 ± 2.60	...	...	...	...	106.7 ± 78.96	26.81 ± 2.01	-23.11 ± 0.31	...
A634	7.14 ± 0.57	$22.81^{+1.24}_{-1.19}$	24.17 ± 0.12	...	...	...	...	24.07 ± 3.09	24.40 ± 0.24	-22.69 ± 0.06	b
A671	3.57 ± 0.16	$44.18^{+1.31}_{-1.28}$	24.05 ± 0.07	...	...	...	...	40.45 ± 1.44	23.76 ± 0.05	-23.99 ± 0.02	...
A688	3.98 ± 0.19	$41.54^{+0.83}_{-0.82}$	23.87 ± 0.04	...	...	...	...	39.34 ± 1.61	23.73 ± 0.09	-24.27 ± 0.03	...
A690	3.88 ± 0.19	$53.45^{+1.73}_{-1.69}$	24.59 ± 0.07	...	...	...	...	41.56 ± 2.17	24.04 ± 0.08	-24.09 ± 0.03	...
A695	3.92 ± 0.25	$20.80^{+0.75}_{-0.73}$	23.11 ± 0.08	...	...	...	...	20.48 ± 0.69	23.02 ± 0.08	-23.40 ± 0.02	d
A734	3.52 ± 0.18	$24.94^{+0.66}_{-0.65}$	23.80 ± 0.06	...	...	...	...	20.49 ± 0.65	23.36 ± 0.07	-23.23 ± 0.02	...
A744	17.44 ± 2.28	$142.8^{+32.98}_{-28.10}$	27.39 ± 0.45	...	...	...	...	114.8 ± 66.44	26.53 ± 1.34	-24.03 ± 0.25	...
A757	9.20 ± 1.09	$38.77^{+10.41}_{-8.66}$	25.53 ± 0.48	0.46 ± 0.16	$227.8^{+14.11}_{-13.49}$	28.93 ± 0.15	0.26 ± 0.05	62.10 ± 12.01	26.30 ± 0.44	-23.04 ± 0.07	...
A834	3.70 ± 0.32	$36.13^{+5.80}_{-5.17}$	24.14 ± 0.27	0.38 ± 0.08	$199.8^{+5.89}_{-5.76}$	26.75 ± 0.09	0.48 ± 0.04	98.28 ± 1.96	25.81 ± 0.07	-23.94 ± 0.01	...
A883	18.08 ± 3.28	$2.1E3^{+2.0E3}_{-1.1E3}$	32.40 ± 1.45	...	...	...	...	9.8E2 ± 8.9E2	29.31 ± 2.90	-24.26 ± 0.54	...
A999	8.02 ± 0.66	$32.61^{+2.37}_{-2.24}$	24.86 ± 0.15	...	...	...	...	20.98 ± 2.34	23.90 ± 0.16	-22.71 ± 0.05	c
A1003	4.31 ± 0.33	$36.78^{+1.82}_{-1.76}$	24.54 ± 0.11	...	...	...	...	25.45 ± 1.36	23.63 ± 0.11	-23.18 ± 0.03	...
A1016	21.23 ± 4.11	$163.0^{+90.82}_{-63.95}$	28.56 ± 0.97	...	...	...	...	79.53 ± 53.95	26.50 ± 1.72	-22.93 ± 0.29	c
A1020	5.62 ± 0.53	$24.36^{+1.17}_{-1.13}$	24.11 ± 0.10	...	...	...	...	19.58 ± 1.57	23.69 ± 0.13	-23.14 ± 0.04	...
A1056	3.55 ± 0.20	$65.15^{+2.44}_{-2.38}$	25.38 ± 0.08	...	...	...	...	43.42 ± 2.53	24.50 ± 0.08	-23.64 ± 0.04	...
A1066	2.20 ± 0.22	$7.67^{+0.90}_{-0.82}$	21.82 ± 0.18	1.91 ± 0.30	$125.9^{+6.42}_{-6.19}$	26.62 ± 0.11	0.73 ± 0.03	72.69 ± 6.01	25.71 ± 0.15	-23.68 ± 0.04	d
A1100	6.87 ± 0.27	$53.62^{+2.03}_{-1.98}$	25.34 ± 0.08	...	...	...	...	33.82 ± 4.71	24.32 ± 0.26	-23.18 ± 0.07	c
A1108	8.45 ± 1.01	$28.66^{+3.57}_{-3.27}$	25.50 ± 0.26	...	...	...	...	24.12 ± 6.22	25.06 ± 0.52	-21.91 ± 0.11	cd
A1142	6.10 ± 0.56	$23.57^{+1.38}_{-1.32}$	23.96 ± 0.13	...	...	...	...	23.30 ± 1.83	23.76 ± 0.10	-22.95 ± 0.04	bcd
A1155	10.04 ± 1.02	$61.36^{+5.66}_{-5.29}$	25.80 ± 0.19	...	...	...	...	34.94 ± 8.40	24.52 ± 0.54	-23.27 ± 0.11	...
A1173	5.52 ± 0.49	$83.91^{+19.15}_{-16.35}$	26.04 ± 0.39	0.35 ± 0.12	$443.2^{+27.33}_{-26.12}$	28.68 ± 0.16	0.39 ± 0.05	174.7 ± 16.46	27.12 ± 0.09	-24.26 ± 0.04	d
A1177	7.46 ± 1.61	$28.62^{+29.08}_{-16.40}$	24.61 ± 1.31	1.38 ± 0.24	$72.57^{+3.32}_{-3.21}$	25.51 ± 0.10	0.53 ± 0.14	40.15 ± 1.45	24.21 ± 0.03	-23.41 ± 0.02	bc
A1185	6.36 ± 1.01	$24.46^{+2.18}_{-2.04}$	23.69 ± 0.19	...	...	...	...	29.76 ± 2.89	24.31 ± 0.17	-23.25 ± 0.05	d
A1187	12.79 ± 2.03	$149.0^{+41.06}_{-34.02}$	27.12 ± 0.52	...	...	...	...	66.69 ± 25.34	25.48 ± 0.90	-23.95 ± 0.16	a
A1190	2.09 ± 0.24	$25.66^{+3.29}_{-3.00}$	23.26 ± 0.21	0.66 ± 0.09	$188.7^{+7.98}_{-7.74}$	26.43 ± 0.12	0.54 ± 0.04	71.25 ± 1.08	24.96 ± 0.02	-24.13 ± 0.01	a
A1203	7.09 ± 0.51	$41.24^{+6.46}_{-5.78}$	24.71 ± 0.29	0.63 ± 0.11	$309.7^{+11.10}_{-10.81}$	28.31 ± 0.09	0.37 ± 0.04	102.5 ± 9.87	26.22 ± 0.13	-24.11 ± 0.04	...
A1213	1.60 ± 0.17	$6.38^{+0.42}_{-0.40}$	21.23 ± 0.08	3.20 ± 1.36	$106.8^{+14.77}_{-13.39}$	27.30 ± 0.28	0.60 ± 0.08	31.21 ± 5.41	24.94 ± 0.24	-23.03 ± 0.06	c

A1218	10.98 ± 1.69	$149.7^{+86.54}_{-60.26}$	28.26 ± 0.92	0.35 ± 0.17	$407.0^{+37.39}_{-34.98}$	29.66 ± 0.22	0.28 ± 0.09	165.7 ± 58.25	27.89 ± 0.61	-23.25 ± 0.15	...
A1228	3.49 ± 0.11	$21.41^{+0.37}_{-0.37}$	23.18 ± 0.04	...	...	...	...	21.59 ± 0.40	23.15 ± 0.04	-23.23 ± 0.01	cd
A1257	2.09 ± 0.32	$2.39^{+0.22}_{-0.20}$	20.77 ± 0.16	1.76 ± 0.16	$52.39^{+1.63}_{-1.60}$	25.56 ± 0.07	0.77 ± 0.02	26.73 ± 0.73	24.39 ± 0.03	-22.35 ± 0.02	c
A1270	2.51 ± 0.10	$18.01^{+0.42}_{-0.41}$	23.28 ± 0.05	...	...	...	...	15.03 ± 0.18	22.94 ± 0.02	-22.89 ± 0.01	...
A1275	14.93 ± 2.60	$9.17^{+1.60}_{-1.41}$	22.32 ± 0.36	...	...	...	...	18.98 ± 4.11	23.89 ± 0.49	-22.76 ± 0.10	...
A1279	2.57 ± 0.10	$20.53^{+0.42}_{-0.42}$	23.55 ± 0.04	...	...	...	...	16.44 ± 0.27	23.16 ± 0.03	-22.70 ± 0.01	...
A1314	6.56 ± 1.51	$7.29^{+2.44}_{-1.95}$	22.05 ± 0.58	1.18 ± 0.07	$71.91^{+0.99}_{-0.98}$	25.23 ± 0.07	0.63 ± 0.05	37.27 ± 0.52	24.10 ± 0.02	-23.29 ± 0.01	c
A1324	6.12 ± 0.72	$19.46^{+2.15}_{-1.98}$	23.54 ± 0.22	0.69 ± 0.19	$478.3^{+50.14}_{-46.48}$	28.83 ± 0.20	0.59 ± 0.04	232.0 ± 33.94	27.96 ± 0.18	-24.38 ± 0.07	...
A1356	4.97 ± 0.38	$22.59^{+0.81}_{-0.79}$	24.30 ± 0.08	...	...	...	...	20.84 ± 1.48	24.15 ± 0.14	-22.68 ± 0.04	...
A1365	7.67 ± 1.11	$20.60^{+4.61}_{-3.95}$	23.93 ± 0.42	0.96 ± 0.18	$347.5^{+23.21}_{-22.10}$	28.67 ± 0.13	0.50 ± 0.05	118.3 ± 22.60	26.94 ± 0.29	-23.67 ± 0.07	d
A1367	9.80 ± 0.77	$74.47^{+9.17}_{-8.40}$	26.12 ± 0.25	...	...	...	...	52.23 ± 15.99	25.32 ± 0.66	-23.32 ± 0.13	...
A1371	2.03 ± 0.63	$3.87^{+0.73}_{-0.64}$	21.24 ± 0.30	2.12 ± 0.21	$104.7^{+4.49}_{-4.35}$	25.62 ± 0.09	0.89 ± 0.02	72.45 ± 3.19	24.77 ± 0.05	-23.89 ± 0.03	a
A1400	16.49 ± 5.48	$15.57^{+2.30}_{-2.07}$	24.50 ± 0.30	...	...	...	...	20.56 ± 6.68	24.98 ± 0.75	-21.67 ± 0.15	...
A1413	16.34 ± 1.91	7256^{+4667}_{-3141}	32.50 ± 1.01	...	...	...	...	3083 ± 2766	29.14 ± 2.90	-26.19 ± 0.53	...
A1423	3.58 ± 0.13	$19.46^{+0.93}_{-0.90}$	23.54 ± 0.09	0.76 ± 0.15	$225.1^{+10.64}_{-10.27}$	28.73 ± 0.10	0.33 ± 0.03	41.62 ± 3.99	25.20 ± 0.29	-23.43 ± 0.04	d
A1424	8.93 ± 1.58	$151.7^{+40.16}_{-33.50}$	26.67 ± 0.51	...	...	...	...	97.78 ± 32.81	25.63 ± 0.95	-24.35 ± 0.15	c
A1435	4.66 ± 0.37	$49.23^{+3.08}_{-2.94}$	25.17 ± 0.13	...	...	...	...	31.17 ± 3.19	24.12 ± 0.32	-23.26 ± 0.05	c
A1436	7.29 ± 2.50	$18.40^{+20.06}_{-10.95}$	23.98 ± 1.50	1.44 ± 0.37	$147.5^{+8.09}_{-7.77}$	27.10 ± 0.21	0.54 ± 0.12	53.41 ± 2.82	25.22 ± 0.08	-23.38 ± 0.03	ac
A1452	7.27 ± 0.72	$51.62^{+4.06}_{-3.83}$	25.15 ± 0.16	...	...	...	...	38.79 ± 6.49	24.48 ± 0.34	-23.50 ± 0.08	a
A1507	5.49 ± 0.41	$35.45^{+1.64}_{-1.59}$	24.48 ± 0.10	...	...	...	...	29.02 ± 2.57	24.00 ± 0.20	-23.30 ± 0.05	...
A1516	4.63 ± 0.22	$63.37^{+2.29}_{-2.23}$	24.89 ± 0.08	...	...	...	...	47.19 ± 3.66	24.27 ± 0.13	-24.16 ± 0.04	...
A1526	15.44 ± 4.15	$56.23^{+47.20}_{-28.84}$	26.32 ± 1.33	0.50 ± 0.14	$265.9^{+15.58}_{-14.92}$	28.53 ± 0.14	0.29 ± 0.11	61.94 ± 12.16	26.22 ± 0.29	-23.20 ± 0.07	...
A1534	4.69 ± 0.30	$38.13^{+1.38}_{-1.35}$	24.33 ± 0.08	...	...	...	...	32.85 ± 2.33	23.95 ± 0.13	-23.62 ± 0.04	...
A1569	4.58 ± 2.62	$3.76^{+1.31}_{-1.04}$	21.05 ± 0.61	2.11 ± 0.25	$146.9^{+8.02}_{-7.70}$	26.31 ± 0.11	0.83 ± 0.04	98.19 ± 5.54	25.42 ± 0.08	-23.79 ± 0.04	c
A1589	6.67 ± 0.66	$160.4^{+23.56}_{-21.22}$	26.39 ± 0.29	...	...	...	...	123.5 ± 30.95	25.91 ± 0.49	-24.59 ± 0.11	bc
A1610	3.74 ± 0.19	$22.92^{+0.57}_{-0.56}$	23.61 ± 0.05	...	...	...	...	16.78 ± 0.48	23.09 ± 0.06	-23.22 ± 0.02	c
A1656	9.00 ± 0.90	$784.0^{+291.1}_{-227.6}$	29.30 ± 0.62	...	...	...	...	421.2 ± 234.7	27.58 ± 1.35	-24.97 ± 0.29	ac
A1668	2.97 ± 0.17	$27.35^{+2.36}_{-2.22}$	23.68 ± 0.15	0.86 ± 0.17	$274.4^{+13.58}_{-13.09}$	28.12 ± 0.11	0.40 ± 0.04	56.30 ± 3.68	25.20 ± 0.12	-23.78 ± 0.03	c
A1691	16.87 ± 3.63	$552.0^{+404.7}_{-260.3}$	29.33 ± 1.19	...	...	...	...	333.8 ± 220.2	27.73 ± 1.61	-24.87 ± 0.33	c
A1749	11.20 ± 0.95	$104.6^{+12.95}_{-11.85}$	26.48 ± 0.25	...	...	...	...	68.99 ± 24.29	25.46 ± 0.82	-23.84 ± 0.15	...
A1767	5.38 ± 0.33	$195.9^{+17.03}_{-15.99}$	26.57 ± 0.17	...	...	...	...	131.7 ± 31.46	25.71 ± 0.37	-24.64 ± 0.11	b
A1775	7.31 ± 0.44	$153.9^{+13.16}_{-12.36}$	26.64 ± 0.17	...	...	...	...	126.1 ± 38.52	26.11 ± 0.69	-24.49 ± 0.14	...
A1795	3.47 ± 1.27	$17.68^{+9.39}_{-6.70}$	23.05 ± 0.79	1.42 ± 0.14	$199.2^{+10.21}_{-9.83}$	26.00 ± 0.14	0.78 ± 0.06	127.7 ± 4.72	25.23 ± 0.05	-24.64 ± 0.02	c
A1800	3.57 ± 0.15	$79.54^{+2.45}_{-2.40}$	24.29 ± 0.07	...	...	...	...	67.94 ± 3.40	23.83 ± 0.08	-24.55 ± 0.03	bc
A1809	9.12 ± 0.90	$111.7^{+33.43}_{-27.30}$	26.16 ± 0.52	0.16 ± 0.01	$71.76^{+3.2E8}_{-2.7E8}$	27.31 ± 0.15	0.24 ± 0.01	85.80 ± 13.65	25.46 ± 0.17	-24.41 ± 0.06	b
A1812	6.03 ± 0.55	$121.9^{+17.05}_{-15.43}$	27.31 ± 0.27	...	...	...	...	90.05 ± 30.34	26.67 ± 0.95	-23.20 ± 0.16	...
A1825	3.87 ± 0.22	$29.28^{+0.85}_{-0.84}$	24.21 ± 0.07	...	...	...	...	23.63 ± 1.06	23.75 ± 0.07	-23.08 ± 0.03	acd

A1828	10.99 ± 2.26	$3.03^{+1.36}_{-1.01}$	19.58 ± 0.90	...	...	...	...	10.07 ± 0.57	22.20 ± 0.14	-22.49 ± 0.03	...
A1831	6.44 ± 0.35	$270.2^{+25.54}_{-23.85}$	27.04 ± 0.18	...	...	...	...	226.1 ± 63.27	26.60 ± 0.56	-25.07 ± 0.16	...
A1890	5.95 ± 0.37	$53.23^{+2.46}_{-2.37}$	24.57 ± 0.10	...	...	...	...	38.85 ± 3.46	23.83 ± 0.23	-23.95 ± 0.05	...
A1899	2.76 ± 0.16	$9.60^{+0.53}_{-0.51}$	22.02 ± 0.11	0.87 ± 0.27	$119.3^{+8.62}_{-8.18}$	27.87 ± 0.15	0.27 ± 0.03	17.13 ± 0.41	23.21 ± 0.07	-22.87 ± 0.01	d
A1904	6.83 ± 0.43	$164.3^{+15.21}_{-14.22}$	26.61 ± 0.18	...	...	...	...	123.6 ± 37.51	25.86 ± 0.68	-24.43 ± 0.13	...
A1913	8.87 ± 0.80	$77.53^{+9.44}_{-8.65}$	26.47 ± 0.24	...	...	...	...	37.30 ± 9.84	24.86 ± 0.49	-23.08 ± 0.12	...
A1982	3.97 ± 0.22	$37.70^{+1.30}_{-1.27}$	24.30 ± 0.08	...	...	...	...	31.80 ± 1.78	24.01 ± 0.10	-23.18 ± 0.03	b
A1983	16.03 ± 2.07	$1047^{+613.8}_{-425.5}$	31.42 ± 0.95	...	...	...	...	431.5 ± 352.1	28.58 ± 2.22	-23.72 ± 0.43	...
A2022	24.43 ± 4.06	$3.3E4^{+5.7E4}_{-2.4E4}$	36.96 ± 2.17	...	...	...	...	1.1E4 ± 1.1E4	31.16 ± 5.02	-25.12 ± 0.80	...
A2029	5.55 ± 0.26	$261.2^{+17.47}_{-16.64}$	26.08 ± 0.14	...	...	...	...	329.3 ± 82.12	26.53 ± 0.73	-25.85 ± 0.12	...
A2052	4.02 ± 0.23	$79.16^{+4.74}_{-4.54}$	25.32 ± 0.12	...	...	...	...	47.87 ± 2.12	24.33 ± 0.11	-23.64 ± 0.03	d
A2061	23.24 ± 6.48	$1.6E5^{+7.8E5}_{-1.5E5}$	38.80 ± 4.12	...	...	...	...	64592 ± 64343	32.39 ± 5.97	-26.02 ± 1.10	b
A2063	8.46 ± 0.64	$345.6^{+68.57}_{-59.69}$	28.41 ± 0.36	...	...	...	...	202.1 ± 103.1	27.00 ± 1.21	-24.02 ± 0.23	...
A2065	7.58 ± 2.29	$25.55^{+23.75}_{-13.92}$	24.42 ± 1.34	1.24 ± 0.30	$189.5^{+10.79}_{-10.35}$	27.35 ± 0.18	0.58 ± 0.13	91.60 ± 6.60	25.79 ± 0.11	-23.78 ± 0.04	...
A2107	3.31 ± 0.11	$35.71^{+1.28}_{-1.24}$	23.78 ± 0.07	0.43 ± 0.08	$352.5^{+11.00}_{-10.75}$	28.74 ± 0.08	0.27 ± 0.02	60.10 ± 3.01	24.85 ± 0.15	-24.09 ± 0.02	c
A2122	3.35 ± 0.13	$58.19^{+1.52}_{-1.49}$	24.53 ± 0.06	...	...	...	...	43.82 ± 1.52	23.86 ± 0.09	-24.03 ± 0.02	...
A2147	1.43 ± 0.39	$6.32^{+0.79}_{-0.73}$	21.78 ± 0.17	1.77 ± 0.16	$85.49^{+2.93}_{-2.86}$	25.26 ± 0.07	0.84 ± 0.03	56.15 ± 1.32	24.44 ± 0.04	-23.50 ± 0.01	a
A2151	8.91 ± 0.70	$152.4^{+23.52}_{-21.08}$	27.21 ± 0.30	...	...	...	...	111.9 ± 42.43	26.48 ± 0.69	-23.80 ± 0.17	...
A2152	5.51 ± 0.30	$11.78^{+0.86}_{-0.81}$	22.89 ± 0.14	0.52 ± 0.03	$188.8^{+3.04}_{-3.00}$	26.92 ± 0.04	0.60 ± 0.01	95.39 ± 2.25	26.13 ± 0.01	-23.56 ± 0.01	a
A2162	6.36 ± 0.51	$20.11^{+3.50}_{-3.09}$	23.52 ± 0.30	0.70 ± 0.09	$99.66^{+2.09}_{-2.06}$	26.38 ± 0.09	0.34 ± 0.03	33.13 ± 1.06	24.15 ± 0.06	-23.22 ± 0.02	c
A2197	5.19 ± 0.29	$35.00^{+1.42}_{-1.37}$	23.89 ± 0.09	...	...	...	...	28.29 ± 1.63	23.51 ± 0.13	-23.48 ± 0.03	b
A2199	7.23 ± 0.19	$144.2^{+6.09}_{-5.90}$	26.31 ± 0.09	...	...	...	...	101.7 ± 27.05	25.50 ± 0.50	-24.22 ± 0.12	d
A2247	6.31 ± 1.29	$72.43^{+24.69}_{-19.65}$	26.30 ± 0.61	...	...	...	...	40.63 ± 5.83	25.14 ± 0.43	-22.93 ± 0.08	...
A2248	4.39 ± 0.27	$39.20^{+1.40}_{-1.36}$	24.60 ± 0.08	...	...	...	...	26.15 ± 1.42	23.66 ± 0.09	-23.27 ± 0.03	...
A2255	23.77 ± 6.61	9338^{+23985}_{-7908}	34.64 ± 2.92	...	...	...	...	5055 ± 4844	30.86 ± 3.90	-25.53 ± 0.75	...
A2256	10.96 ± 1.14	$217.4^{+45.73}_{-39.50}$	27.41 ± 0.40	...	...	...	...	169.2 ± 71.65	26.54 ± 0.77	-24.61 ± 0.20	a
A2271	6.17 ± 0.29	$111.9^{+6.54}_{-6.26}$	25.99 ± 0.12	...	...	...	...	56.83 ± 7.09	24.61 ± 0.22	-23.96 ± 0.07	c
A2293	8.59 ± 1.13	$85.51^{+14.85}_{-13.14}$	26.10 ± 0.34	...	...	...	...	89.57 ± 27.84	26.16 ± 0.64	-23.81 ± 0.12	d
A2308	10.92 ± 1.49	$270.9^{+83.32}_{-67.68}$	27.92 ± 0.56	...	...	...	...	130.0 ± 66.38	26.34 ± 1.32	-24.39 ± 0.21	...
A2319	1.34 ± 0.13	$22.61^{+2.12}_{-1.98}$	22.69 ± 0.13	1.18 ± 0.25	$168.6^{+11.88}_{-11.29}$	26.39 ± 0.14	0.64 ± 0.04	92.40 ± 3.15	25.40 ± 0.05	-24.64 ± 0.02	d
A2388	11.08 ± 0.79	$526.6^{+173.4}_{-139.0}$	29.52 ± 0.54	0.16 ± 0.06	$141.0^{+1.7E11}_{-1.6E11}$	28.87 ± 0.12	0.25 ± 0.04	327.4 ± 123.1	27.79 ± 0.51	-24.06 ± 0.19	...
A2469	4.08 ± 0.34	$50.30^{+3.65}_{-3.46}$	25.99 ± 0.15	...	...	...	...	31.83 ± 2.92	25.14 ± 0.24	-22.47 ± 0.06	...
A2495	3.81 ± 0.22	$157.7^{+12.03}_{-11.38}$	25.78 ± 0.15	...	...	...	...	104.2 ± 9.91	25.02 ± 0.17	-24.61 ± 0.05	...
A2506	4.06 ± 0.17	$23.76^{+0.67}_{-0.66}$	23.81 ± 0.06	...	...	...	...	16.66 ± 0.59	23.14 ± 0.07	-22.61 ± 0.02	d
A2513	3.50 ± 0.09	$23.07^{+0.41}_{-0.40}$	23.47 ± 0.04	...	...	...	...	20.22 ± 0.43	23.19 ± 0.04	-23.20 ± 0.01	...
A2516	4.21 ± 0.29	$16.82^{+0.61}_{-0.59}$	22.91 ± 0.08	...	...	...	...	17.31 ± 0.53	23.02 ± 0.05	-23.38 ± 0.02	...
A2524	5.11 ± 0.36	$39.90^{+1.74}_{-1.69}$	24.37 ± 0.09	...	...	...	...	32.46 ± 2.48	23.96 ± 0.18	-23.73 ± 0.04	...

A2558	6.25 ± 0.39	$79.90^{+5.94}_{-5.63}$	26.25 ± 0.15	...	...	...	...	55.86 ± 12.99	25.46 ± 0.59	-23.32 ± 0.11	...
A2572	8.43 ± 0.47	$109.3^{+10.50}_{-9.80}$	26.67 ± 0.19	...	...	...	...	73.14 ± 24.10	25.79 ± 0.74	-23.57 ± 0.14	d
A2589	5.92 ± 0.26	$276.8^{+24.84}_{-23.27}$	27.32 ± 0.17	...	...	...	...	113.7 ± 26.69	25.45 ± 0.50	-24.14 ± 0.12	c
A2593	5.78 ± 0.47	$72.58^{+6.14}_{-5.77}$	25.41 ± 0.17	...	...	...	...	45.63 ± 6.32	24.52 ± 0.36	-23.56 ± 0.07	d
A2618	6.97 ± 0.48	$129.4^{+12.31}_{-11.49}$	26.17 ± 0.19	...	...	...	...	88.33 ± 19.27	25.32 ± 0.49	-24.50 ± 0.10	...
A2622	5.05 ± 0.21	$37.77^{+3.01}_{-2.84}$	24.35 ± 0.15	0.67 ± 0.19	$410.8^{+38.95}_{-36.36}$	28.76 ± 0.18	0.32 ± 0.04	62.06 ± 6.46	25.28 ± 0.19	-23.83 ± 0.04	...
A2625	2.82 ± 0.13	$13.16^{+0.34}_{-0.33}$	22.40 ± 0.05	...	...	...	...	13.08 ± 0.16	22.42 ± 0.02	-22.75 ± 0.01	...
A2626	4.97 ± 0.33	$61.03^{+3.34}_{-3.21}$	24.83 ± 0.11	...	...	...	...	47.21 ± 3.63	24.34 ± 0.19	-23.83 ± 0.04	d
A2630	5.87 ± 0.63	$7.17^{+0.52}_{-0.49}$	22.18 ± 0.15	...	...	...	...	7.16 ± 0.18	22.08 ± 0.04	-22.16 ± 0.02	...
A2634	4.79 ± 0.28	$56.56^{+3.38}_{-3.23}$	24.73 ± 0.13	...	...	...	...	42.75 ± 3.31	24.05 ± 0.17	-23.67 ± 0.04	bd
A2637	9.63 ± 1.09	$46.50^{+3.79}_{-3.57}$	24.82 ± 0.17	...	...	...	...	36.44 ± 7.56	24.21 ± 0.35	-23.76 ± 0.09	...
A2657	3.17 ± 0.17	$48.52^{+2.05}_{-1.99}$	24.86 ± 0.09	...	...	...	...	32.94 ± 1.36	23.98 ± 0.08	-23.04 ± 0.03	b
A2665	4.29 ± 0.15	$61.63^{+4.77}_{-4.51}$	24.81 ± 0.13	0.19 ± 0.04	$170.1^{+33.40}_{-29.11}$	27.30 ± 0.10	0.22 ± 0.04	75.08 ± 4.43	24.97 ± 0.17	-24.25 ± 0.03	...
A2666	4.79 ± 0.36	$33.19^{+1.90}_{-1.82}$	24.06 ± 0.13	...	...	...	...	27.40 ± 1.89	23.80 ± 0.14	-23.25 ± 0.04	cd
A2675	4.24 ± 0.38	$27.48^{+5.41}_{-4.71}$	23.85 ± 0.32	1.87 ± 0.31	$751.8^{+96.65}_{-88.15}$	28.28 ± 0.22	0.80 ± 0.03	430.4 ± 69.07	27.31 ± 0.28	-24.91 ± 0.10	...
A2678	5.76 ± 0.40	$9.59^{+0.74}_{-0.70}$	22.44 ± 0.15	1.02 ± 0.08	$370.7^{+14.97}_{-14.53}$	27.69 ± 0.08	0.74 ± 0.02	235.4 ± 19.22	26.89 ± 0.07	-24.04 ± 0.05	d
AWM1	4.99 ± 0.16	$14.47^{+0.33}_{-0.32}$	23.00 ± 0.05	...	...	...	...	16.51 ± 0.69	23.28 ± 0.11	-22.73 ± 0.02	bc
AWM5	6.53 ± 0.16	$58.72^{+1.98}_{-1.93}$	24.69 ± 0.07	...	...	...	...	41.67 ± 4.22	23.91 ± 0.20	-23.96 ± 0.05	...
AWM7	6.49 ± 0.17	$150.4^{+7.30}_{-7.04}$	26.22 ± 0.10	...	...	...	...	82.44 ± 16.77	24.94 ± 0.43	-24.22 ± 0.09	c
L2027	12.12 ± 1.66	$465.2^{+193.4}_{-147.3}$	29.58 ± 0.72	...	...	...	...	271.1 ± 199.8	27.66 ± 1.95	-23.85 ± 0.35	...
L2030	2.47 ± 0.11	$34.97^{+1.04}_{-1.02}$	24.28 ± 0.07	...	...	...	...	30.65 ± 0.67	23.96 ± 0.02	-22.75 ± 0.02	...
L2069	5.04 ± 0.29	$64.08^{+2.87}_{-2.77}$	24.82 ± 0.10	...	...	...	...	56.18 ± 6.74	24.43 ± 0.24	-24.34 ± 0.06	d
L2093	5.60 ± 0.55	$21.45^{+1.50}_{-1.42}$	24.00 ± 0.15	...	...	...	...	15.73 ± 1.15	23.50 ± 0.15	-22.49 ± 0.04	bd
L2211	5.34 ± 0.36	$26.18^{+1.03}_{-1.00}$	23.73 ± 0.09	...	...	...	...	21.23 ± 1.21	23.32 ± 0.11	-23.28 ± 0.03	c
L3009	77.14 ± 111.1	$3426^{+1.8E5}_{-805.4}$	34.51 ± 14.30	...	...	...	...	3446 ± 3405	30.51 ± 5.51	-23.87 ± 0.67	d
L3055	5.39 ± 0.60	$57.26^{+6.39}_{-5.90}$	25.96 ± 0.23	...	...	...	...	49.05 ± 7.94	25.73 ± 0.33	-22.96 ± 0.08	...
L3152	5.39 ± 0.22	$30.84^{+2.33}_{-2.20}$	24.09 ± 0.14	0.25 ± 0.05	$175.1^{+4.82}_{-4.73}$	27.70 ± 0.09	0.22 ± 0.03	39.91 ± 1.59	24.52 ± 0.08	-23.41 ± 0.02	...
L3186	5.38 ± 0.42	$40.78^{+2.01}_{-1.94}$	24.59 ± 0.10	...	...	...	...	32.27 ± 3.29	24.02 ± 0.19	-23.49 ± 0.05	c
MKW4	4.20 ± 0.15	$39.32^{+1.00}_{-0.98}$	23.76 ± 0.06	...	...	...	...	31.81 ± 1.12	23.29 ± 0.07	-23.46 ± 0.02	b

Table D.1: All parameters are corrected for PSF broadening, dust extinction, cosmic dimming and are K-corrected. The parameters of the single Sérsic fits (cf. Eq. 4.3) or double Sérsic fits (cf. Eq. 4.4) are given in columns (2)–(7). The errors are calculated solely from the covariance matrices of the fits. The fraction of the integrated outer Sérsic component (column 8) compared to the total galaxy light $S_2/(S_1 + S_2)$ is calculated by integrating both semimajor axis Sérsic functions out to infinite radius. Both components are assumed to have the same ellipticity profiles. The parameters from 2D profile integration are listed in columns (9)–(11). They are corrected for undetected ICL (see Sec. 5.4) and the errors are estimated from that correction. Column (12) lists the found types of accretion signatures: a = 2 BCGs, b = shells, c = tidal streams and d = multiple nuclei.

Appendix E

Host Cluster Parameters

Table E.1: Host Cluster Parameters.

Cluster	σ_C (km s^{-1})	S	r_g (kpc)	M_{sat} (g' mag)	$\log(\mathcal{M}_g)$ ($\log(\mathcal{M}_\odot)$)	v_{syst} (km s^{-1})	r_{syst} (kpc)	$\log(\rho)$ ($\log(\mathcal{M}_\odot$kpc^{-3}))	$\log(s)$ ($\log$(kpc^{-3}))	$\log(f_\mathcal{M})$ ($\log(\mathcal{M}_\odot$ kpc^{-3} km^{-3} s^3))	$\log(f_s)$ ($\log$(kpc^{-3} km^{-3} s^3))
(1)	(2)	(3)	(4)	(5)	(6)	(7)	(8)	(9)	(10)	(11)	(12)
A76	491 ± 120	...	...	-24.94 ± 0.40	...	686 ± 149.0	467	...	...	...	...
A85	1009 ± 31	314	1324 ± 195	-25.58 ± 0.40	15.07 ± 0.07	41 ± 83.5	1	5.08 ± 0.07	-6.87 ± 0.11	-3.93 ± 0.07	-15.88 ± 0.11
A150	664 ± 151	...	...	-25.59 ± 0.40	...	4 ± 194.7	34	...	...	...	...
A152	844 ± 59	...	...	-24.90 ± 1.18	...	120 ± 105.0	...	...	...	...	...
A154	988 ± 146	...	...	-25.61 ± 0.40	...	...	...	...	...	...	...
A158	...	...	...	-25.43 ± 0.55	...	...	...	...	...	...	...
A160	...	122	923 ± 100	-24.67 ± 0.40	...	...	...	...	-6.81 ± 0.10	...	...
A161	...	...	...	-25.49 ± 0.86	...	0 ± 63.6	...	...	...	...	...
A171	...	...	...	-24.00 ± 1.33	...	0 ± 63.6	...	...	...	...	...
A174	...	...	...	-25.57 ± 0.70	...	0 ± 60.8	...	...	...	...	...
A179	284 ± 100	...	...	-24.98 ± 0.53	...	...	...	...	...	...	...
A193	776 ± 62	93	968 ± 100	-25.04 ± 0.40	14.71 ± 0.06	135 ± 89.1	1	5.13 ± 0.06	-6.99 ± 0.10	-3.54 ± 0.06	-15.66 ± 0.11
A225	660 ± 272	...	...	-25.31 ± 0.81	...	13 ± 272.1	...	...	...	...	...
A240	...	...	...	-25.07 ± 0.41	...	0 ± 50.9	...	...	...	...	...
A245	...	...	...	-25.31 ± 0.96	...	...	...	...	...	...	...
A257	499 ± 42	...	...	-24.94 ± 1.57	...	89 ± 83.4	...	...	...	...	...
A260	754 ± 74	...	...	-24.38 ± 1.15	...	289 ± 92.0	...	...	...	...	...
A262	540 ± 38	150	1313 ± 100	-23.11 ± 0.93	14.52 ± 0.05	47 ± 60.1	2	4.55 ± 0.05	-7.18 ± 0.09	-3.65 ± 0.05	-15.38 ± 0.10
A292	...	...	...	-24.96 ± 0.81	...	0 ± 67.9	...	...	...	...	...
A347	627 ± 61	...	...	-23.61 ± 0.40	...	394 ± 81.2	...	...	...	...	...
A376	830 ± 59	135	1303 ± 100	-24.90 ± 1.23	14.89 ± 0.05	166 ± 80.5	75	4.93 ± 0.05	-7.21 ± 0.09	-3.83 ± 0.05	-15.97 ± 0.10
A397	638 ± 85	...	...	-24.41 ± 1.09	...	461 ± 112.3	...	...	...	...	...
A399	1224 ± 62	...	...	-25.73 ± 0.51	...	135 ± 120.4	26	...	...	...	...
A400	683 ± 39	133	887 ± 100	-24.10 ± 0.49	14.56 ± 0.06	31 ± 63.8	5	5.09 ± 0.06	-6.72 ± 0.10	-3.41 ± 0.06	-15.22 ± 0.10
A407	762 ± 62	...	...	-26.11 ± 0.44	...	187 ± 139.0	...	...	...	...	...
A426	...	254	721 ± 139	-23.88 ± 0.96	...	...	...	...	-6.17 ± 0.12	...	...
A498	...	...	...	-24.64 ± 0.56	...	0 ± 77.8	...	...	...	...	...
A505	...	...	...	-26.02 ± 0.40	...	0 ± 66.5	...	...	...	...	...
A539	833 ± 40	161	1097 ± 265	-24.34 ± 1.01	14.82 ± 0.11	...	...	5.08 ± 0.11	-6.91 ± 0.14	-3.68 ± 0.11	-15.68 ± 0.14
A553	...	...	...	-26.44 ± 0.47	...	...	...	...	...	...	...
A559	...	...	...	-25.62 ± 0.48	...	...	...	...	...	...	...
A568	687 ± 100	...	...	-25.87 ± 0.74	...	471 ± 263.4	...	...	...	...	...
A569	394 ± 25	...	...	-22.20 ± 2.78	...	...	...	...	...	...	...
A582	324 ± 56	...	...	-25.60 ± 1.02	...	182 ± 74.2	...	...	...	...	...
A592	123 ± 100	...	...	-25.93 ± 0.40	...	149 ± 65.2	...	...	...	...	...
A595	601 ± 56	...	...	-25.16 ± 1.09	...	...	...	...	...	...	...
A600	...	...	...	-25.25 ± 1.00	...	0 ± 48.1	...	...	...	...	...
A602	796 ± 61	69	1476 ± 100	-25.14 ± 0.75	14.91 ± 0.04	...	...	4.78 ± 0.04	-7.67 ± 0.09	-3.92 ± 0.04	-16.37 ± 0.10
A607	...	...	...	-25.14 ± 1.84	...	...	...	...	...	...	...
A612	...	...	...	-25.62 ± 0.89	...	...	...	...	...	...	...
A634	331 ± 25	...	...	-23.56 ± 0.40	...	218 ± 40.2	...	...	...	...	...
A671	850 ± 33	133	1314 ± 181	-25.36 ± 0.40	14.92 ± 0.06	93 ± 141.5	111	4.94 ± 0.06	-7.23 ± 0.11	-3.85 ± 0.06	-16.02 ± 0.11
A688	...	...	...	-25.54 ± 2.41	...	...	...	...	...	...	...
A690	546 ± 46	79	1512 ± 275	-25.11 ± 0.63	14.59 ± 0.09	295 ± 258.6	...	4.43 ± 0.09	-7.64 ± 0.12	-3.78 ± 0.09	-15.85 ± 0.13
A695	402 ± 52	...	...	...	...	278 ± 116.0	...	...	...	...	...
A734	...	...	...	-25.29 ± 0.92	...	...	...	...	...	...	...
A744	445 ± 920	...	...	-25.02 ± 1.40	...	21 ± 80.0	2	...	...	...	...
A757	360 ± 32	...	...	-24.60 ± 0.74	...	5 ± 46.0	...	...	...	...	...
A834	392 ± 100	...	...	...	...	397 ± 84.4	...	...	...	...	...
A999	286 ± 25	...	...	-23.69 ± 0.78	...	129 ± 39.3	...	...	...	...	...
A1003	501 ± 50	...	...	-24.75 ± 0.83	...	427 ± 82.4	...	...	...	...	...
A1016	204 ± 53	...	...	-23.73 ± 0.84	...	18 ± 30.4	...	...	...	...	...
A1020	314 ± 41	...	...	-25.26 ± 0.81	...	13 ± 68.7	481	...	...	...	...
A1056	...	...	...	-26.85 ± 0.46	...	...	...	...	...	...	...
A1066	817 ± 55	...	...	-25.55 ± 0.40	...	498 ± 79.3	...	...	...	...	...

A1100	451 ± 100	...	...	-24.57 ± 0.40	...	34 ± 58.6	...	...	...	...	...
A1108	...	...	...	...	...	...	...	...	...	...	...
A1142	757 ± 44	...	...	-24.19 ± 0.40	...	457 ± 88.1	52	...	...	...	...
A1155	277 ± 41	...	...	-23.77 ± 3.73	...	76 ± 108.3	...	...	...	...	...
A1173	...	...	...	-23.39 ± 2.52	...	...	...	...	...	...	...
A1177	331 ± 59	...	...	-23.24 ± 0.92	...	36 ± 55.5	...	...	...	...	...
A1185	758 ± 54	292	1335 ± 283	-24.86 ± 0.40	14.83 ± 0.10	730 ± 63.5	161	4.83 ± 0.10	-6.91 ± 0.13	-3.81 ± 0.10	-15.55 ± 0.13
A1187	952 ± 55	...	...	-25.04 ± 1.43	...	1317 ± 118.0	428	...	...	...	...
A1190	671 ± 43	60	1106 ± 260	-25.55 ± 0.60	14.64 ± 0.11	905 ± 73.4	...	4.88 ± 0.11	-7.35 ± 0.14	-3.60 ± 0.11	-15.83 ± 0.14
A1203	552 ± 36	...	...	-24.51 ± 0.68	...	90 ± 66.9	...	...	...	...	...
A1213	572 ± 43	154	1132 ± 246	-25.24 ± 0.40	14.51 ± 0.10	516 ± 61.9	...	4.73 ± 0.10	-6.97 ± 0.13	-3.55 ± 0.10	-15.25 ± 0.14
A1218	...	...	...	-25.90 ± 0.57	...	...	...	...	...	...	...
A1228	246 ± 23	...	...	-24.62 ± 0.40	...	...	...	...	...	...	...
A1257	1202 ± 58	...	...	-24.23 ± 0.43	...	...	...	...	...	...	...
A1270	...	...	...	-24.98 ± 1.33	...	...	...	...	...	...	...
A1275	...	...	...	-25.59 ± 0.42	...	...	...	...	...	...	...
A1279	186 ± 30	...	...	-24.08 ± 1.05	...	35 ± 42.0	...	...	...	...	...
A1314	648 ± 25	76	909 ± 100	-25.14 ± 0.40	14.52 ± 0.05	122 ± 65.8	71	5.02 ± 0.05	-7.00 ± 0.10	-3.41 ± 0.05	-15.43 ± 0.10
A1324	...	...	...	-25.81 ± 1.63	...	...	...	...	...	...	...
A1356	...	...	...	-25.95 ± 1.51	...	...	...	...	...	...	...
A1365	369 ± 61	...	...	-25.45 ± 1.11	...	195 ± 88.1	91	...	...	...	...
A1367	872 ± 42	374	1176 ± 234	-23.95 ± 1.11	14.89 ± 0.09	286 ± 62.6	354	5.06 ± 0.09	-6.64 ± 0.13	-3.76 ± 0.09	-15.46 ± 0.13
A1371	577 ± 50	...	...	...	...	...	...	...	...	...	...
A1400	332 ± 53	...	...	-25.57 ± 0.57	...	...	...	...	...	...	...
A1413	...	142	1219 ± 146	-27.39 ± 0.53	...	...	...	...	-7.11 ± 0.10	...	...
A1423	...	...	...	-24.57 ± 1.26	...	...	...	...	...	...	...
A1424	697 ± 55	...	...	-25.61 ± 0.85	...	442 ± 78.1	168	...	...	...	...
A1435	...	...	...	-24.79 ± 0.51	...	...	...	...	...	...	...
A1436	703 ± 36	...	...	-24.82 ± 1.37	...	...	...	...	...	...	...
A1452	560 ± 63	...	...	-24.71 ± 0.62	...	...	...	...	...	...	...
A1507	405 ± 48	...	...	-25.37 ± 0.40	...	414 ± 58.3	139	...	...	...	...
A1516	...	...	...	-25.08 ± 0.88	...	...	...	...	...	...	...
A1526	...	...	...	-25.47 ± 1.12	...	...	...	...	...	...	...
A1534	371 ± 55	...	...	-25.93 ± 0.40	...	25 ± 64.4	157	...	...	...	...
A1569	622 ± 1314	73	1002 ± 226	-25.02 ± 0.43	...	...	...	...	-7.14 ± 0.14	...	...
A1589	899 ± 546	...	...	-26.01 ± 0.40	...	688 ± 99.0	...	...	...	...	...
A1610	292 ± 403	...	...	-24.82 ± 0.68	...	485 ± 62.0	...	...	...	...	...
A1656	1035 ± 25	...	...	-25.02 ± 0.40	...	...	...	...	...	...	...
A1668	...	75	1426 ± 129	-25.02 ± 0.86	...	...	...	...	-7.59 ± 0.10	...	...
A1691	784 ± 45	93	1450 ± 202	-26.06 ± 0.40	14.89 ± 0.07	37 ± 80.6	45	4.78 ± 0.07	-7.52 ± 0.11	-3.90 ± 0.07	-16.20 ± 0.11
A1749	707 ± 66	92	1238 ± 243	-24.44 ± 1.07	14.73 ± 0.10	43 ± 94.3	28	4.83 ± 0.10	-7.31 ± 0.13	-3.72 ± 0.10	-15.86 ± 0.13
A1767	887 ± 31	...	...	-25.87 ± 0.45	...	44 ± 169.1	25	...	...	...	...
A1775	568 ± 60	79	993 ± 197	-25.59 ± 0.40	14.45 ± 0.10	35 ± 74.9	48	4.83 ± 0.10	-7.09 ± 0.13	-3.43 ± 0.10	-15.36 ± 0.13
A1795	861 ± 56	175	1011 ± 100	-26.05 ± 0.53	14.82 ± 0.05	222 ± 112.1	12	5.18 ± 0.05	-6.77 ± 0.10	-3.63 ± 0.05	-15.58 ± 0.10
A1800	767 ± 190	...	...	-25.46 ± 0.66	...	36 ± 93.9	83	...	...	...	...
A1809	745 ± 30	77	1105 ± 191	-26.30 ± 0.40	14.73 ± 0.08	204 ± 81.5	47	4.98 ± 0.08	-7.24 ± 0.12	-3.64 ± 0.08	-15.86 ± 0.12
A1812	...	...	...	-25.30 ± 1.25	...	...	...	...	...	...	...
A1825	1024 ± 100	...	...	-25.20 ± 0.40	...	869 ± 154.3	...	...	...	...	...
A1828	388 ± 84	...	...	-24.52 ± 1.02	...	94 ± 96.1	...	...	...	...	...
A1831	1176 ± 118	...	...	-26.03 ± 0.94	...	133 ± 118.3	51	...	...	...	...
A1890	550 ± 59	...	...	-25.45 ± 0.45	...	275 ± 63.1	236	...	...	...	...
A1899	646 ± 100	...	...	...	...	649 ± 97.2	...	...	...	...	...
A1904	772 ± 31	...	...	-25.77 ± 0.40	...	22 ± 66.0	289	...	...	...	...
A1913	636 ± 130	86	1136 ± 383	-25.64 ± 0.40	14.60 ± 0.18	...	...	4.81 ± 0.18	-7.23 ± 0.18	-3.60 ± 0.18	-15.64 ± 0.21
A1982	1325 ± 100	...	...	-24.11 ± 1.11	...	281 ± 248.8	...	...	...	...	...
A1983	541 ± 27	184	1520 ± 234	-24.07 ± 0.67	14.59 ± 0.07	...	...	4.42 ± 0.07	-7.28 ± 0.11	-3.78 ± 0.07	-15.48 ± 0.11
A2029	1222 ± 75	587	1625 ± 323	-25.63 ± 0.58	15.33 ± 0.09	215 ± 124.3	1	5.07 ± 0.09	-6.86 ± 0.13	-4.19 ± 0.09	-16.12 ± 0.13
A2052	681 ± 41	186	798 ± 281	-24.70 ± 0.47	14.51 ± 0.16	92 ± 66.5	0	5.18 ± 0.16	-6.44 ± 0.19	-3.32 ± 0.16	-14.94 ± 0.19
A2061	851 ± 28	164	1461 ± 217	-25.99 ± 0.40	14.96 ± 0.07	270 ± 74.2	176	4.85 ± 0.07	-7.28 ± 0.11	-3.94 ± 0.07	-16.07 ± 0.11
A2063	930 ± 57	189	1237 ± 264	-24.75 ± 0.40	14.97 ± 0.10	205 ± 85.9	11	5.07 ± 0.10	-7.00 ± 0.13	-3.84 ± 0.10	-15.91 ± 0.13
A2065	1286 ± 140	...	...	-26.46 ± 0.40	...	927 ± 110.0	105	...	...	...	...
A2107	629 ± 46	134	1301 ± 110	-24.21 ± 0.64	14.65 ± 0.05	182 ± 89.2	1	4.69 ± 0.05	-7.22 ± 0.10	-3.71 ± 0.05	-15.61 ± 0.10

A2122	...	99	1305 ± 100	-25.07 ± 0.40	...	...	...	...	-7.35 ± 0.09	...	...
A2147	1033 ± 33	362	1279 ± 369	-24.28 ± 1.55	15.08 ± 0.13	361 ± 68.4	0	5.13 ± 0.13	-6.76 ± 0.16	-3.91 ± 0.13	-15.80 ± 0.16
A2151	842 ± 30	336	474 ± 106	-24.93 ± 0.71	14.47 ± 0.10	385 ± 51.4	1	5.82 ± 0.10	-5.50 ± 0.13	-2.96 ± 0.10	-14.28 ± 0.14
A2152	456 ± 62	...	...	-24.70 ± 0.92	...	6 ± 77.3	63	...	...	...	...
A2162	435 ± 37	...	...	-23.82 ± 0.77	...	98 ± 57.2	49	...	...	...	...
A2197	615 ± 21	...	...	...	...	268 ± 41.8	886	...	...	...	...
A2199	819 ± 32	714	1444 ± 291	-24.50 ± 0.87	14.93 ± 0.09	229 ± 39.3	1	4.83 ± 0.09	-6.63 ± 0.13	-3.91 ± 0.09	-15.37 ± 0.13
A2247	353 ± 59	...	...	-23.94 ± 0.96	...	...	...	...	...	...	...
A2248	1224 ± 1758	...	...	-25.59 ± 0.40	...	...	...	...	...	...	...
A2255	...	457	1612 ± 260	-26.66 ± 0.46	...	...	...	...	-6.96 ± 0.11	...	...
A2256	1301 ± 42	392	1501 ± 109	-26.59 ± 0.40	15.35 ± 0.03	347 ± 91.8	143	5.19 ± 0.03	-6.94 ± 0.09	-4.15 ± 0.03	-16.28 ± 0.09
A2271	538 ± 135	...	...	-24.96 ± 0.82	...	171 ± 168.1	17	...	...	...	...
A2293	754 ± 100	...	...	...	...	...	...	...	...	...	...
A2308	...	...	...	-26.39 ± 0.40	...	0 ± 55.2	...	...	...	...	...
A2319	...	334	1651 ± 100	-25.63 ± 0.53	...	...	...	...	-7.13 ± 0.09	...	...
A2388	...	...	...	-25.05 ± 1.50	...	0 ± 50.9	...	...	...	...	...
A2469	...	...	...	-24.82 ± 1.15	...	...	...	...	...	...	...
A2495	638 ± 188	168	1506 ± 267	-26.23 ± 0.60	14.73 ± 0.16	151 ± 216.7	...	4.57 ± 0.16	-7.31 ± 0.12	-3.84 ± 0.16	-15.72 ± 0.18
A2506	...	...	...	...	...	...	...	...	...	...	...
A2513	...	...	...	-22.74 ± 1.22	...	...	...	...	...	...	...
A2516	...	...	...	...	...	...	...	...	...	...	...
A2524	627 ± 175	...	...	-26.03 ± 0.43	...	402 ± 176.1	...	...	...	...	...
A2558	...	...	...	-24.92 ± 1.02	...	0 ± 53.7	...	...	...	...	...
A2572	593 ± 36	...	...	-23.58 ± 1.73	...	...	...	...	...	...	...
A2589	872 ± 60	164	1123 ± 100	-24.45 ± 0.40	14.87 ± 0.05	48 ± 101.5	3	5.10 ± 0.05	-6.94 ± 0.10	-3.72 ± 0.05	-15.76 ± 0.10
A2593	644 ± 23	182	1216 ± 316	-24.79 ± 0.40	14.64 ± 0.12	25 ± 51.3	10	4.77 ± 0.12	-7.00 ± 0.15	-3.66 ± 0.12	-15.42 ± 0.15
A2618	...	...	...	-25.02 ± 1.88	...	0 ± 50.9	...	...	...	...	...
A2622	860 ± 121	59	1068 ± 100	-24.88 ± 1.04	14.84 ± 0.07	121 ± 120.2	55	5.13 ± 0.07	-7.31 ± 0.10	-3.67 ± 0.07	-16.12 ± 0.12
A2625	1506 ± 171	...	...	-23.82 ± 2.06	...	863 ± 239.5	2065	...	...	...	...
A2626	648 ± 53	116	1471 ± 144	-24.57 ± 1.14	14.73 ± 0.06	54 ± 82.3	2	4.61 ± 0.06	-7.44 ± 0.10	-3.83 ± 0.06	-15.87 ± 0.11
A2630	420 ± 1336	...	...	-26.28 ± 0.40	...	...	...	...	...	...	...
A2634	919 ± 45	236	1126 ± 147	-24.34 ± 0.90	14.92 ± 0.06	238 ± 79.3	24	5.14 ± 0.06	-6.78 ± 0.11	-3.75 ± 0.06	-15.67 ± 0.11
A2637	361 ± 59	...	...	-24.63 ± 1.21	...	179 ± 97.3	177	...	...	...	...
A2657	807 ± 52	61	1046 ± 100	-24.51 ± 0.48	14.77 ± 0.05	...	...	5.09 ± 0.05	-7.27 ± 0.10	-3.63 ± 0.05	-15.99 ± 0.10
A2665	...	118	1517 ± 100	-24.46 ± 0.70	...	0 ± 80.6	...	...	-7.47 ± 0.09	...	...
A2666	377 ± 47	104	728 ± 467	-22.54 ± 1.70	13.95 ± 0.34	75 ± 78.8	65	4.75 ± 0.34	-6.57 ± 0.35	-2.98 ± 0.34	-14.30 ± 0.36
A2675	372 ± 156	...	...	-24.55 ± 1.79	...	609 ± 125.0	176	...	...	...	...
A2678	361 ± 156	...	...	...	...	...	...	...	...	...	...
AWM1	...	116	1397 ± 225	-24.11 ± 0.40	...	...	...	...	-7.37 ± 0.11	...	...
AWM5	...	88	1204 ± 100	-24.32 ± 1.09	...	...	...	...	-7.30 ± 0.10	...	...
AWM7	...	193	1171 ± 208	-23.66 ± 0.40	...	...	...	...	-6.92 ± 0.12	...	...
L2027	...	...	...	-25.29 ± 0.73	...	...	...	...	...	...	...
L2030	...	...	...	-22.97 ± 1.43	...	...	...	...	...	...	...
L2069	...	...	...	-24.48 ± 1.78	...	...	...	...	...	...	...
L2093	...	...	...	-25.59 ± 0.40	...	...	...	...	...	...	...
L2211	...	...	...	-24.48 ± 0.67	...	...	...	...	...	...	...
L3055	...	...	...	-24.25 ± 1.44	...	...	...	...	...	...	...
L3152	...	...	...	-23.68 ± 0.40	...	...	...	...	...	...	...
L3186	...	...	...	...	...	...	...	...	...	...	...
MKW4	...	...	...	-22.56 ± 1.09	...	...	...	...	...	...	...

Table E.1: Host cluster parameters. The columns show the velocity dispersion of the cluster galaxies $\sigma_{\rm C}$ (2), richness S, i.e., number of cluster galaxies (3), gravitational radius $r_{\rm g}$ (4), integrated absolute brightness of all cluster galaxies $M_{\rm sat}$ excluding the BCG+ICL (5), gravitational mass $\mathcal{M}$ (6), systemic velocity offset $v_{\rm syst}$ (7), radial X-ray emission peak offset $r_{\rm syst}$ (8), mass density ρ (9), number density of cluster galaxies s (10), mass phase space density $f_{\mathcal{M}}$ (11), and number phase space density of the cluster galaxies $f_{\rm s}$ (12).

Appendix F

BCG/ICL vs. host cluster parameter correlations

X	Y	Slope α	Offset β	R
(1)	(2)	(3)	(4)	(5)
$M_{BCG+ICL}$	σ_C	-3.89E+02 ± 5.18E+01	-8557.01	-0.40
$M_{BCG+ICL}$	log(S)	-3.54E-01 ± 7.80E-02	-6.34	-0.17
$M_{BCG+ICL}$	$\log(r_g)$	-1.37E-01 ± 2.75E-02	-0.23	-0.39
$M_{BCG+ICL}$	M_{sat}	1.19E+00 ± 1.17E-01	3.36	0.43
$M_{BCG+ICL}$	$\log(\mathcal{M}_g)$	-3.55E-01 ± 6.58E-02	6.26	-0.46
$M_{BCG+ICL}$	$\log(\lvert v_{syst}\rvert)$	4.10E-01 ± 9.59E-02	12.22	0.13
$M_{BCG+ICL}$	$\log(\lvert r_{syst}\rvert)$	1.27E+00 ± 2.87E-01	32.01	0.22
$M_{BCG+ICL}$	$\log(\rho)$	-3.28E-01 ± 1.01E-01	-2.93	-0.12
$M_{BCG+ICL}$	log(s)	4.97E-01 ± 1.28E-01	4.91	0.13
$M_{BCG+ICL}$	$\log(f_{\mathcal{M}})$	3.57E-01 ± 6.98E-02	4.85	0.49
$M_{BCG+ICL}$	$\log(f_s)$	6.34E-01 ± 1.31E-01	-0.46	0.51
M_{ICL}^{MT}	σ_C	-3.20E+02 ± 4.42E+01	-6825.41	-0.38
M_{ICL}^{MT}	log(S)	-3.11E-01 ± 6.89E-02	-5.24	-0.17
M_{ICL}^{MT}	$\log(r_g)$	-1.21E-01 ± 2.43E-02	0.20	-0.39
M_{ICL}^{MT}	M_{sat}	9.81E-01 ± 9.56E-02	-1.93	0.44
M_{ICL}^{MT}	$\log(\mathcal{M}_g)$	-3.10E-01 ± 5.75E-02	7.39	-0.46
M_{ICL}^{MT}	$\log(\lvert v_{syst}\rvert)$	3.45E-01 ± 8.04E-02	10.60	0.13
M_{ICL}^{MT}	$\log(\lvert r_{syst}\rvert)$	1.10E+00 ± 2.47E-01	27.75	0.22
M_{ICL}^{MT}	$\log(\rho)$	-2.95E-01 ± 8.99E-02	-2.08	-0.12

M_{ICL}^{MT}	log(s)	4.36E-01 ± 1.13E-01	3.36	0.13
M_{ICL}^{MT}	$\log(f_{\mathcal{M}})$	3.11E-01 ± 6.12E-02	3.71	0.49
M_{ICL}^{MT}	$\log(f_s)$	5.53E-01 ± 1.14E-01	-2.49	0.51
M_{ICL}^{SB25}	σ_C	-2.86E+02 ± 4.02E+01	-5891.93	-0.36
M_{ICL}^{SB25}	log(S)	-2.70E-01 ± 5.92E-02	-4.13	-0.20
M_{ICL}^{SB25}	$\log(r_g)$	-1.05E-01 ± 2.11E-02	0.63	-0.37
M_{ICL}^{SB25}	M_{sat}	8.84E-01 ± 8.70E-02	-4.66	0.42
M_{ICL}^{SB25}	$\log(\mathcal{M}_g)$	-2.73E-01 ± 4.99E-02	8.40	-0.44
M_{ICL}^{SB25}	$\log(\lvert v_{syst}\rvert)$	2.85E-01 ± 6.94E-02	9.01	0.06
M_{ICL}^{SB25}	$\log(\lvert r_{syst}\rvert)$	9.20E-01 ± 2.02E-01	23.00	0.22
M_{ICL}^{SB25}	$\log(\rho)$	-2.68E-01 ± 8.07E-02	-1.31	-0.12
M_{ICL}^{SB25}	log(s)	3.77E-01 ± 9.80E-02	1.75	0.10
M_{ICL}^{SB25}	$\log(f_{\mathcal{M}})$	2.74E-01 ± 5.34E-02	2.70	0.48
M_{ICL}^{SB25}	$\log(f_s)$	4.88E-01 ± 1.00E-01	-4.29	0.48
M_{ICL}^{SB28}	σ_C	-2.25E+02 ± 3.32E+01	-4261.98	-0.29
M_{ICL}^{SB28}	log(S)	-1.93E-01 ± 4.11E-02	-2.12	-0.28
M_{ICL}^{SB28}	$\log(r_g)$	-7.47E-02 ± 1.45E-02	1.41	-0.41
M_{ICL}^{SB28}	M_{sat}	6.88E-01 ± 6.74E-02	-9.83	0.40
M_{ICL}^{SB28}	$\log(\mathcal{M}_g)$	-1.98E-01 ± 3.88E-02	10.34	-0.42
M_{ICL}^{SB28}	$\log(\lvert v_{syst}\rvert)$	1.86E-01 ± 4.80E-02	6.55	0.04
M_{ICL}^{SB28}	$\log(\lvert r_{syst}\rvert)$	6.83E-01 ± 1.56E-01	16.86	0.20
M_{ICL}^{SB28}	$\log(\rho)$	-1.30E-01 ± 4.54E-02	2.03	-0.03
M_{ICL}^{SB28}	log(s)	2.70E-01 ± 6.97E-02	-1.01	0.08
M_{ICL}^{SB28}	$\log(f_{\mathcal{M}})$	1.99E-01 ± 4.01E-02	0.75	0.49
M_{ICL}^{SB28}	$\log(f_s)$	3.53E-01 ± 8.00E-02	-7.75	0.39
M_{ICL}^{DV}	σ_C	-2.76E+02 ± 3.98E+01	-5642.01	-0.35
M_{ICL}^{DV}	log(S)	-2.70E-01 ± 6.79E-02	-4.07	-0.21
M_{ICL}^{DV}	$\log(r_g)$	-1.04E-01 ± 2.69E-02	0.66	-0.21
M_{ICL}^{DV}	M_{sat}	8.28E-01 ± 9.94E-02	-6.09	0.33
M_{ICL}^{DV}	$\log(\mathcal{M}_g)$	-2.97E-01 ± 6.75E-02	7.90	-0.36
M_{ICL}^{DV}	$\log(\lvert v_{syst}\rvert)$	-1.73E-01 ± 5.09E-02	-1.51	-0.02
M_{ICL}^{DV}	$\log(\lvert r_{syst}\rvert)$	9.41E-01 ± 2.67E-01	23.39	0.11
M_{ICL}^{DV}	$\log(\rho)$	-2.95E-01 ± 9.24E-02	-1.90	-0.14

M_{ICL}^{DV}	log(s)	5.60E-02 ± 6.03E-02	-5.75	-0.04
M_{ICL}^{DV}	$\log(f_{\mathcal{M}})$	2.93E-01 ± 7.12E-02	3.08	0.43
M_{ICL}^{DV}	$\log(f_s)$	5.18E-01 ± 1.22E-01	-3.68	0.40
$M_{ICL}^{S\times}$	σ_C	-3.32E+02 ± 1.08E+02	-6976.68	-0.14
$M_{ICL}^{S\times}$	log(S)	-3.91E-01 ± 1.32E-01	-6.96	-0.11
$M_{ICL}^{S\times}$	$\log(r_g)$	-1.41E-01 ± 5.20E-02	-0.20	-0.21
$M_{ICL}^{S\times}$	M_{sat}	9.52E-01 ± 1.96E-01	-3.07	0.30
$M_{ICL}^{S\times}$	$\log(\mathcal{M}_g)$	-2.74E-01 ± 8.87E-02	8.41	-0.41
$M_{ICL}^{S\times}$	$\log(\lvert v_{syst}\rvert)$	-4.54E-01 ± 1.79E-01	-7.96	-0.41
$M_{ICL}^{S\times}$	$\log(\lvert r_{syst}\rvert)$	1.01E+00 ± 4.90E-01	24.90	-0.21
$M_{ICL}^{S\times}$	$\log(\rho)$	-2.39E-01 ± 1.03E-01	-0.55	-0.30
$M_{ICL}^{S\times}$	log(s)	-3.91E-01 ± 1.92E-01	-16.12	-0.03
$M_{ICL}^{S\times}$	$\log(f_{\mathcal{M}})$	2.49E-01 ± 9.20E-02	2.09	0.31
$M_{ICL}^{S\times}$	$\log(f_s)$	4.70E-01 ± 2.18E-01	-4.82	0.31
$\log(r_e)$	σ_C	6.08E+02 ± 9.31E+01	-415.44	0.28
$\log(r_e)$	log(S)	4.93E-01 ± 9.98E-02	1.17	0.49
$\log(r_e)$	$\log(r_g)$	1.91E-01 ± 4.53E-02	2.68	0.12
$\log(r_e)$	M_{sat}	-1.84E+00 ± 2.59E-01	-21.68	-0.03
$\log(r_e)$	$\log(\mathcal{M}_g)$	4.81E-01 ± 1.14E-01	13.79	0.42
$\log(r_e)$	$\log(\lvert v_{syst}\rvert)$	-5.51E-01 ± 1.32E-01	3.45	-0.12
$\log(r_e)$	$\log(\lvert r_{syst}\rvert)$	-1.73E+00 ± 4.02E-01	4.89	-0.36
$\log(r_e)$	$\log(\rho)$	4.58E-01 ± 1.41E-01	4.01	0.23
$\log(r_e)$	log(s)	6.79E-01 ± 1.79E-01	-8.43	0.33
$\log(r_e)$	$\log(f_{\mathcal{M}})$	-4.84E-01 ± 1.19E-01	-2.72	-0.40
$\log(r_e)$	$\log(f_s)$	-8.59E-01 ± 2.35E-01	-13.92	-0.18
SB_e	σ_C	1.89E+02 ± 3.14E+01	-4056.48	0.19
SB_e	log(S)	1.51E-01 ± 3.47E-02	-1.68	0.20
SB_e	$\log(r_g)$	5.87E-02 ± 1.30E-02	1.58	0.25
SB_e	M_{sat}	-5.53E-01 ± 6.32E-02	-11.07	-0.25
SB_e	$\log(\mathcal{M}_g)$	1.54E-01 ± 3.65E-02	10.82	0.33
SB_e	$\log(\lvert v_{syst}\rvert)$	-1.65E-02 ± 2.43E-02	2.87	-0.01
SB_e	$\log(\lvert r_{syst}\rvert)$	-5.46E-01 ± 1.36E-01	15.39	-0.22
SB_e	$\log(\rho)$	8.58E-02 ± 3.32E-02	2.74	0.10

SB_e	log(s)	-1.69E-01 ± 4.71E-02	-2.74	-0.01
SB_e	$\log(f_{\mathcal{M}})$	-1.55E-01 ± 3.72E-02	0.27	-0.37
SB_e	$\log(f_s)$	-2.76E-01 ± 6.82E-02	-8.61	-0.32
log(n)	σ_C	-1.11E+03 ± 2.35E+02	1557.29	-0.01
log(n)	log(S)	1.09E+00 ± 3.05E-01	1.29	0.21
log(n)	$\log(r_g)$	4.45E-01 ± 1.35E-01	2.71	0.14
log(n)	M_{sat}	-3.89E+00 ± 6.13E-01	-21.88	-0.10
log(n)	$\log(\mathcal{M}_g)$	1.20E+00 ± 3.69E-01	13.75	0.25
log(n)	$\log(\lvert v_{syst}\rvert)$	1.14E+00 ± 2.92E-01	1.56	0.10
log(n)	$\log(\lvert r_{syst}\rvert)$	-6.64E-01 ± 7.10E-01	2.14	0.04
log(n)	$\log(\rho)$	1.22E+00 ± 4.49E-01	3.88	0.11
log(n)	log(s)	1.04E+00 ± 4.00E-01	-7.92	0.05
log(n)	$\log(f_{\mathcal{M}})$	-1.22E+00 ± 3.97E-01	-2.68	-0.22
log(n)	$\log(f_s)$	-2.14E+00 ± 7.05E-01	-13.82	-0.18
$\log(r_\times)$	σ_C	-5.67E+02 ± 1.42E+02	1567.66	-0.30
$\log(r_\times)$	log(S)	-5.74E-01 ± 1.99E-01	3.06	-0.30
$\log(r_\times)$	$\log(r_g)$	2.06E-01 ± 7.35E-02	2.71	0.37
$\log(r_\times)$	M_{sat}	1.04E+00 ± 3.45E-01	-26.76	0.04
$\log(r_\times)$	$\log(\mathcal{M}_g)$	-1.73E-01 ± 1.43E-01	15.04	0.09
$\log(r_\times)$	$\log(\lvert v_{syst}\rvert)$	-8.57E-01 ± 3.44E-01	3.99	-0.24
$\log(r_\times)$	$\log(\lvert r_{syst}\rvert)$	1.94E+00 ± 8.72E-01	-1.86	0.13
$\log(r_\times)$	$\log(\rho)$	-3.58E-01 ± 1.50E-01	5.56	-0.41
$\log(r_\times)$	log(s)	-7.99E-01 ± 2.34E-01	-5.73	-0.58
$\log(r_\times)$	$\log(f_{\mathcal{M}})$	-3.71E-01 ± 1.95E-01	-3.07	-0.29
$\log(r_\times)$	$\log(f_s)$	-7.05E-01 ± 2.49E-01	-14.58	-0.50
$SB_\times$	σ_C	-1.42E+02 ± 3.43E+01	4279.70	-0.40
$SB_\times$	log(S)	-1.48E-01 ± 4.46E-02	5.86	-0.48
$SB_\times$	$\log(r_g)$	5.31E-02 ± 2.03E-02	1.71	0.25
$SB_\times$	M_{sat}	3.42E-01 ± 1.01E-01	-33.84	0.06
$SB_\times$	$\log(\mathcal{M}_g)$	-1.02E-01 ± 5.17E-02	17.34	-0.13
$SB_\times$	$\log(\lvert v_{syst}\rvert)$	-2.09E-01 ± 8.48E-02	7.90	-0.28
$SB_\times$	$\log(\lvert r_{syst}\rvert)$	4.56E-01 ± 1.95E-01	-10.26	0.17
$SB_\times$	$\log(\rho)$	-8.92E-02 ± 3.31E-02	7.23	-0.54

$\mathrm{SB}_{\times}$	$\log(\mathrm{s})$	-2.06E-01 ± 5.76E-02	-1.84	-0.63
$\mathrm{SB}_{\times}$	$\log(\mathrm{f}_{\mathcal{M}})$	-3.88E-02 ± 3.24E-02	-2.69	-0.08
$\mathrm{SB}_{\times}$	$\log(\mathrm{f_s})$	-1.76E-01 ± 7.00E-02	-11.29	-0.36
σ_0	σ_{C}	6.52E+00 ± 1.38E+00	-1213.19	0.19
σ_0	$\log(\mathrm{S})$	5.23E-03 ± 1.76E-03	0.69	0.17
σ_0	$\log(\mathrm{r_g})$	-3.18E-05 ± 4.22E-04	3.07	-0.07
σ_0	$\mathrm{M_{sat}}$	-1.81E-02 ± 3.57E-03	-19.75	-0.15
σ_0	$\log(\mathcal{M}_{\mathrm{g}})$	4.88E-03 ± 1.56E-03	13.32	0.24
σ_0	$\log(\lvert\mathrm{v_{syst}}\rvert)$	-5.07E-03 ± 1.47E-03	3.89	0.03
σ_0	$\log(\lvert\mathrm{r_{syst}}\rvert)$	-2.07E-02 ± 5.23E-03	7.60	-0.11
σ_0	$\log(\rho)$	4.79E-03 ± 1.50E-03	3.56	0.31
σ_0	$\log(\mathrm{s})$	7.62E-03 ± 2.69E-03	-9.18	0.33
σ_0	$\log(\mathrm{f}_{\mathcal{M}})$	-4.97E-03 ± 1.81E-03	-2.22	-0.10
σ_0	$\log(\mathrm{f_s})$	-8.54E-03 ± 3.15E-03	-13.09	-0.01

Table F.1: Correlations between BCG/ICL and host cluster parameters. The correlations are in the form of $Y = \alpha X + \beta$. Orthogonal distance regression was applied to find the best-fit parameters. The Spearman coefficient R for each correlation is given in column (5). The BCG/ICL parameters are given in column (1). They are: absolute brightness of the BCGs+ICL $M_{\mathrm{BCG+ICL}}$ [g' mag], absolute brightness of the ICL only M_{ICL} [g' mag], dissected via the total magnitude threshold of –21.85 g' mag $M_{\mathrm{ICL}}^{\mathrm{MT}}$, via the surface brightness threshold of 25 g' mag $M_{\mathrm{ICL}}^{\mathrm{SB25}}$, via the surface brightness threshold of 28 g' mag $M_{\mathrm{ICL}}^{\mathrm{SB28}}$, via the light excess above the inner de Vaucouleurs fit $M_{\mathrm{ICL}}^{\mathrm{DV}}$, and via the double Sérsic fit $M_{\mathrm{ICL}}^{\mathrm{S}\times}$. The methods are explained in Sec. 7.4. The BCG/ICL parameters are measured along the major axis. They are: effective radius r_{e} [kpc], effective surface brightness SB_{e} [g' mag arcsec^{-2}], Sérsic index n (for SS BCGs), transition radius $r_{\times}$ [kpc] and transition surface brightness $SB_{\times}$ [g' mag arcsec^{-2}] between the two Sérsic profiles of DS BCGs, and central velocity dispersion (data taken from Lauer et al. 2014). The cluster parameters are given in column (2). They are: velocity dispersion of the cluster galaxies σ_{C} [km s^{-1}] (taken from Lauer et al. 2014), richness S, i.e., number of satellite galaxies, gravitational radius r_{g} [kpc], integrated absolute brightness of all satellite galaxies (excluding the BCG+ICL) M_{sat} [g' mag], gravitational mass $\mathcal{M}$ [M$_{\odot}$], absolute systemic velocity offset $|v_{\mathrm{syst}}|$ (data taken from Lauer et al. 2014), radial X-ray emission peak offset r_{syst} (data also taken from Lauer et al. 2014), mass density ρ [$M_{\odot}$ kpc^{-3}], number density of satellite galaxies s [kpc^{-3}], mass phase space density $f_{\mathcal{M}}$ [M$_{\odot}$ kpc^{-3} km^{-3} s^{3}], and number phase space density of the satellite galaxies f_{s} [kpc^{-3} km^{-3} s^{3}].

Acknowledgments

I wish to thank Prof. Dr. Ralf Bender, who was my supervising professor, for making this thesis possible. His patience and trust allowed me to follow creative approaches to many problems that I have encountered on the way. His foresight on the significance of effects like background subtraction errors and PSF broadening helped me a lot to keep the systematics in check.

I also want to thank Dr. Ulrich Hopp. His calm, focused and appreciating mind gave me a lot of reassurance during the years. As the scientific director of the Wendelstein observatory, he allowed me to use 300+ hours of telescope time during the best dark and photometric conditions. My gratitude is naturally also directed towards the University Observatory Munich for providing the amazing opportunity to gain observing experience first-hand.

Michael Schmidt and Christoph Ries have done most of the observations that have built the foundation for this work. Special thanks are directed to Michael, who trained me to become an observer back in 2014. Also, from studying the amazing complexity of his telescope operating scripts, I have leaned a lot of useful bash programming tricks. Much of that knowledge went into the development of the WWFI data reduction pipeline.

I also wish to thank Bianca Neureiter who developed the background matching program `skyalign` during her bachelor's thesis and which is now permanently implemented into the WWFI pipeline. She also verified the WWFI surface brightness profile of one BCG using Wendelstein 40cm Telescope data during her master's thesis. Her company and support made the observing runs both, at Wendelstein and McDonald Observatory really enjoyable.

Furthermore, I would like to thank Christian Obermeier for the competitive challenges that we had. Be it noise reduction, sky subtraction or just creating colorful pictures. We always ended with the best (average) of both worlds. I have learned a lot from you about image processing.

I also appreciate the many fruitful discussions with Dr. Stella Seitz, Dr. Rhea-Silvia Remus as well as the constructive feedback on the paper by John Kormendy and Tod Lauer.

Last but not least, my thanks go to the rest of the Wendelstein Team: Arno, Claus, Christoph, Wolfgang, Hanna, Vanessa, Jana, Marco, Raphael, Benjamin, Flo, and Anna. I feel proud to be part of such an amazing team.